Forschungszentrum Karlsruhe
Technik und Umwelt

Wissenschaftliche Berichte
FZKA 5572

Cold Lower End Test CORA-10: Test Results

S. Hagen, P. Hofmann, V. Noack, L. Sepold, G. Schanz, G. Schumacher

Hauptabteilung Ingenieurtechnik
Institut für Materialforschung
Institut für Neutronenphysik und Reaktortechnik
Projekt Nukleare Sicherheitsforschung

November 1997

Forschungszentrum Karlsruhe
Technik und Umwelt
Wissenschaftliche Berichte

FZKA 5572

Cold Lower End Test CORA-10: Test Results

S. Hagen, P. Hofmann, V. Noack, L. Sepold,
G. Schanz, G. Schumacher

Hauptabteilung Ingenieurtechnik
Institut für Materialforschung
Institut für Neutronenphysik und Reaktortechnik
Projekt Nukleare Sicherheitsforschung

Forschungszentrum Karlsruhe GmbH, Karlsruhe
1997

Als Manuskript gedruckt
Für diesen Bericht behalten wir uns alle Rechte vor

Forschungszentrum Karlsruhe GmbH
Postfach 3640, 76021 Karlsruhe

Mitglied der Hermann von Helmholtz-Gemeinschaft
Deutscher Forschungszentren (HGF)

ISSN 0947-8620

ABSTRACT

PWR Cold Lower End Test CORA-10: Test Results

The CORA out-of-pile experiments are part of the international Severe Fuel Damage (SFD) program. They should provide information on the damage development of Light Water Reactor (LWR) fuel elements in the temperature range from 1200°C to 2400°C.

In test CORA-10 it was intended to simulate TMI-2 accident conditions with the lower end of the bundle in water. The aim of this experiment was to obtain information on the solidification of molten relocated material and the formation of blockages at the lower end of the core above the water level. Due to safety restrictions it was however not possible to perform the test as initially planned. Instead of increasing the water level to 250 mm elevation, the bundle insulation was removed up to 300 mm elevation, which should cause a strong axial temperature gradient. To simulate the evaporation from the water an additional steam flow rate of 2 g/s was added.

Due to the strong heat losses in the lower part of the bundle the temperature escalation was restricted to the upper part of the bundle, above 500 mm elevation. The escalation started in the range 750 mm to 950 mm and spread down to 550 mm elevation within about 200 s. The highest temperature of the bundle, 2100°C, was reached at 1050 mm elevation at the end of the transient. As a consequence, the damage was concentrated to the upper half of the bundle. The damage of the bundle started with the failure of the absorber rods at 1230°C. At the end of the test the absorber rods were completely destroyed above 250 mm elevation. The total hydrogen production was about 180 g.

The molten material which formed in the upper part of the bundle relocated and solidified in the lower part by forming a blockage between 310 mm and 430 mm bundle elevation. Test CORA-10 confirms that the blockage formation is determined mainly by the axial temperature gradient and the amount of molten and relocated material. No obstacles, like spacers, are necessary to stop the relocation of the melt.

Zusammenfassung

DWR Versuch CORA-10 mit kühlem unteren Bündelende: Testergebnisse

Die CORA-Out-of-pile-Experimente wurden im Rahmen des international geplanten "Severe-Fuel-Damage"-Programms durchgeführt. Sie sollten Informationen über die Schadensmechanismen bei Leichtwasser-Reaktor-(LWR)-Brennelementen im Temperaturbereich von 1200°C bis 2400°C liefern.

Im Versuch CORA-10 sollten die Bedingungen des TMI-2-Störfalls simuliert werden, bei dem sich zeitweilig nur das untere Bündelende im Wasser befand. Insbesondere sollte das Experiment Informationen liefern über das Erstarrungsverhalten von verlagerter Schmelze und die Ausbildung von möglichen Blockaden im unteren Bündelbereich oberhalb des Wasserspiegels. Aufgrund von Sicherheitsüberlegungen wurde der Versuch aber nicht, wie ursprünglich geplant, mit einem Wasserspiegel in 250 mm Bündelhöhe durchgeführt. Um den starken axialen Temperaturgradienten zu simulieren, wurde die Bündelisolation bis zu einer Höhe von 300 mm entfernt. Die Verdampfung des Flutwassers wurde durch einen zusätzlichen Dampfstrom von 2 g/s simuliert.

Aufgrund der starken Wärmeverluste im unteren Bereich des Bündels beschränkte sich die Temperatureskalation auf den oberen Bereich des Bündels, d.h. oberhalb 550 mm. Die Eskalation begann im Bereich von 750 mm bis 950 mm Bündelhöhe und breitete sich in ca. 200 s nach unten bis zu einer Höhe von 550 mm aus. Die höchste Temperatur im Bündel, 2100°C, wurde in der Bündelhöhe 1050 mm am Ende des Versuchs erreicht. Aufgrund der axialen Temperaturverteilung konzentrierte sich die Zerstörung des Bündels auf die obere Hälfte. Die Zerstörung des Bündels begann mit dem Versagen der Absorberstäbe bei 1230°C. Am Ende des Versuchs waren die Absorberstäbe oberhalb 250 mm vollkommen zerstört. Die beim Versuch erzeugte Wasserstoffmenge betrug ca. 180 g.

Die im oberen Bereich des Bündels entstandene Schmelze verlagerte sich und erstarrte unter Bildung einer Blockade zwischen 310 mm und 430 mm Bündelhöhe. Der Versuch CORA-10 bestätigt, daß die Blockadenbildung im Bündel im wesentlichen durch die axiale Temperaturverteilung und die Schmelzmenge bestimmt wird. Die untere Grenze der Blockade bildet sich unabhängig von Hindernissen, wie z.B. Abstandhaltern, aus.

Contents

1. Introduction

The TMI-2 accident has demonstrated that a severe fuel damage transient will not necessarily escalate to an uncontrolled core melt down accident if the design basis accident limits are exceeded. Therefore, comprehensive research programs have been initiated in various countries to investigate the relevant fuel rod bundle damage mechanisms that occur in an uncovered core, after an increase of temperature.

In the Federal Republic of Germany at the Forschungszentrum Karlsruhe (FZK) the Severe Fuel Damage (SFD) Program is now co-ordinated by the project Nuclear Safety Research (PSF) as successor of Project Nuclear Safety (PNS) and LWR Safety Project Group (PRS). As part of this program, out-of-pile experiments (the CORA-Program) were conducted at the Hauptabteilung Ingenieurtechnik (HIT), These experiments have been designed to provide information on the behaviour of Light water Reactor (LWR) fuel elements under severe fuel damage (SFD) conditions, up to meltdown. The results of the out-of-pile experiments can be used for the assessment of the SFD computer codes.

Within the framework of international co-operation the out-of-pile experiments are contributing confirmatory and complementary information to the results obtained from the limited number of inpile tests. The investigation of the basic phenomena of the damage process is supported by separate-effect tests.

The most important aspects concerning fuel rod failure and subsequent core degradation are the chemical interactions amongst the fuel element components in competition with the oxidation of the cladding in steam, which causes also the temperature escalation. Melt formation starts around 1200°C by chemical interactions of the Inconel spacer grids and absorber materials (Ag, In, Cd) for PWRs and B_4C/stainless steel for BWRs with the Zircaloy cladding. The dissolution of the UO_2 pellets by liquid Zircaloy starts far below the UO_2 melting point.

Melt formation, relocation, blockage formation and finally fragmentation of fuel elements during reflooding characterise the degraded core and the potential of long term coolability. Furthermore the influence of internal pressure of the fuel rods (ballooning and bursting) and external pressure of the system (solid contact between pellets and cladding) on the bundle meltdown behaviour was investigated.

Further on, the investigation of the influence of pre-oxidation, initial heat-up rate, steam availability, water level in the bundle and bundle size was included in the program. The damage behaviour of VVER fuel elements was the subject of the last two CORA-tests.

The tests performed in the CORA-facility are listed in the test matrix (Table 1). The original test matrix was directed towards the behaviour of PWR fuel elements only. In 1988 discussion showed that in most countries using nuclear energy, information on the behaviour of BWRs in severe accident conditions was needed. In consequence, five planned PWR experiments were replaced by BWR tests in the revised test matrix. Also the original sequence of tests was changed, as one can see from the test numbers.

In this paper, the results of test CORA-10 are reported and discussed. The experiment CORA-10 should investigate the blockage behaviour of a bundle with its lower end in water. Due to safety limitations, we could not run the test - as originally planned - with a water level increased to 250 mm elevation. Instead the cold lower end was simulated by removing the insulation around the shroud up to 300 mm and simulating the evaporation of water by a steam input of two g/s. Otherwise the bundle arrangement and test procedure was the normal one.

2. Description of the CORA test facility

The CORA out-of-pile facility was designed to investigate the behaviour of LWR fuel elements under severe fuel damage accident conditions. In the experiments the decay heat was simulated by electrical heating. Great emphasis was placed on the

fact that the test bundles contain the original materials used in light-water reactor fuel elements to investigate the different material interactions.

Pellets, cladding, grid spacers, absorber rods and channel box walls were typical of those of the investigated LWRs with respect to their compositions and radial dimensions.

The CORA facility was situated within the reactor hall of the now disused FR2 reactor at the Nuclear Research Center Karlsruhe. Figure 1 gives a simplified flow diagram of the facility. The geometrical arrangement of the different CORA components is given in Figure 2.

The central part of the facility was the fuel rod bundle. The bundle was enclosed in a Zry shroud with ZrO_2 fibre insulation. A high temperature radiation shield surrounded the bundle and shroud assembly, leaving an annular space for introduction of the quench cylinder. The bundle was connected to the power supply system at the upper and lower ends.

Below the bundle was the quench unit with a water filled quench cylinder, which can be raised around the bundle at a controlled speed. The cylinder was guided by three rods, which also connected the electric power to the bundle lower end. At the beginning of the test the water level was 220 mm below the "zero elevation" of the bundle. The "zero elevation" corresponds to the lower end of the pellets in the heated rods.

The bundle upper end was fixed in the bundle head plate. The plate was connected by a funnel shaped tube to the surge condenser. The surge condenser was double-walled, leaving access to the bundle end fittings above the bundle head funnel.

The steam was produced in the steam generator, superheated and guided to the lower end of the bundle, entering at "zero elevation": The steam not consumed within the bundle was condensed in two parallel condensers and the hydrogen produced was fed into the off-gas system after dilution by air to a low H_2 concentration.

Bundle Design

The location of the bundle within the facility is shown in Figures 2 and 4. Details of the high temperature shield are given in Figures 3 and 4. The arrangement of the fuel rod simulators within the bundle is given in Figure 5. Figure 6a presents the individual main components of the bundle; i.e. the heated and unheated fuel rods and the (Ag, In, Cd) absorber rods. Characteristic data of the bundle are given in Tables 2-4.

Fuel rod simulator

Two types of fuel rod simulators are used: electrically heated rods and unheated solid rods. Altogether 25 rods made up of 16 heated and 7 unheated rods and two absorber rods have been used. Vertical cross sections of the rods are shown in Fig. 6a. The heated fuel rod simulator has a standard PWR Zircaloy cladding tube. The central internal heater consists of a 6 mm diameter tungsten rod surrounded by UO_2 annular pellets. The tungsten heater has an effective length of 1024 mm. At the top and bottom the tungsten heater is screwed into Mo-electrodes of 300 mm length which fit directly into the Zircaloy cladding. The molybdenum electrodes are connected to copper electrodes. The upper electrode consists of 669 mm copper and the lower electrode of 189 mm copper. The electrodes have a diameter of 8.6 mm. The diameter of the copper electrodes is reduced from 8.6 mm to 7.5 mm for 82 mm at the top and for 155 mm at the bottom. The rod arrangement is insulated from the Zircaloy cladding by a flame-sprayed ZrO_2 layer. The Zircaloy cladding is sealed to the copper electrodes by swage-lock fittings with an insulating sleeve. To the upper and lower copper electrodes flexible copper power cables are connected. The fuel rod simulator is screwed into the bundle flange from the top, sealing it hermetically. The bundle flange thus gives the fixed point for the axial thermal movement of the rod.

The resistivities R of tungsten, molybdenum and copper are given respectively in the following three equations:

$$R_w = 2.61 \bullet 10^{-2} + 2.63 \bullet 10^{-4} T_w + 2.20 \bullet 10^{-8} T^2_w$$

$$R_{Mo} = 2.29 \bullet 10^{-2} + 5.36 \bullet 10^{-5} T_{mo} + 1.38 \bullet 10^{-7} T^2_{Mo} - 2.22 \bullet 10^{-11} T^3_{Mo}$$

$$R_{cu} = 7.89 \bullet 10^{-3} + 9.90 \bullet 10^{-5} T_{cu} - 5.49 \bullet 10^{-8} T^2_{Cu} + 3.16 \bullet^{-11} T^3_{Cu}$$

with T in [Kelvin] and R in [$\Omega mm^2/m$].

The resistance of the flexible cables to the points where the voltage is measured for the determination of the power, was less than 1 mΩ per rod (recommended value: 0.5 mΩ).

The unheated fuel rod simulator has the same configuration as the fuel rods in PWR-type reactors: solid UO_2 pellets inside the original Zry-4 cladding. The unheated fuel rod simulator is introduced through the bundle flange from below. At the lower end it extends to -200 mm elevation i.e. to 20 mm above the initial water level of the quench cylinder.

The two absorber rods are also made from original components. The (Ag80, In15,Cd5) absorber material is sheathed in stainless steel and this rod is surrounded by a Zry-4 guide tube. The absorber rods are connected in the same way to the bundle flange as the unheated rods.

Three spacers are used in the bundle to maintain the positions of the rods. Original PWR-type spacers have been used. The material of the middle spacer is Inconel 718. The upper and lower spacer are made of Zircaloy-4. The distances from the top end of the spacers to "zero elevation" are +880 mm, +496 mm and -5 mm.

The bundle head funnel (Fig. 2) is made of copper and is water-cooled by the double-walled outer chamber. To make the cooling more effective the space around the rods inside this chamber is filled with water. In consequence, the upper ends of the heated rods (the copper electrode inside the Zry-cladding) and the connectors for the pressure capillaries and thermocouples of the unheated rods are surrounded by water. The water was cooled by a heat exchanger. Argon was blown against the lower surface of the plate to protect the sealing in the bundle head plate.

At the lower end the heated fuel rod simulators are cooled by the water inside the quench cylinder. The gross volume of water inside the quench cylinder (230 mm ID) amounts to about 70 l. The initial water level is at the -220 mm elevation. The electrode is made of molybdenum from 0 to 300 mm length and the remaining part consists of copper. The electrode is flame-sprayed with a 0.2 mm thick layer of ZrO_2 and surrounded by the Zry-4 cladding. The unheated rod contacts the water of the quench cylinder only through the thermocouple connections.

The bundle is surrounded by a Zry-4 shroud of 1.2 mm thickness (Figure 5). The shroud conducts the steam through the bundle. The steam enters at 180° into the lower end (0 mm). To minimise the heat losses from the shroud, it is surrounded by an insulation layer of ZrO_2 fibre of 19 mm (0.75 inch) thickness. Since the ZrO_2 fibre has a low heat conductivity and heat capacity, the shroud temperature can follow the bundle temperature closely. Consequently the Zry shroud participates in the interaction with steam and the resulting oxidation energy contributes substantially to the bundle heat-up.

Test CORA-10 was foreseen to investigate the blockage behaviour of the bundle with its lower end in water. Due to safety limitations the cold lower end was simulated by leaving the shroud below 300 mm without insulation (Figure 7).

The steam inlet at 8 mm elevation is connected to the stainless steel steam distribution tube (Figures 3, 4 and 7). This tube extends down into the water of the quench cylinder thus forming a lower closure. The time history of the water level in the quench cylinder shows that there is no net condensation of steam in the quench cylinder.

At an elevation of 40 mm the steam distribution tube joins into the shroud. From here the shroud extends in vertical direction for 1195 mm. The shroud is covered by 19 mm of ZrO_2 fibre insulation from 300 mm to 1060 mm elevation.

The annuli between the shroud and the high temperature shield on one hand and the high temperature shield and pressure containment on the other hand are closed at the upper end by fibre ceramic layers of 38 mm thickness.

High temperature shield

To keep the heat losses as low as possible, the bundle was surrounded by an additional high temperature shield (HTS). The vertical and the horizontal cross-sections of the high temperature shield are given in Figures 3 and 4. The high temperature shield consisted mainly of ceramic fibre plates. The inner layer of plates consisted of ZrO_2, and the outer layer of Al_2O_3. The fibre ceramics were excellent insulators and had a low density which resulted in a low heat capacity. The thermal shock behaviour of the fibre ceramics was also extremely low.

The mechanical strength of the high temperature shield was ensured by external walls of stainless steel (0.9 mm). The fibre ceramic plates were attached to the stainless steel cover by ceramic nails. The inner ZrO_2 layer was 38 mm thick, and the outer Al_2O_3 layer was 76 mm. They were separated by a gap of 23 mm. The distance from the inner insulation surface to the centre of the bundle was 153 mm.

The high temperature shield was located within the pressure tube. In the pressure tube a large number of flanges allowed access to the bundle. Through these holes and their extensions in the temperature shield, the bundle could be inspected during the test with the help of the videoscope systems. In test CORA-10 two windows were used: in the 120° direction at the 590 and 790 mm elevations. The size of the windows was 30 mm high and 40 mm wide.

Power Supply

In CORA-10 16 rods out of 25 were heated. The rods can be separately connected to three available power systems, each of which can supply a different voltage. Thus the radial power distribution of the bundle can be varied. In this test the power input was the same for all rods. Since the voltages and currents of the individual rods are measured, the power input for each rod can be determined.

The power input is controlled by computer. The time-dependent power history is programmed before the test. The power is controlled by measuring the currents of the group and setting the voltage necessary to obtain the desired power. The electric heating is done by direct current to avoid generating eddy currents in the containment structures.

3. Test conduct and initial boundary condition

The test sequence can be divided into three phases (Fig. 10):

1. 0 - 3000 s: gas preheat phase;
2. 3000 - 4900 s: transient phase;
3. 4900 s: cooling phase.

During the gas preheat phase 8 g/s preheated argon flows through the bundle and a low constant electric power input of about 0.65 kW was used (Fig. 10). During this period the temperature in the insulation reaches a level which is high enough to avoid steam condensation. To keep the videoscope windows clear, a total flow of 0.35 g/s argon is directed to the front of the windows of the videoscopes. 0.26 g/s is flowing in addition through the channel between bundle insulation and HTS. 5.39 g/s is directed to the lower side of the bundle head plate for cooling. The sum of this three contributions not directed into the bundle 6 g/s is signified as "videoscopes" in Figure 10 and 11. The pressure in the system is controlled to 0.22 MPa.

During the transient phase the temperature increase is initiated by raising the electric power input from 6 to 27 kW at a constant rate (Figures 10 + 13). At 3300 s a steam flow of 2 g/s is added to the system. The shut down of the electric power is initiated at 4900 s. At the same time the steam input is stopped.

The voltage input of the three rod groups (Figure 14) is chosen by the controlling system in a way that the foreseen electric power input (Figure 13) is resulting. The total current through the heated rods is given in Figure 17. The current is only increasing from 3300 A to 3900 A, though the voltage is growing by a factor of 3.5 in the same time. This is due to the large increase of the resistance of the tungsten heater rods with the increasing temperature (Figure 18).

In Figure 19 the currents of the single rods are given. After about 4100 s the smooth flow is disturbed. The scatter is produced by melt formations allowing flow of current in neighbouring unheated rods as well. The effect can also be seen in Figure 14 in the voltage input.

The resistance of the bundle, of the rod groups and of the single rods are given in Figure 18 and 20 to 23. The resistance increases by a factor of about 3 during the test. The stronger increase of the resistance in the second half of the test is caused by the influence of the chemical power production as a result of the exothermal Zry-steam interaction.

Also for the resistance the irregularities in the smooth increase can clearly be seen at the start of melting. The sharp spikes during power shut down are artificial due to measurement of voltage and current not taken exactly at the same time.

In Figure 24 the water temperature in the quench cylinder at -300 mm elevation is given. The increase of temperature is caused by melt falling into the water and disturbing the stratification of the quench water heated from the top. In Figure 25 temperatures at 0 mm elevation 15 mm inside the inner surface and 9 mm outside the outer surface of the steam tube are given. A difference of about 300°C can be recognised.

4. Temperature measurement

The temperatures in the bundle were measured by high-temperature thermocouples of WRe5/WRe26 wires and HfO_2 insulating material. The sheath was made of tantalum and Zircaloy. Thermocouples with "Ker" in the name (see e.g. Figures 29, 41, 43) were additionally shielded with a ZrO_2 sheath. The measurements in the high temperature shield were performed with NiCrNi-thermocouples sheathed with stainless steel. Also the compensation cables were sheathed with stainless steel. The positions of the thermocouples in the bundle are given in Table 5 and Figure 26, on the shroud in Figure 34 and those in the high temperature shield in Figures 49 and 50.

The temperature measurements of the bundle are presented as functions of time in the following way: on one hand, the temperatures of the components (heated rods, unheated rods, channel box walls, absorber blade, etc. are given in Figures 27 - 37, on the other hand - for comparison reasons - the temperature measurements for different components are grouped by axial elevations in (Figures 38 - 46). The temperature measurements of the high temperature shield are given in Figures 51-70.

The failure of the thermocouples is mainly caused by the oxidising atmosphere and the interaction with the melts formed during the temperature escalation. After failure new junctions may be formed. Therefore the smooth temperature traces during cooldown must be handled with caution.

4.1 Temperature in the bundle

Due to the bundle arrangement with a Zircaloy shroud - participating in the exothermic reaction with steam - and the low-heat conductivity and heat capacity of the fibre insulation, a flat radial temperature profile was obtained. The measurements at the same elevation can therefore been combined to give a representative temperature of the bundle. The results of this combination are given in Figure 47 as best-estimate temperatures of the bundle as function of time for different elevations. In Figure 48 these values are rearranged as axial temperature distributions for different times in the test sequence.

Before 3000 s the temperature in the bundle was mainly determined by the heating effect of the incoming gas of about 500°C. The result was a axial temperature profile with the maximum at the lower end and decreasing temperature with increasing elevation. With increasing power input and temperature level the incoming gas and steam was cooler than the bundle and acted as coolant. The maximum of the temperature moved to the upper end of the bundle. Beginning at 850 mm elevation the temperature escalation developed first in the interval 750 mm to 950 mm elevation. Within the next 200 s the escalation spread to 550 mm and 1050 mm elevation. The maximum temperature in the bundle was reached at 1050 mm at the end of the transient. At 1150 mm elevation a maximum temperature of about 1800°C was reached at the end of the transient. Below 450 mm elevation the temperature remained smaller than 1400°C.

Compared to the other CORA tests the axial temperature distribution has clearly moved to the upper part of the bundle, due to the increased heat losses caused by the removal of the insulation below 300 mm. In addition in test CORA-10 the temperature escalation started about 100 s earlier than in the other tests with similar conditions in the transient phase.

In respect to the axial boundary conditions of the bundle we have measured the following maximum temperatures. At the lower end we got 90°C at -220 mm (quench water) and 600°C at 0 mm. At the upper end a maximum temperature of about 100°C was found at the upper surface (1571 mm) of the bundle head plate. On the lower surface (1471 mm) the temperature had increased to about 200°C. At the

elevations 1350 mm and 1250 mm the maximal temperatures of about 450°C and 1200°C were found.

4.2 Temperatures of the High Temperature Shield

The temperatures in the high temperature shield are given in Figures 51 to 70. The general tendency for the axial distribution at the inner surface (153 mm radius) was the same as in the other tests. A strong monotonous increase of the maximum temperature from -50 mm to 950 mm elevation was found. But for test CORA-10 the maximum values reached at the upper part of the insulation were much higher than in equivalent tests. For instance for CORA-29 a maximum temperature at 153 mm radius at 890 to 990 mm elevation of 1300°C was found. In CORA-10 the temperature at 850 and 950 mm is clearly higher than 1400°C, the upper limit of the measurement range. From the shape of the measurement traces one can assume that a maximum temperature of at least 1500°C was reached.

Measurements at the same elevation at different azimuthal directions gave temperature differences less than 100 °C. In direction of 165° the temperature has the tendency to show higher values at all elevations.

5. Failure of the absorber and fuel rod simulators

On the two absorber rods 4.6 and 6.2, the three unheated rods 4.4, 6.4 and 6.6 and the heated rod 3.3 the internal pressure was measured to determine the time of rod failure. The results are shown in Figures 73 and 74. In Figure 75 these times are compared with the times of first melt movement, seen in the videoscope investigations. The temperature traces of Figures 76 and 77 allow by their irregularities to determine the time of failure and also give the temperature at which this failure takes place. The temperature graphs of heated and unheated rods in the time span of failure in Figure 78 finally give the failure temperature of the unheated and heated fuel rods.

From Figure 74 can be seen, that the absorber rods 4.6 and 6.2 failed at 3980 s and 3990 s. These times correspond to the initiation of decrease of pressure in the two absorber rods to the pressure of the system. In Figure 75 is given, that melt movement was seen 2 s later (3982 s) at 800 mm and 600 mm elevation. The pressure loss at 3990 s could be attributed to melt movement at 4000 s by the videoscope at 800 mm. The failure of the stainless steel absorber rod cladding inside the Zircaloy guide tube may have two reasons. First with increasing temperature the steam pressure of Cd may cause the contact of stainless steel cladding and Zry guide tube by ballooning. Loss of the central position of the absorber rod inside the guide tube can favour the contact between stainless steel and Zry. The eutectic reaction between these materials is responsible for the final failure of the absorber rod. The delay of 2 s and 10 s between absorber failure and melt movement recognition is explained by the assumption, that the AgInCd melt, filling up the gap between absorber rod and guide tube, needs this extra time to dissolve a hole into the Zircaloy.

The failure of the absorber rods can also be recognised in irregularities of the temperature traces of the absorber rods and guide tubes. At 3900 s the temperature of absorber rod 6.2 showed a decrease at 950 mm elevation and an increase at 450 mm and 550 mm elevation, caused by the flowing melt, which has formed in the temperature region above about 800°C. For absorber rod 4.6 the irregularities can be seen at 3980 s. The temperature in the upper part of the absorber rod at the time of failure corresponds to 1230 °C.

The temperature graphs of the unheated and heated fuel rods in Figure 78 give in combination with the failure times of Figure 74 failure temperatures of 1280°C to 1330°C. The heated rod 3.3 failed 10 s later at a temperature of 1450°C.

6. Hydrogen generation

The hydrogen produced during the test by the steam/zirconium reaction was measured with mass spectrometer systems installed at two positions, i.e. above the test section, and in the mixing chamber after the gas had passed the condenser (see Figure1). The gas at the test section outlet could contain a high steam partial pressure and had therefore to be diluted by helium before it entered the analyser

through a capillary tube. For this purpose a dilution chamber with flow meters was installed.

A schematic diagram of the probes, gas lines, and gas analysis system is provided in Figure 9. The off-gas mixture which contained hydrogen among other gases is transported to the spectrometer via capillary tubes. It was analysed by quadrupole mass spectrometers of the type Leibold PQ 100. The ion currents representing the concentration of the respective gases were determined. The production rate of a gas component was calculated with the ratio of the partial pressure of the particular gas to that of argon (carrier gas) and multiplied by the argon flow rate through the test bundle. The hydrogen generation rate was evaluated as follows:

$R_m = 2 \bullet p_H F_{Ar} / (22.4 \bullet p_{Ar})$ [g/s]

with

R_m = mass production rate of hydrogen [g/s]

p_H = partial pressure of hydrogen

p_{AR} = partial pressure of argon

F_{ar} = volumetric argon flow through mixing chamber [l/s]

Based on a calibration test with bundle CORA-7, in which a mixture of argon and 30 % hydrogen was radially injected into the test section, the delay time of monitoring the gas was estimated to be 80 s. This time was taken into account for the measured hydrogen production in all CORA experiments. The same calibration test, however, shows lower increases in the rate of hydrogen production than would be expected from the injected gas flow. For this reason the measured data were corrected based on the actual gas concentration, i.a. on the gas input during the calibration test. A transfer function was determined and applied to the measured data. The result is a corrected curve that better represents the H2 production rate in the test section.

For test CORA-10 the measured as well as the corrected hydrogen production rate are given in Figure 71. The measured data were obtained from the gas probes of the mixing chambers. The corrected data are based on the transfer function of the CORA-7 calibration test. The temperature escalation started at about 3800 s (Figure

47). This corresponds to the start of the hydrogen production (Figure 71). Integral values of the hydrogen production are shown in Figure 72. The total produced hydrogen were to about 180 g.

From the best estimate temperature distributions in Fig. 47 and Fig. 48 it can be seen, that the high temperature region was restricted to an axial region from about 350 to about 1250 mm. Assuming, that this was also the region of the Zirconium/steam reaction one can deduce, that 67% of the Zircaloy in the high temperature area is oxidised. Referring the corrected hydrogen production rates to the steam input, it can be seen, that during escalation an average value of 62% and a maximum of 82% of steam was consumed.

The chemical power due to the corrected hydrogen production rate is compared with the electric power in Fig. 15. Both curves are integral values for the length of the bundle and do not reflect the axial variations. Especially the Zirconium/steam reaction is a local process. This means that at the region of escalation the local chemical power will be distinctly higher than the mean value.

The 180 g of hydrogen produced corresponds to an oxidation energy release of 27,4 MJ. The total electric input was to 34.9 MJ. This means that the energy from the exothermic reaction contributed to heating with 78,5 % of the electric input.

Of interest may be a comparison to test CORA-29 (Figure 72a). The test procedure of CORA-29 was the same as CORA-10, only 6 g/s steam input was used in CORA-29 instead 2 g/s in CORA-10. The bundle of CORA-29 was slightly pre-oxidised with a axial layer of about 10 μm. The large integral hydrogen production of 225 g shows that the slight pre-oxidation has no preventive influence on the hydrogen production. The important difference between the two tests are the flatter escalation shape and the lower maximal production rate for CORA-10. This behaviour is most likely an indication of local steam starvation.

7. Posttest appearance of the bundle

The post-test appearance of the bundle is given in Figures 84 to 124. Figure 84 show the bundle with insulation at the four different orientations 300° to 30°. This

demonstrates the state of the bundle in its original position after the test. Only the surrounding high temperature shield was moved down, to give access to the bundle. The pieces of insulation missing in these photographs were broken away after the test.

The state of the inner side of the insulation material (0,75 inch ZrO_2 fibre) is shown in Figures 85 to 89. A strong interaction between shroud and insulation has taken place over the whole length of the insulation. The remnants of the strongly deformed and embrittled shroud are glued to the strongly attacked insulation and are broken away during dismantling of the bundle.

Figure 90 shows photographs of the windows in 120° direction at 600 and 800 mm. The smooth surfaces on the left side are oxidised claddings of the fuel rod simulator. The strongly deformed surfaces in the middle more to the right side, are the remnants of the oxidised guide tube. This can clearly be seen from Figures 103 - 104, showing the bundle without shroud.

Figures 91-93 give an overview of the bundle after removal of the insulation. Due to its strong embrittlement the shroud is broken away with the insulation nearly over the whole insulated region. At 300 mm elevation, the support for the insulation (made of Zircaloy) can be recognised. The failure of the shroud represents the fast increase of the axial temperature due to Zr-fibre insulation. Below about 500 mm one can recognise the relocated melt. From about 500 mm to 900 mm the oxidised "flowered" smooth cladding is the most predominant appearance. Above 900 mm the cladding has disappeared. In this area interaction and melting has clearly dominated the oxidation of the cladding.

In Figures 94 to 124 details of the bundle are given. The bundle is photographed in 4 sections, starting from the top. The directions are shown in the sequence 300°, 210°, 120°, 30° (Figure 94 to 109). Special more enlarged sections of the bundle selected again in decreasing direction are given in Figures 110-124.

The upper spacer was made of Zircaloy. A large part of the spacer survived. The spacer formed the border of a region with preferential "flowered" cladding on the outside against the above region with much interaction (Figures: 99, 103, 107, 108). This damage structure, together with the late temperature increase in the upper part

of the bundle (Figure 47, 950 mm elevation) suggest, that the steam was initially consumed preferentially in the region below 950 mm elevation.

Figures 109, 112, 115, 118, 121 and 122 point to a strong blockage formation within the bundle below about 500 mm elevation. This is in agreement with the information from the much more detailed results in the next section on the cross sections. In Figure 124 material dropped from the bundle unto the comb fixing the radial rod positions is shown. During the test this region is inside the water of the quench cylinder. This photograph shows, that only a small amount of the melt formed is dropping in free fall out of the bundle. The major part is refreezing between the rods of the bundle according to the temperature profiles as can be seen from cross sections (Figure 126).

The damage in the bundle can best be seen from the horizontal and vertical cross sections. To enable the cutting of the cross sections a Lucite box was set around the bundle for encapsulation with epoxy resin. The lower end of this box was closed by a paraffin layer which was produced by refreezing paraffin floating on the water of the quench cylinder. Mutapox 0273 with the hardener LC (Backelite GmbH, Iserlohn) was used as epoxy. This epoxy was chosen, as its reaction time was slow enough that the shrinkage effect is negligible. The hardening time was one week. The bundle was filled starting from the bottom through the steam inlet. A saw with 2.3 mm thick diamond blade of 500 mm OD (mean diamond grain size 138 μm) was used to cut the bundle at 3200 rpm.

From the horizontal and vertical cross-sections in comparison to the post-test photographs one can obtain the following information:

- In accordance with the temperature profile damage on the bundle is found between about 250 mm and 1200 mm elevation. In the cross section at 238/240 mm elevation the fuel rod cladding and the absorber and guide tubes are intact. There is only some minor damage in the neighbourhood of the absorber rods due to relocated melt (preferential absorber material) (Figures 125, 129, A36, A40, A42). At 290 mm elevation the absorber rods have disappeared in the cross section and the attack on the cladding has reached a larger area around the positions of absorber rods. For the upper end at 1198 mm elevation again the

absorber rods are disappeared with only minor damage to the fuel rods, while at 1056/1058 mm large damage can be recognised on all fuel rods.

- The damage within the bundle is starting from the absorber channel, as clearly can be seen from all cross sections. The immediate surrounding of the absorber rods is shown in Figures 129 and A39-A42. The absorber rods have disappeared above about 250 mm.
- The horizontal cross sections (Figure 125) show that the formation of the oxide layers takes place up to about 900 mm elevation on the outer surface of the bundle in the "flowered" form. In the inner region of the bundle the oxidation of the cladding has to compete with the interaction of the cladding with the absorber material.
- A large blockage has formed in the bundle between 300 mm and 430 mm elevation (Figures 125 + 126). A radially less pronounced relocation can be recognised down to about 100 mm elevation. The lower blockage was formed mainly by an absorber-rich metallic melt coming down first caused by the failure of the absorber rods. The upper larger blockage has formed later from Zr and U rich more ceramic melts. The melt with the higher refreezing temperature relocates to the higher elevation. This refreezing behaviour shows, that relocation in the bundle is mainly determined by the axial temperature profile. The fact, that the melt relocated to a region between the spacers, shows that no additional obstacles are necessary to form the blockage, though spacers influence the relocation of the melt.

8. Blockage formation and mass distribution

The relocation of molten material is also determined by measuring the axial distribution of the blocked area and bundle mass. These measurements were performed in connection with the epoxying process. As can be seen in Figure 79 the resin is poured into the Lucite mould from the bottom end. By weighing the resin - left in the supply container - after each step, i.e. when the resin level has raised in the bundle by 1 cm, the difference of mass allows the calculation of the void volume of

the bundle as a function of axial height. The filling process is slow enough so that the reading at the scale can be taken per cm.

The error of this measured mass distribution amounts to about 15 %. 10 % with respect to the measurement of 1 cm increments of the epoxy level and 5% due to the error of mass measurement. The error, however, is alternating, i.e. epoxy not measured at one step is certainly included in the next reading at the scale. A filtering method using a Fourier transformation, where higher frequencies were cut off by a low pass filter, was performed to deal with these errors.

The data of the mass of resin as a function of elevation (g/cm) in Figure 80 demonstrate the scatter. The smoothed solid-line curve in Figure 80 was obtained from the data (crosses) by filtering. The axial distribution in Figure 80 is the distribution of the epoxy bundle fill-up, i.e. a complement to blockage in the bundle.

Using the density of the epoxy and the cross sectional area inside the Lucite mould the structural area of the bundle end state can be evaluated. Referred to the area of the shroud, it is given in Figure 82b as „relative blockage".

The blocked area is defined as (cross section mould inside - cross section epoxy - cross-section of shroud remnants) referred to cross section of shroud inside.

As part of the shroud was removed together with the fibre insulation after the test, the remnants of the shroud - which were present during the filling process - were excluded in the evaluation by measuring their contribution to the cross section separately. The areas are given as percentages, where 100 % means complete blockage.

To determine the axial mass distribution, the epoxy filled bundle was cut into horizontal slices and these bundle segments were weighed. The distribution is shown in Figure 81. Knowing the axial epoxy distribution, the contribution of the resin is subtracted from the measured weight, to give the mass distribution of the bundle. Also this distribution is corrected for the share of the shroud. The results are given in the left picture of Figure 82. These data represent the mass of the rods and spacer. The measured curve is compared with the mass distribution of the intact bundle.

The specific mass is defined as (mass of weighed samples - epoxy mass - mass of shroud remnants) referred to the pertinent axial segment.

If one compares the uncertainty of the axial mass distribution with the axial volume distribution, one can see, that the method using the weighed samples is the more accurate one. The uncertainty of the measurement of the filled-in epoxy mass contains the same absolute error, however, the relative error is only one fifth, because the epoxy resin is referred to a 5 cm block compared with the reference of 1 cm for the volume method. Because of the lower density of the epoxy resin in comparison with the density of the structural material the relative error is further reduced. On the other hand in the mass distribution the resolution is reduced.

The axial distribution of mass and blocked area in the bundle (Figure 82) are very similar and in accordance with the results from the cross sections. An upper larger blockage at about 400 mm elevation and a similar lower relocation extending to about 100 mm.

In Figure 83 the axial mass distribution is compared with the axial temperature distribution. One can recognise the strong correlation between the axial temperature profile and the melt relocation. The relocation is related to the decreasing temperature of the axial distribution. The lower blockage has formed earlier. One can recognise the change of the profile in time, showing that the relocated melt again is influencing the axial temperature profile. The influence of the relocating melt on the temperature profile is caused basically due to the heat transported by the melt coming from a region of higher temperature. In addition the resulting increase of the temperature may enhance the heat production due to the exothermic Zry/steam reaction.

9. Summary and discussion

Test CORA-10 should investigate the blockage behaviour of a bundle with its lower end in water. Due to safety limitations the test was not run - as originally planned - with a water level increased to 250 mm elevation. Instead the cold lower end was simulated by removing the insulation around the shroud up to 300 mm and

simulating the evaporation of water by a steam input of two g/s. The following results should be mentioned:

- Due to the absence of insulation below 300 mm elevation, the temperature escalation is restricted to the upper part of the bundle above 500 mm. The escalation starts at 750 to 950 mm elevation (maximum reached at 4100 s). The maximum for the escalation at 650 mm and 550 mm are reached at 4150 s and 4200 s. The highest temperature of the bundle is measured at 1050 mm at the end of the transient (4900 s).
- Accordingly, the damage to the bundle is concentrated to its upper half: The absorber rods have survived below 250 mm. Increasing damage to the fuel rod simulator starts at 300 mm up to about 1200 mm. The damage within the bundle started from the absorber rods.
- A large blockage has formed in the bundle between 310 mm and 430 mm. A radially less pronounced relocation has formed in the region below down to about 100 mm. The lower blockage was formed first by mainly metallic melt. The upper blockage resulted from Zr and U rich partly ceramic melts.
- Only a negligible amount of melt has fallen out of the bundle.
- Test CORA-10 confirms that the relocation of molten material within a bundle is mainly determined by the axial temperature distribution. On the other hand the axial temperature profile is influenced by the heat transported by the relocated melt and by the additional energy, resulting from the increasing exothermic reaction due to the increased temperature.
- 180 g hydrogen produced in test CORA-10. This amount of hydrogen corresponds to an oxidation energy release of 27.4 MJ. The total electric input amounted to 34.9 MJ, which means that the energy produced in the exothermic reaction contributed to heating by 78% of the electric input.

10. References

1. J.M. Broughton; P. Kuan, D.A. Petti; "A Scenario of the Three Mile Island Unit 2 Accident", *Nuclear Technology*, Vol. 87, 34-53 (1989).

2. S. Hagen, K. Hain: "Out-of-pile Bundle Experiments on Severe Fuel Damage (CORA-Program)", *KfK* 3677 (1986).

3. S. Hagen, P. Hofmann, G. Schanz, L. Sepold; "Interactions in Zircaloy/UO_2 Fuel Rod Bundles with Inconel Spacers at Temperatures above 1200°C (CORA-2 and CORA-3)", *KfK* 4378 (1990).

4. S. Hagen, P. Hofmann, V. Noack, G. Schanz, G. Schumacher, L. Sepold; "Results of SFD Experiment CORA-13 (OECD International Standard Problem 31)" *KfK* 5054 (1993).

5. M. Firnhaber, K. Trambauer, S. Hagen, P. Hofmann, G. Schanz, L. Sepold:ISP-31, "CORA-13 Experiment on Severe Fuel Damage GRS-106", *KfK* 5287, NEA/CSNI/R (93) 17 (1993).

6. S. Hagen, P. Hofmann, V. Noack, G. Schanz, G. Schumacher, L. Sepold; "BWR Slow Heat-up Test CORA-31: Test Results", *KfK* 5383 (1994)

7. S. Hagen, P. Hofmann, V. Noack, G. Schanz, G. Schumacher, L. Sepold; "Dry Core BWR Test CORA-33: Test Results", *KfK* 5261 (1994).

8. S. Hagen, P. Hofmann, V. Noack, G. Schanz, G. Schumacher, L. Sepold; "Behaviour of a VVER Fuel Element Tested under Severe Accident Conditions in the CORA Facility (Test Results of Experiment CORA-W1)" *KfK* 5212 (1994).

9. S. Hagen, P. Hofmann, V. Noack, G. Schanz, G. Schumacher, L. Sepold; "Behaviour of a VVER-1000 Fuel Element with Boron Carbide/Steel Absorber Tested under Severe Fuel Damage Conditions in the CORA Facility (Results of Experiment CORA-W2)", *KfK* 5363 (1994).

10. J. Burbach; "Results of SEM/EDX Microrange Analyses of the PWR Fuel Element Meltdown Experiment CORA-13", *KfK* 5162 (1993).

11. J. Burbach; "Results of SEM/EDX Microrange Analyses of the BWR Fuel Element Meltdown Experiment CORA-16", *KfK* 5282 (1994).

12. S. Hagen, P. Hofmann, V. Noack, L. Sepold, G. Schanz, G. Schumacher;" Comparison of the Quench Experiments CORA-12, CORA-13, CORA-17", *FZKA* 5679, (1996).

13. S. Hagen, P. Hofmann, V. Noack, L. Sepold, G. Schanz, G. Schumacher; "Impact of absorber rod material on bundle degradation seen in CORA experiments", *FZKA* 5680 (1996).

14. S. Hagen, P. Hofmann, V. Noack, L. Sepold, G. Schanz, G. Schumacher; "Pre-oxidised BWR Test CORA-28: Test Results"; FZKA 5571 (1997)

15. S. Hagen, P. Hofmann, V. Noack, L. Sepold, G. Schanz, G. Schumacher; "Pre-oxidised PWR Test CORA-29: Test Results"; FZKA 5928 (1997)

16. S. Hagen, P. Hofmann, V. Noack, L. Sepold, G. Schanz, G. Schumacher; "Slow Heatup PWR Test CORA-30: Test Results" FZKA 5929 (1997)

11. Acknowledgements

At the Forschungszentrum Karlsruhe a variety of support needed for preparation, conduct, and evaluation of the experiment is hereby gratefully acknowledged.
The facility was designed by K. Hain and his team. The special bundle set up was designed by Mr. H. Junker. The test rods were assembled by Mr. E. Mackert, the test bundles by Messrs. H. Gießmann and R. Röder. The authors would like to thank Messrs. H. Benz, C. Grehl and H.J. Röhling for test preparations and conduct.
Mr. K. P. Wallenfels was responsible for arrangement of camera and video systems and for the preparation of temperature measurements. Messrs. R. Huber and H. Malauschek prepared and conducted the on-line measurements of the off-gas composition.
Finally we would like to express our gratitude to Mrs. U. Ivanitsch for the careful typing of this report.

List of tables

Table 1: CORA Test Matrix

Test No.	Max. Cladding Tempera-tures	Absorber Material	Other Test Conditions	Date of Test
2	≈ 2000°C	-	UO_2 refer., inconel spacer	Aug. 6, 1987
3	≈ 2400°C	-	UO_2 refer., high temperature	Dec. 3, 1987
5	≈ 2000°C	Ag, In, Cd	PWR-absorber	Febr. 26, 1988
12	≈ 2000°C	Ag, In, Cd	quenching	June 9, 1988
16	≈ 2000°C	B_4C	BWR-absorber	Nov. 24, 1988
15	≈ 2000°C	Ag, In, Cd	rods with internal pressure	March 2, 1989
17	≈ 2000°C	B_4C	quenching	June 29, 1989
9	≈ 2000°C	Ag, In, Cd	10 bar system pressure	Nov. 9, 1989
7	< 2000°C	Ag, In ,Cd	57-rod bundle, slow cooling	Febr. 22, 1990
18	< 2000°C	B_4C	59-rod bundle, slow cooling	June 21, 1990
13	≈ 2200°C	Ag, In, Cd	OECD/ISP; quench initiation at higher temperature	Nov. 15, 1990
29*	≈ 2000°C	Ag, In, Cd	pre-oxidised,	April 11, 1991
31*	≈ 2000°C	B_4C	slow initial heat-up (≈ 0.3 K/s)	July 25, 1991
30*	≈ 2000°C	Ag, In, Cd	slow initial heat-up (≈ 0.2 K/s)	Oct. 30, 1991
28*	≈ 2000°C	B_4C	pre-oxidised	Febr. 25, 1992
10	≈ 2000°C	Ag, In, Cd	cold lower end 2 g/s steam flow rate	July 16, 1992
33	≈ 2000°C	B_4C	dry core conditions, no extra steam input	Oct. 1, 1992
W1	≈ 2000°C	-	WWER-test	Febr. 18, 1993
W2	≈ 2000°C	B_4C	WWER test with absorber	April 21, 1993

Initial heat-up rate: ≈ 1,0 K/s; Steam flow rate, PWR: 6 g/s BWR: 2 g/s;
CORA 10: 2g/s; CORA W1 + W2: 4 g/s; quench rate (from the bottom) ≈1 cm/s

Table 2: Design characteristics of bundle CORA-10

Bundle type		PWR
Bundle size		25 rods
Number of heated rods		16
Number of unheated rods		7
Pitch		14.3 mm
Cladding material		Zircaloy-4
Cladding thickness		0.725 mm
Rod length	- heated rods (elevation	1960 mm - 489 to 1471 mm)
	- unheated rods (elevation	1672 mm - 201 to 1471 mm)
Heated pellet stack		0 to 1000 mm
Heater material		Tungsten (W)
Heater	- length	1000 mm
	- diameter	6 mm
Fuel pellets	- heated rods	UO_2 annular pellets
	- unheated rods	UO_2 full pellets
Pellet stack	- heated rods	0 to 1000 mm
	- unheated rods:	- 199 to 1295 mm
U-235 enrichment		0.2 %
Pellet outer diameter (nominal)		9.1 mm
Grid spacer	- material	Zircaloy -4, Inconel 718
	- length	Zry 42 mm Inc 38 mm
	- location	lower (Zry) -5 mm center (Inc) +496 mm top (Zry) +880 mm
Shroud	- material	Zircaloy -4
	- wall thickness	1.2 mm
	- outside dimensions	90.4 x 90.4 mm
	- elevation	40 - 1235 mm

Table 2 (continuation)

Shroud insulation	- material	ZrO_2 fibre
	- insulation thickness	19 mm
	- elevation	300 mm to 1060 mm
Mo electrode	- length	300 mm
	- diameter	8.6 mm
Cu electrode	- length	189 mm (lower end)
	- length	669 mm (upper end)
	- diameter	8.6 mm
Absorber rod	- number of rods	2
	- material and composition	80Ag, 15In, 5Cd (wt.%)
	- cladding	Stainless steel
	- cladding OD	11.2 mm
	- cladding ID	10.2 mm
	- length	1660 mm
	- absorber material	-189 mm to +1300 mm
Absorber rod guide tube	- material - OD	Zircaloy -4 13.8 mm
	- wall thickness of tube	0.8 mm
Plenum Volume	- heated rods	$19.8\ 10^{-6}\ m^3$
	- unheated rods	$39.0\ 10^{-6}\ m^3$

Table 3: Total specific mass data of bundle CORA-10

Specific mass [kg/m]	
Tungsten heater elements	8.74
UO_2	10.85
Zircaloy in rods	3.45
Zircaloy in absorber rods	0.43
Stainless steel in absorber rods	0.26
Ag/In/Cd absorber	1.59
Inconel grid spacer	0.11
Zircaloy grid spacer	0.14
Zircaloy of shroud	2.77
Total zircaloy	6.65

Table 4: Areas of bundle CORA-10

Cross section areas [m^2]	
Tungsten	$4.524\ 10^{-4}$
UO_2	$1.043\ 10^{-3}$
Zircaloy cladding	$5.252\ 10^{-4}$
Absorber, Ag/In/Cd	$1.634\ 10^{-4}$
Absorber, Stainless steel cladding	$3.36\ 10^{-5}$
Absorber, Zircaloy guide tube	$6.54\ 10^{-5}$
Zircaloy shroud	$4.22\ 10^{-4}$
Total area inside the shroud	$7.535\ 10^{-3}$

Table 5: Position of Thermocouples

Positions of thermocouples in unheated rods (CORA -10)		
Slot Number	Elevation [mm]	Rod Number
131	1350	2.6
101	1150	6.6
102	1050	2.2
103	950	6.4
104	850	2.4
105	750	4.4
106	650	4.2
221	550	2.6
222	550	6.6
223	550	4.4
231	450	4.2
232	350	6.4
234	250	2.2
233	150	2.4

Positions of thermocouples in absorber rods (CORA-10)		
Slot Number	Elevation [mm]	Rod Number
107	950	6.2
108	750	4.6
235	450	6.2
236	350	4.6

Positions of thermocouples at heated rods (CORA-10)		
Slot Number	Elevation [mm]	Rod Number
109	1150	5.3
110	950	5.5
111	750	3.5
224	550	5.5
237	500	5.5
238	450	5.3
239	400	3.5
261	350	3.3
262	300	5.1
263	250	7.3
264	150	3.7

Positions of thermocouples at inside shroud (CORA-10)		
Slot Number	Elevation [mm]	Direction of TE
121	950	300°
122	750	300°
226	650	300°
227	550	300°

Positions of thermocouples at guide tube(CORA-10)		
Slot Number	Elevation [mm]	Rod Number
112	1150	4.6
113	950	6.2
114	750	4.6
225	550	6.2
265	350	4.6
266	150	4.6
267	50	6.2

Positions of thermocouples at grid spacer (CORA-10)		
Slot Number	Elevation [mm]	Direction of TE
115	860	210°
116	860	30°
268	475	210°
269	475	30°

Positions of thermocouples at shroud outer surface		
Slot Number	Elevation [mm]	Direction of TE
123	1150	30°
124	950	30°
125	750	210°
228	550	210°
270	500	210°
271	450	30
272	400	30
273	350	210°
274	300	210°
275	250	210°
276	150	210°

Positions of thermocouples in shroud insulation(CORA-10)		
Slot Number	Elevation [mm]	Direction of TE
128	1050	30°
229	950	30°
230	750	30°
241	650	300°
242	550	300°
277	450	210°
278	350	210°
279	300	210°

Positions of thermocouples btw. bundle+shroud (C. -10)		
Slot Number	Elevation [mm]	Direction of TE
280	240	120°
137	230	120°
138	220	120°

Positions of thermocouples in cer. tube,shroud+bundle		
Slot Number	Elevation [mm]	Direction of TE
117	950	30°
118	960	210°
119	750	30°
120	721	210°

Positions of thermocouples at bundle flange (CORA-10)		
Slot Number	Elevation [mm]	Direction of TE
132	1491	210°
133	1471	300°
134	1471	330°
135	1511	30°
136	1511	300°

Positions of thermocouples for gas (CORA-10)		
Slot Number	Elevation [mm]	Direction of TE
126	1350	120°
127	1250	300°
139	220	120°

Positions of thermocouples steam distribution tube		
Slot Number	Elevation [mm]	Direction of TE
141	0	345°

Table 6: List of cross sections for test bundle CORA-10

Sample	Sample length	Elevation bottom	Elevation top	Remarks
10-a	115 mm	-167 mm	-52 mm	Lower remnant
Cut	2 mm			Lower grid spacer
10-01	13 mm	-50 mm	-37 mm	Top polished
Cut	2 mm			
10-b	50 mm	-35 mm	15 mm	
Cut	2 mm			
10-c	50 mm	17 mm	67 mm	
Cut	2 mm			
10-d	50 mm	69 mm	119 mm	
Cut	2 mm			
10-02	13 mm	121 mm	134 mm	
Cut	2 mm			
10-e	35 mm	136 mm	171 mm	Additional vertical cut
Cut	2 mm			
10-09	13 mm	173 mm	186 mm	Top polished
Cut	2 mm			
10-f	35 mm	188 mm	223 mm	Additional vertical cut
Cut	2 mm			
10-10	13 mm	225 mm	238 mm	Top polished
Cut	2 mm			
10-g	50 mm	240 mm	290 mm	Additional vertical cut
Cut	2 mm			
10-03	13 mm	292 mm	305 mm	Top polished
Cut	2 mm			
10-h	50 mm	307 mm	357 mm	Additional vertical cut
Cut	2 mm			

10-i	35 mm	359 mm	394 mm	Additional vertical cut
Cut	2 mm			
10-11	13 mm	396 mm	409 mm	Top polished
Cut	2 mm			
10-j	50 mm	411 mm	461 mm	Additional vertical cut
Cut	2 mm			
10-04	13 mm	463 mm	476 mm	Top polished
Cut	2 mm			
10-k	50 mm	478 mm	528 mm	
Cut	2 mm			
10-l	50 mm	530 mm	580 mm	
Cut	2 mm			
10-m	50 mm	582 mm	632 mm	
Cut	2 mm			
10-05	13 mm	634 mm	647 mm	Top polished
Cut	2 mm			
10-n	50 mm	649 mm	699 mm	
Cut	2 mm			
10-o	50 mm	701 mm	751 mm	
Cut	2 mm			
10-p	50 mm	753 mm	803 mm	
Cut	2 mm			
10-06	13 mm	805 mm	818 mm	Top polished
Cut	2 mm			
10-q	50 mm	820 mm	870 mm	
Cut	2 mm			
10-07	13 mm	872 mm	885 mm	Top polished

Cut	2 mm			
10-r	50 mm	887 mm	937 mm	
Cut	2 mm			
10-s	50 mm	939 mm	989 mm	
Cut	2 mm			
10-08	13 mm	991 mm	1004 mm	Top polished
Cut	2 mm			
10-t	50 mm	1006 mm	1056 mm	
Cut	2 mm			
10-u	140 mm	1058 mm	1198 mm	
Cut	2 mm			
10-v	xxx mm	1200 mm	xxxx mm	Upper remnant

Table 7: Temperatures [°C] of test CORA-10 at 0 seconds for different components

	Components						
Elevation [mm]	Heated rod	Unheated rod	Absorber rod	Guide tube	Shroud	Shroud insulation	HTS 153 mm
1350		50					
1250							83
1150	262	264		244			93
1050		306				121	90
950	301	318	315	315	286		89
850		331					86
750	324	337	314	315	297	125	84
650		346			312		83
550	354	353		353	310	127	82
450		353	350			126	79
350	361	365	360	361		134	75
300						126	
250		357					71
150	374	383		390			71
50				415			60
-50							56

Table 8: Temperatures [°C] of test CORA-10 at 3000 seconds for different components

	Components						
Elevation [mm]	Heated rod	Unheated rod	Absorber rod	Guide tube	Shroud	Shroud insulation	HTS 153 mm
1350		53					
1250							90
1150	328	325		301			104
1050		378				137	100
950	401	400	391	395	355		97
850		412					94
750	417	421	388	393	362	135	92
650		426			378		90
550	437	422		422	368	138	89
450		412	407			139	85
350	428	415	412	415		147	79
300						140	
250		395					76
150	415	411		419			76
50				428			70
-50							59

Table 9: Distribution of void volumes in unheated and heated rods

Void volume of one unheated rod

	elevation [mm]	volume [cm^3]	relative volume [cm^3/cm]
dishing of uranium pellets; gap between pellet stack and cladding	-201 to 1315	4.083	0.027
void volume above pellet stack	1315 to 1439	8.378	0.678
	1439 to 1456	0.711	0.419
	1456 to 1522	3.658	0.55
	1522 to 1531	0.387	0.43
	1531 to 1762	6.531	0.283
	1762 to 1764	0.084	0.419
system for pressure measurement		15.120	
total void volume		38.952	

Void volume of one heated rod

	elevation [mm]	volume [cm^3]	relative volume [cm^3/cm]
void volume below pellet stack	-369 to -334	0.826	0.236
	-334 to 0	1.391	0.0417
gap between pellet stack and cladding and between pellet stack and heater	0 to 1024	2.311	0.023
void above pellet stack	1024 to 1875	3.545	0.0417
	1875 to 1911	0.852	0.24
system of pressure measurement		10.860	
total void volume		19.785	

List of figures

22 : Resistance of rods group 2

23 : Resistance of rods group 3

24 : Water temperature in the quench cylinder

25 : Temperature on inner side and outer side of steam tube at 0 mm elevation

26 : Thermocouple locations within the bundle (CORA-10)

27 : Temperatures of heated rods

28 : Temperatures of unheated rods

29 : Temperatures measured with ceramic protected TCs

30 : Temperatures of the spacers used in test CORA-10

31 : Temperatures on the guide tube and in the absorber

32 : Temperatures at the bundle head plate and of the lower end of the bundle (0 mm) between bundle and shroud

33 : Temperatures at lower end of bundle and shroud

34 : Location of the thermocouples at shroud and shroud insulation (CORA-10)

35 : Temperatures on the inner side of shroud

36 : Temperatures of the outer side of the shroud

37 : Temperatures on and in shroud insulation

38 : Temperatures at elevations given (1511-1471, 1350-1150 mm)

39 : Temperatures at elevations given (1471, 1350 mm)

40 : Temperatures at elevations given (1250, 1150 mm)

41 : Temperatures at elevations given (1050 - 960, 950 mm)

42 : Temperatures at elevations given (860 - 850, 750 mm)

43 : Temperatures at elevations given (721 - 650, 550 mm)

44 : Temperatures at elevations given (500 - 475, 450 - 400 mm)

45 : Temperatures at elevations given (350, 300 - 250 mm)

46 : Temperatures at elevations given (240 - 220, 150 - 0 mm)

47 : Best-estimate bundle temperatures at different elevations

48 : Axial temperature distribution during the transient of test CORA-10

49 : Locations of thermocouples in the high temperature shield (CORA-10)

50 : Position of thermocouples in high temperature shield for test CORA-10

51 : Temperatures of HTS at inner surface, 153 mm radius

52 : Temperatures of HTS, inner surface at 153 mm radius (550 mm)

53 : Temperatures of HTS, inner surface at 153 mm radius (950 mm)

54 : Temperatures of HTS, inner surface at 153 mm radius (50 mm)

55 : Temperatures of HTS at inner surface, 153 mm radius

56 : Temperatures of HTS at 172 mm radius

57 : Temperatures of HTS at 172 mm radius (0-15000s)

58 : Temperatures of HTS at 192 mm radius

59 : Temperatures of HTS at 255 mm radius

60 : Temperatures of HTS at 192 mm radius (0-20000s)

61 : Temperatures of HTS at 255 mm radius (0-20000s)

62 : Temperatures of HTS at 293 mm radius

63 : Temperatures of HTS at the outer surface, 380 mm radius

64 : Temperatures of HTS at 293 mm radius (0-15000s)

65 : Temperatures of HTS at the outer surface, 380 mm radius (0-15000s)

66 : Temperatures of HTS, Radial dependence at 950 mm elevation (0-10000s)

67 : Temperatures of HTS, Radial dependence at 550 mm elevation (0-10000s)

68 : Temperatures of HTS, Radial dependence at 950 mm elevation (3000-6000s)

69 : Temperatures of HTS, Radial dependence at 550 mm elevation (3000-6000s)

70 : Temperatures of HTS, Radial dependence at 50 mm elevation (3000-6000s)

71 : Hydrogen production rate in test CORA-10

72 : Hydrogen production in test CORA-10; integral values

72a Hydrogen production in test CORA-29; production rate (top) and integral values (bottom)

73 : Internal pressure of fuel rod simulators and absorber rods

74 : Determination of failure time by pressure loss measurement

75 : Determination of failure of absorber rods

76 : Determination of failure of absorber rod 6.2 by irregularities in absorber and guide tube temperature measurement

77 : Determination of failure of absorber rod 4.6 by irregularities in absorber and guide tube temperature measurement

78 : Determination of failure of fuel rods by pressure loss measurement

79 : Epoxying process of the tested bundle

80 : Axial distribution of the bundle fill-up with epoxy resin

81 : Axial mass distribution of bundle segments filled with epoxy resin

82 : Comparison of axial mass distribution and axial volume distribution after the test

83 : Axial mass distribution after the test and axial temperature distribution during the test

84 : Post-test appearance of the entire bundle length with the shroud insulation

85 : Post-test view of the inner side of shroud insulation

86 : view of the inner side of shroud insulation, 30° and 120° orientation, 720 - 1100 mm elevation

87 : view of the inner side of shroud insulation, 30° and 120° orientation, 320 - 700 mm elevation

88 : view of the inner side of shroud insulation, 210° and 300° orientation, 720 - 1100 mm elevation

89 : view of the inner side of shroud insulation, 210° and 300° orientation, 320 - 700 mm elevation

90 : Windows at 800 mm and 600 mm

91 : Post-test appearance of the entire bundle length after removal of the shroud insulation

92 : Post test view 300° and 210° orientation

93 : Post test view 120° and 30° orientation

94 : Post test view 300° orientation, 1080 - 1350 mm elevation

95 : Post test view 300° orientation, 780 - 1050 mm elevation

96 : Post test view 300° orientation, 480 - 750 mm elevation

97 : Post test view 300° orientation, 180 - 450 mm elevation

98 : Post test view 210° orientation, 1080 - 1350 mm elevation

99 : Post test view 210° orientation, 780 - 1050 mm elevation

100 : Post test view 210° orientation, 480 - 750 mm elevation

101 : Post test view 210° orientation, 180 - 450 mm elevation

102 : Post test view 120° orientation, 1080 - 1350 mm elevation

103 : Post test view 120° orientation, 780 - 1050 mm elevation

104 : Post test view 120° orientation, 480 - 750 mm elevation

105 : Post test view 120° orientation, 180 - 450 mm elevation

106 : Post test view 30° orientation, 1080 - 1350 mm elevation

107 : Post test view 30° orientation, 880 - 1150 mm elevation

108 : Post test view 30° orientation, 580 - 850 mm elevation

109 : Post test view 30° orientation, 280 - 550 mm elevation

110 : Post test view 300° orientation, 920 - 1110 mm elevation

111 : Post test view 300° orientation, 770 - 920 mm elevation

112 : Post test view 300° orientation, 380 - 550 mm elevation

113 : Post test view 210° orientation, 930 - 1110 mm elevation

114 : Post test view 210° orientation,770 - 910 mm elevation

115 : Post test view 210° orientation, 440 - 530 mm elevation

116 : Post test view 105° orientation, 920 - 1110 mm elevation

117 : Post test view 105° orientation, 760 - 940 mm elevation

118 : Post test view 105° orientation, 350 - 540 mm elevation

119 : Post test view 30° orientation, 770 - 920 mm elevation

120 : Post test view 30° orientation, 580 - 760 mm elevation

121 : Post test view 30° orientation, 390 - 580 mm elevation

122 : Post test view 30° orientation, 320 - 500 mm elevation

123 : Post test view 160° orientation, -190 - 50 mm elevation

124 : Refrozen melt at the lower end of the bundle

125 : Horizontal cross sections of bundle CORA-10, top view (1198 to -37 mm)

126 : Vertical cross section from 307 to 461 mm elevation

127 : Vertical cross section from 136 to 290 mm elevation

128 : Vertical cross section from 136 to 290 mm elevation and
from 307 to 461 mm elevation

128a : Locations of vertical cuts through samples
CORA - 10-e, 10-f, 10-g, 10-h, 10-i and 10-j

129 : Horizontal cross section of absorber region of absorber rod 6.2

Appendix

A1 : Argon input before the test

A2 : Temperature at the entrance of the bundle prior to test

A3 : Power input during pre-heat phase

A4 : Resistance during the pre-heat phase

A5 : Temperatures of heated rods, pre-heat phase

A6 : Temperatures of unheated rods, pre-heat phase

A7 : Temperatures measured with ceramic protected TCs; pre-heat phase

A8 : Temperatures on the guide tubes and in the absorbers, pre-heat phase

A9 : Temperatures of the spacers; pre-heat phase

A10 : Temperatures at lower end of bundle and shroud; pre-heat phase

A11 : Temperatures on the inner side of shroud; pre-heat phase

A12 : Temperatures on the outer side of shroud; pre-heat phase

A13 : Temperatures on shroud insulation; pre-heat phase

A14 : Temperatures at elevations given; pre-heat phase (1511-1471, 1350-1150 mm)

A15 : Temperatures at elevations given; pre-heat phase (1050 - 960, 950 mm)

A16 : Temperatures at elevations given; pre-heat phase (860 - 850, 750 mm)

A17 : Temperatures at elevations given; pre-heat phase (721 - 650, 550 mm)

A18 : Temperatures at elevations given; pre-heat phase (500 - 475, 450 - 400 mm)

A19 : Temperatures at elevations given; pre-heat phase (350, 300 - 250 mm)

A20 : Temperatures at elevations given; pre-heat phase (240 - 220, 150 - 0 mm)

A21 : Temperatures of HTS, pre-heat phase, inner surface at 153 mm radius

A22 : Temperatures of HTS, pre-heat phase, inner surface at 153 mm radius

A23 : Temperatures of HTS, pre-heat phase, inner surface at 153 mm radius

A24 : Temperatures of HTS, pre-heat phase, at 192 mm radius

A25 : Temperatures of HTS, pre-heat phase, at 192 mm radius

A26 : Temperatures of HTS, pre-heat phase, at 255 mm radius

A27 : Temperatures of HTS, pre-heat phase, at 950 mm elevation

A28 : Temperatures of HTS, pre-heat phase, at 550 mm elevation

A29 : Temperatures of HTS, pre-heat phase, at 50 mm elevation

A30 : Temperatures of HTS, pre-heat phase, on outer surface, 380 mm radius

A31 : Horizontal cross sections of bundle CORA-10, 1198 to 989 mm elevation

A32 : Horizontal cross sections of bundle CORA-10, 939 to 818 mm elevation

A33 : Horizontal cross sections of bundle CORA-10, 805 to 647 mm elevation

A34 : Horizontal cross sections of bundle CORA-10, 634 to 476 mm elevation

A35 : Horizontal cross sections of bundle CORA-10, 463 to 305 mm elevation

A36 : Horizontal cross sections of bundle CORA-10, 292 to 134 mm elevation

A37 : Horizontal cross sections of bundle CORA-10, 121 to -37 mm elevation

A38 : Horizontal cross sections of bundle CORA-10, -50 to -52 mm elevation

A39 : Horizontal cross section of absorber region of absorber rod 4.6,
1198 to 476 mm elevation

A40 : Horizontal cross section of absorber region of absorber rod 4.6,
461 to -52 mm elevation

A41 : Horizontal cross section of region of absorber rod 6.2,
1198 to 476 mm elevation

A42 : Horizontal cross section of region of absorber rod 6.2,
461 to -52 mm elevation

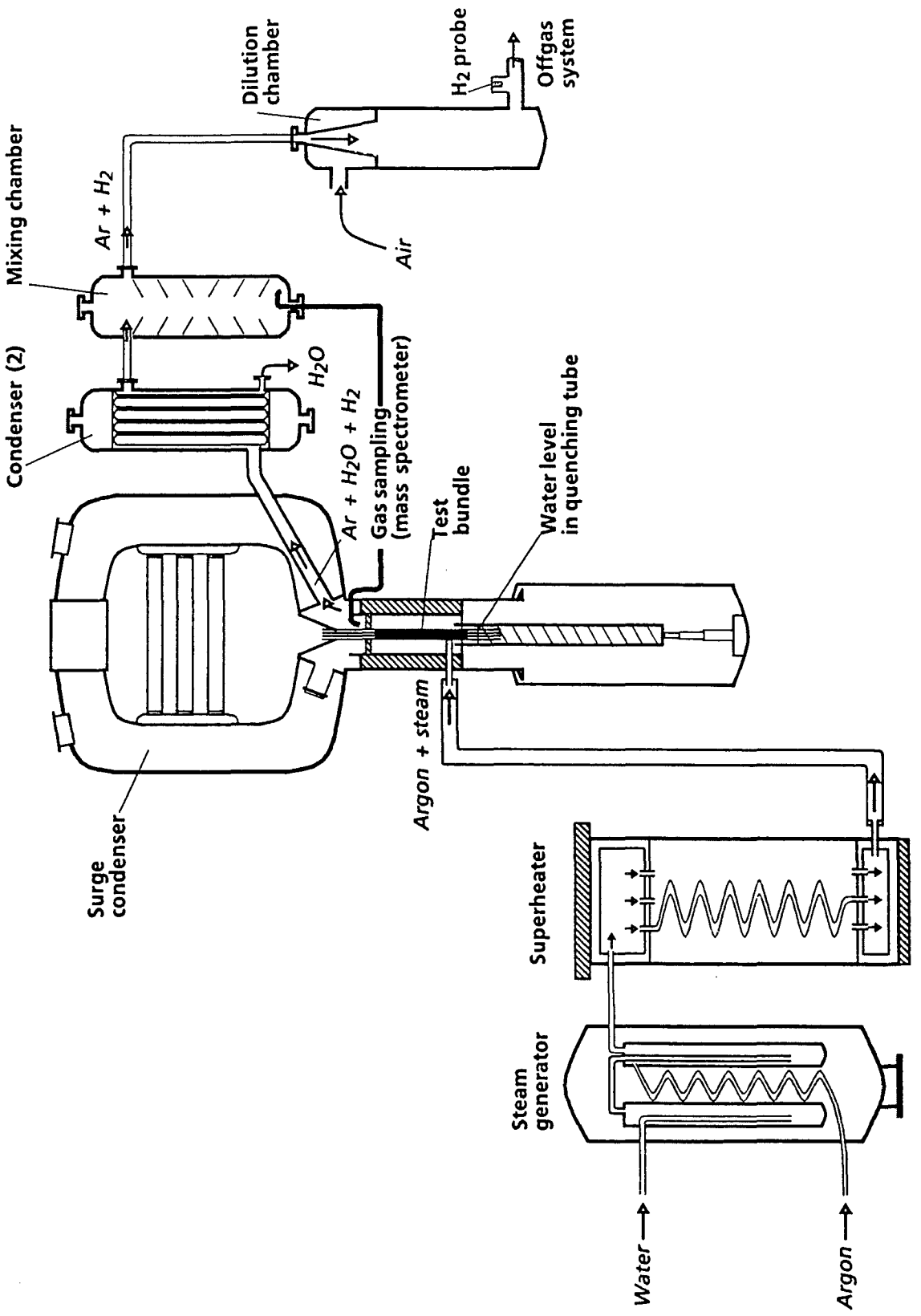

Fig. 1: SFD Test Facility (simplified flow diagram)

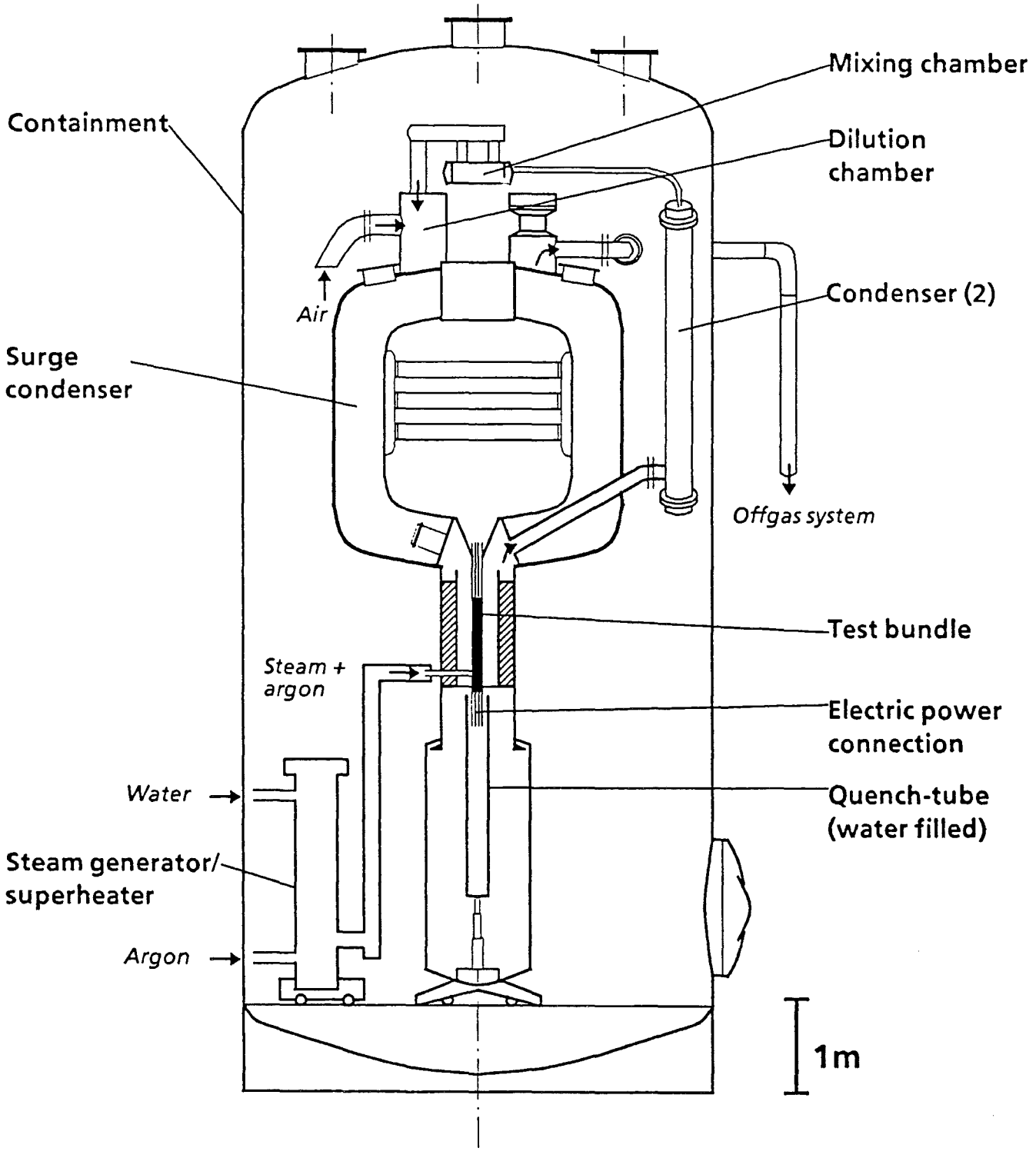

Fig. 2: SFD Test Facility CORA (Main Components)

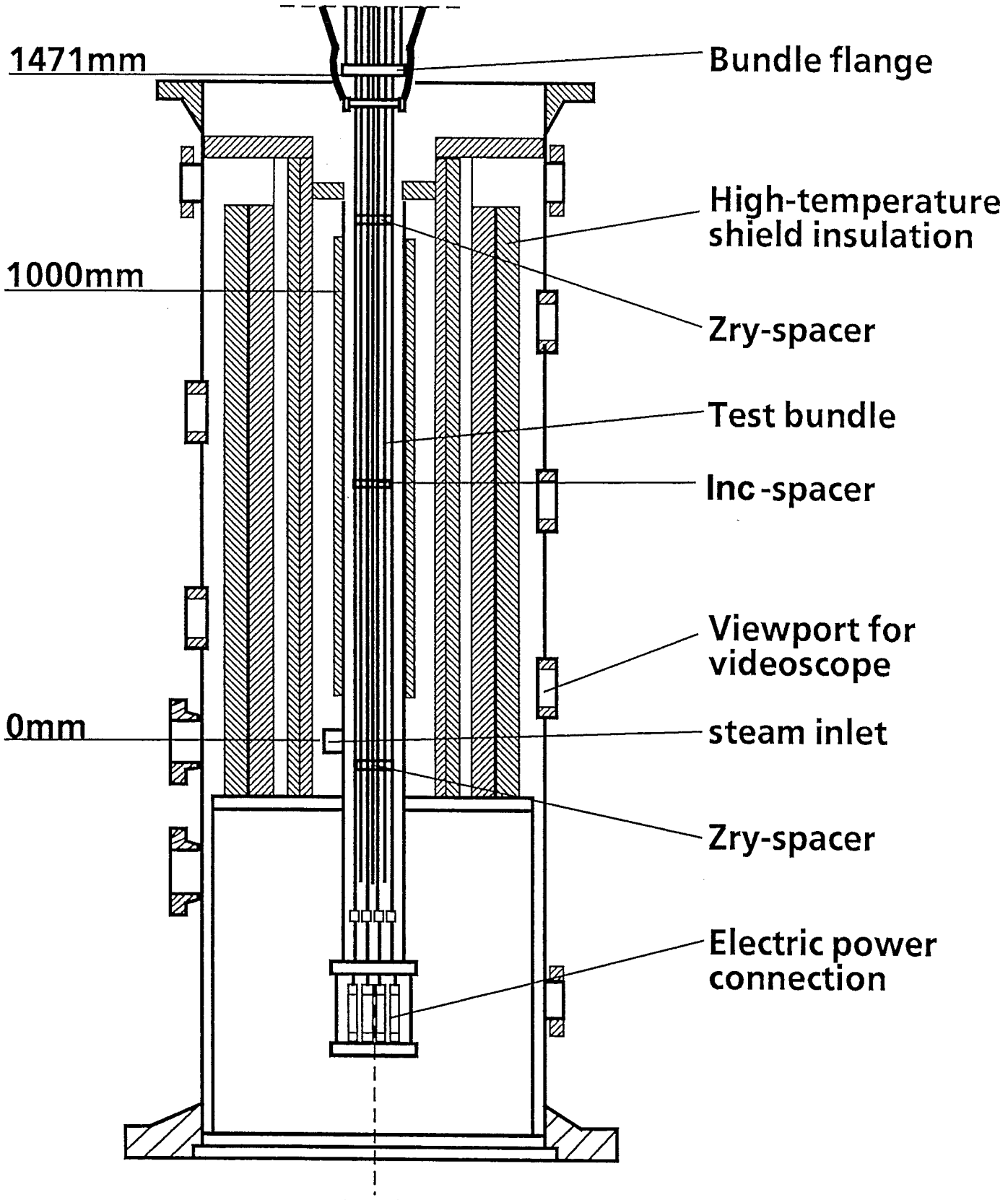

Fig. 3: CORA bundle arrangement

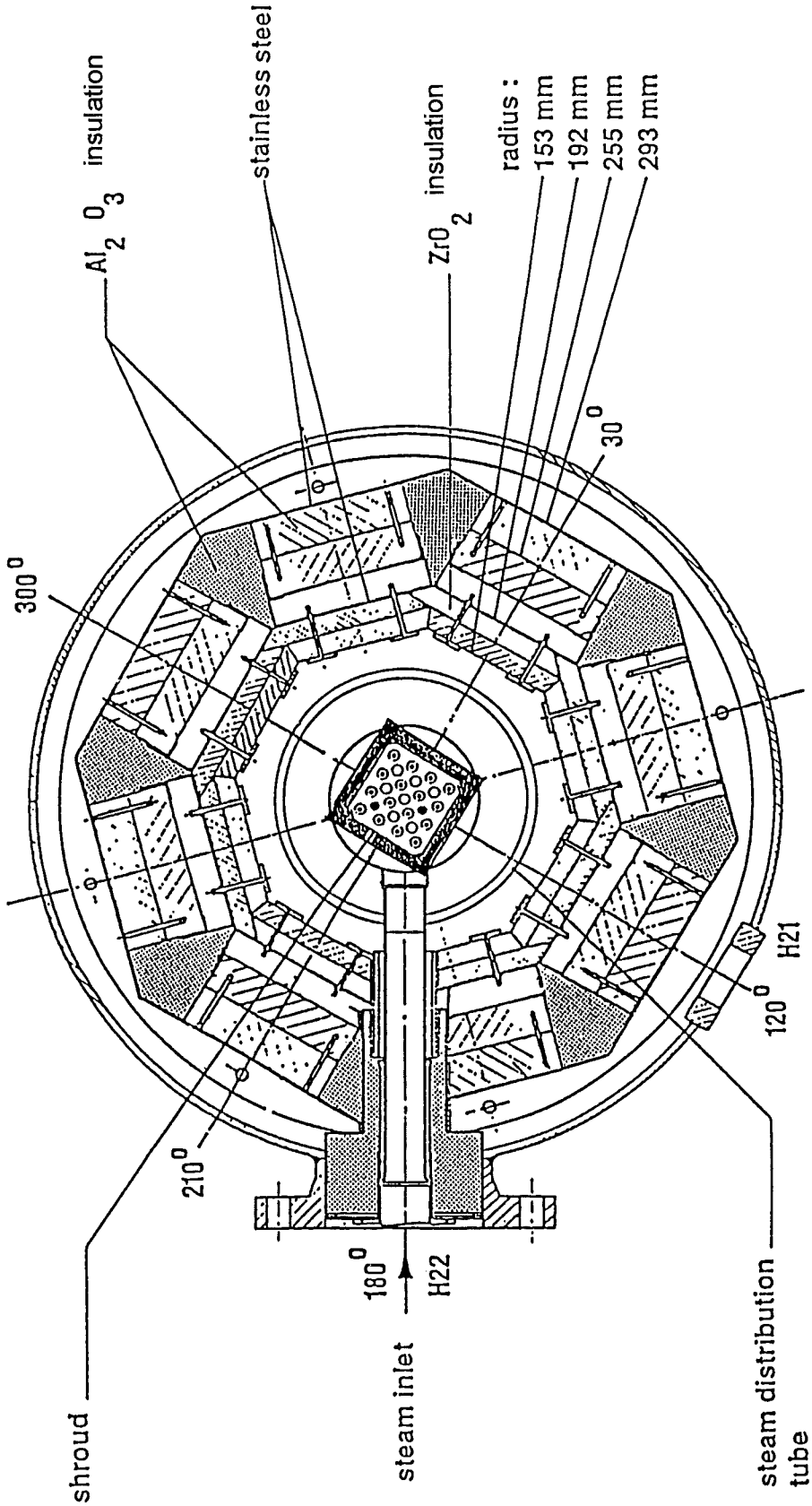

Fig. 4: Horizontal cross section of the high-temperature shield

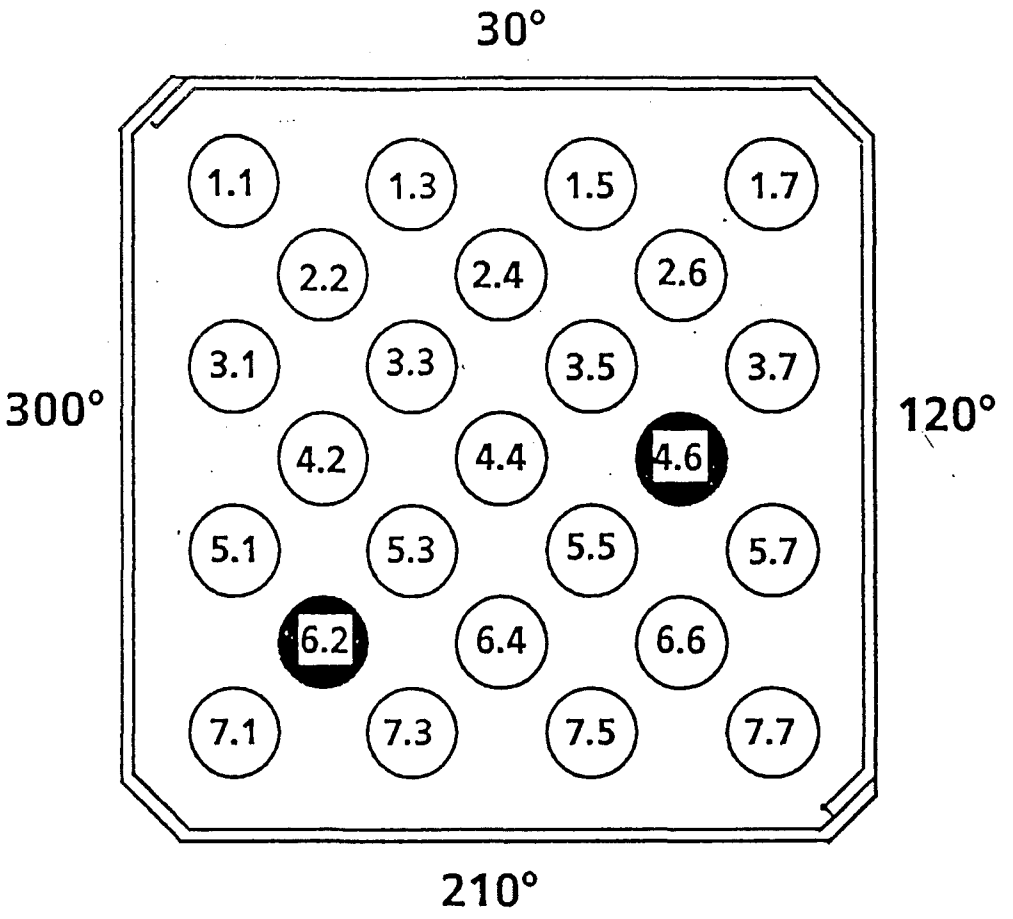

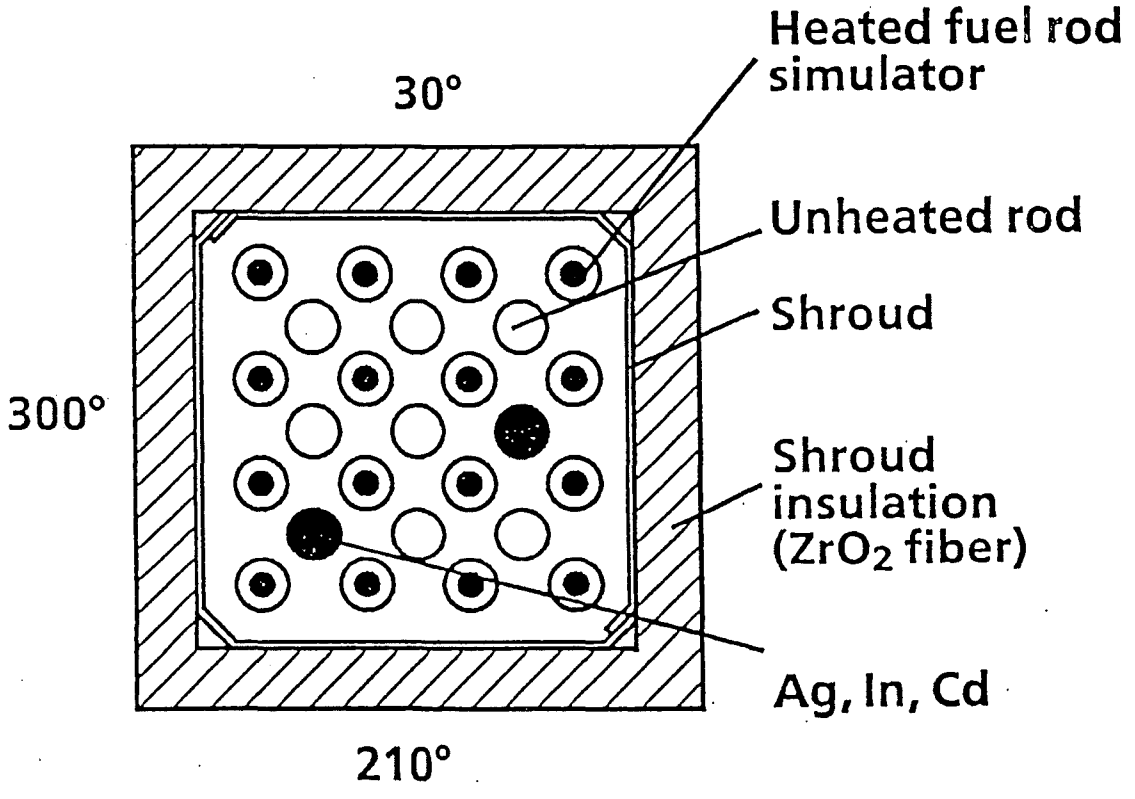

Fig. 5: Rod arrangement and test rod designation of bundle CORA-10

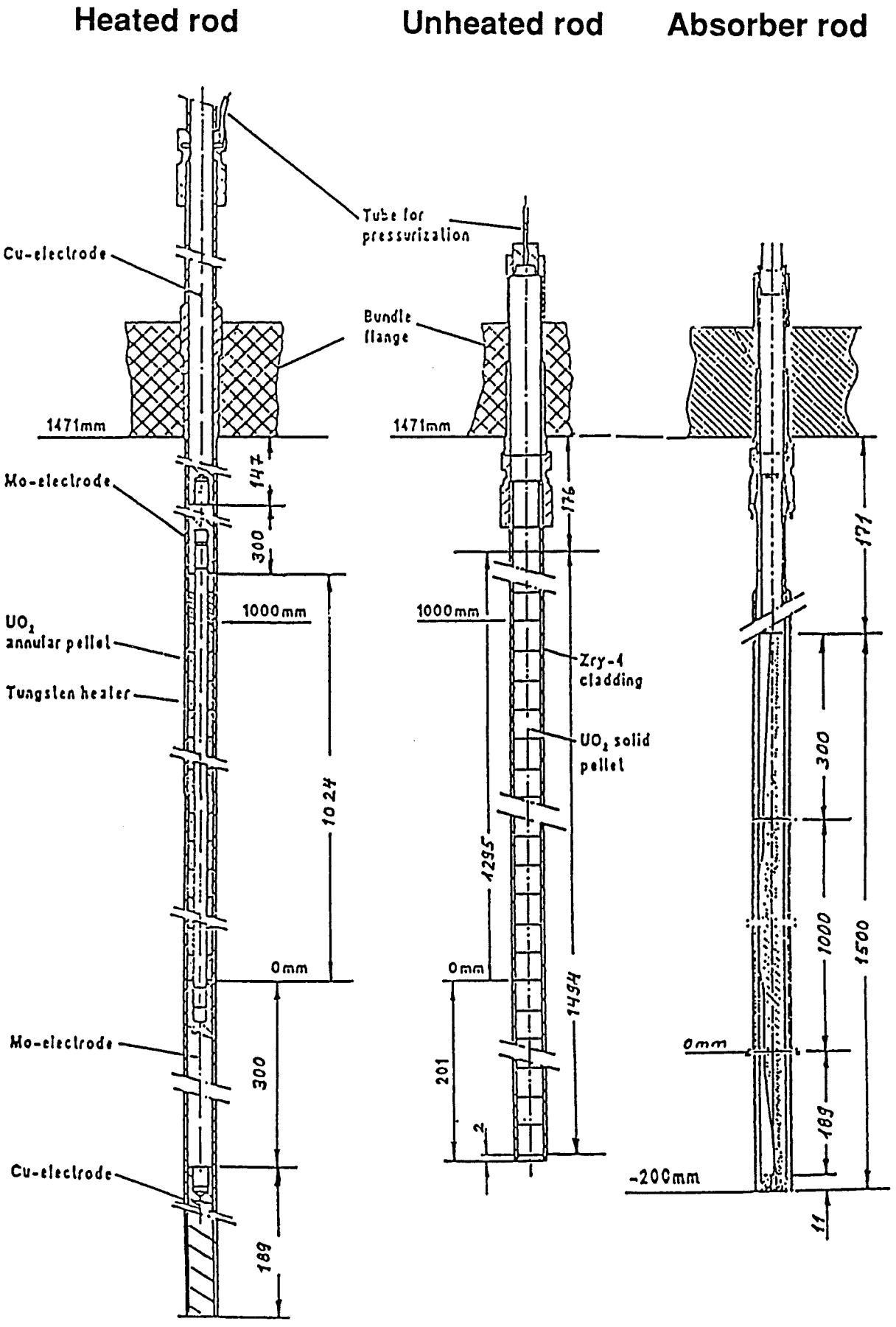

Fig. 6a: Rod types used in the CORA experiments

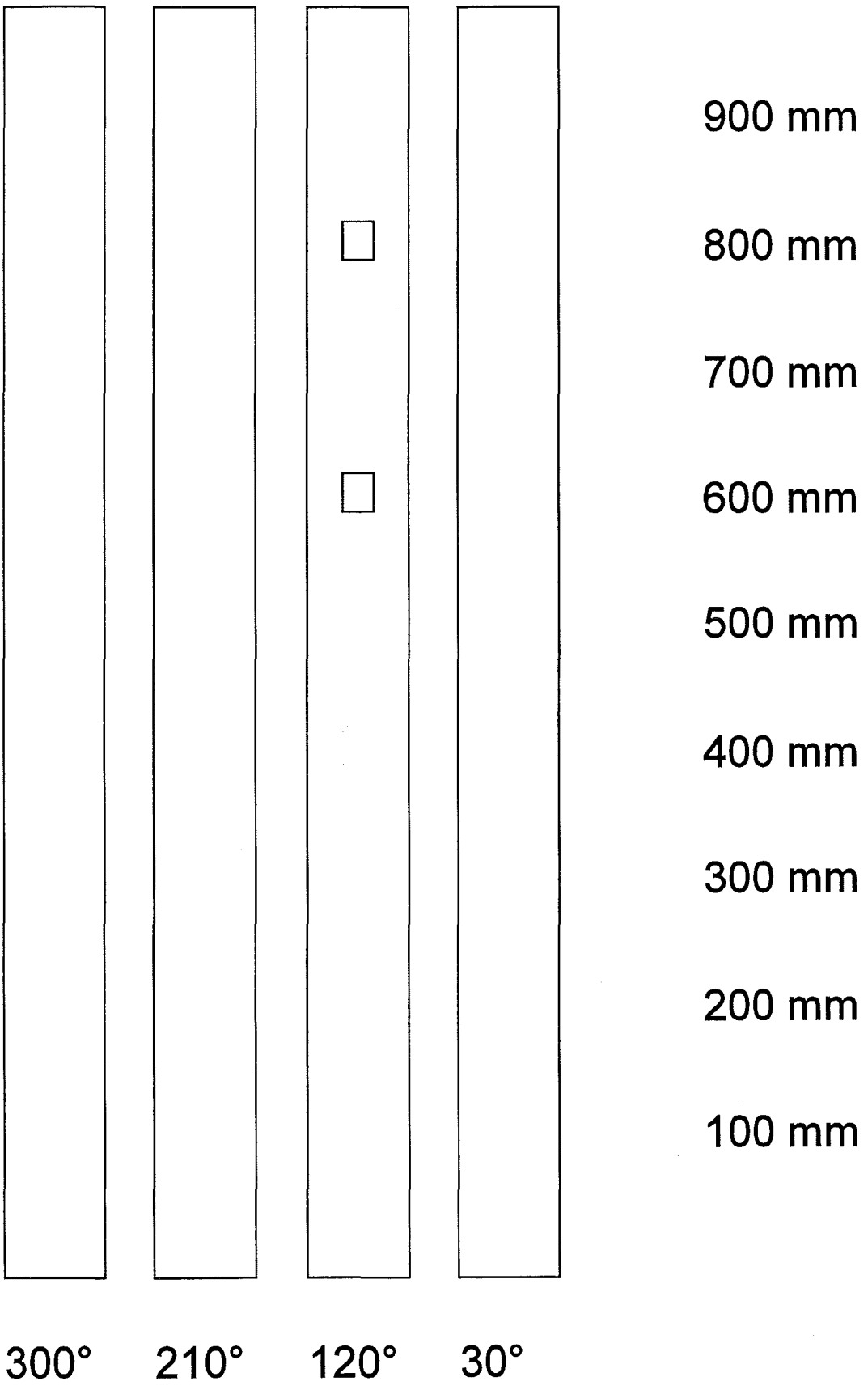

Fig. 6b: CORA-10; Position of windows in the shroud

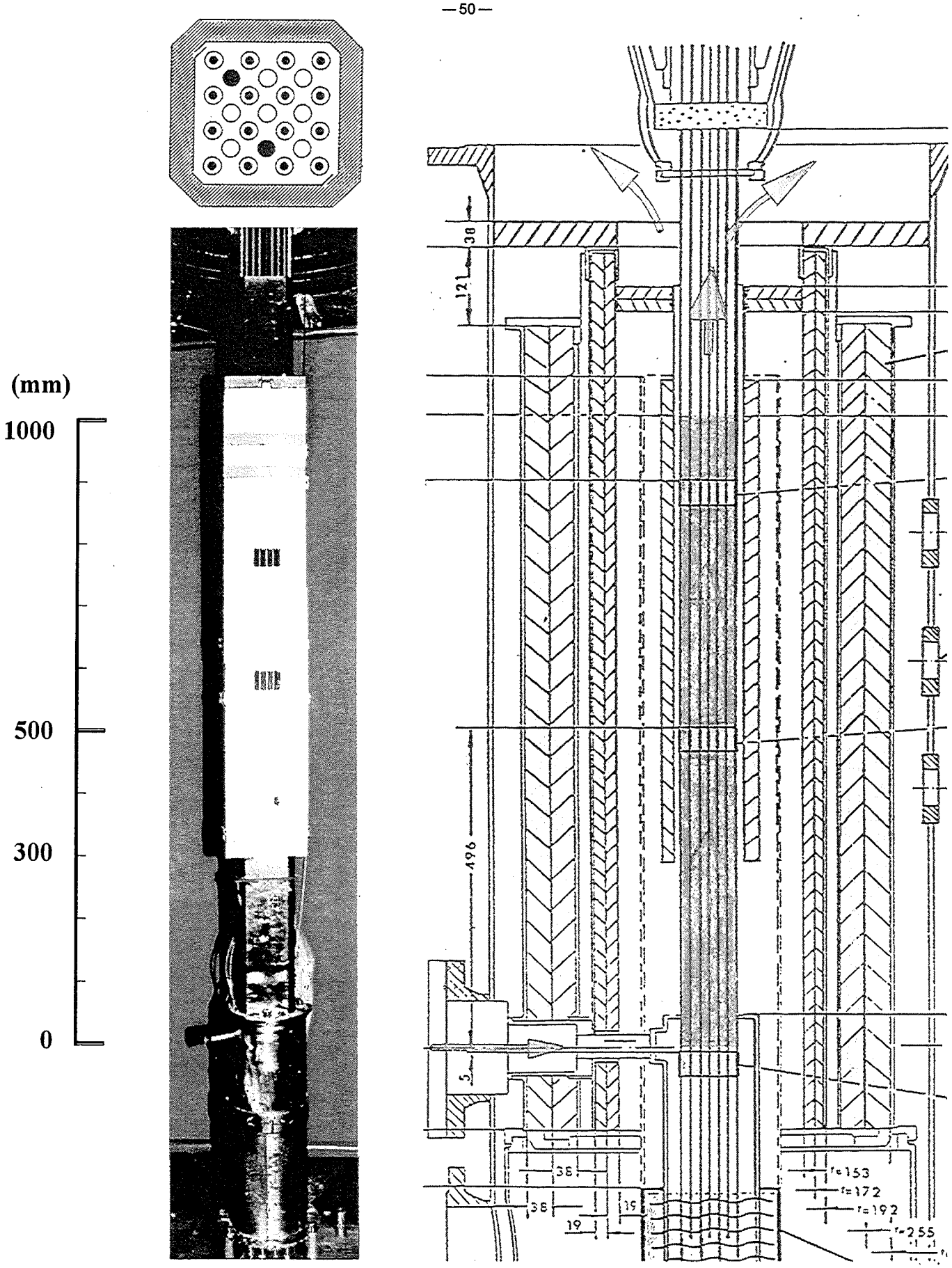

Fig. 7: CORA-10; Bundle insulation geometry

CORA - "Normal" **CORA - 10**

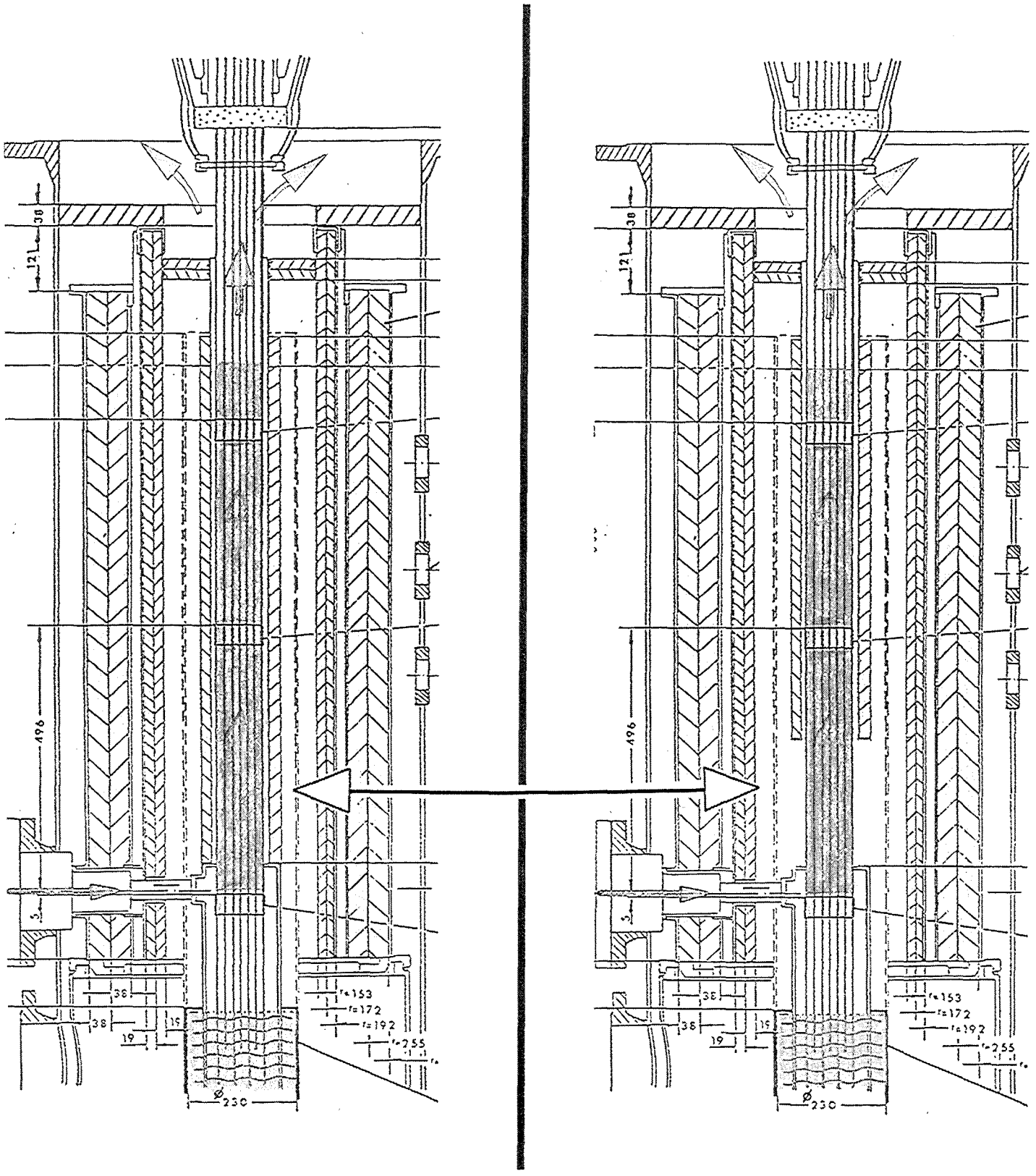

Fig. 8: Comparison of insulation geometry in test CORA-10 with normal conditions

(a)

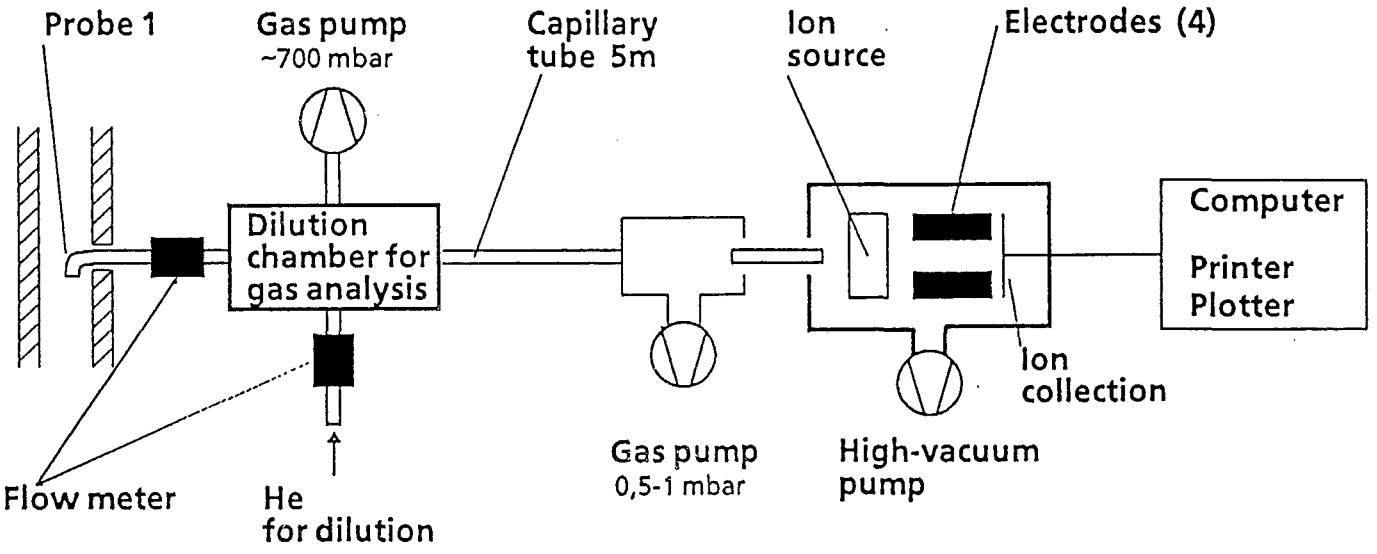

(b)

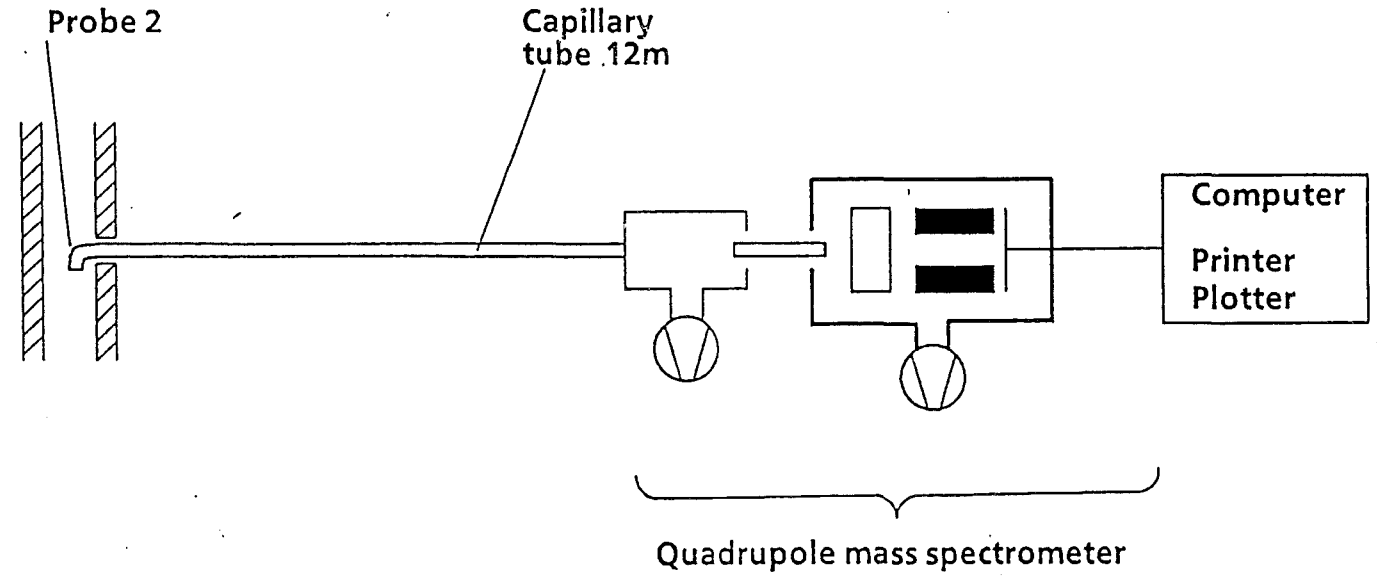

Location (a): Outlet of test section

Location (b): Mixing chamber

Fig. 9: Hydrogen measurement

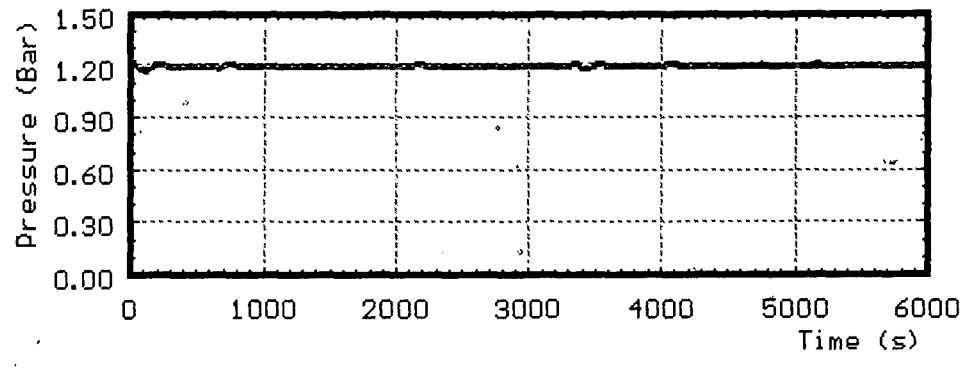

system overpressure

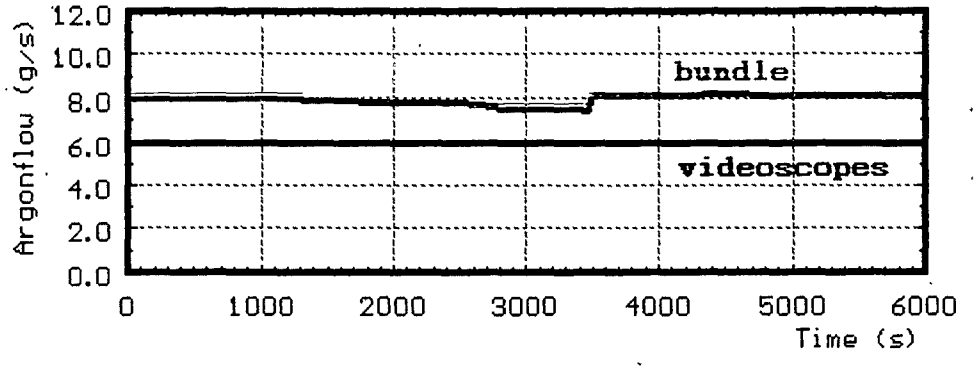

argonflow

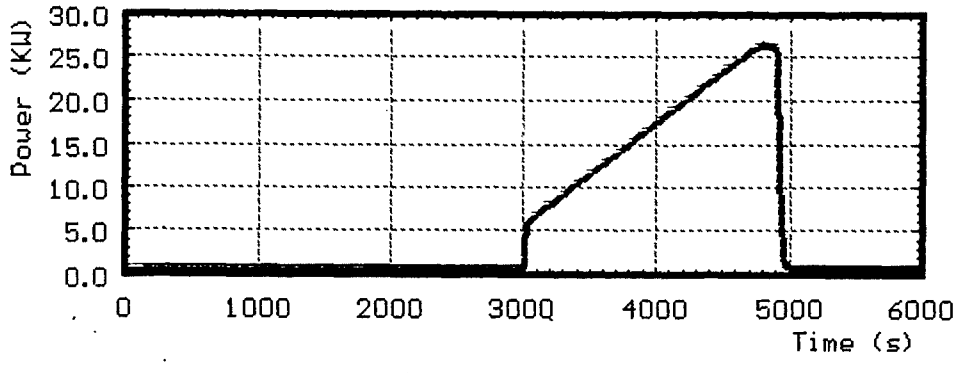

power

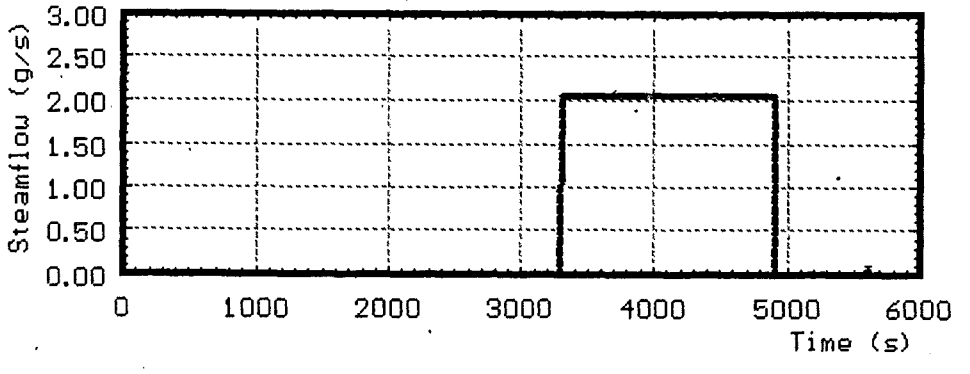

steam input

Fig. 10: CORA-10; System pressure, argon flow, steam input and power

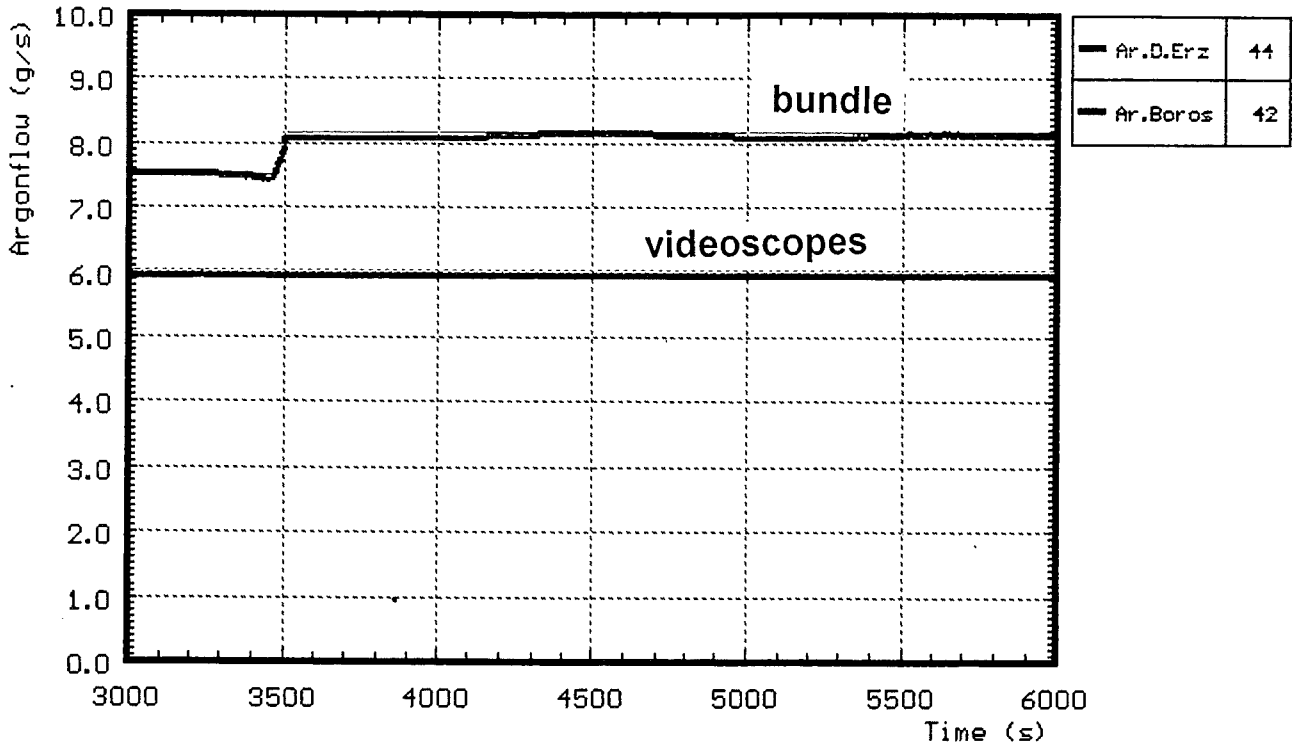

Fig. 11: CORA-10; Argon flow through bundle and videoscopes

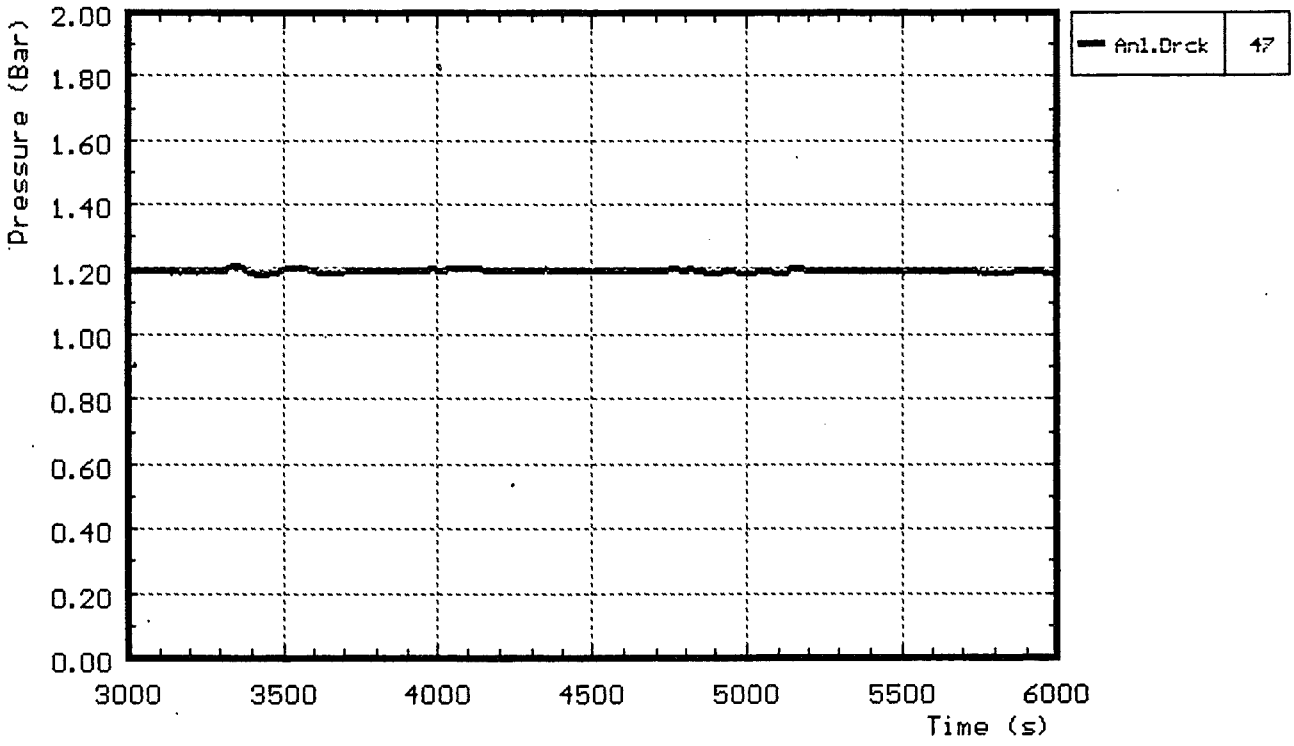

Fig. 12: CORA-10; System pressure (gauge)

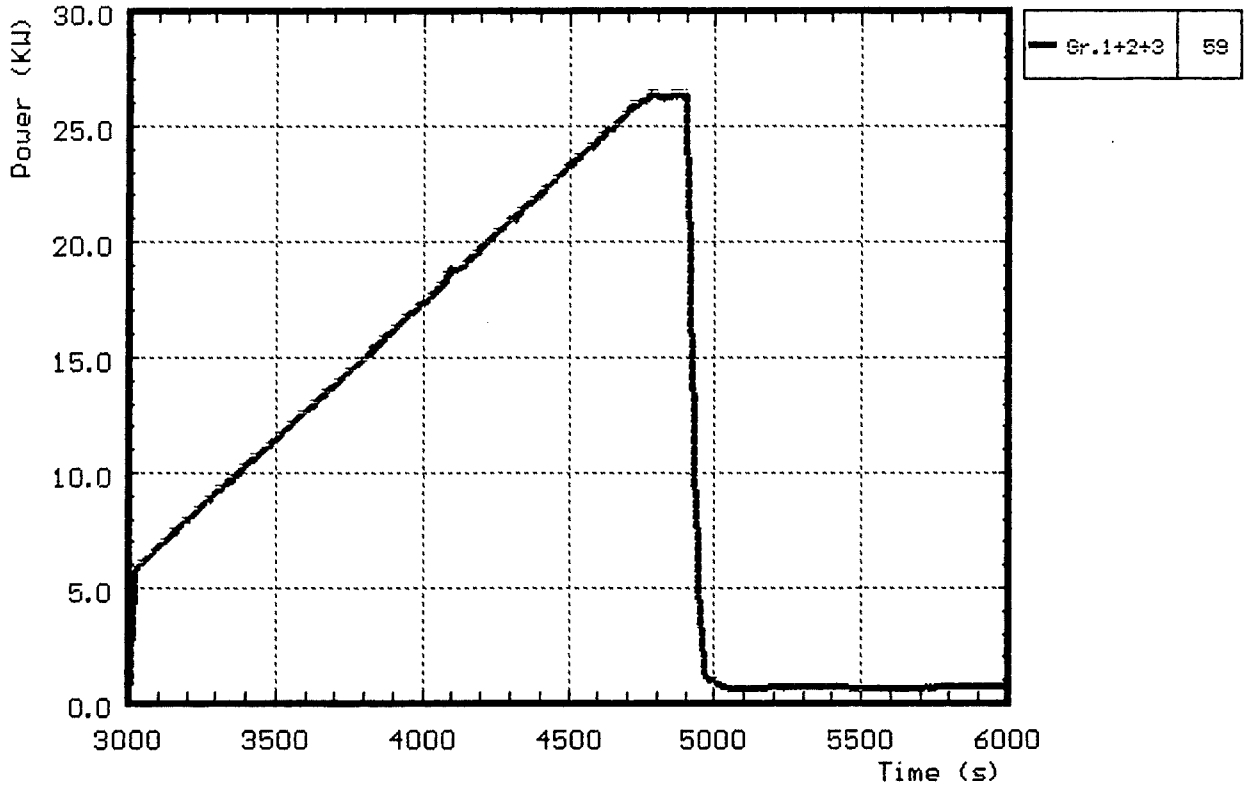

Fig. 13: CORA-10; Total electric power input

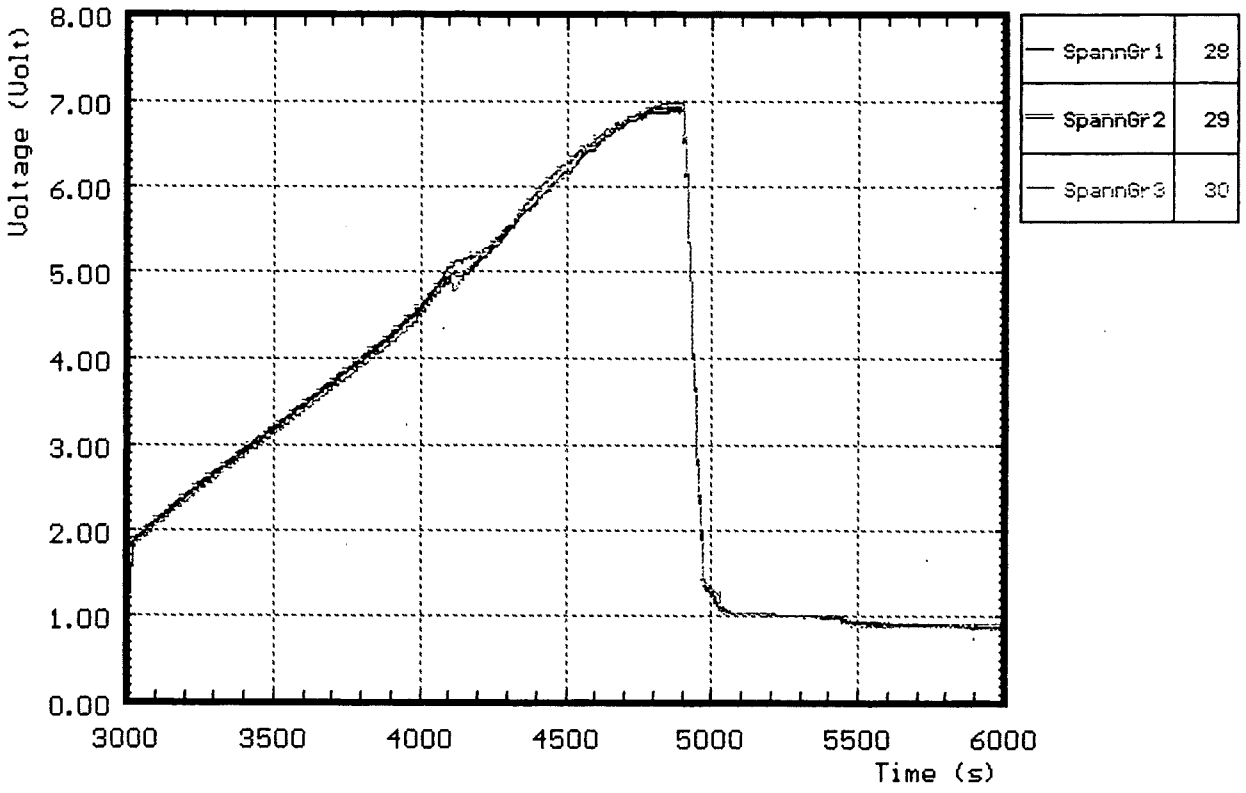

Fig. 14: CORA-10; Voltage input for the 3 rod groups

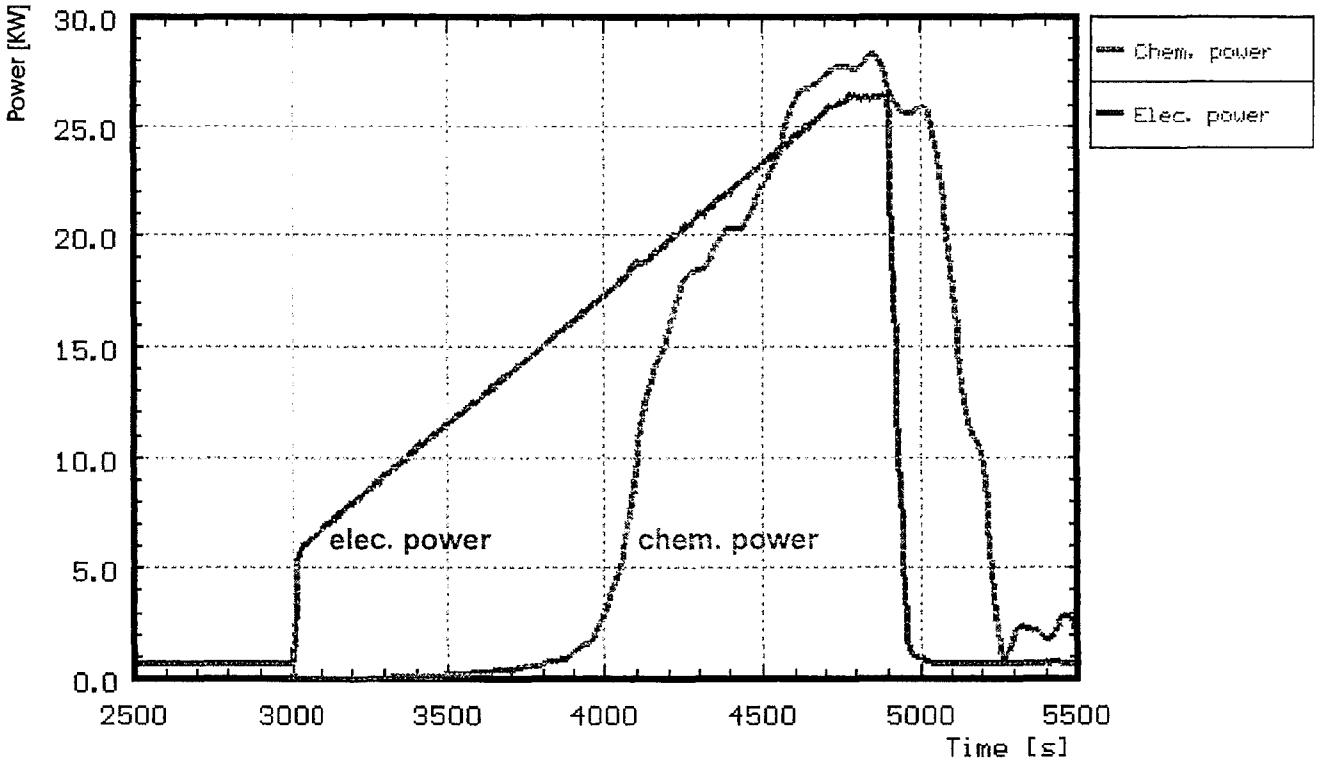

Fig. 15: Comparison of chemical and electric power c10f15.cdr

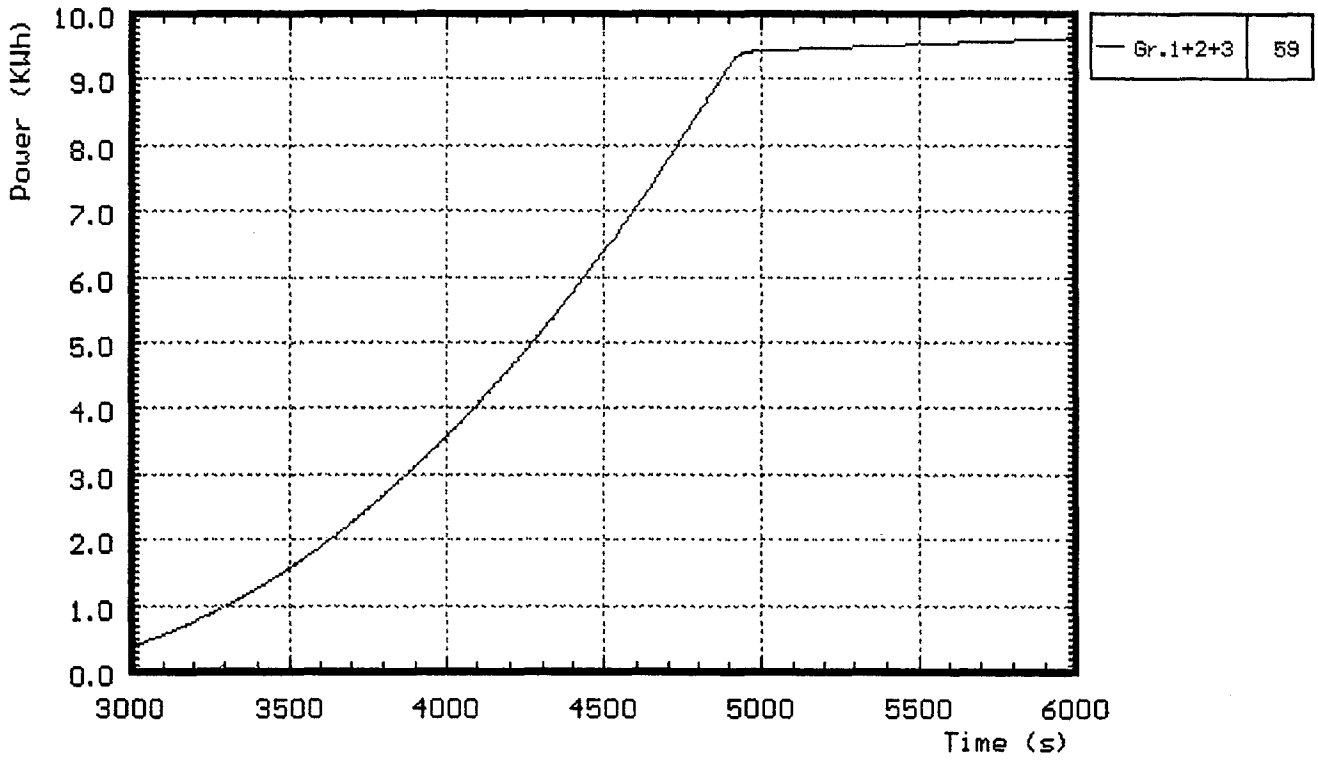

Fig. 16: Total electric energy input

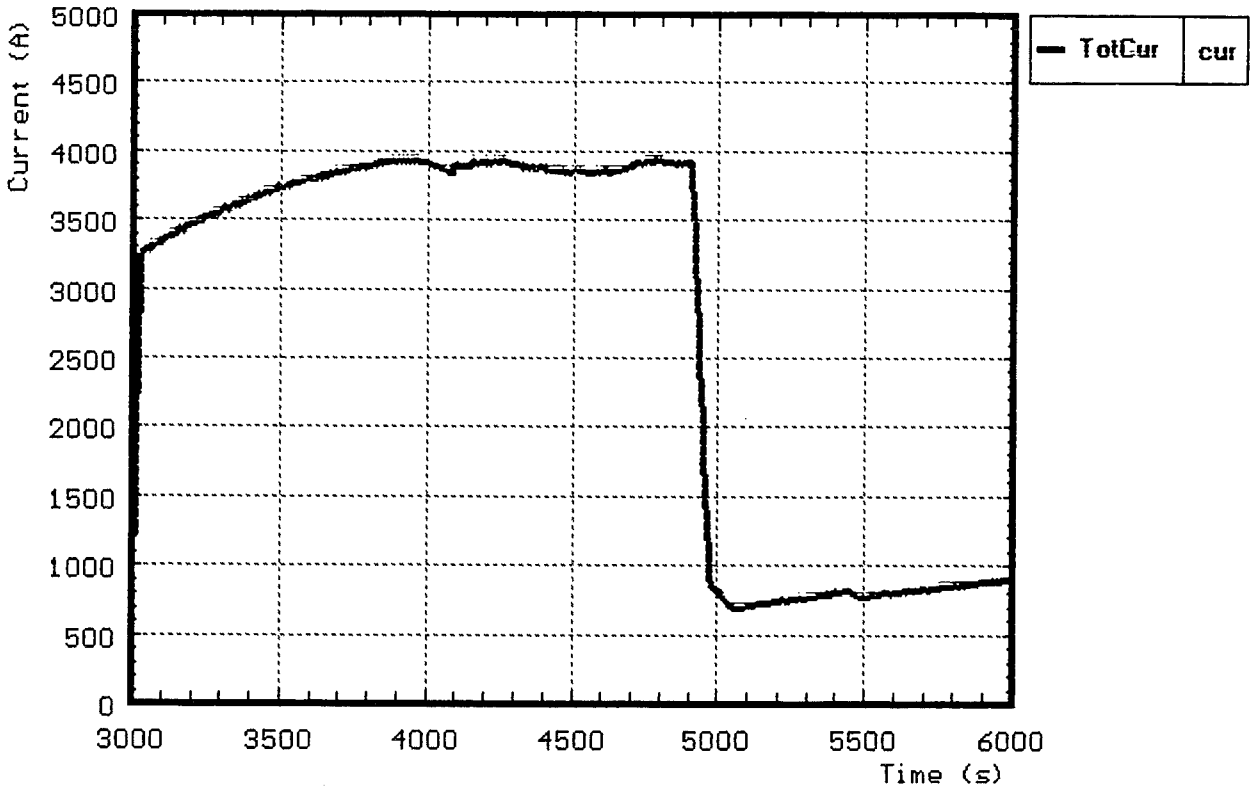

Fig. 17: Total current

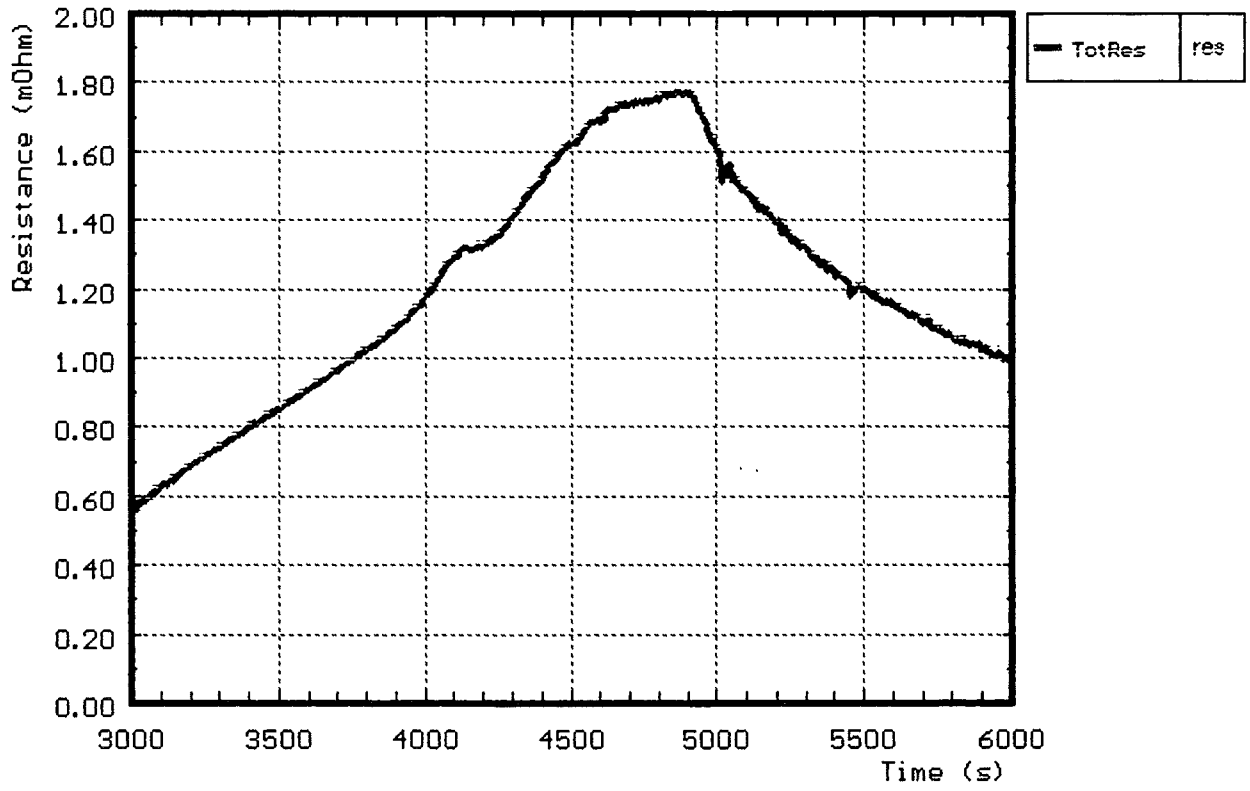

Fig. 18: Resistance of bundle
(Voltage group 1 / total current)

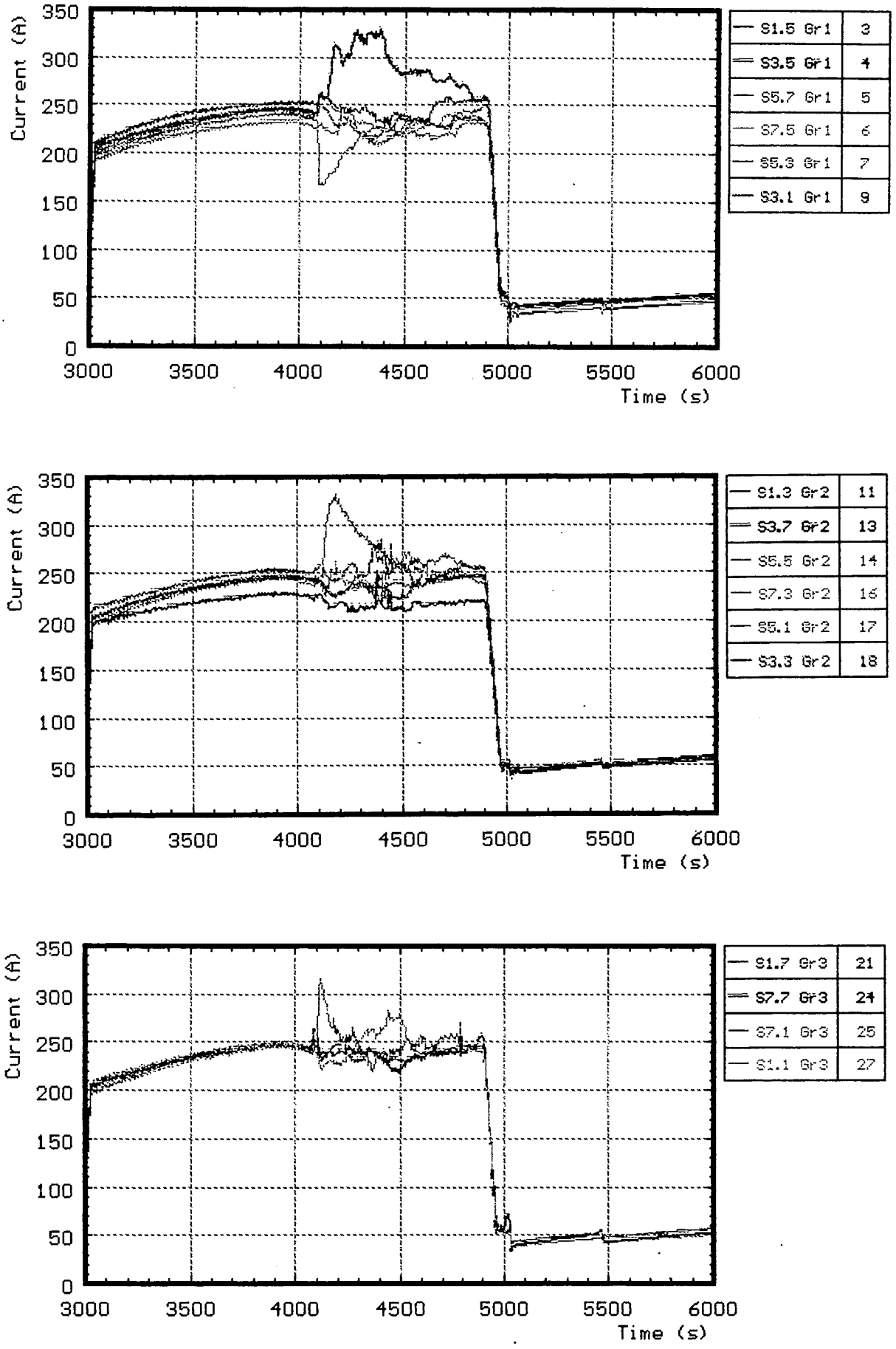

Fig. 19: Variations of currents within the rod groups

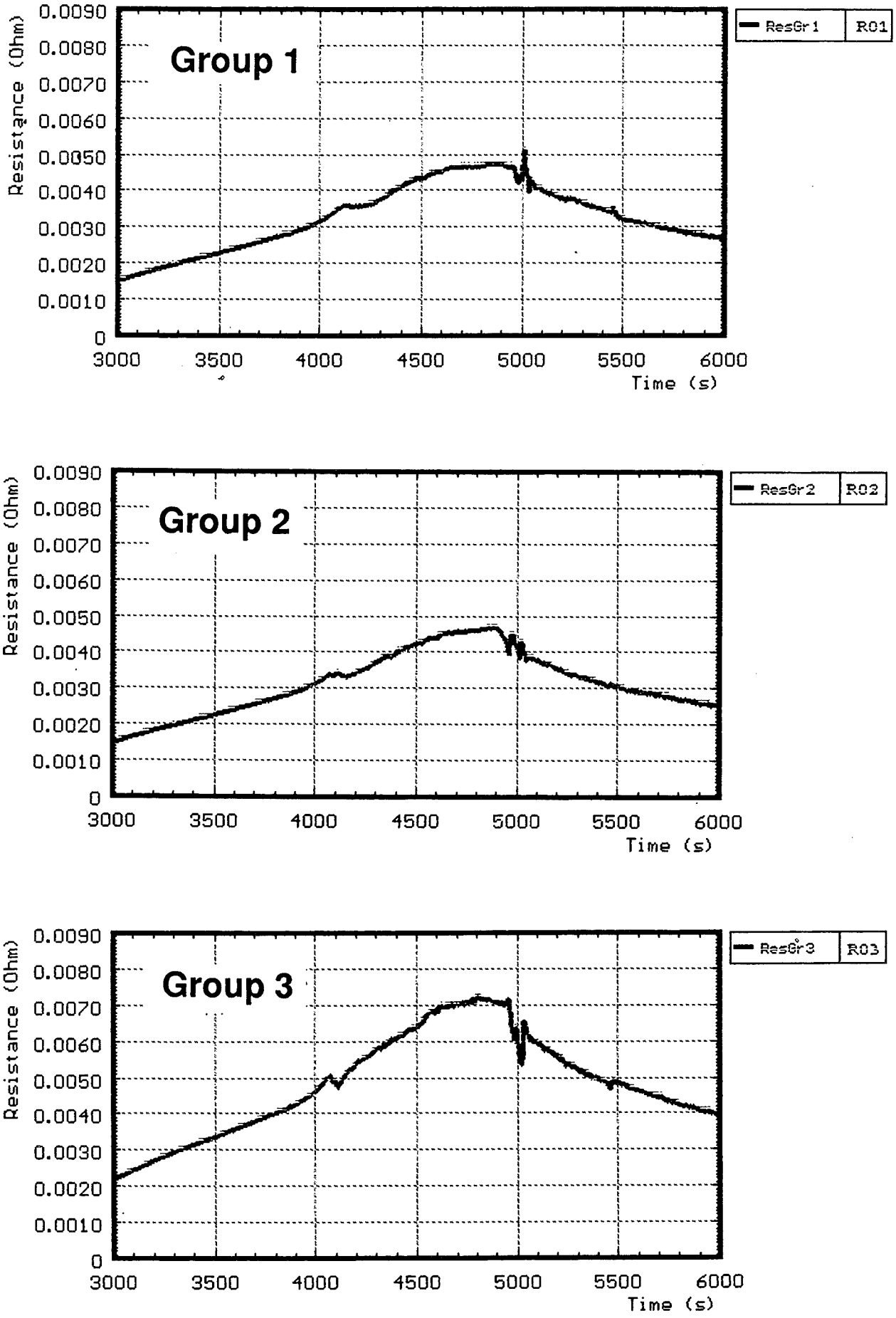

Fig. 20: CORA-10; Resistance of the rod groups

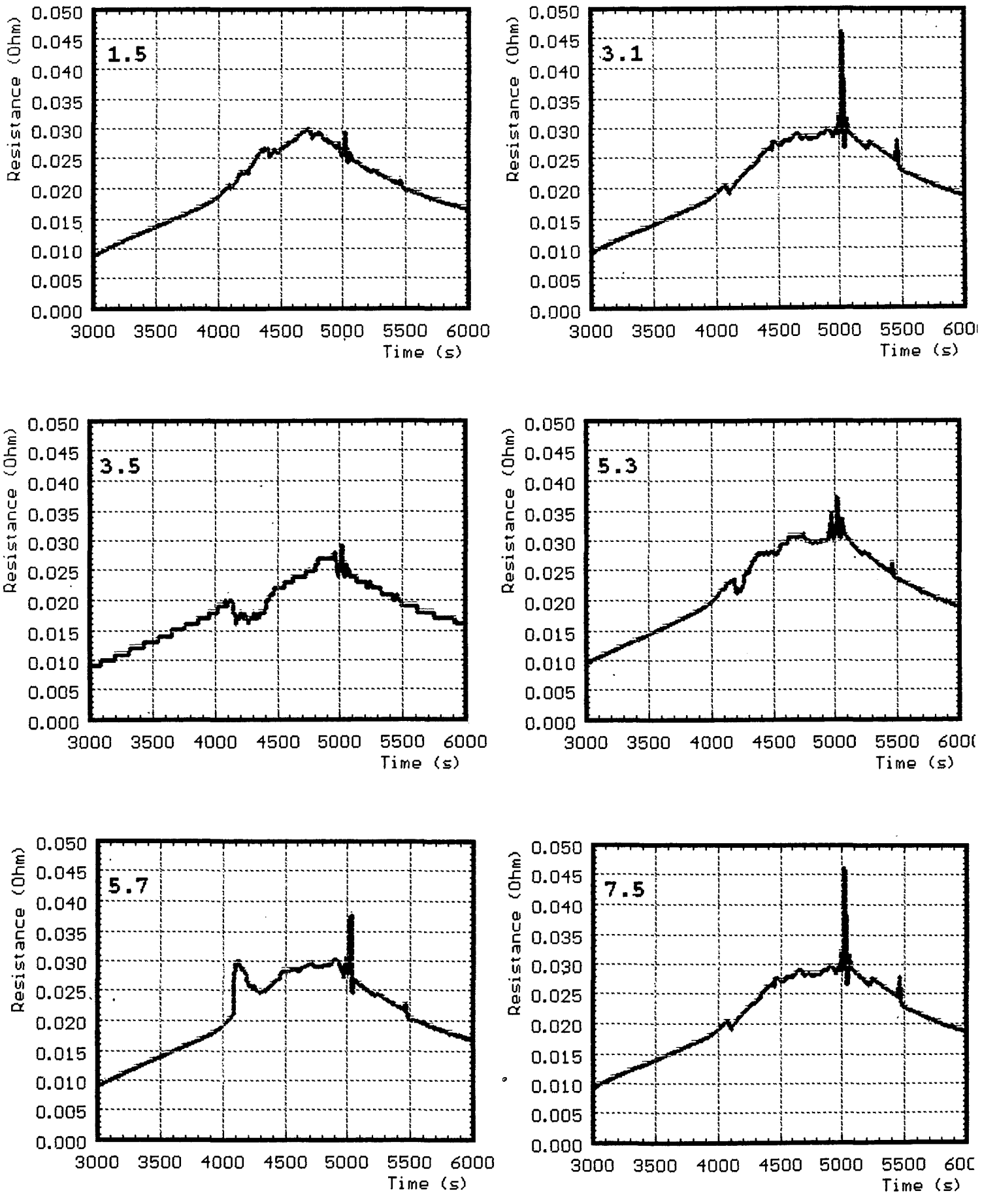

Fig. 21: CORA-10; Resistance of rods group 1

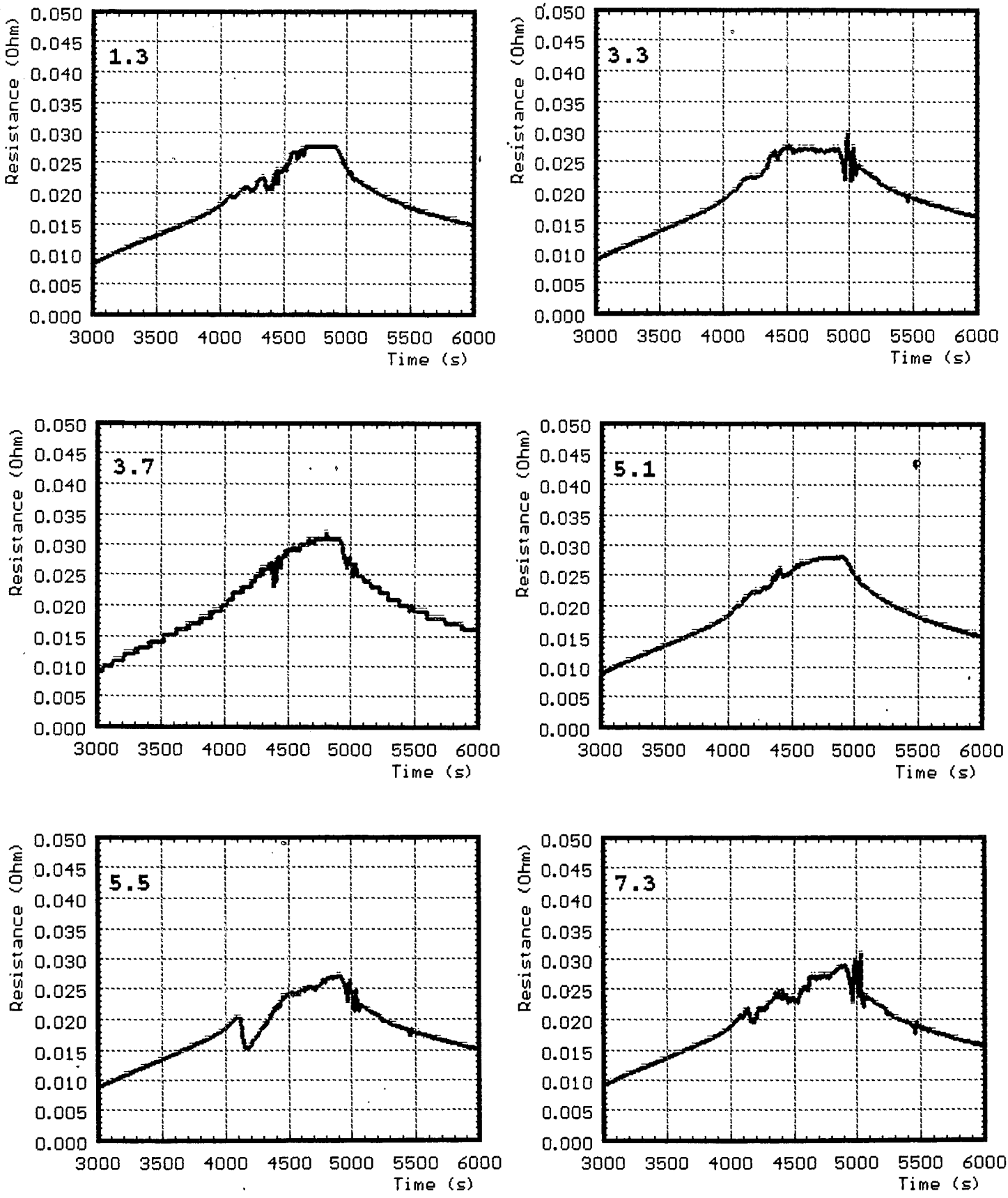

Fig. 22: CORA-10; Resistance of rods group 2

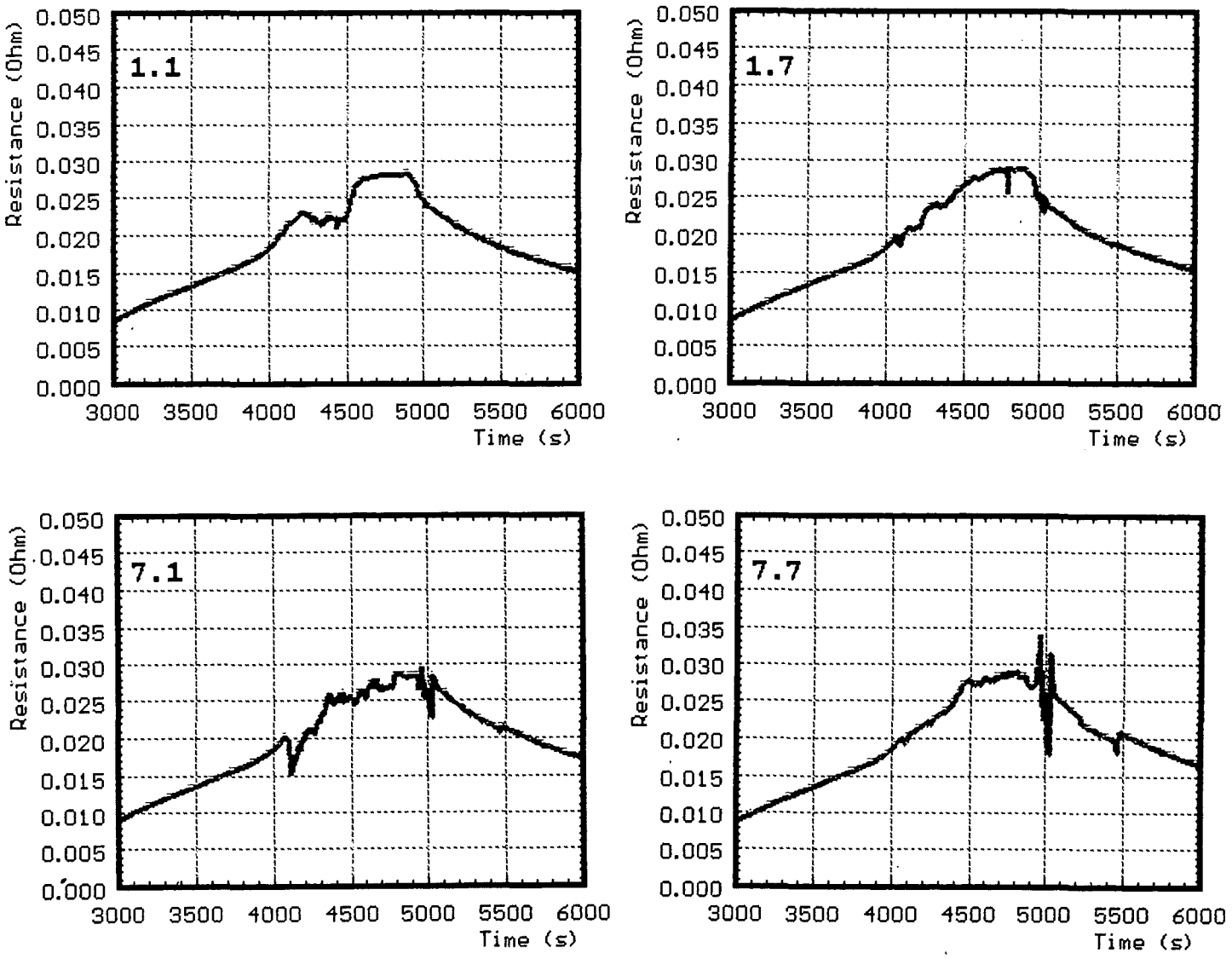

Fig. 23: CORA-10; Resistance of rods group 3

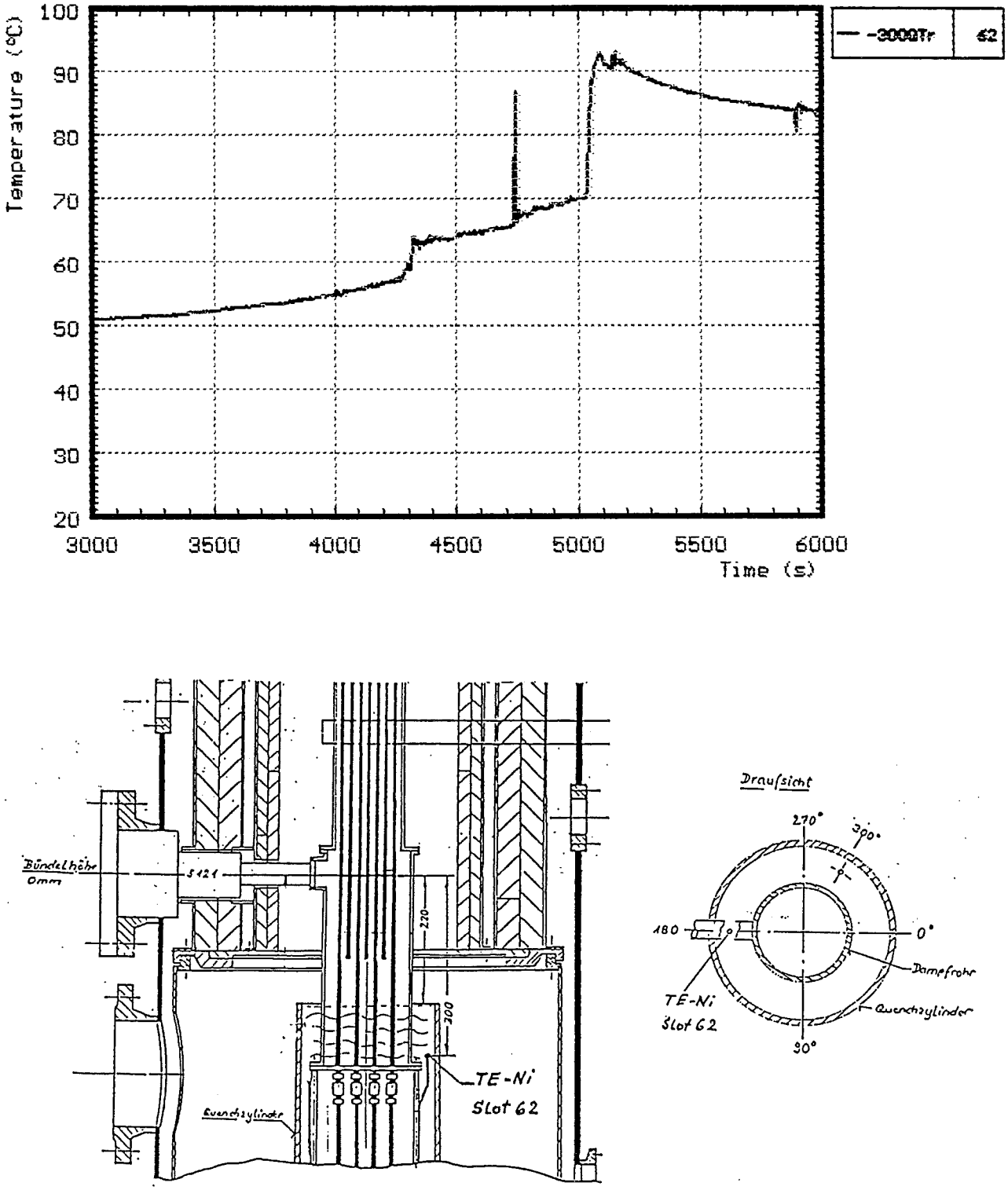

Fig. 24: CORA-10; Water temperature in the quench cylinder

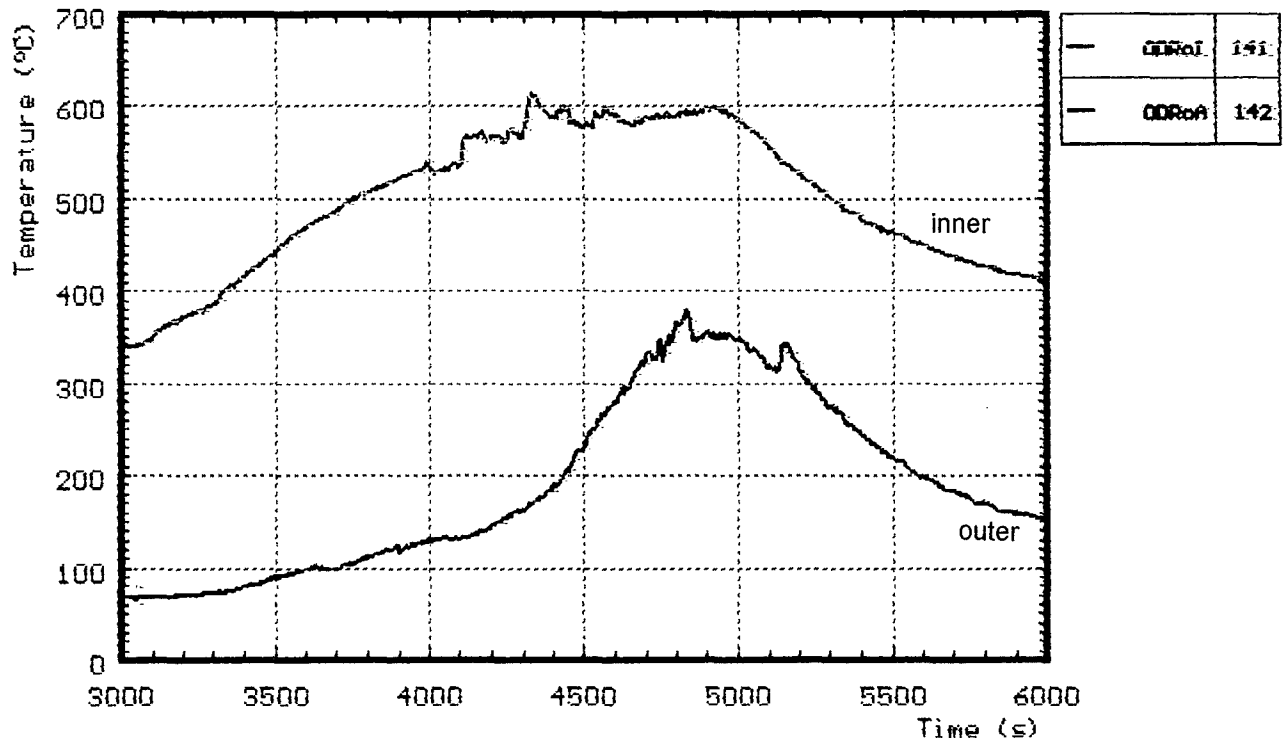

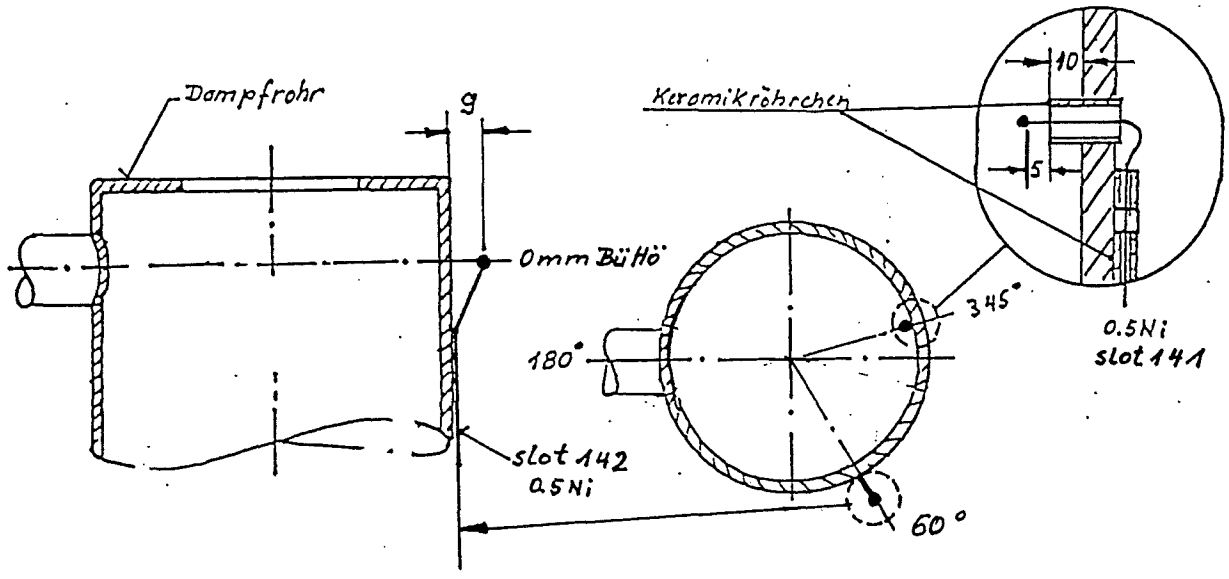

Fig. 25: CORA-10; Temperature on inner side and outer side of steam tube at 0mm elevation

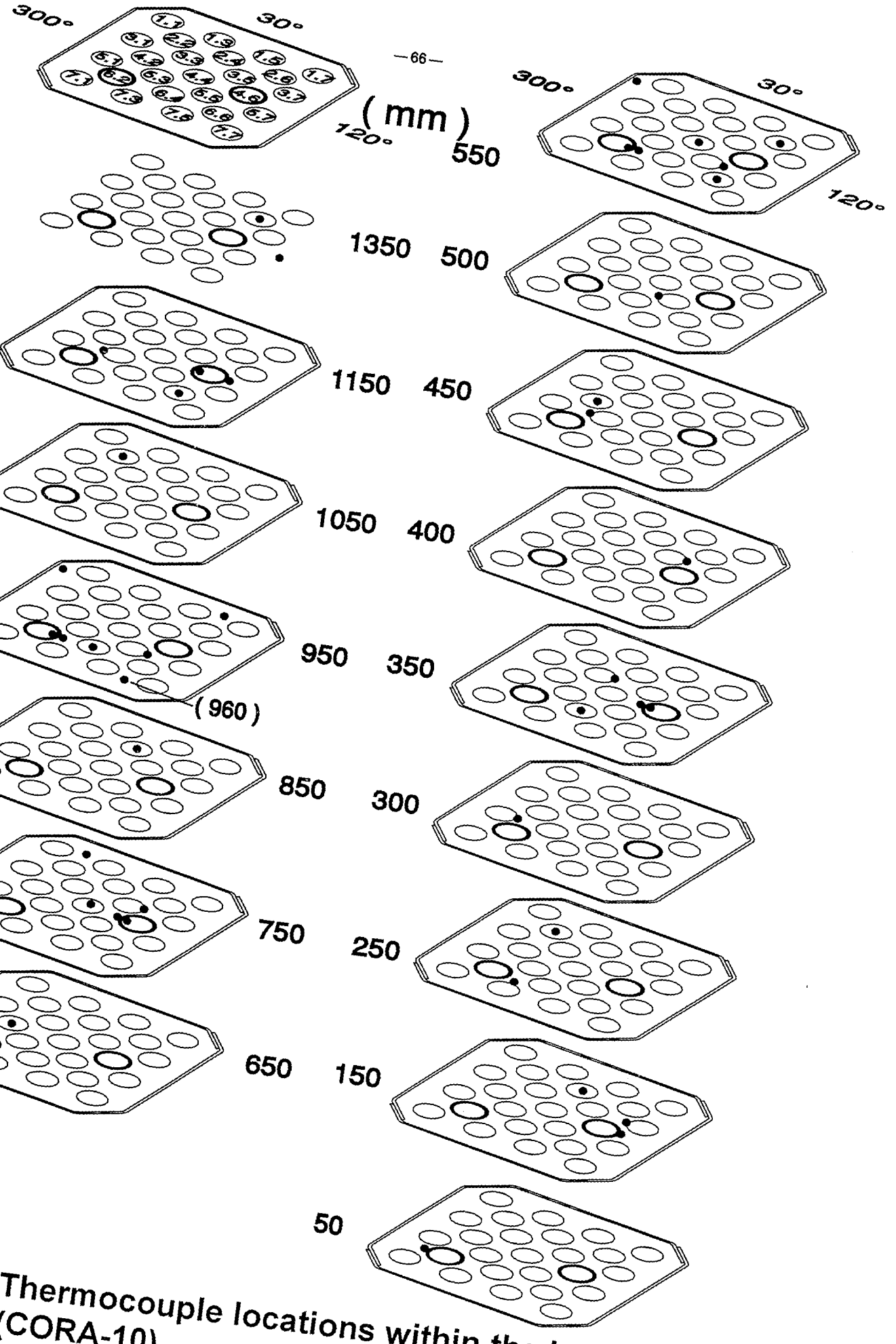

Fig. 26: Thermocouple locations within the bundle (CORA-10)

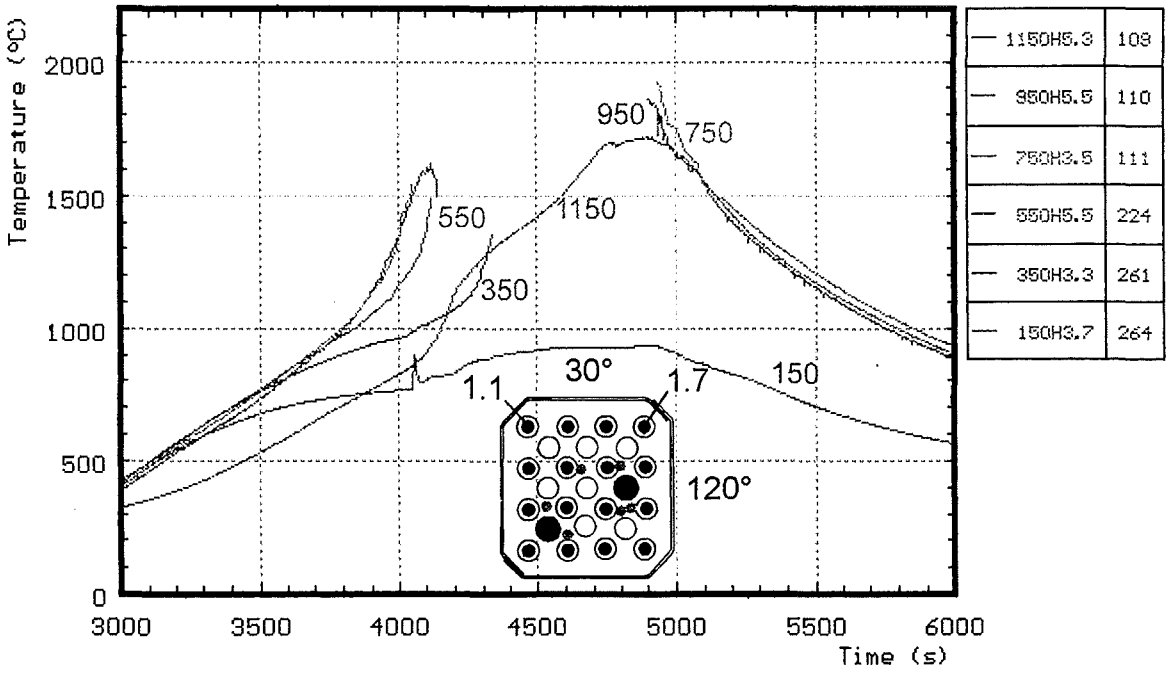

Fig. 27: CORA-10; Temperatures of heated rods

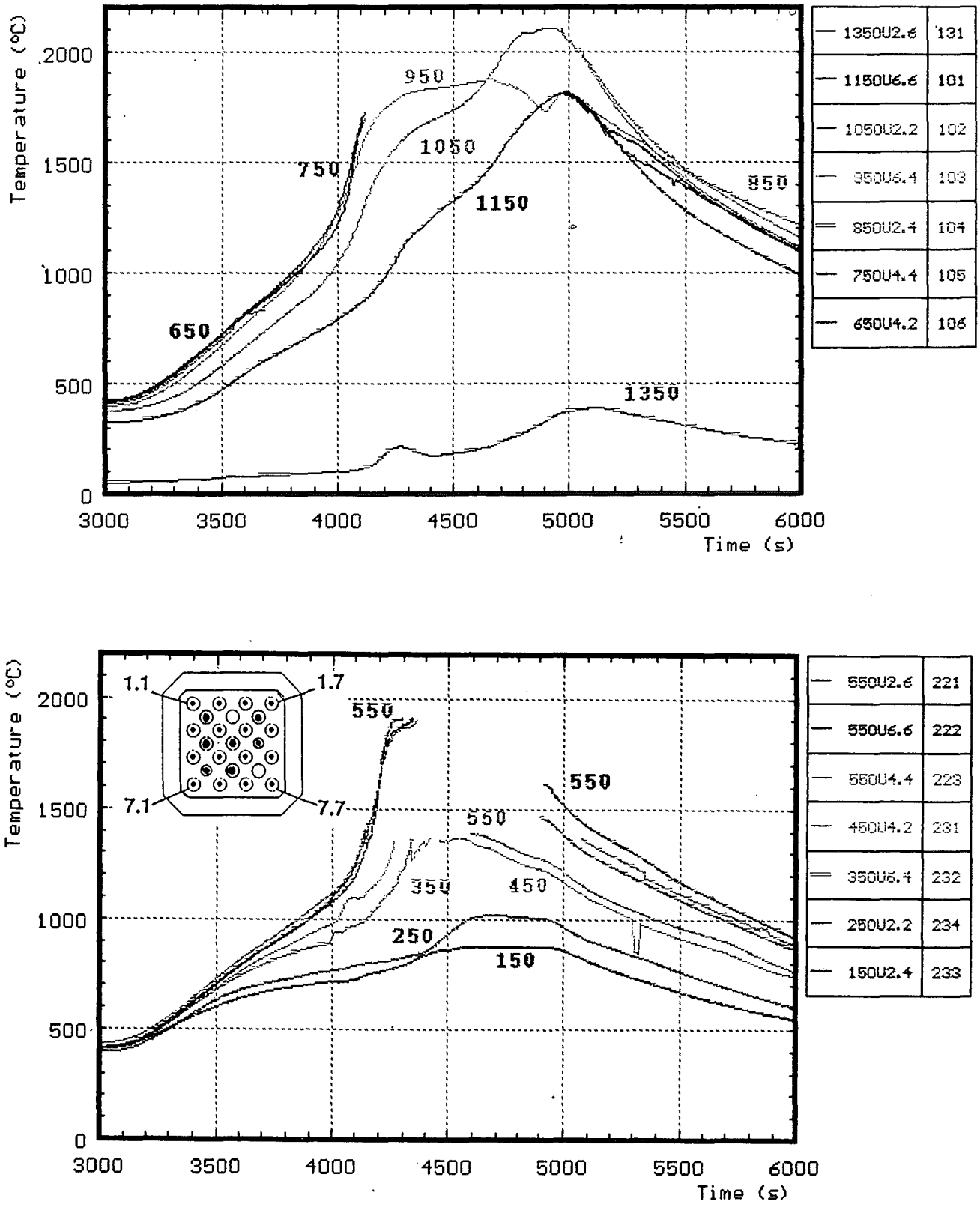

Fig. 28: CORA-10; Temperatures of unheated rods

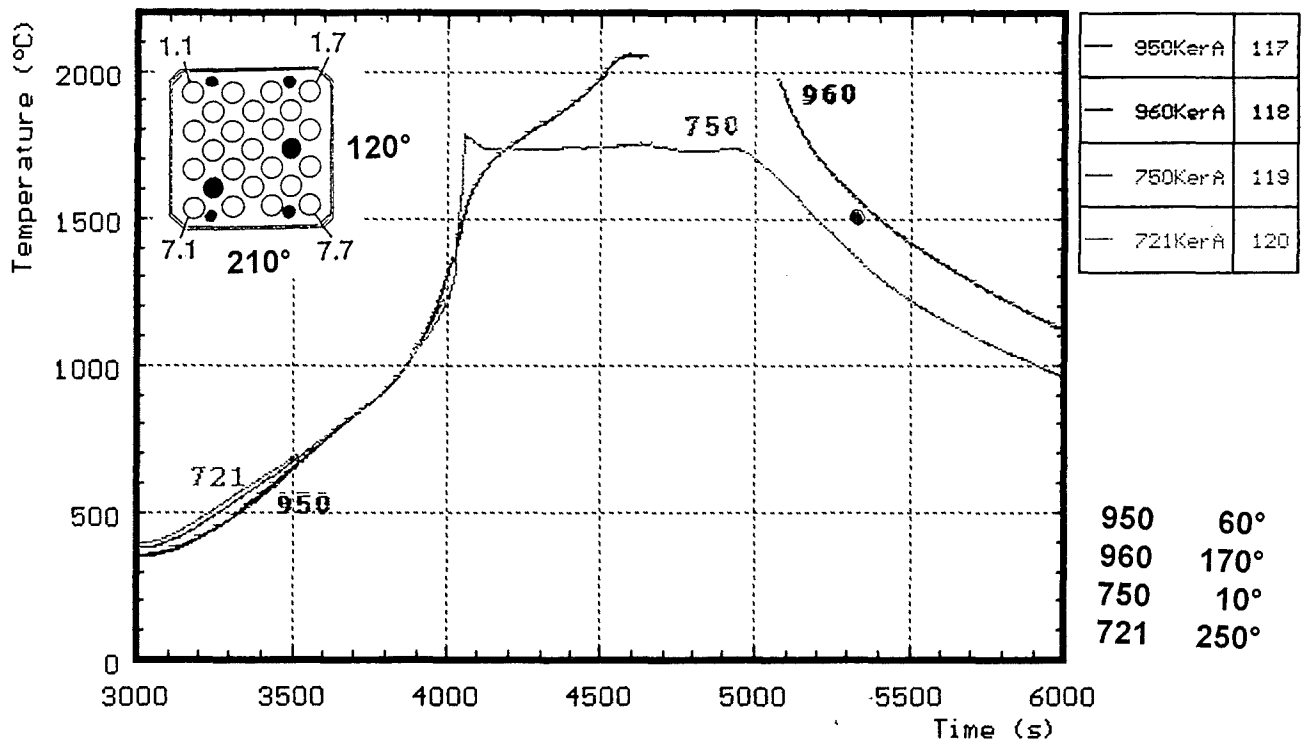

Fig. 29: CORA-10; Temperatures measured with ceramic protected TCs

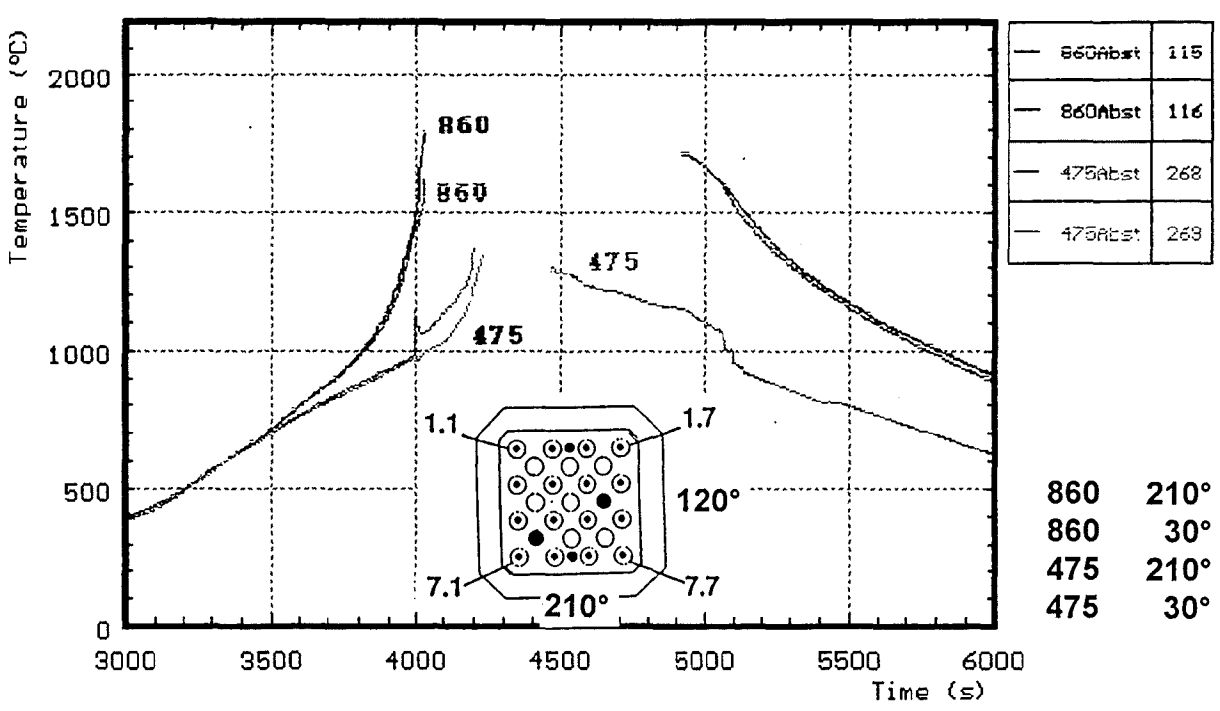

Fig. 30: CORA-10; Temperatures on the spacers used in test CORA-10

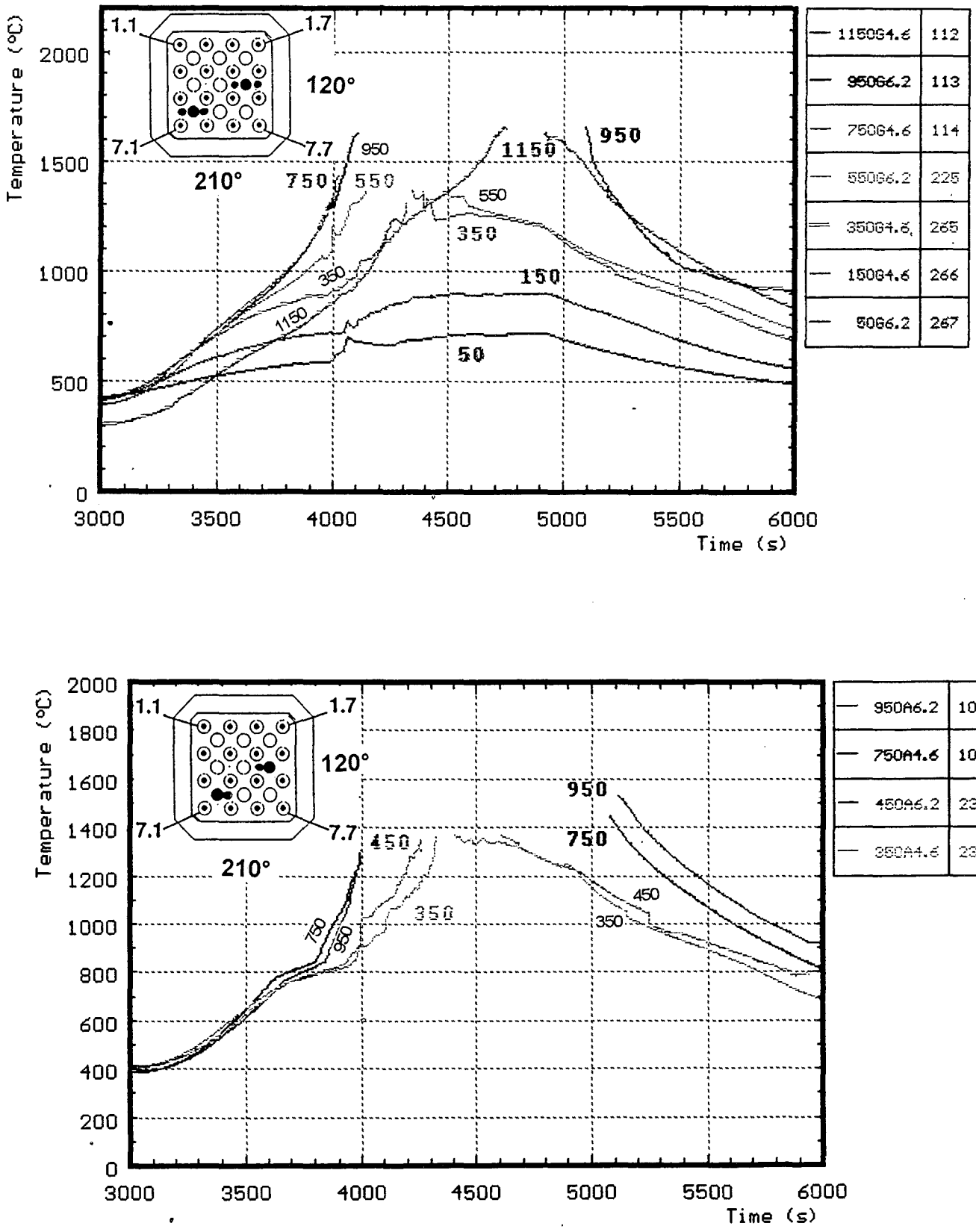

Fig. 31: CORA-10; Temperatures on the guide tube and in the absorber

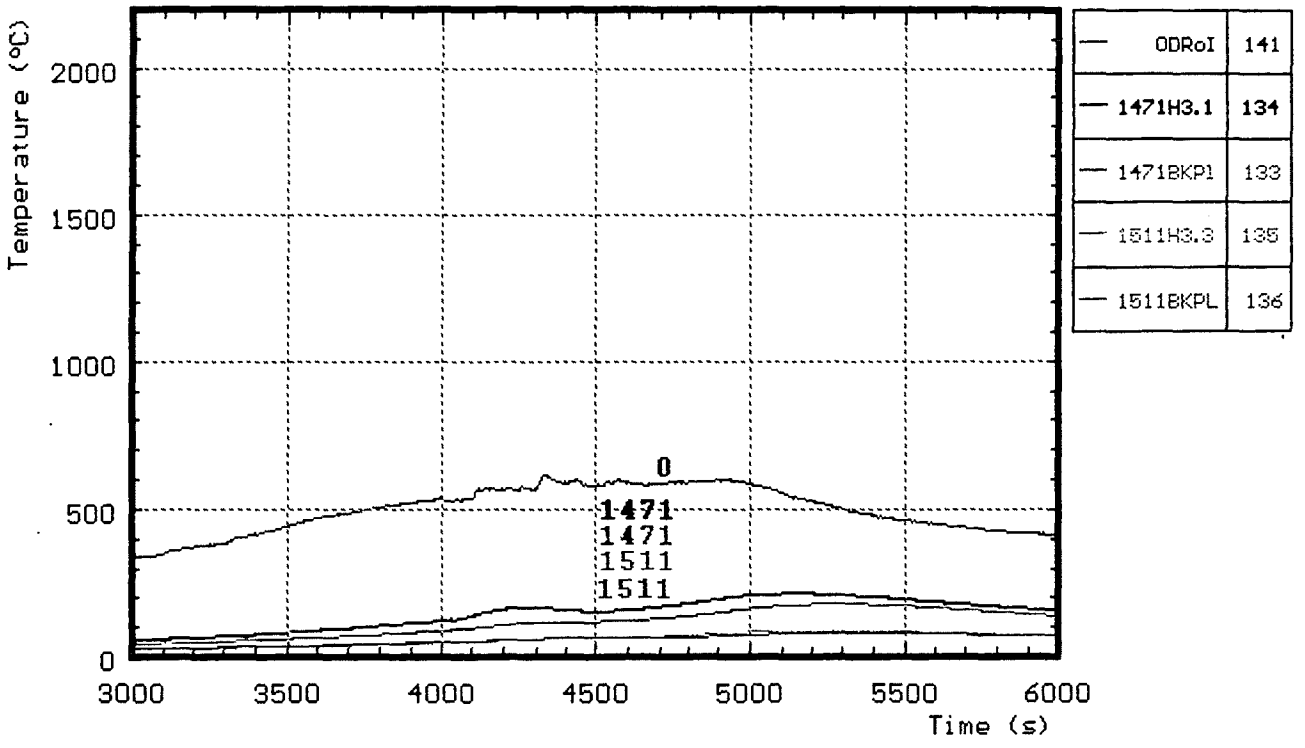

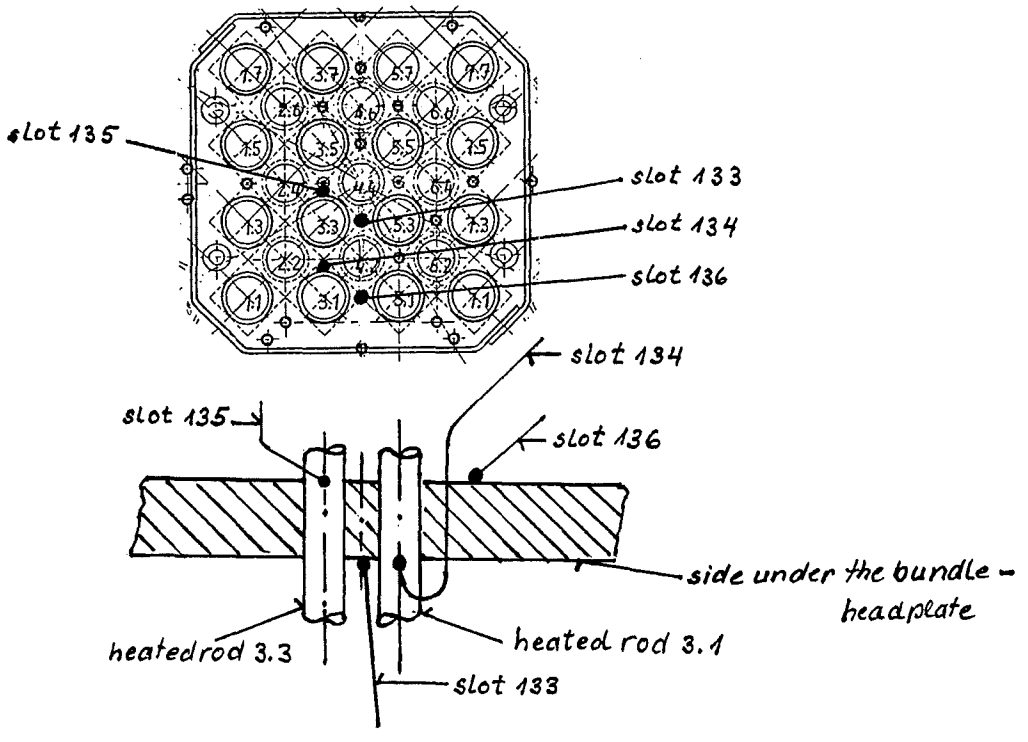

Fig. 32: CORA-10; Temperatures at the bundle head plate and of the lower end of the bundle (0mm) between bundle and shroud.

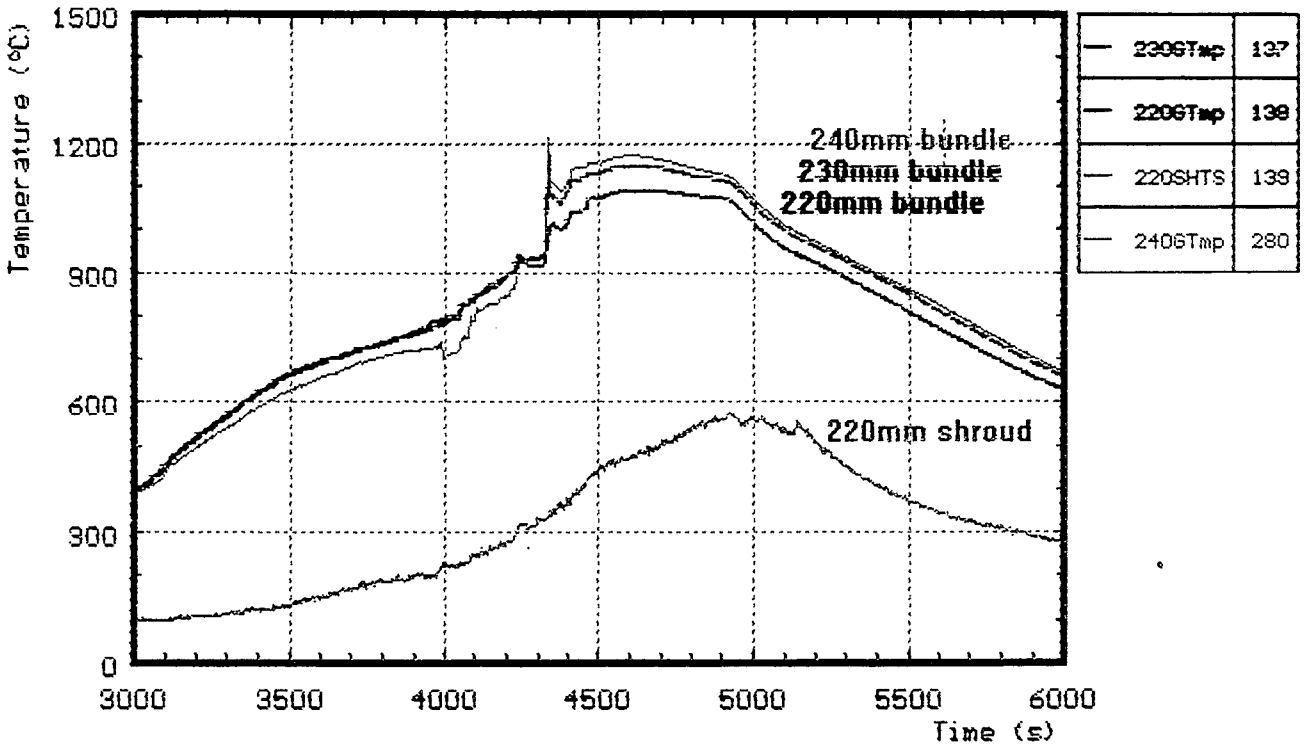

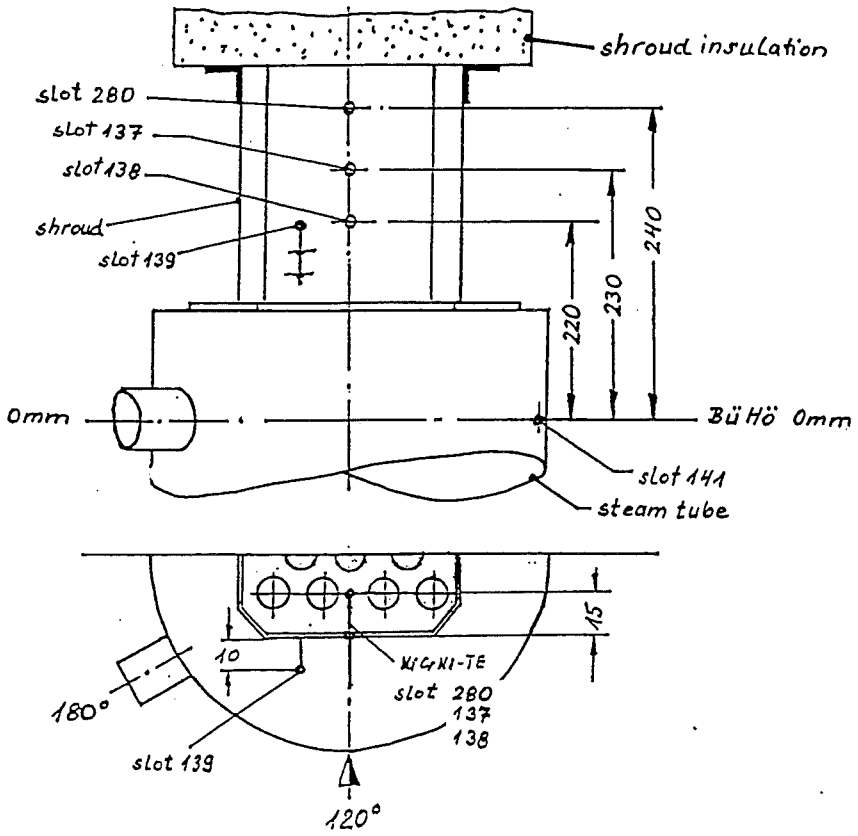

Fig. 33: CORA-10; Temperatures at lower end of bundle and shroud

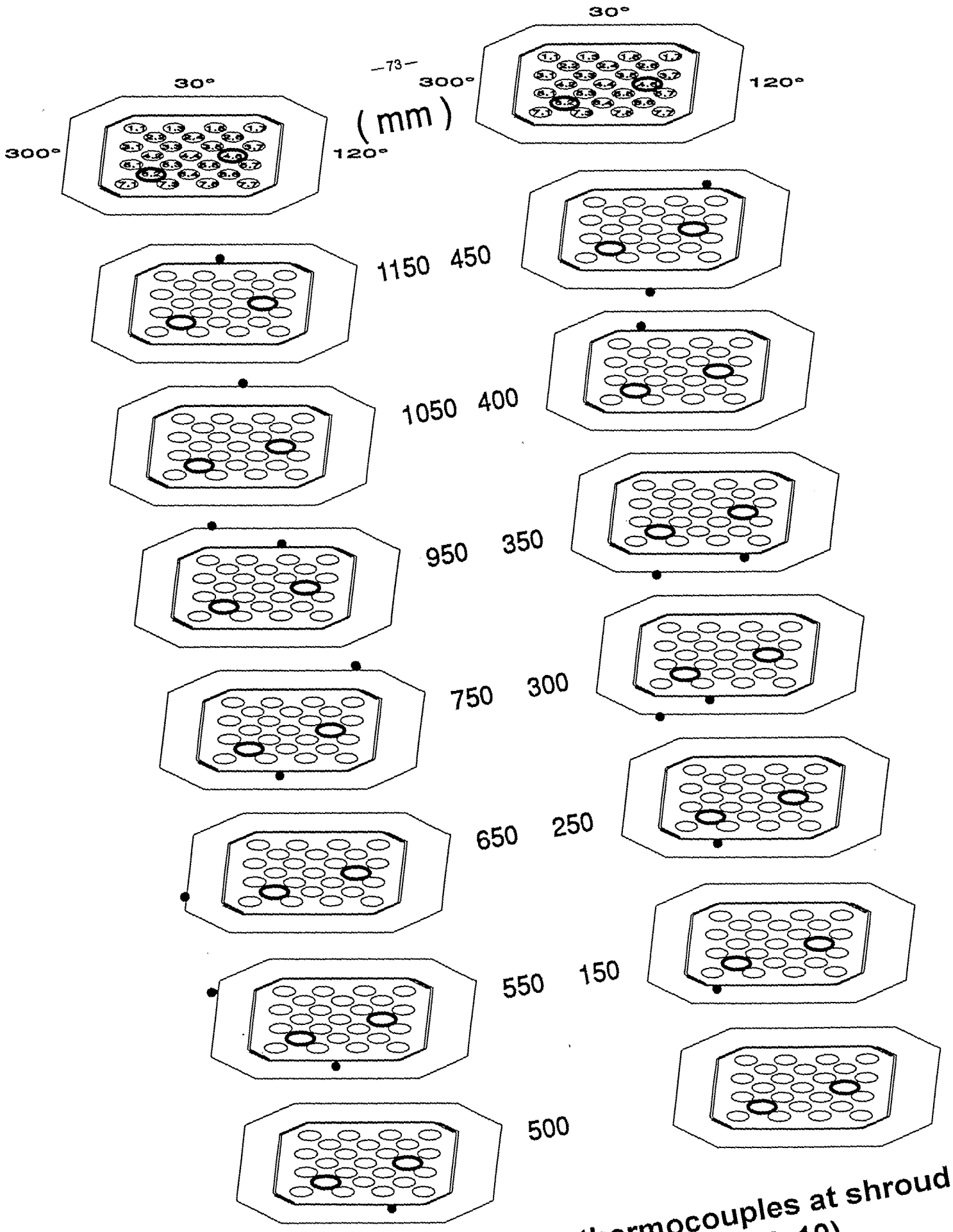

Fig. 34: Location of the thermocouples at shroud and shroud insulation (CORA-10)

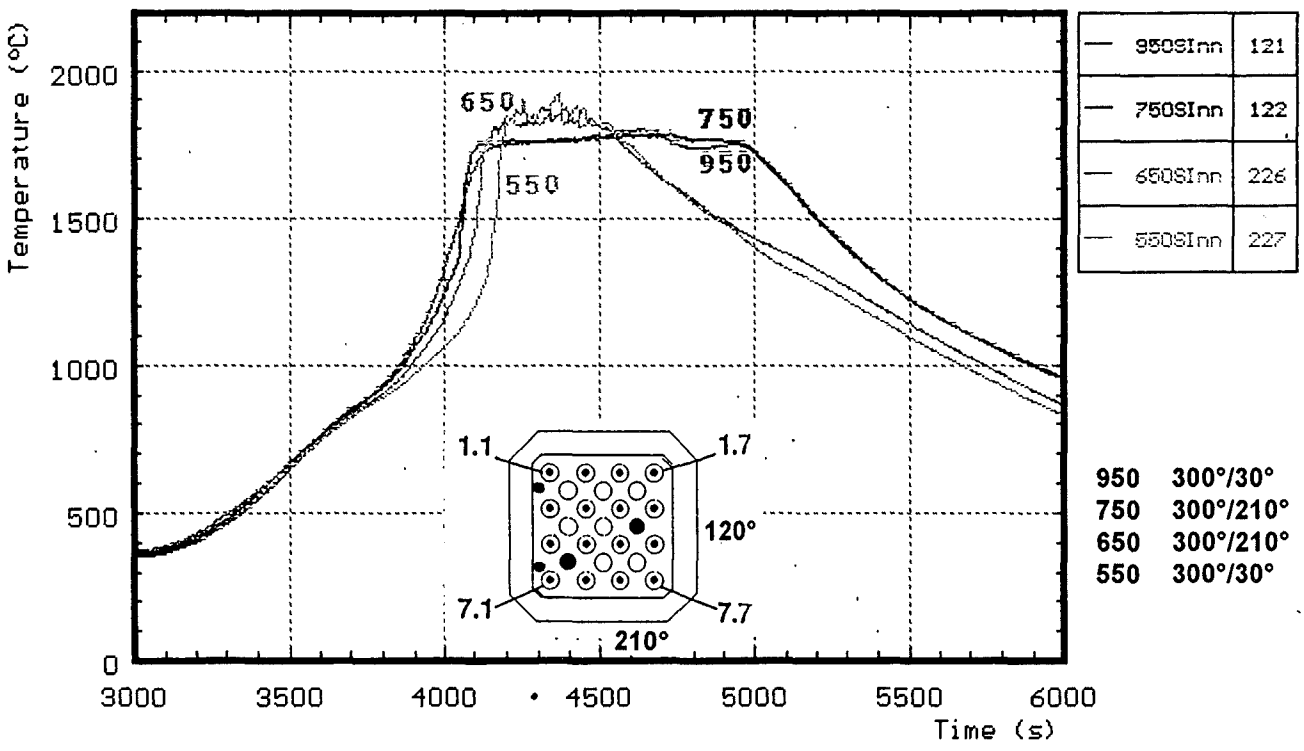

Fig. 35: CORA-10; Temperatures on the inner side of shroud

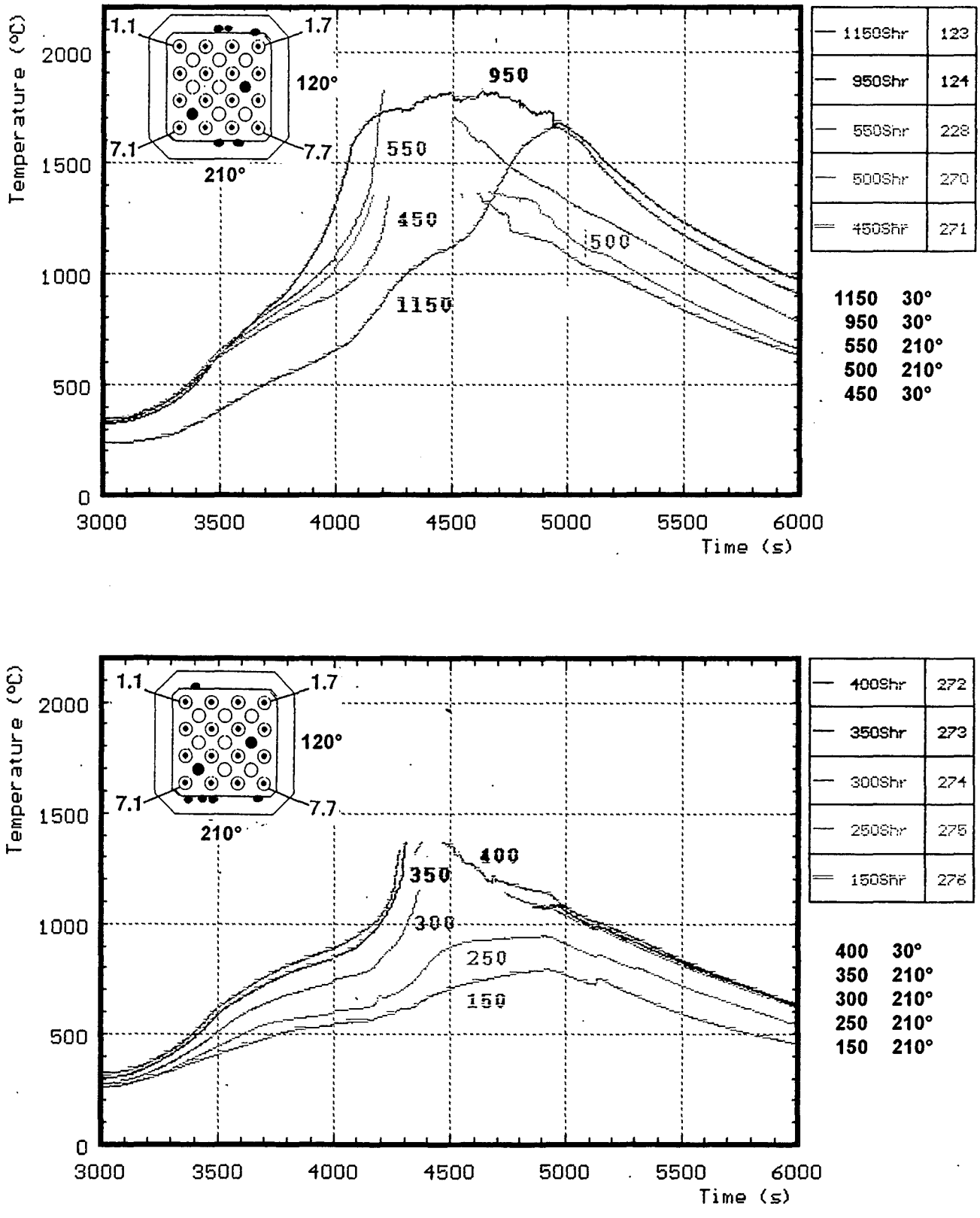

Fig. 36: CORA-10; Temperatures of the outer side of the shroud

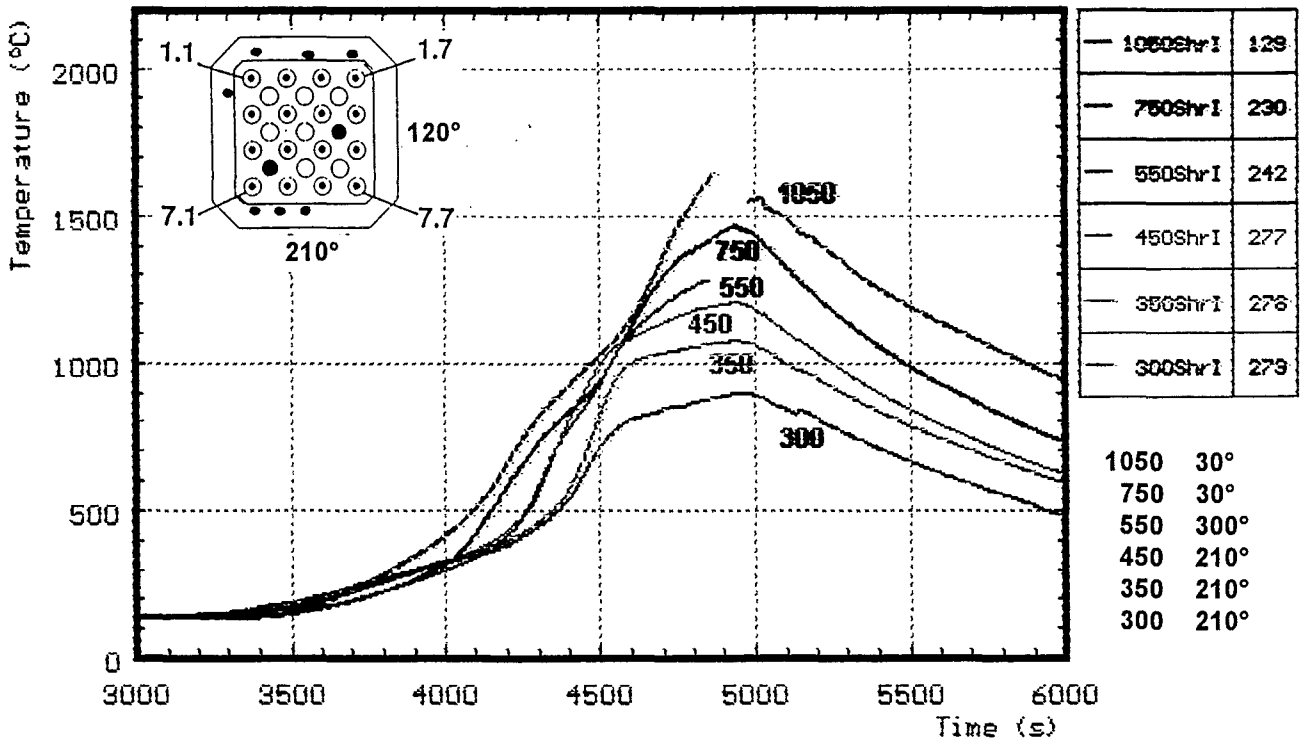

Fig. 37: CORA-10; Temperatures on and in shroud insulation

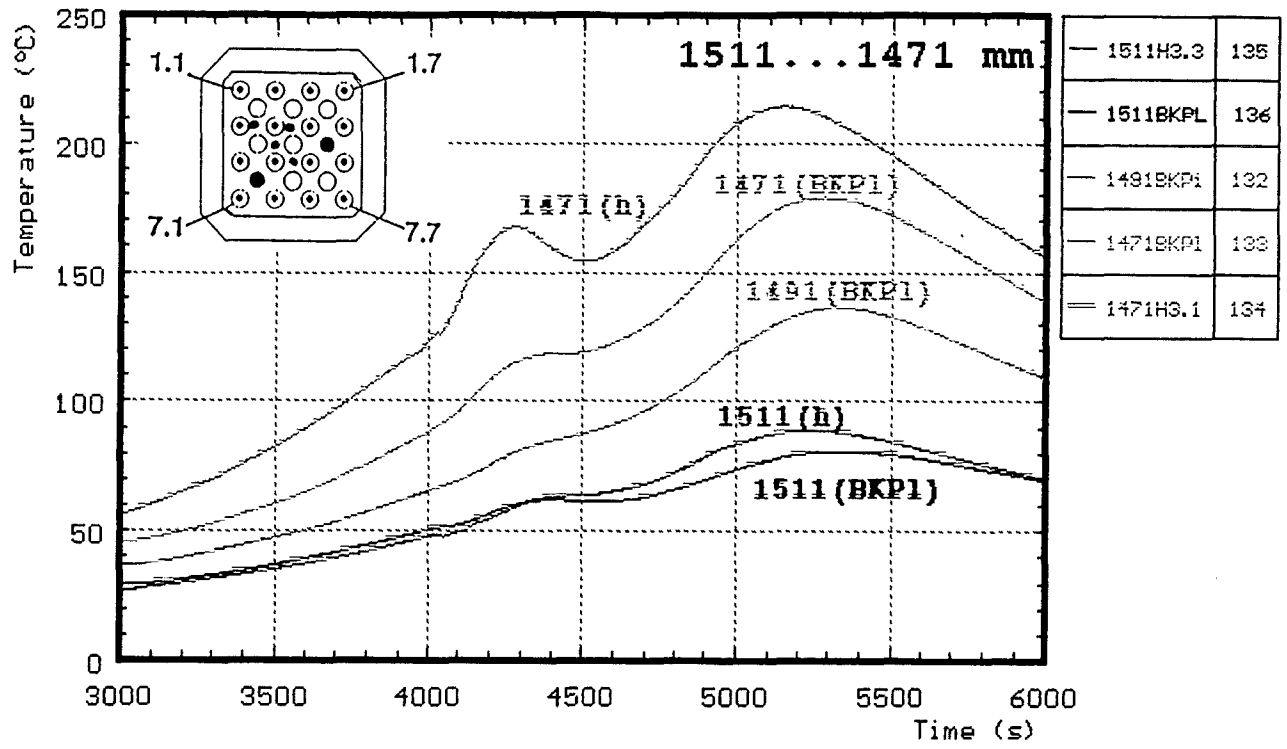

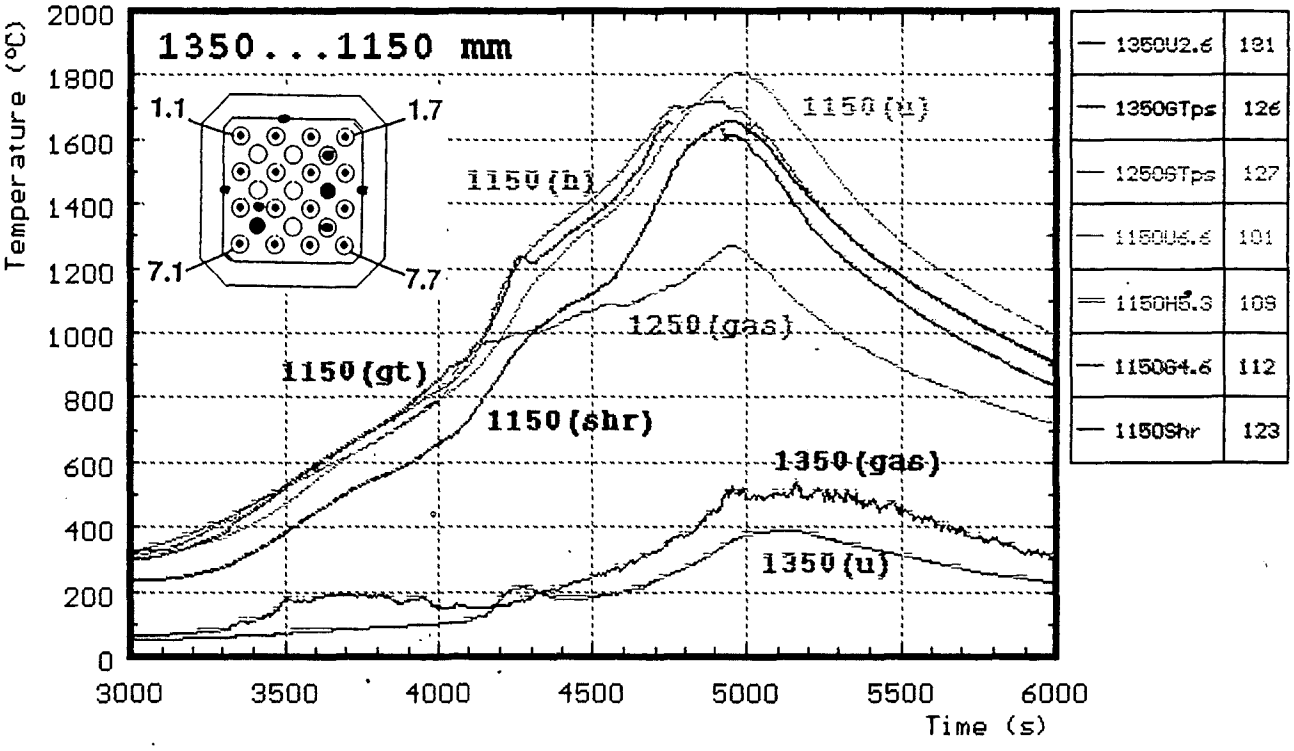

h : heated rods
u : unheated rods
gt : guide tube
shr : on shroud
BKPl : bundle heat plate
gas : gas temperature

Fig. 38: CORA-10; Temperatures at elevations given (1511-1471mm, 1350-1150mm)

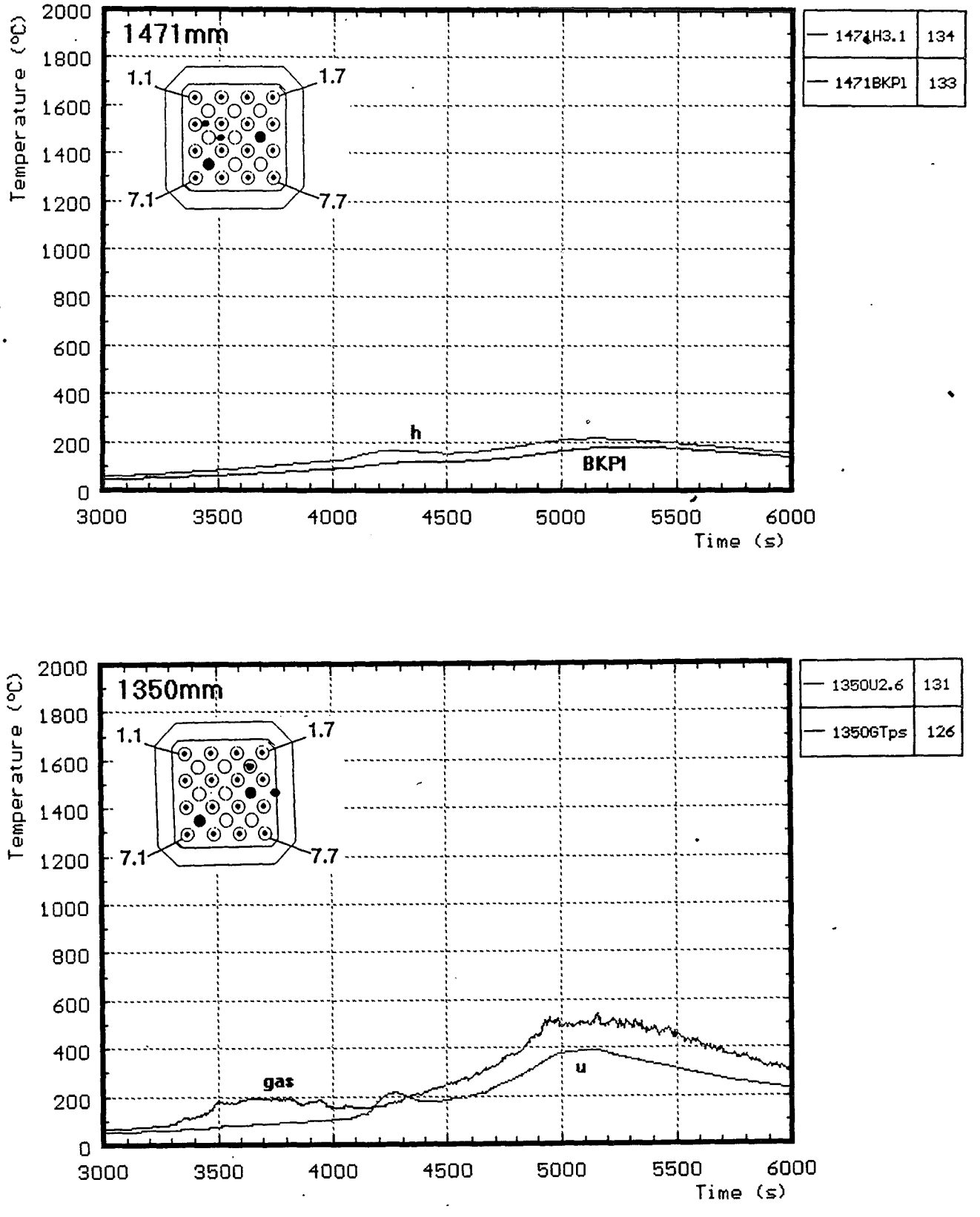

h : heated rods
BKPl : bundle head plate
u : unheated rods
gas : gas temperature

Fig. 39: CORA-10; Temperatures at elevations given (1471, 1350mm)

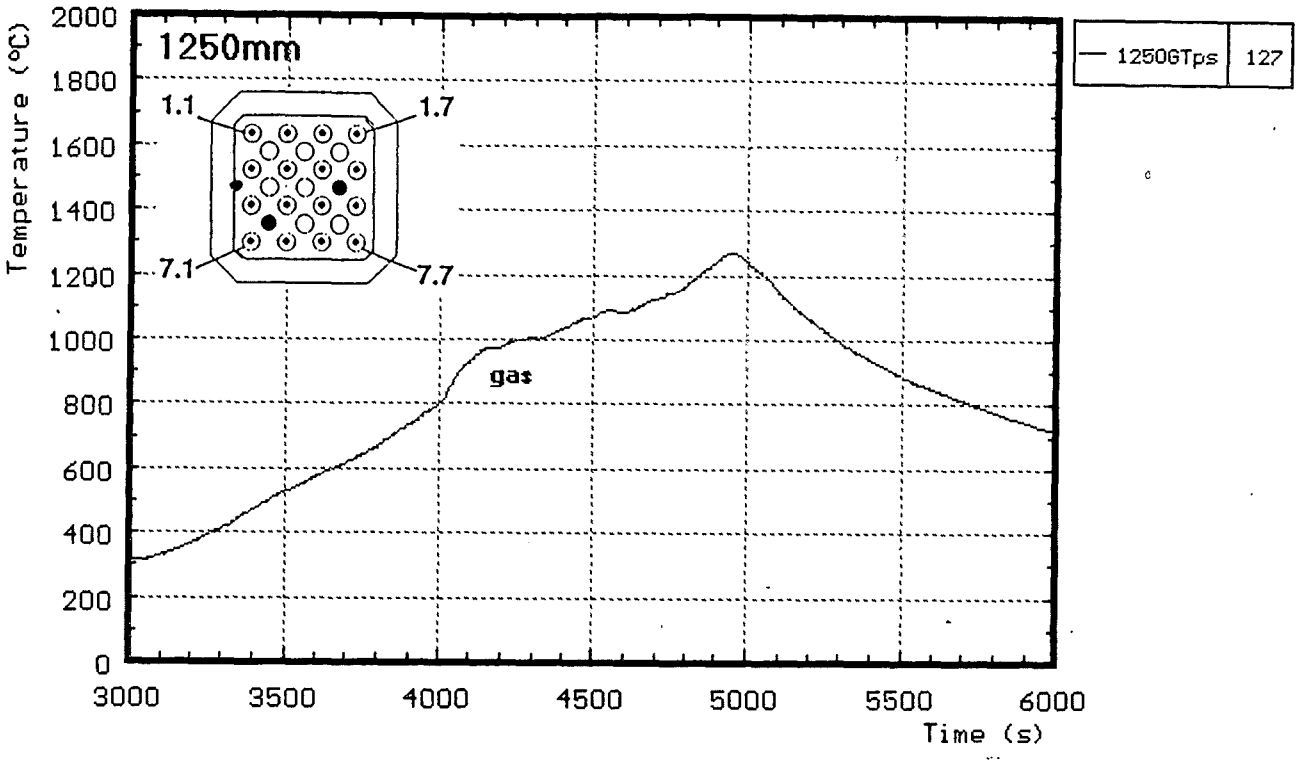

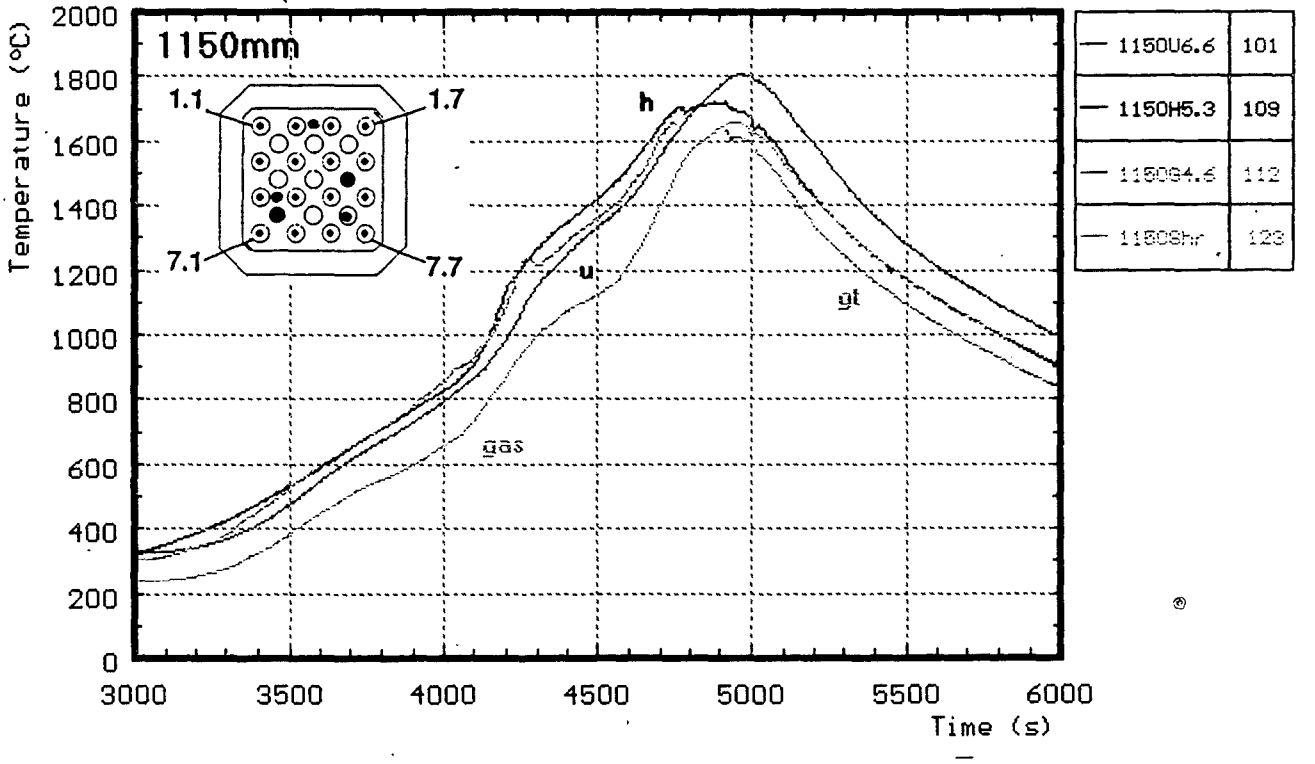

h : heated rods
shr : on shroud
gt : guide tube
u : unheated rods
gas : gas temperature

Fig. 40: CORA-10; Temperatures at elevations given (1250, 1150mm)

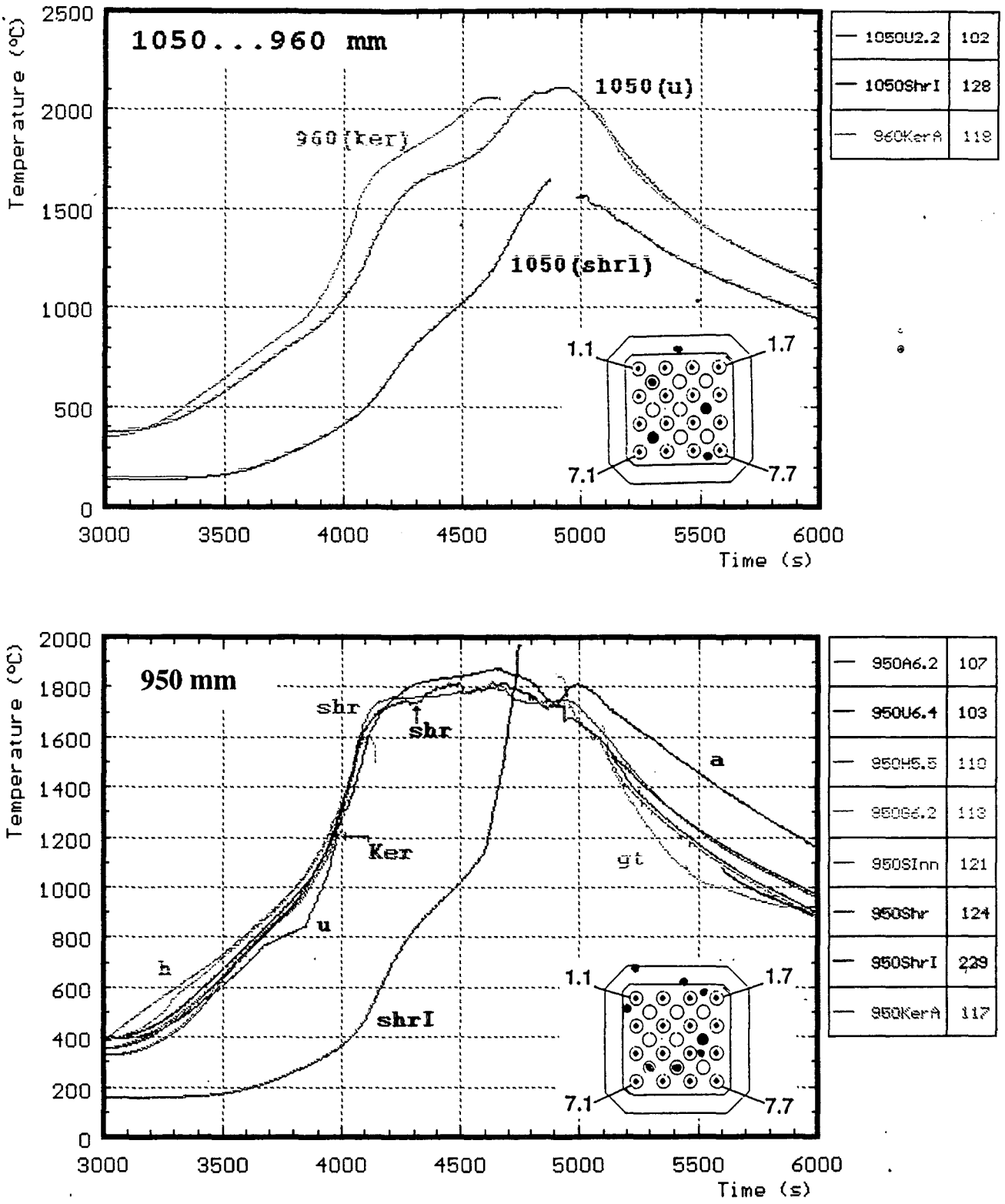

h : heated rods
u : unheated rods
gt : guide tube
a : in absorber

shr : on shroud
shrl : shroud insulation
ker : ceramic protected thermocouples

Fig. 41: CORA-10; Temperatures at elevations given (1050-960, 950mm)

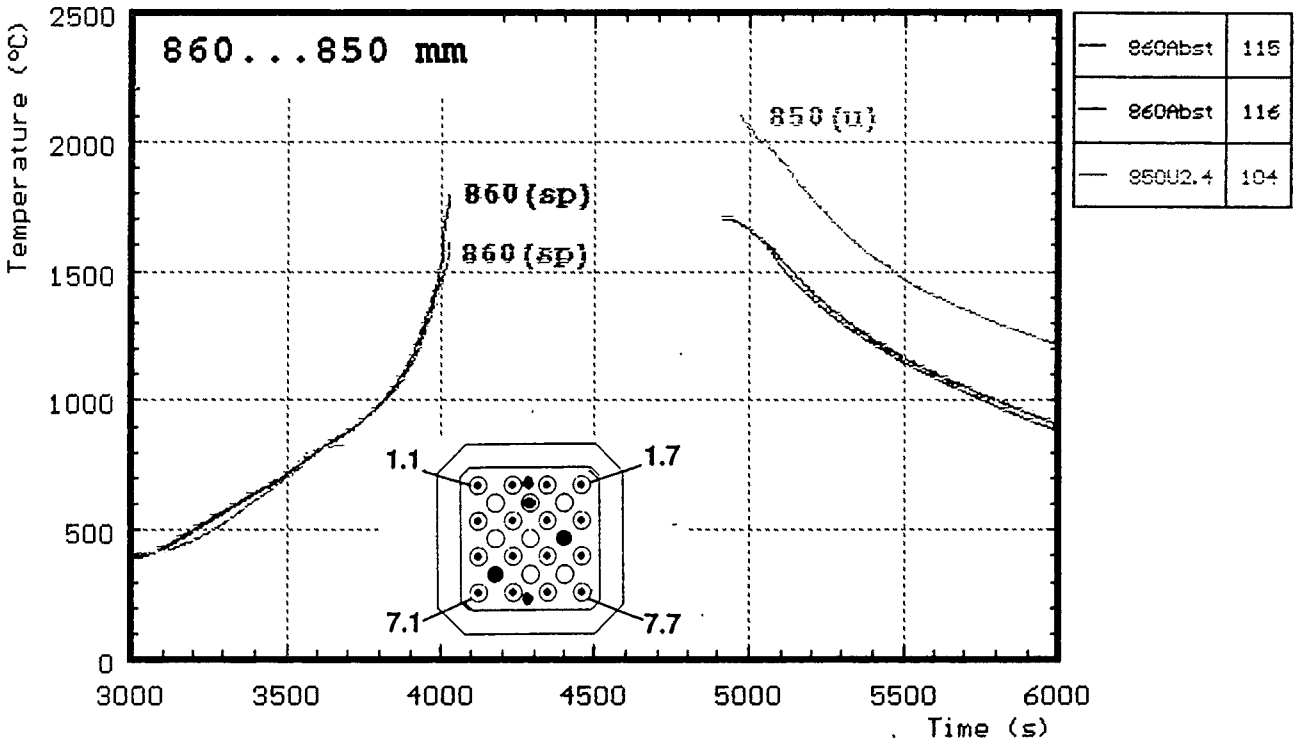

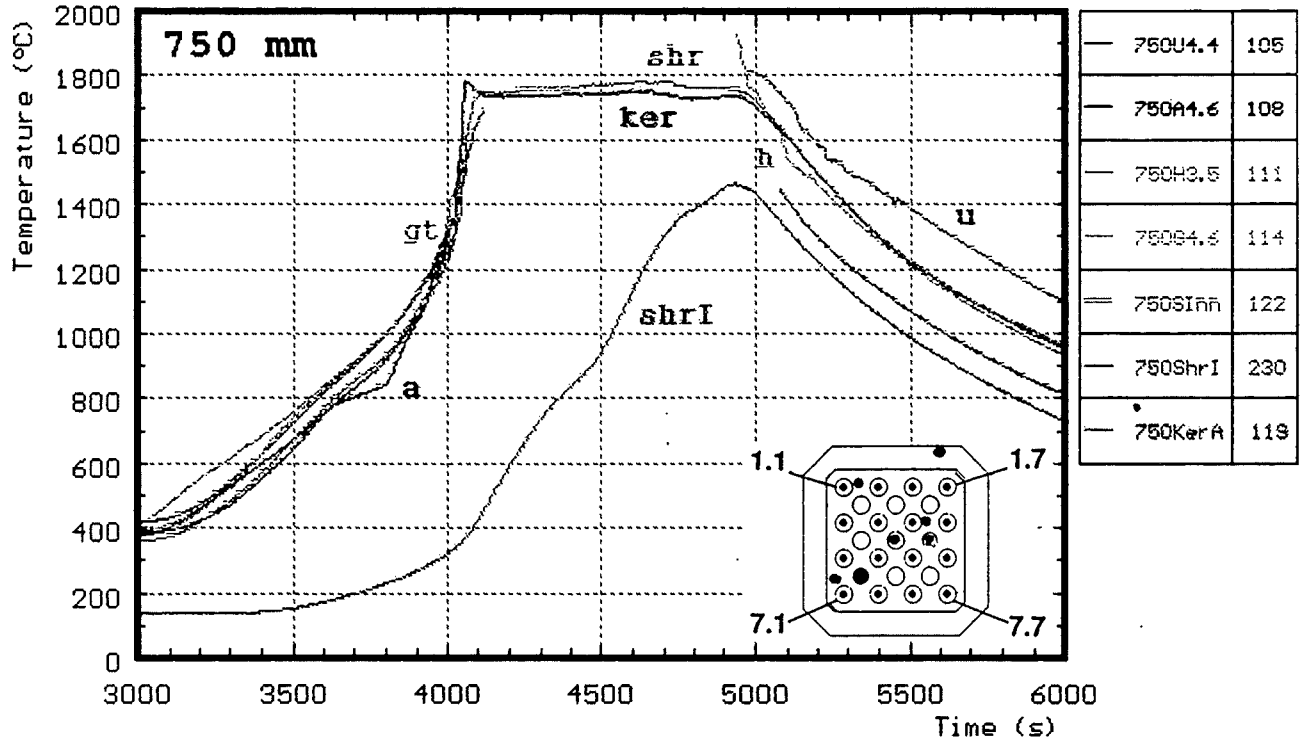

h : heated rods
u : unheated rods
gt : guide tube
a : in absorber

shr : on shroud
shrI : shroud insulation
ker : ceramic protected thermocouples
sp : spacer

Fig. 42: CORA-10; Temperatures at elevations given (860-850, 750 mm)

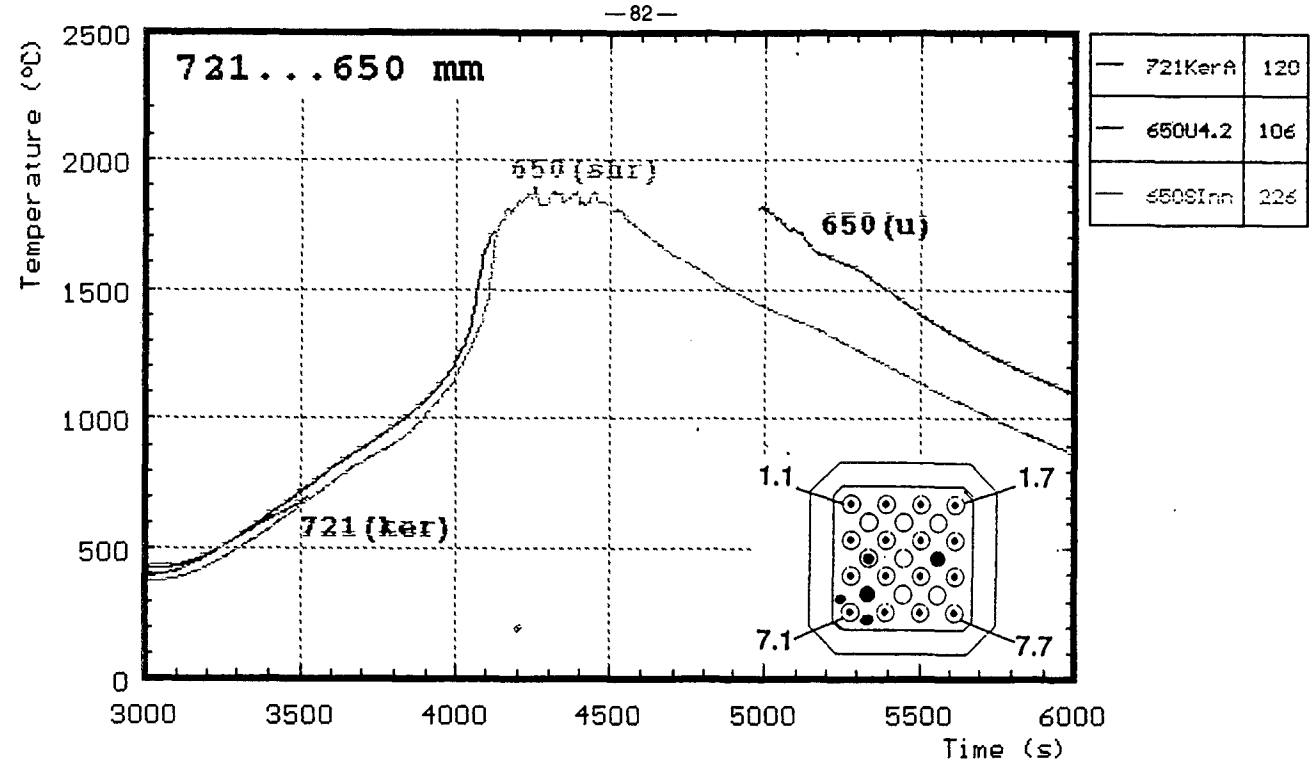

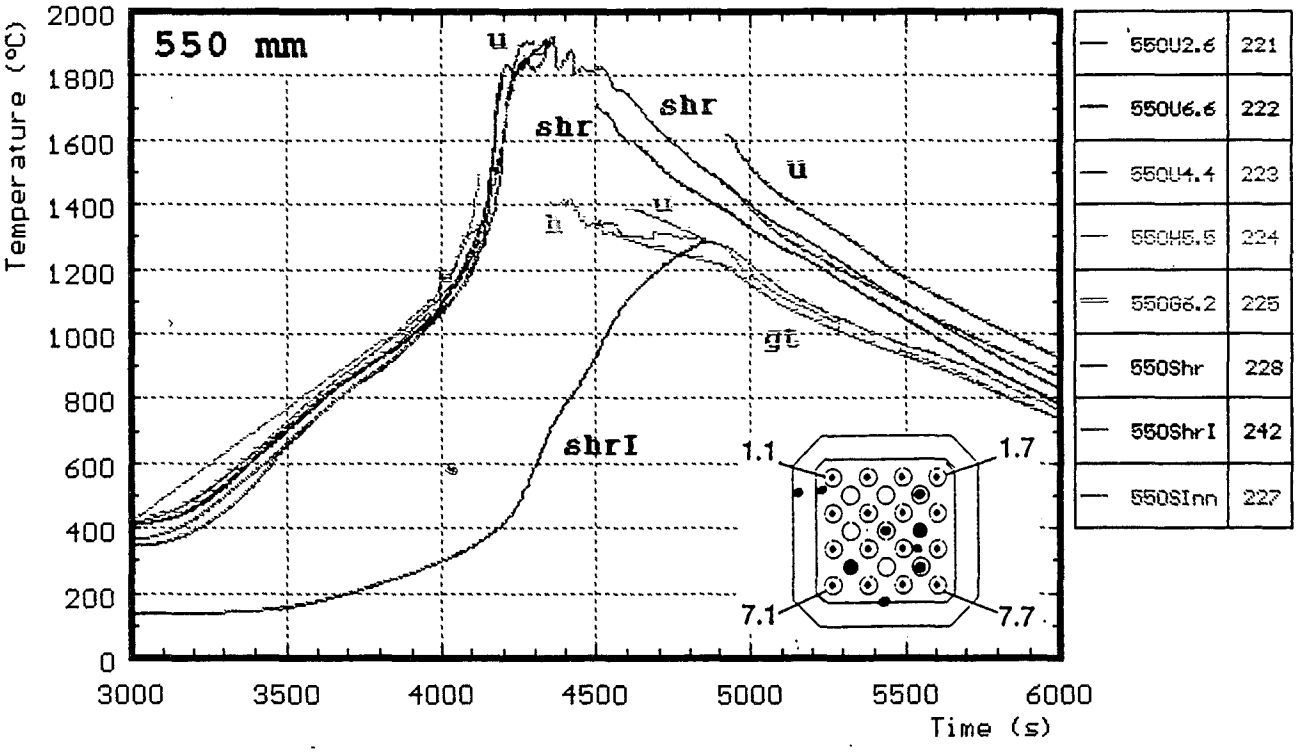

h : heated rods
u : unheated rods
gt : guide tube

shr : on shroud
shrl : shroud insulation
ker : ceramic protected thermocouples

Fig. 43: CORA-10; Temperatures at elevations given (721-650, 550mm)

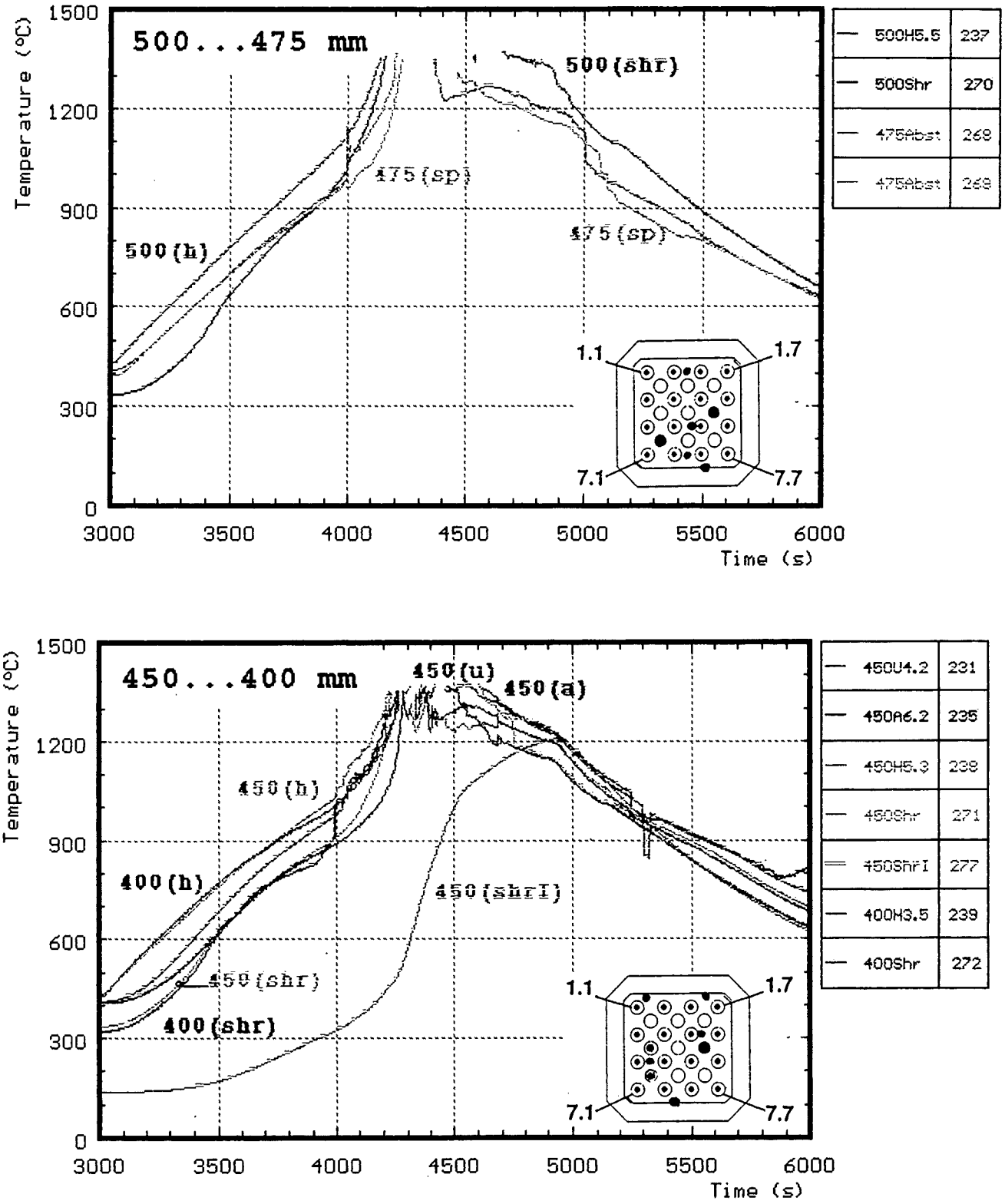

h : heated rods
u : unheated rods
a : in absorber

shr : on shroud
shrl : shroud insulation
sp : spacer

Fig. 44: CORA-10; Temperatures at elevations given (500-475, 450-400mm)

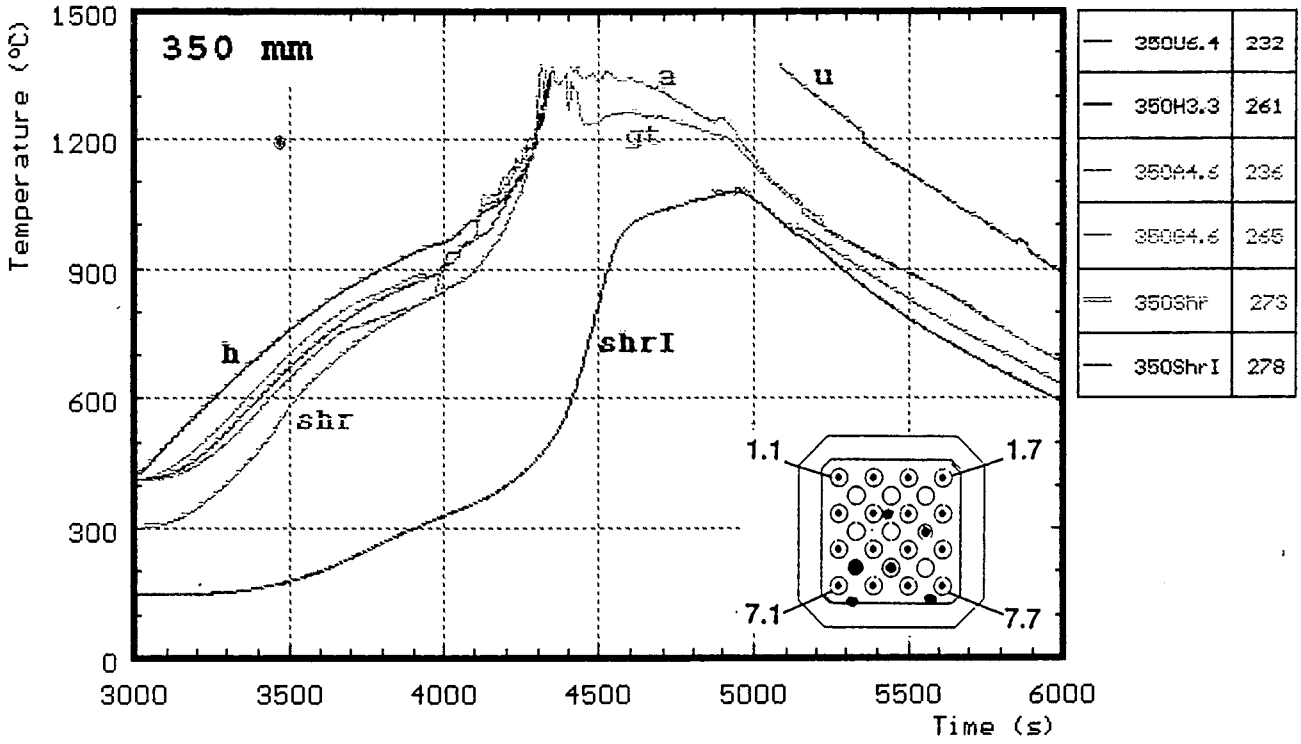

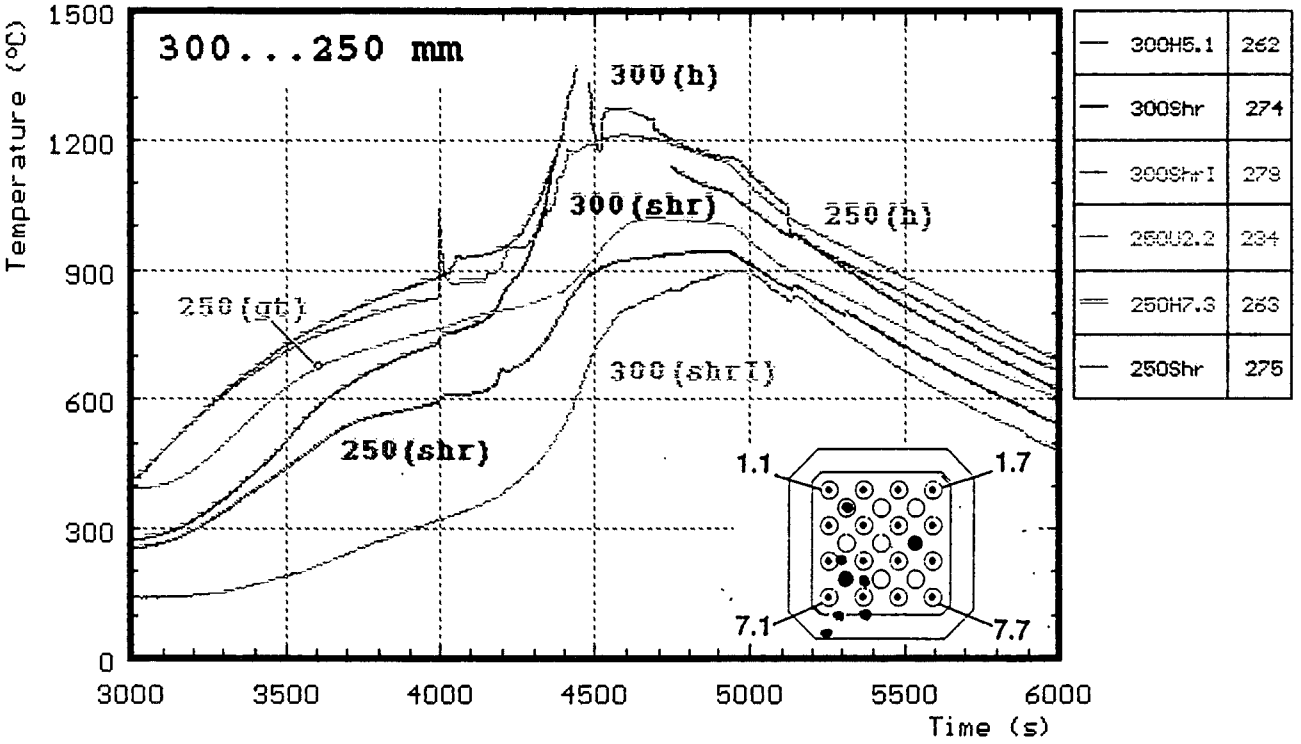

h : heated rods
u : unheated rods
gt : guide tube
shr : on shroud
shrI : shroud insulation
a : in absorber

Fig. 45: CORA-10; Temperatures at elevations given (350, 300-250mm)

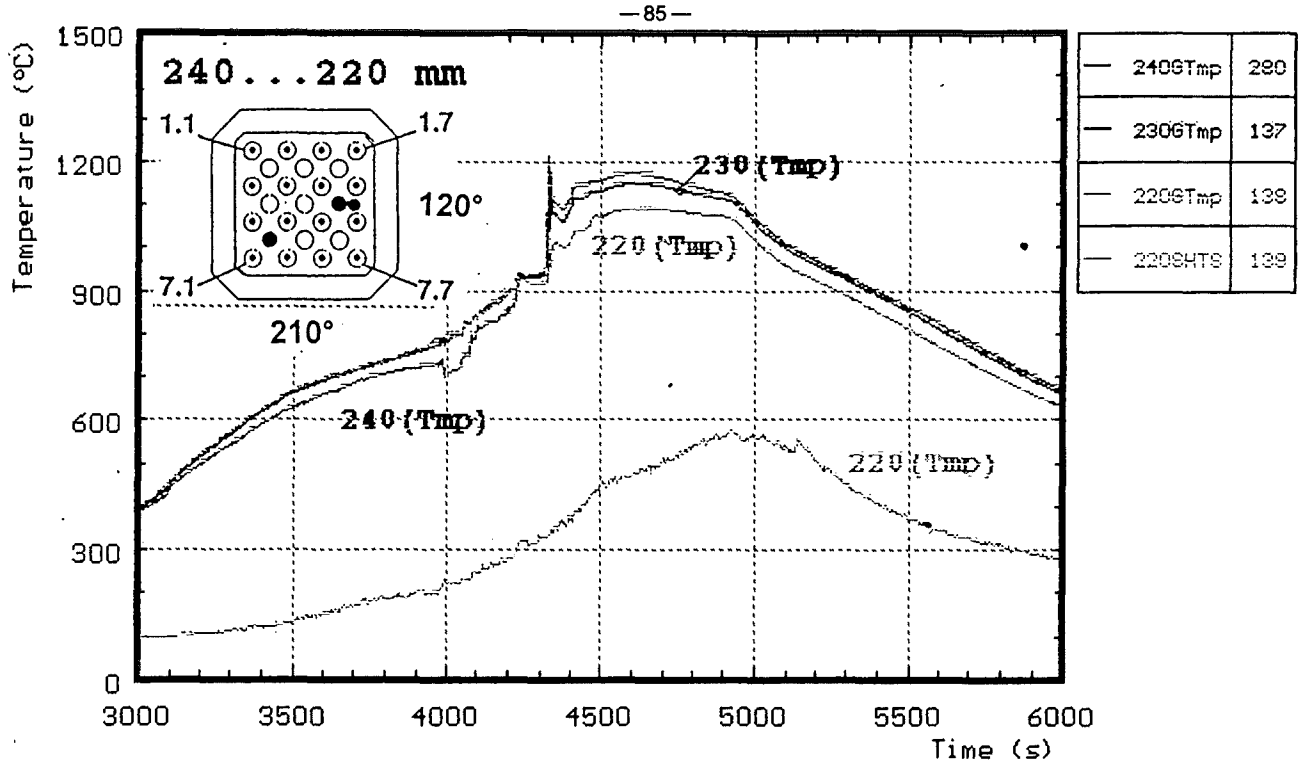

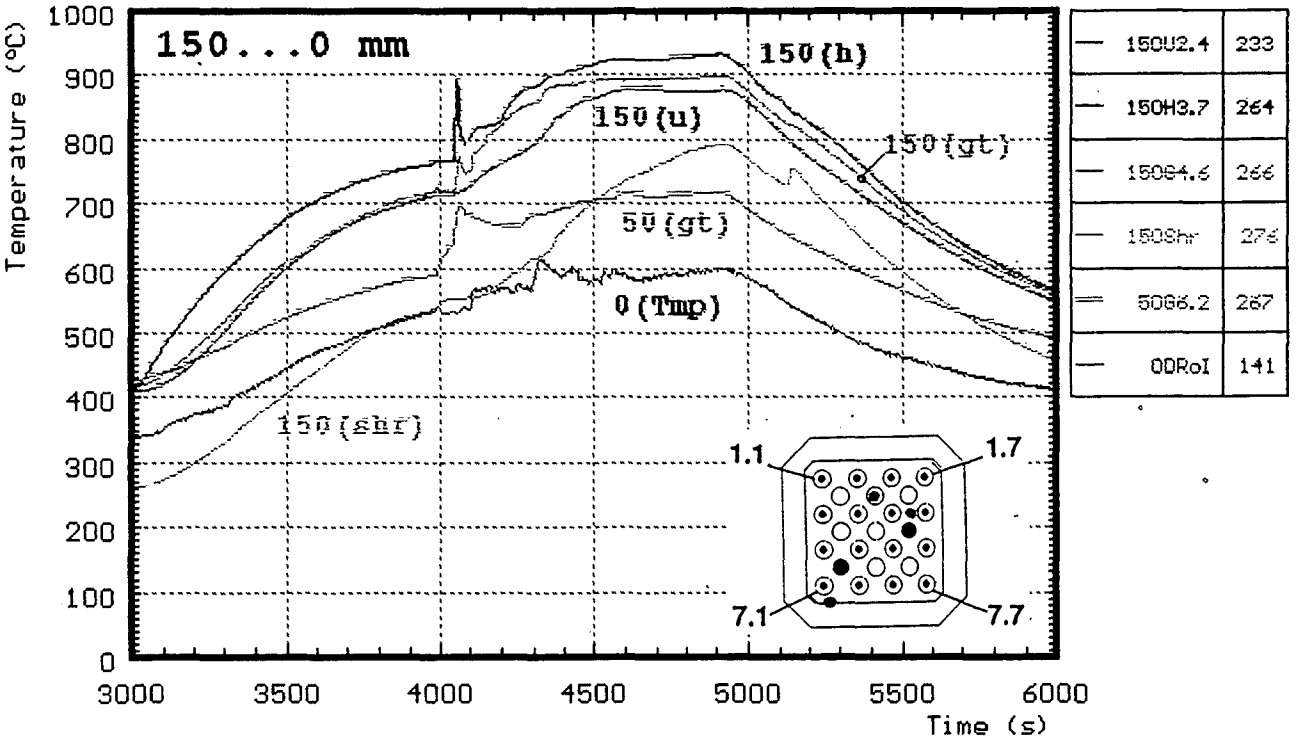

h : heated rods
u : unheated rods
gt : guide tube

shr : on shroud
Tmp : between bundle and shroud

Fig. 46: CORA-10; Temperatures at elevations given (240-220, 150-0mm)

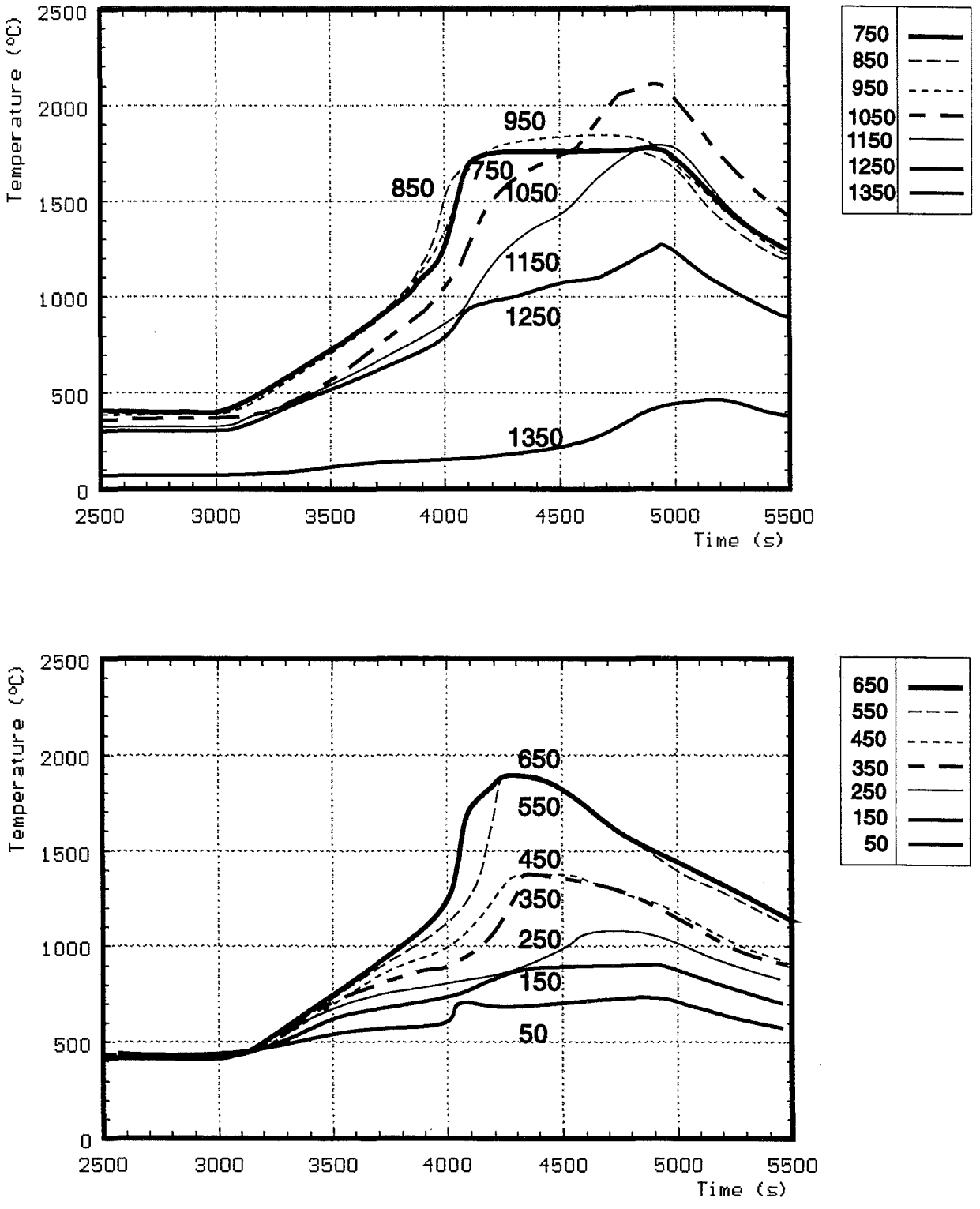

Fig. 47: CORA-10; Best-estimate bundle temperatures at different elevations

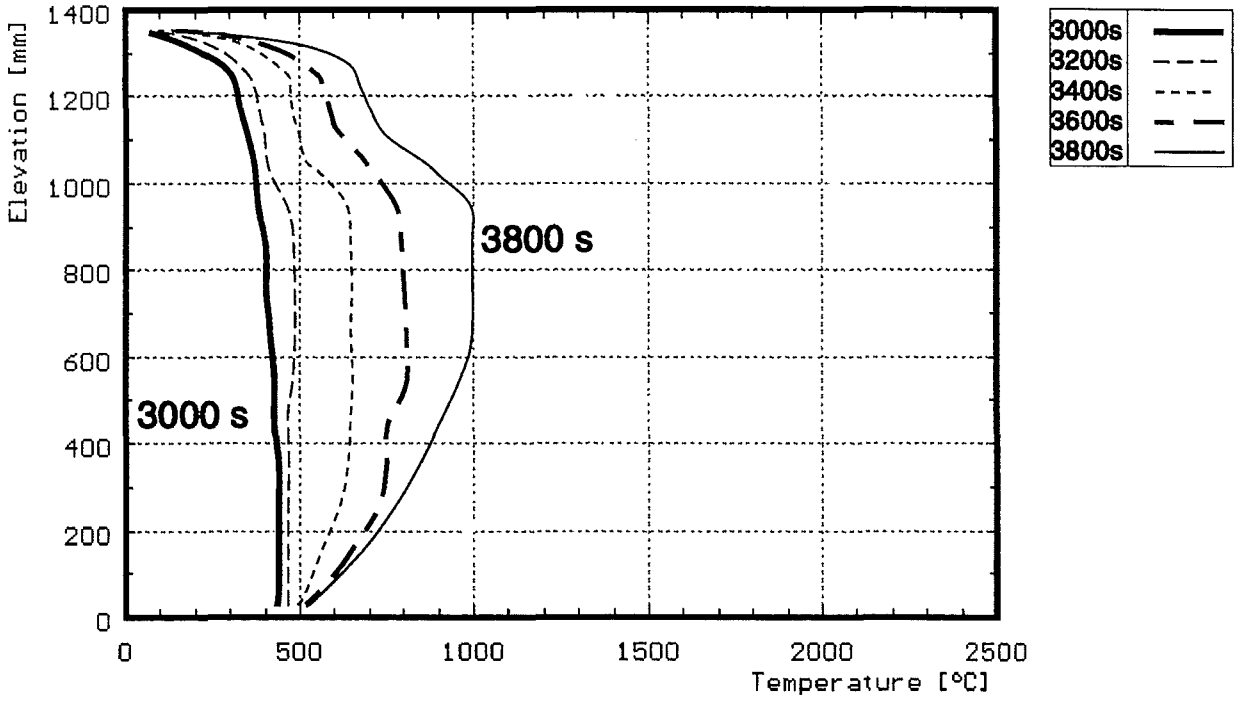

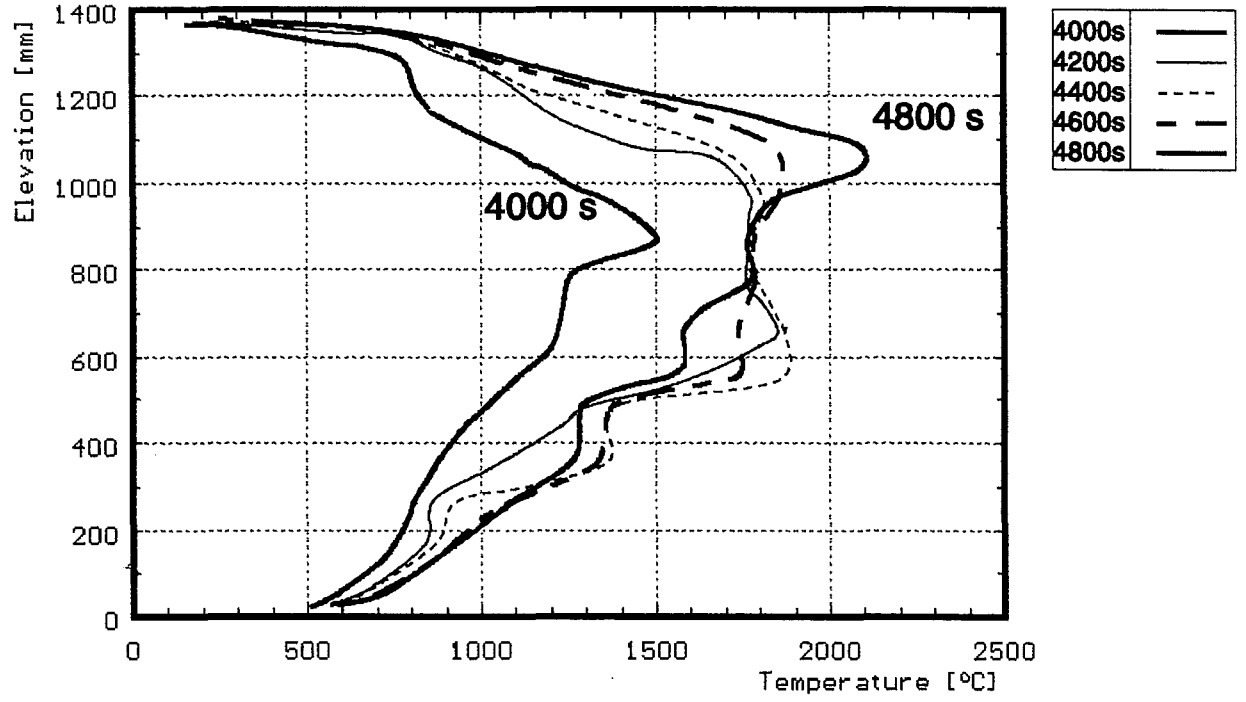

Fig. 48: Axial temperature distribution during the transient of test CORA-10

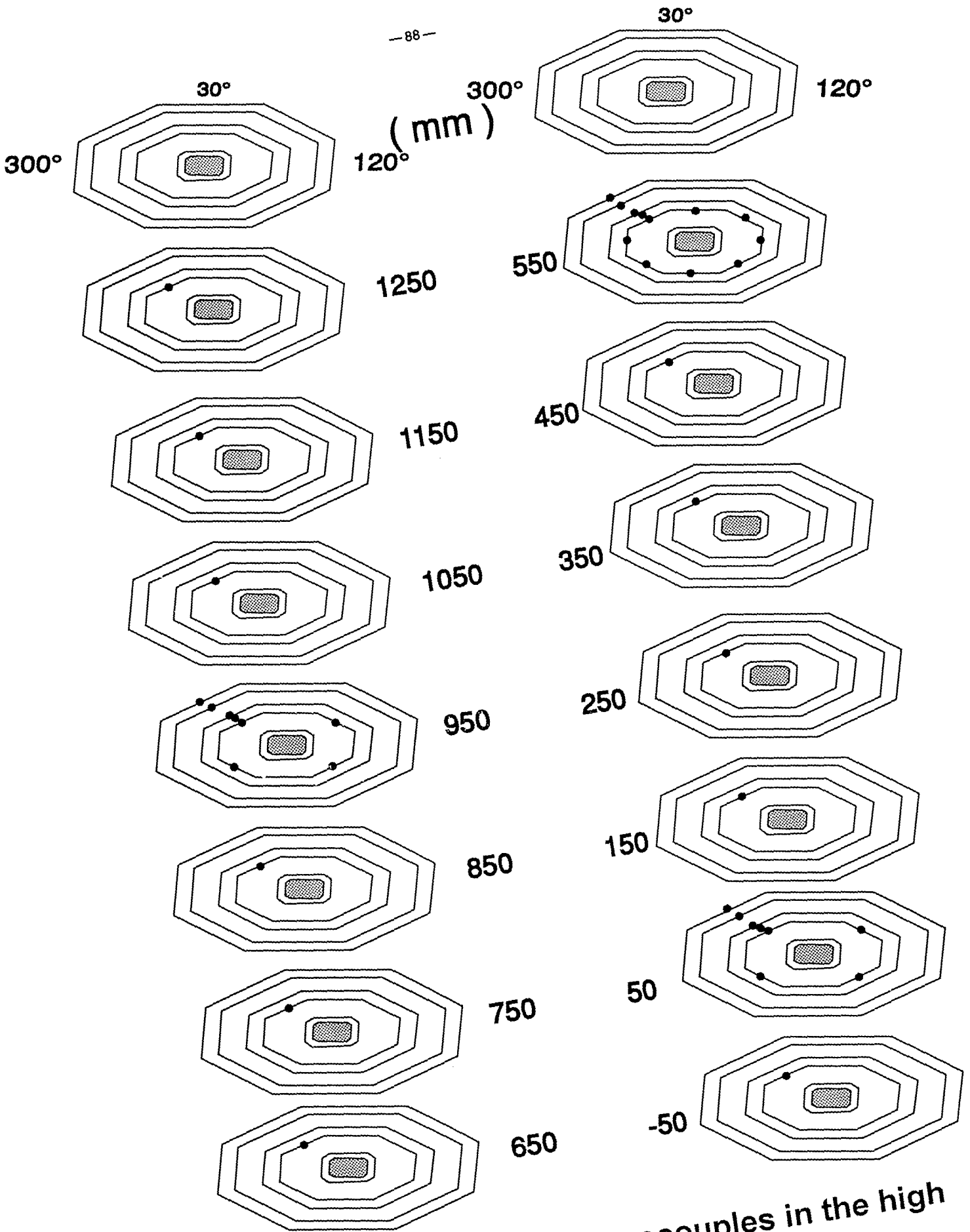

Fig. 49: Locations of thermocouples in the high temperature shield (CORA-10)

ANGLE ∠		30°	75°	120°	165°	210°	255°	300°	345°				
RADIUS		153	153	153	153	153	153	153	153	172	192	255	293
Elevation in bundle	mm												
	1250								**174** *33Ni*				
	1150								**175** *32Ni*				
	1050								**176** *31Ni*				
	950		**slot162** *28Ni*		**166** *27Ni*		**170** *26Ni*		**177** *25Ni*	**188** *29Ni*	**191** *30Ni*	**194** *38Ni*	**197** *39Ni*
	850								**178** *24Ni*				
	750								**179** *23Ni*				
	650								**180** *22Ni*				
	550	**slot161** *19Ni*	**163** *18Ni*	**165** *17Ni*	**167** *16Ni*	**169** *15Ni*	**171** *14Ni*	**173** *13Ni*	**181** *12Ni*	**189** *20Ni*	**192** *21Ni*	**195** *36Ni*	**198** *37Ni*
	450								**182** *11Ni*				
	350								**183** *10Ni*				
	250								**184** *9Ni*				
	150								**185** *8Ni*				
	50		**164** *5Ni*		**168** *4Ni*		**172** *3Ni*		**186** *2Ni*	**190** *6Ni*	**193** *7Ni*	**196** *34Ni*	**199** *35Ni*
	- 50								**187** *1Ni*				

Fig. 50: Position of thermocouples in high temperature shield for test CORA10

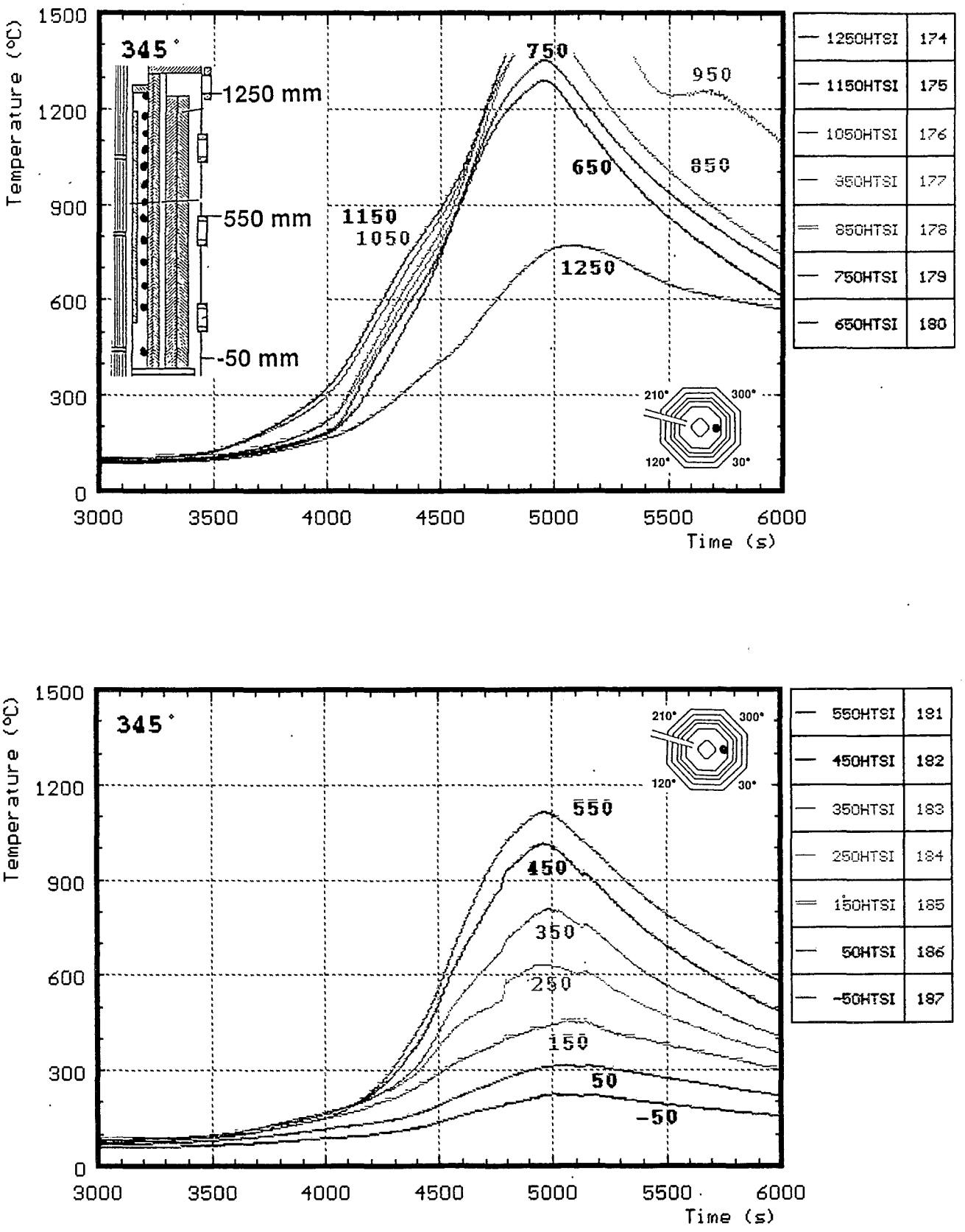

Fig. 51: CORA-10; Temperatures of HTS at inner surface, 153 mm radius

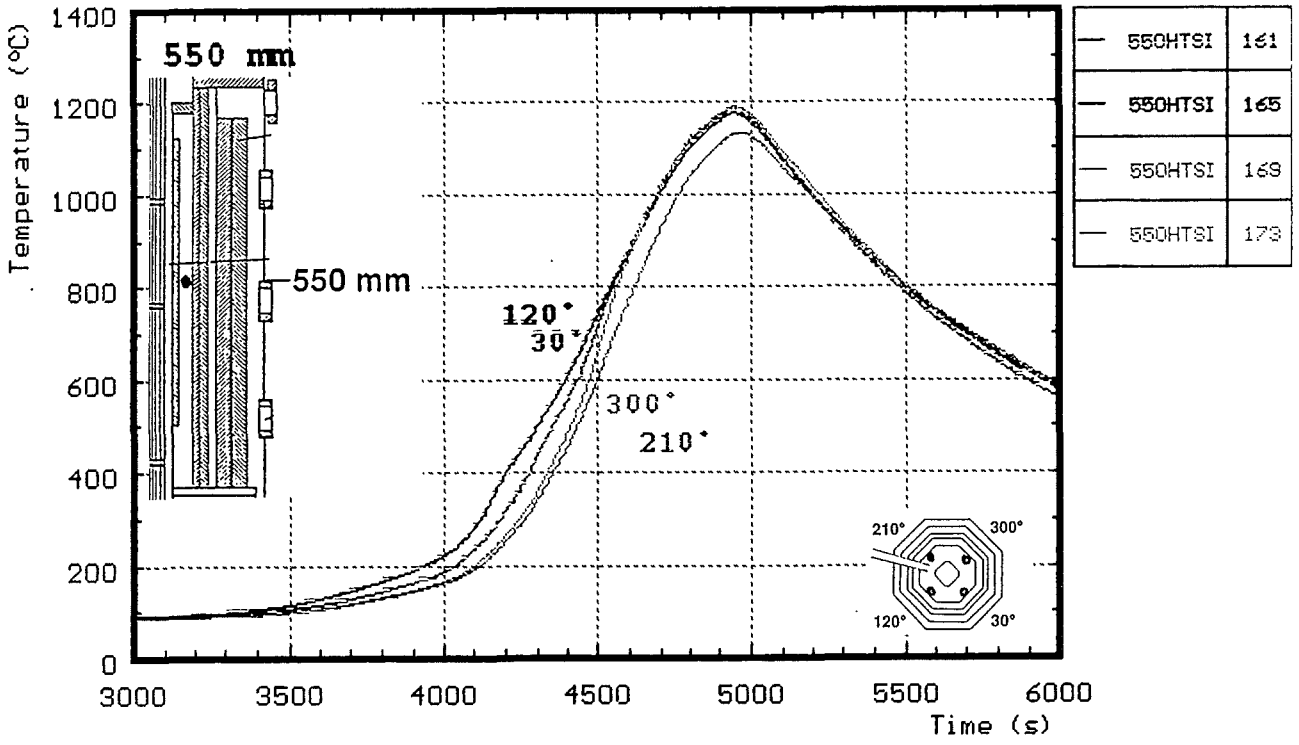

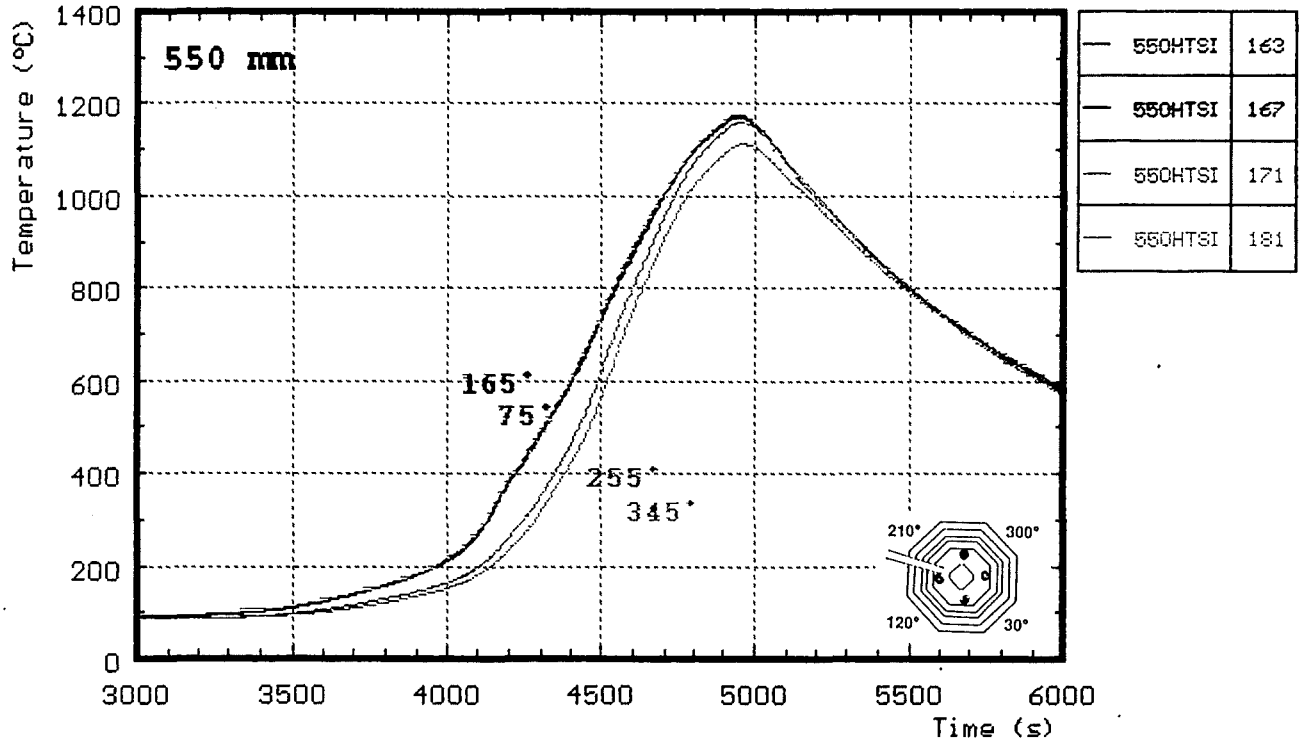

Fig. 52: CORA-10; Temperatures of HTS, inner surface at 153 mm radius (550 mm)

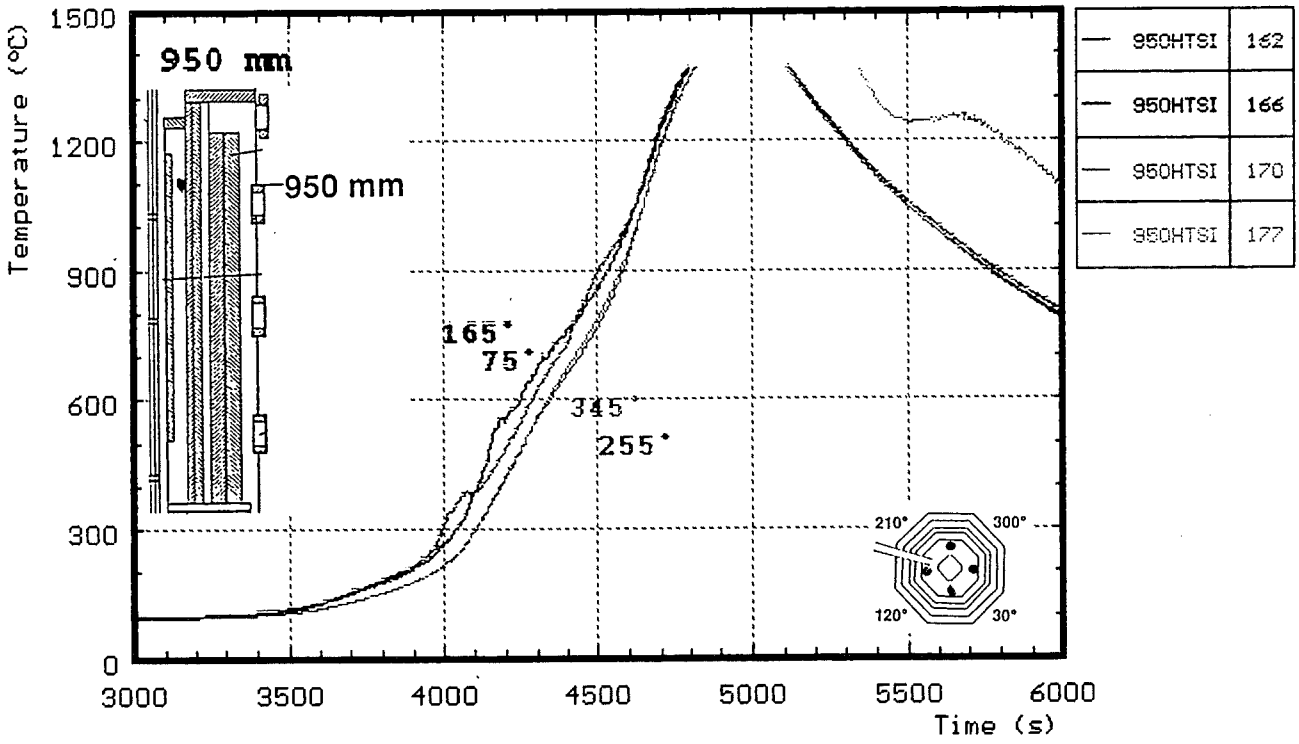

Fig. 53: CORA-10; Temperatures of HTS, inner surface at 153 mm radius (950mm)

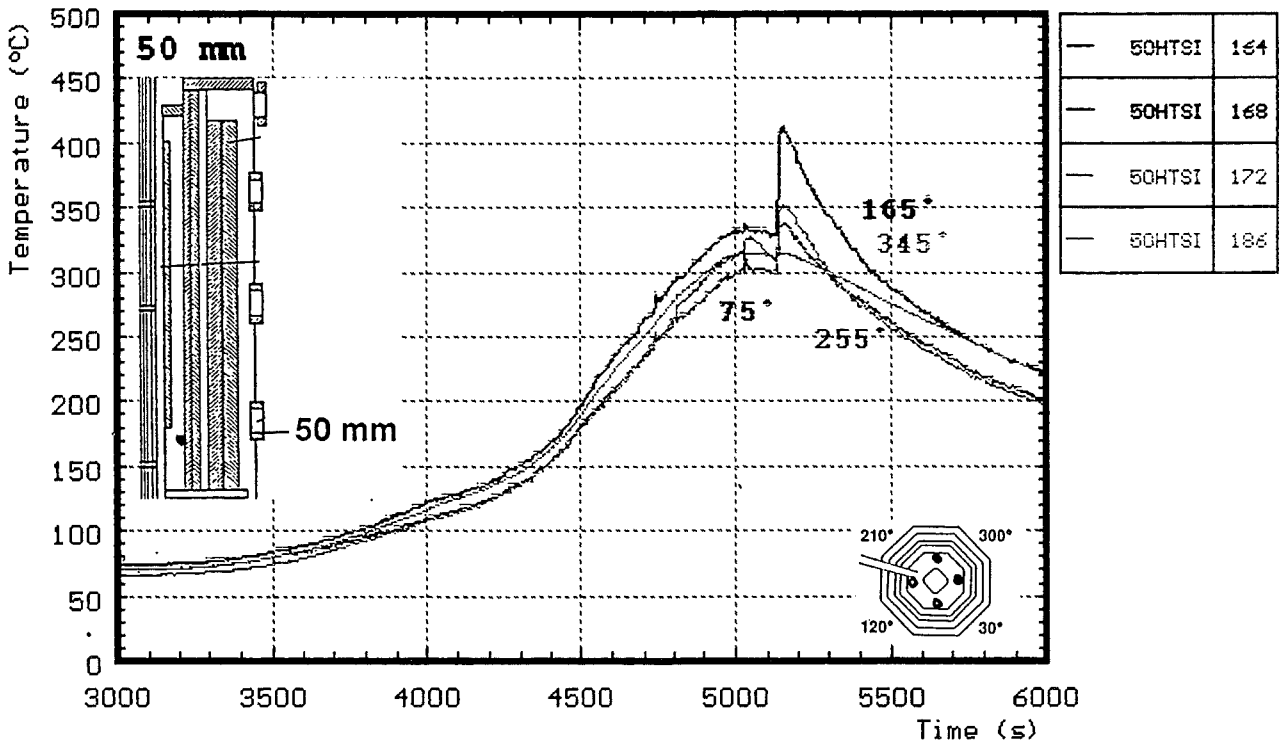

Fig. 54: CORA-10; Temperatures of HTS, inner surface at 153 mm radius (50mm)

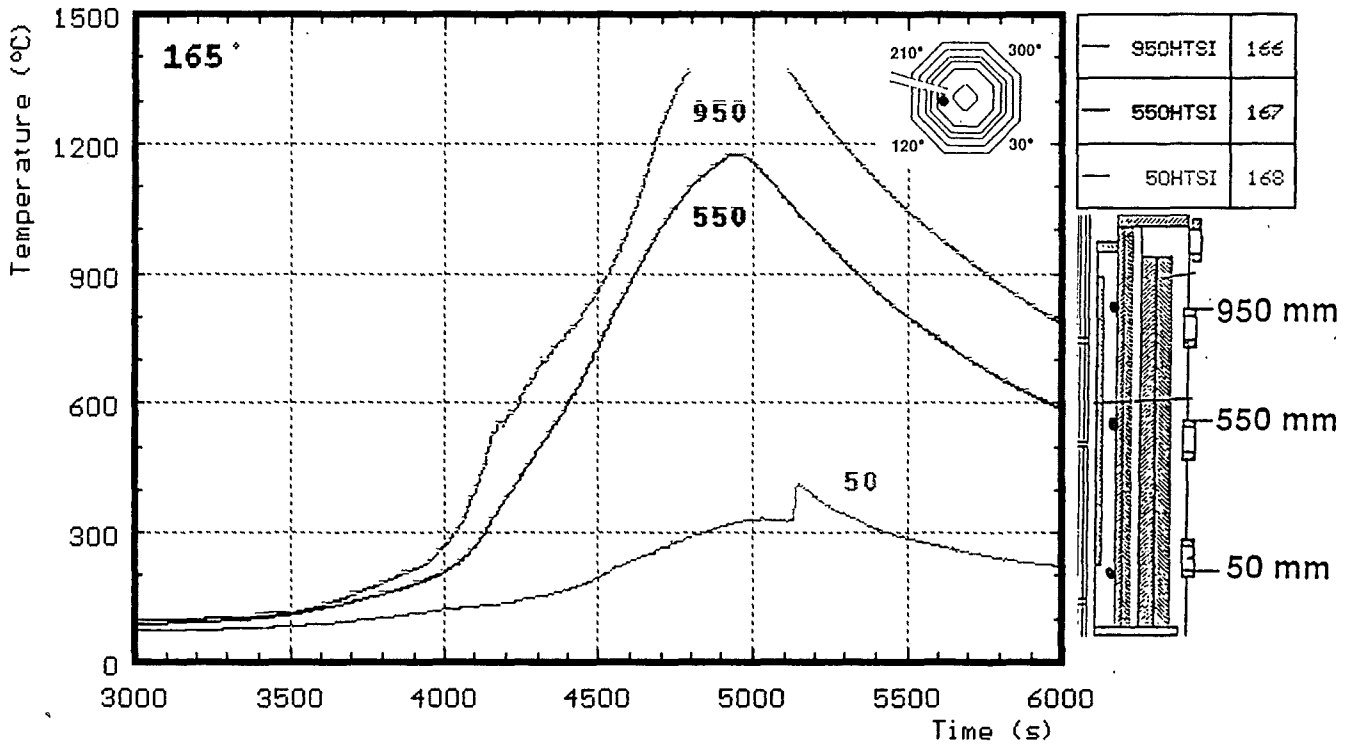

Fig. 55: CORA-10; Temperatures of HTS at inner surface; 153 mm radius

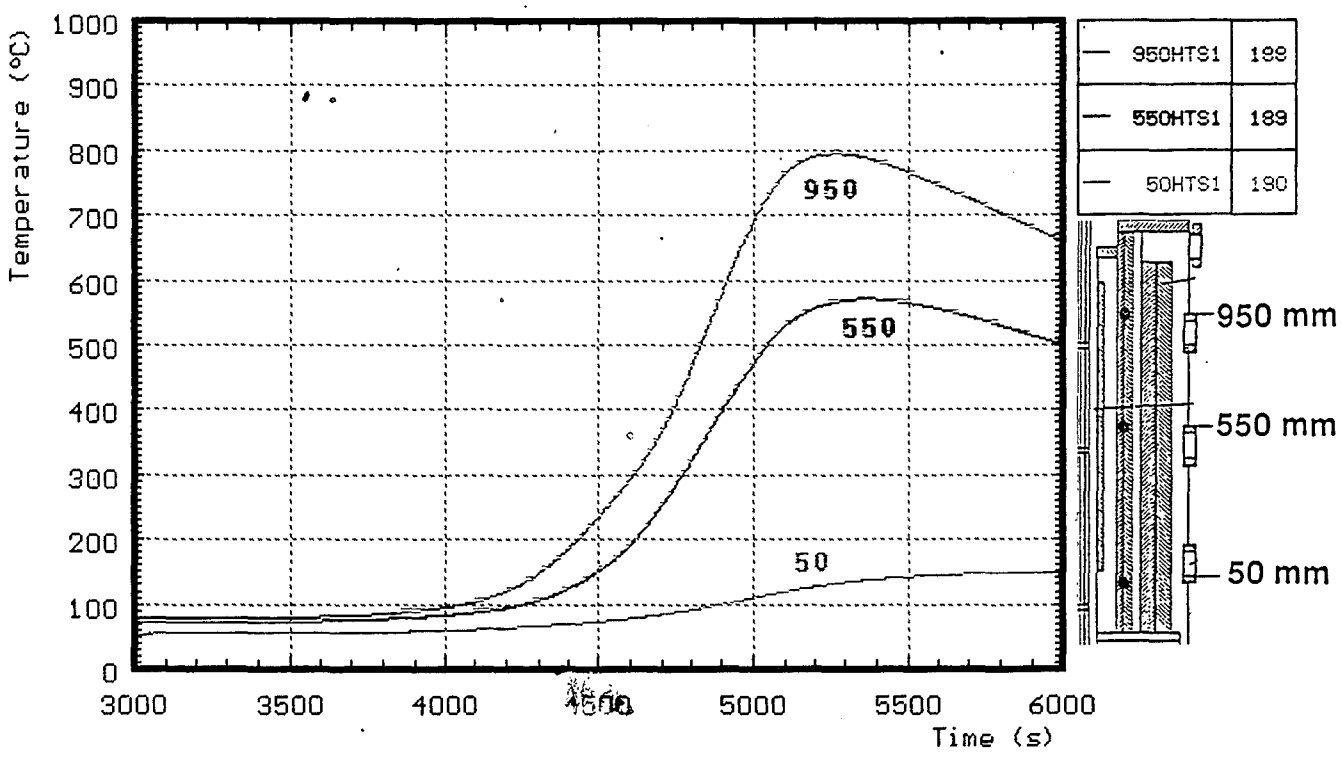

Fig. 56: CORA-10; Temperatures of HTS at 172 mm radius

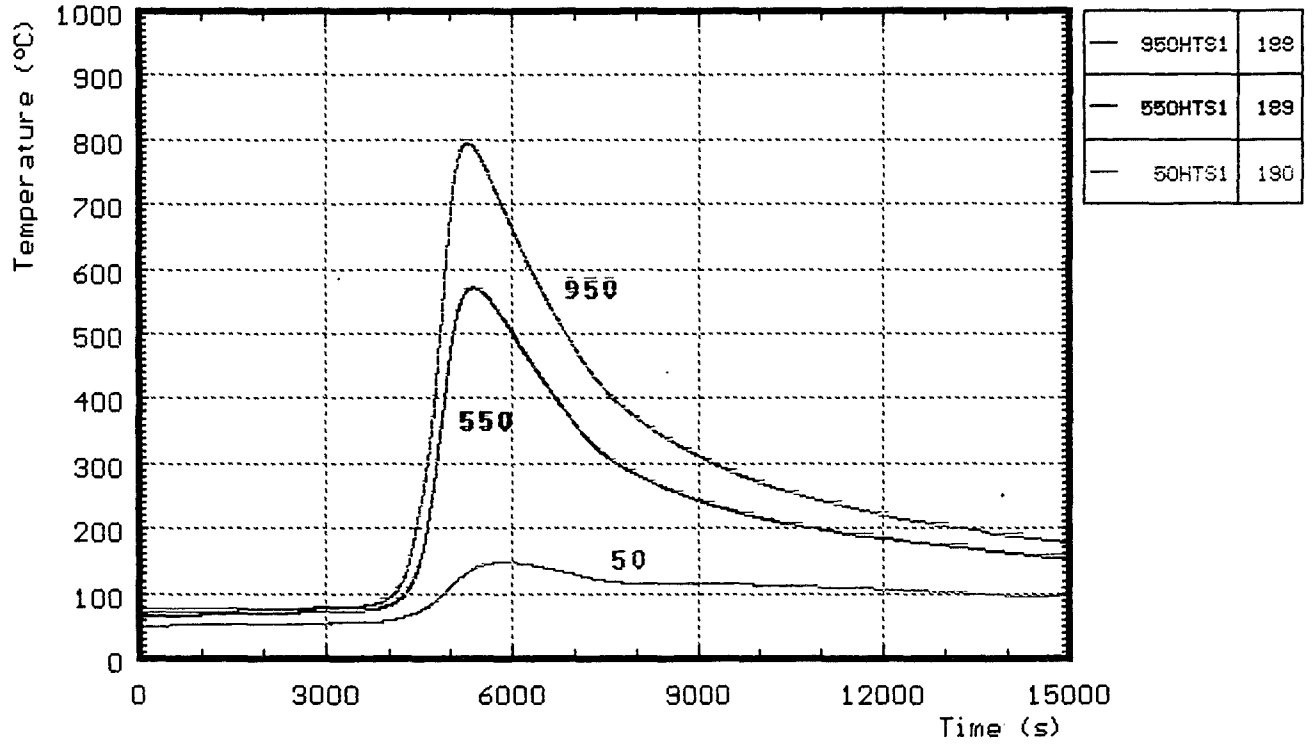

Fig. 57: CORA-10; Temperatures of HTS at 172 mm radius (0-15000 s)

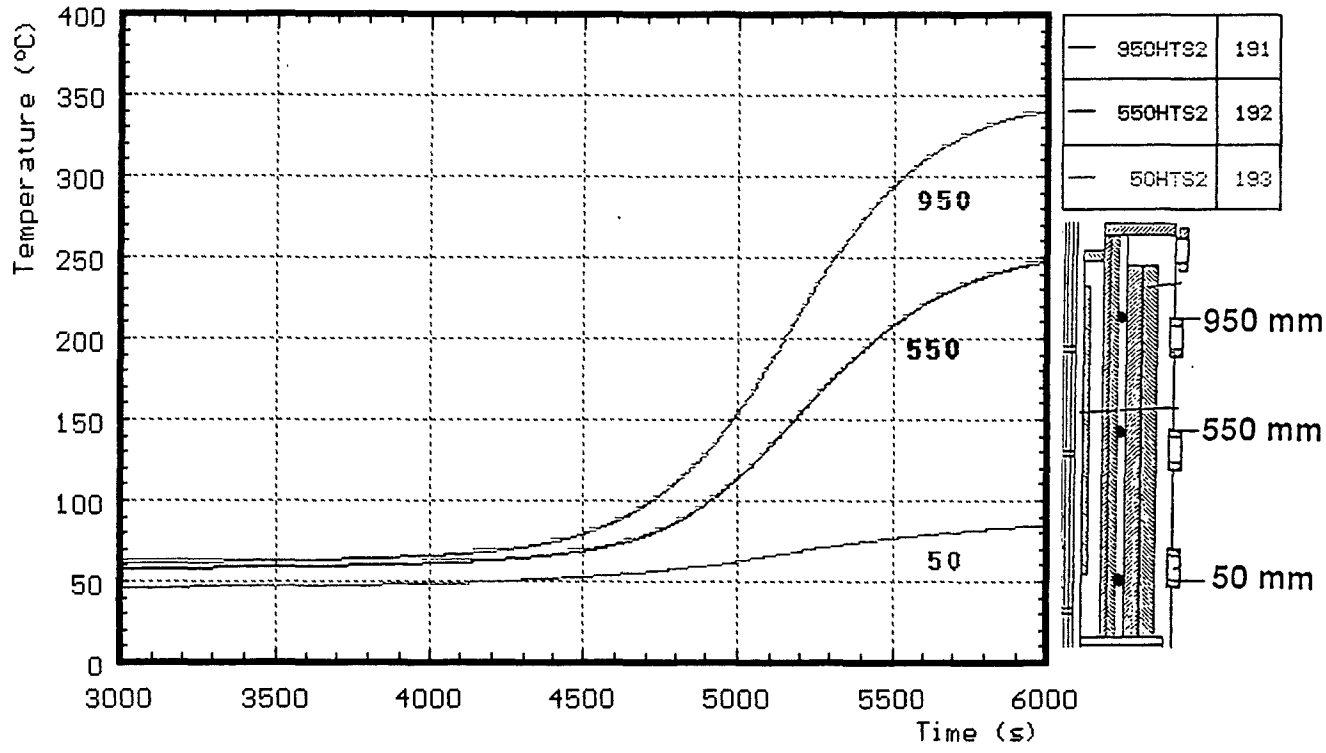

Fig. 58: CORA-10; Temperatures of HTS at 192 mm radius

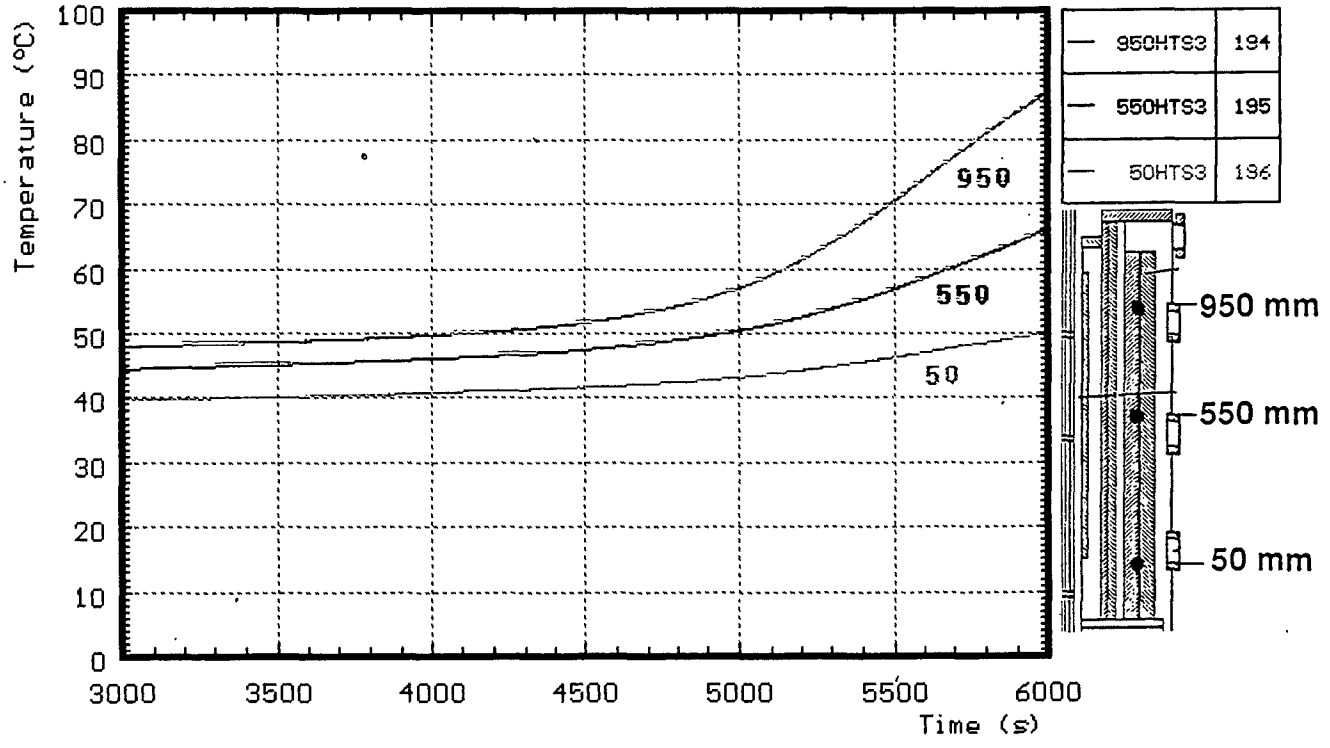

Fig. 59: CORA-10; Temperatures of HTS at 255 mm radius

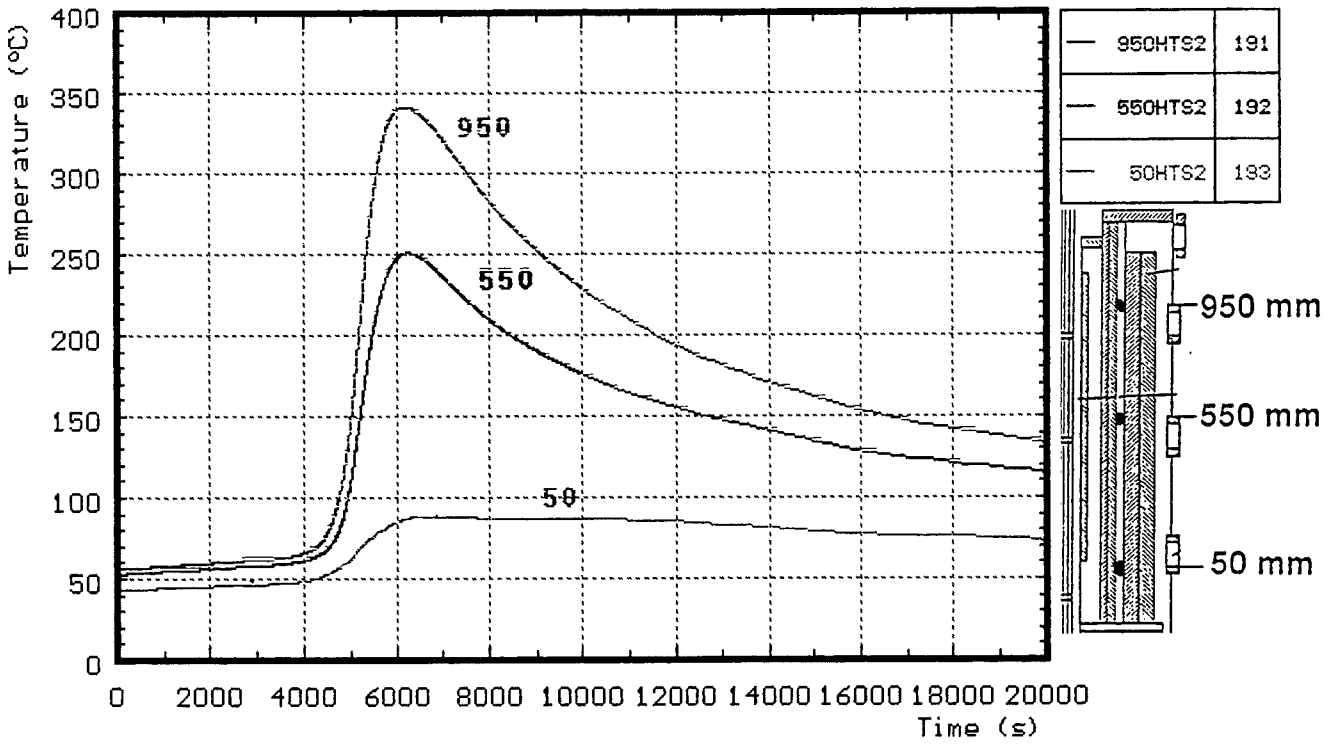

Fig. 60: CORA-10; Temperatures of HTS at 192 mm radius (0-20000 s)

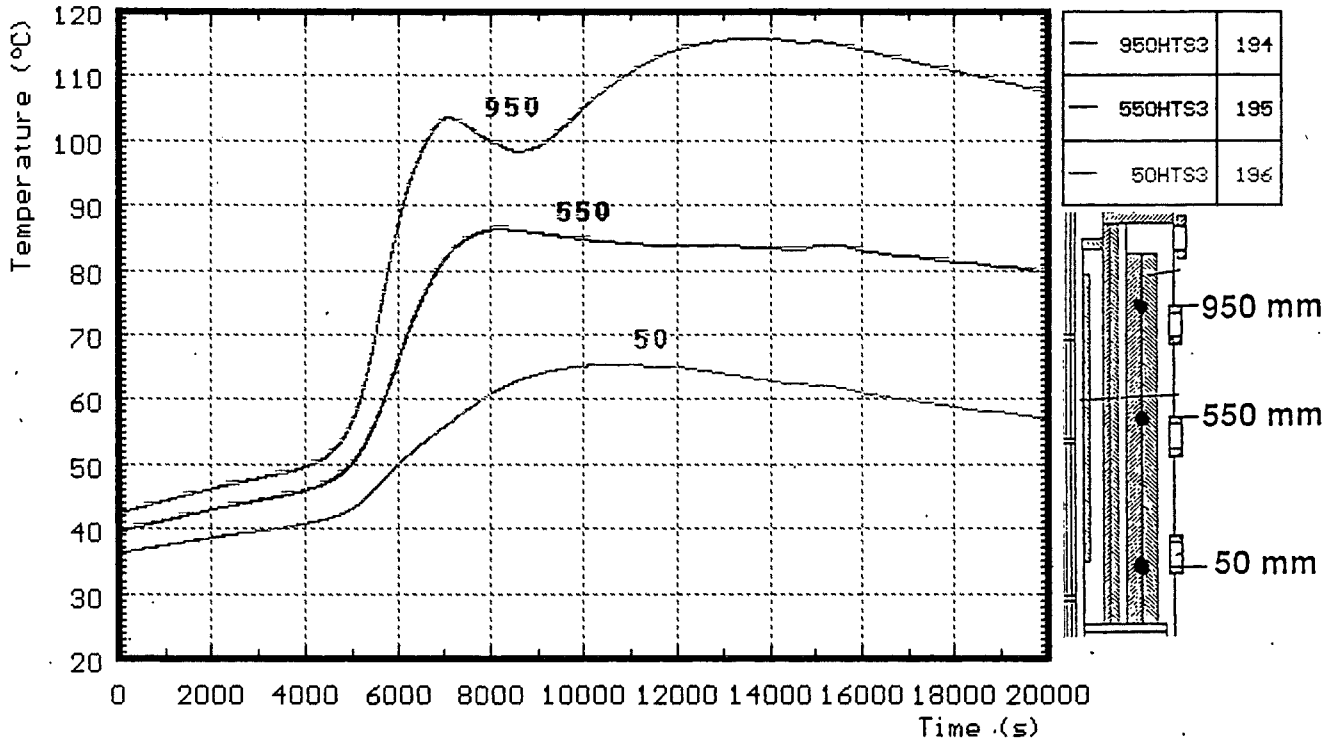

Fig. 61: CORA-10; Temperatures of HTS at 255 mm radius (0-20000 s)

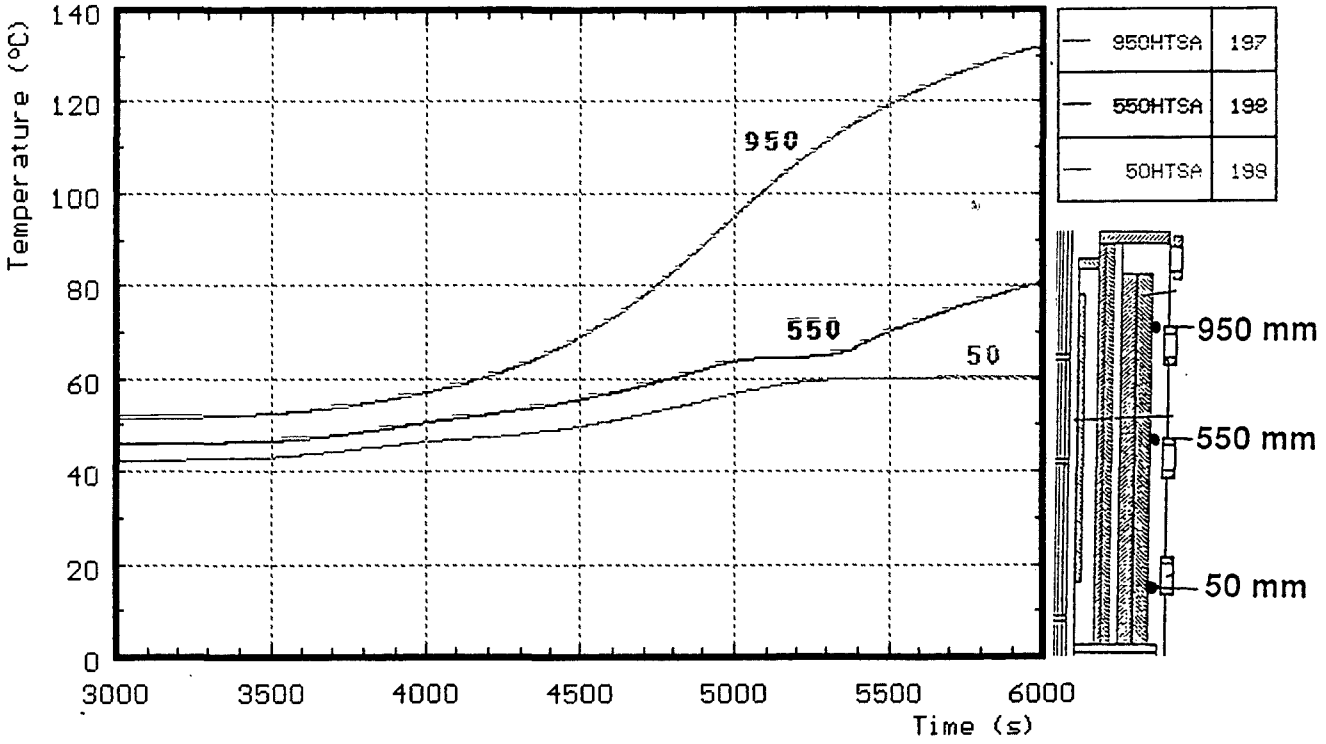

Fig. 62: CORA-10; Temperatures of HTS at 293 mm radius

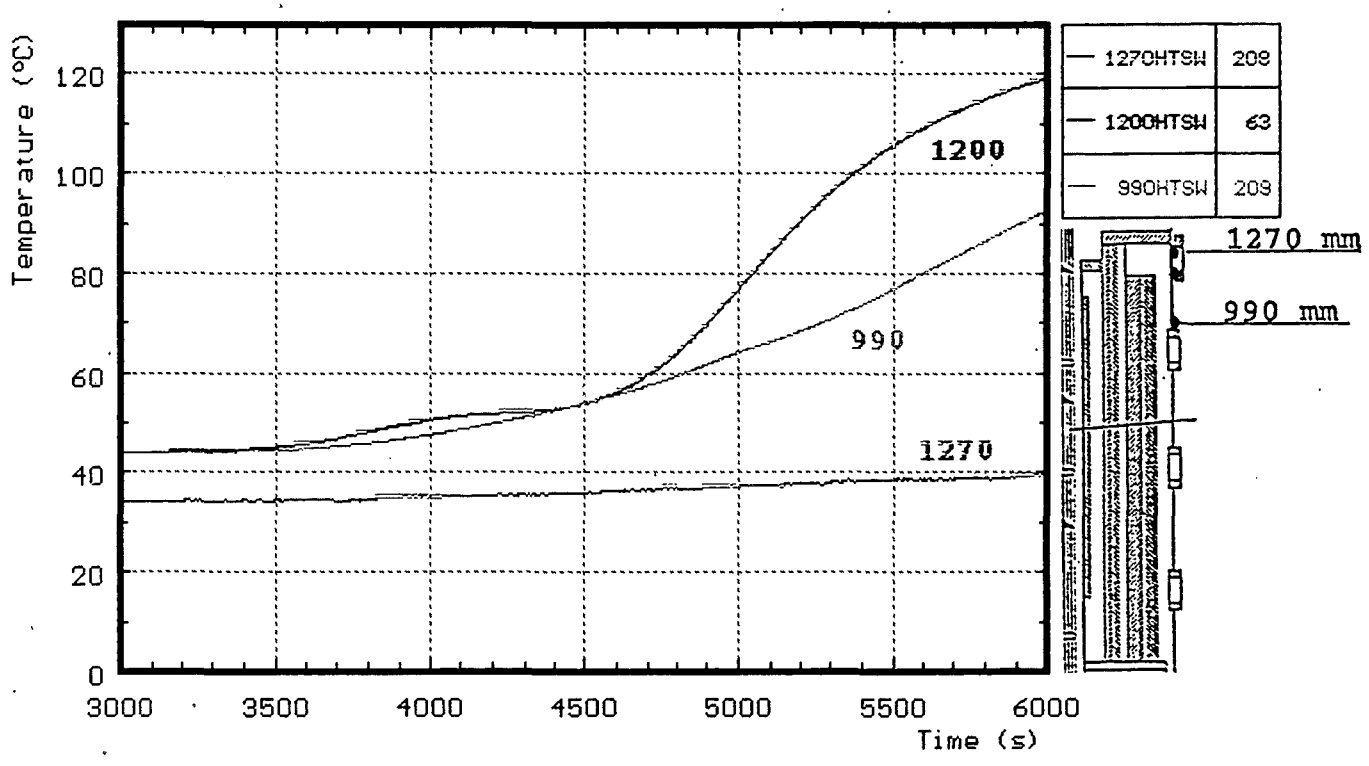

Fig. 63: CORA-10; Temperatures of HTS at the outer surface , 380 mm radius

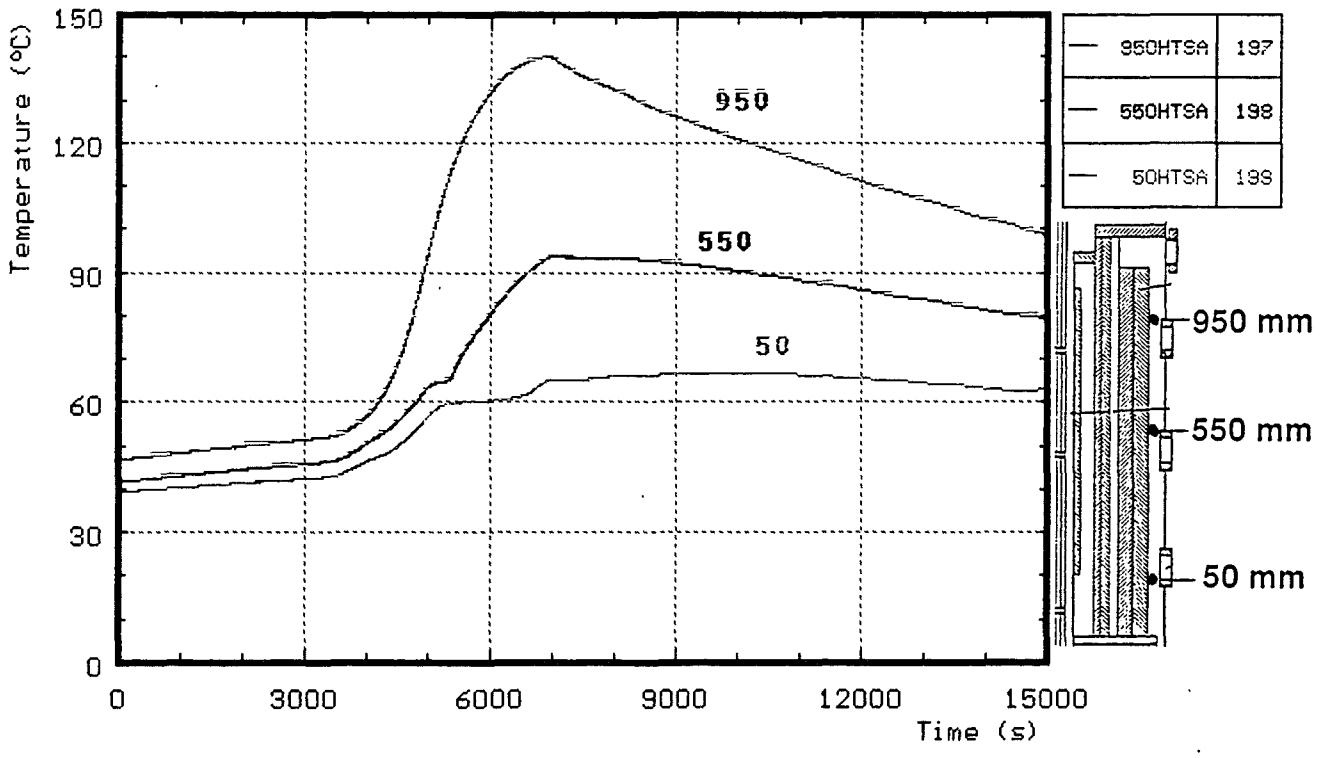

Fig. 64: CORA-10; Temperatures of HTS at 293 mm radius (0-15000 s)

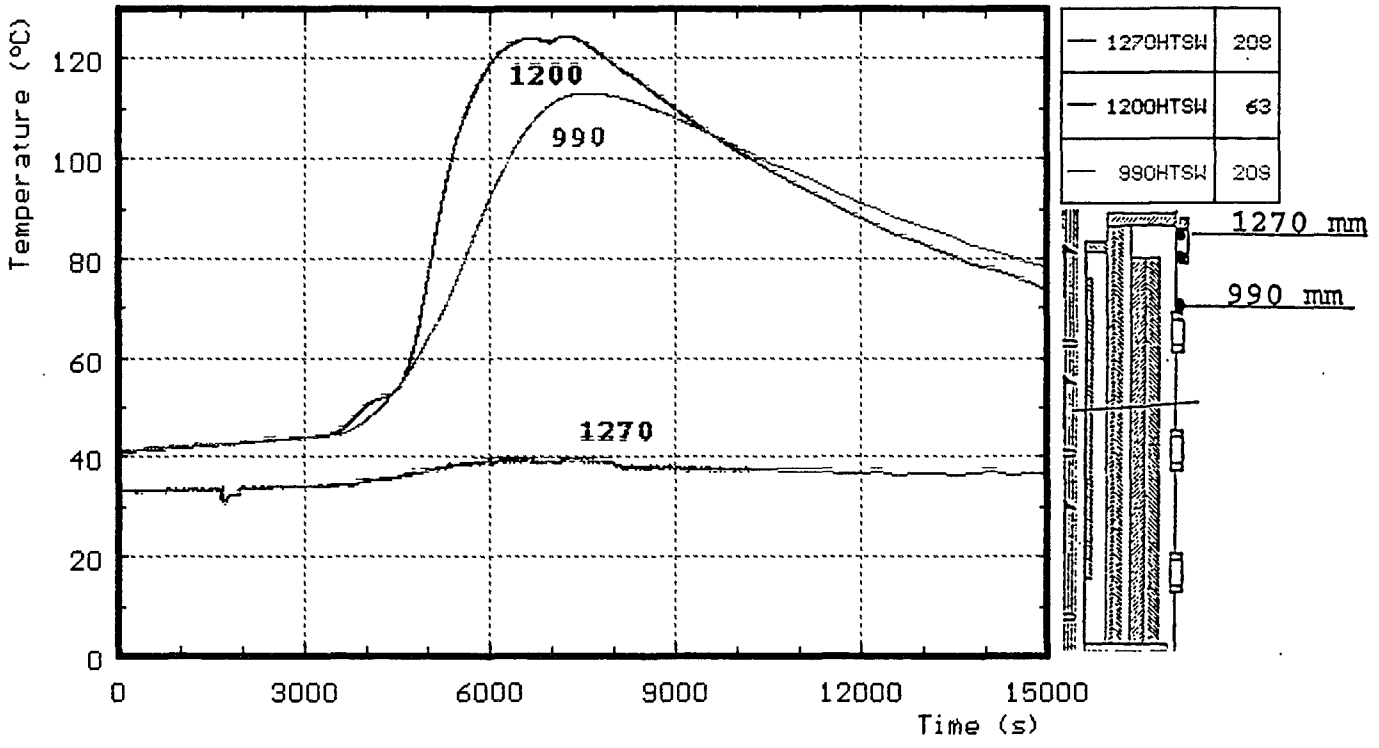

Fig. 65: CORA-10; Temperatures of HTS at the outer surface, 380 mm radius (0-15000 s)

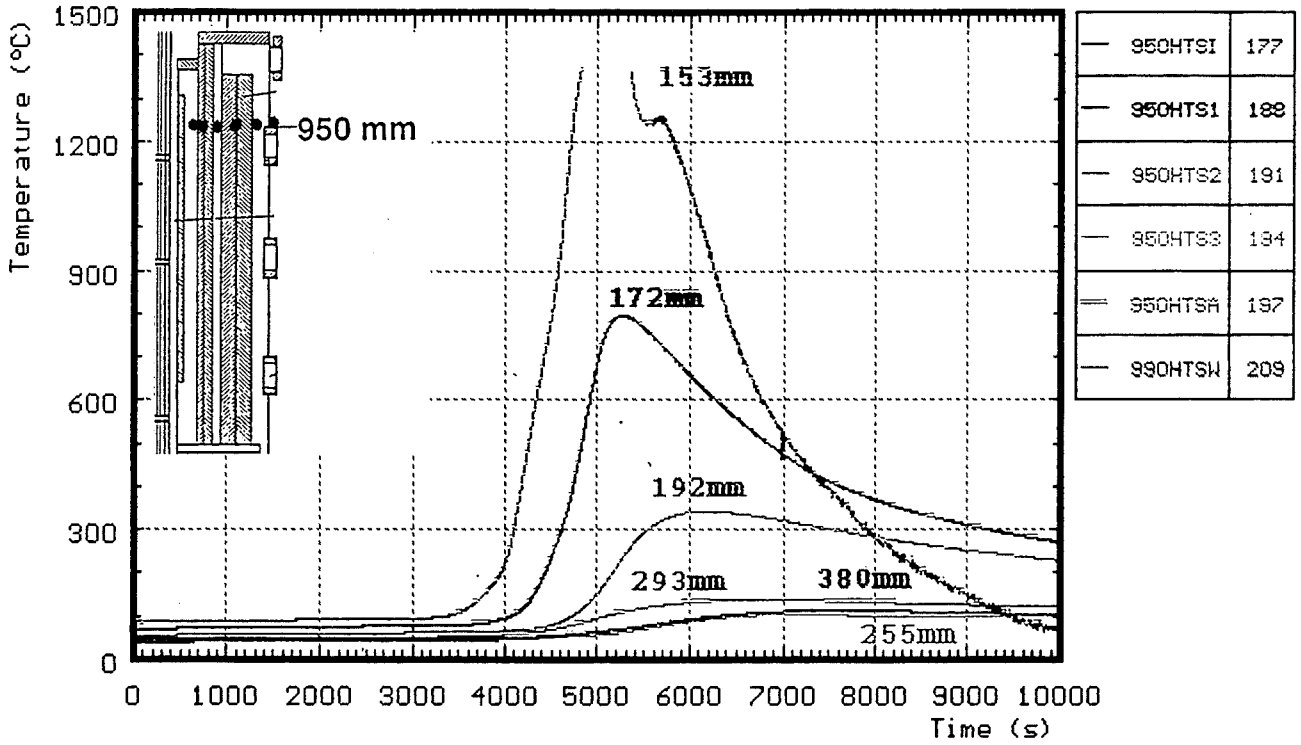

Fig. 66: CORA-10; Temperatures of HTS, Radial dependence at 950 mm elevation (0-10000 s)

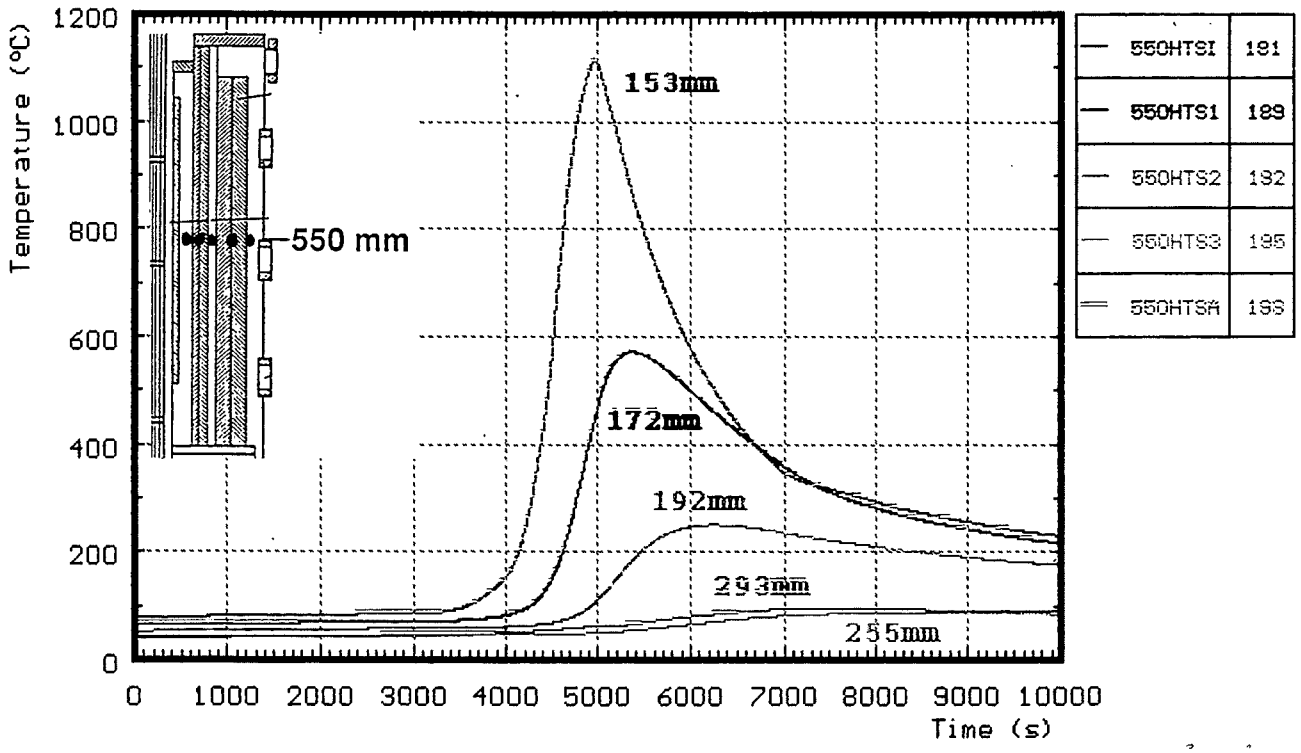

Fig. 67: CORA-10; Temperatures of HTS, Radial dependence at 550 mm elevation (0-10000 s)

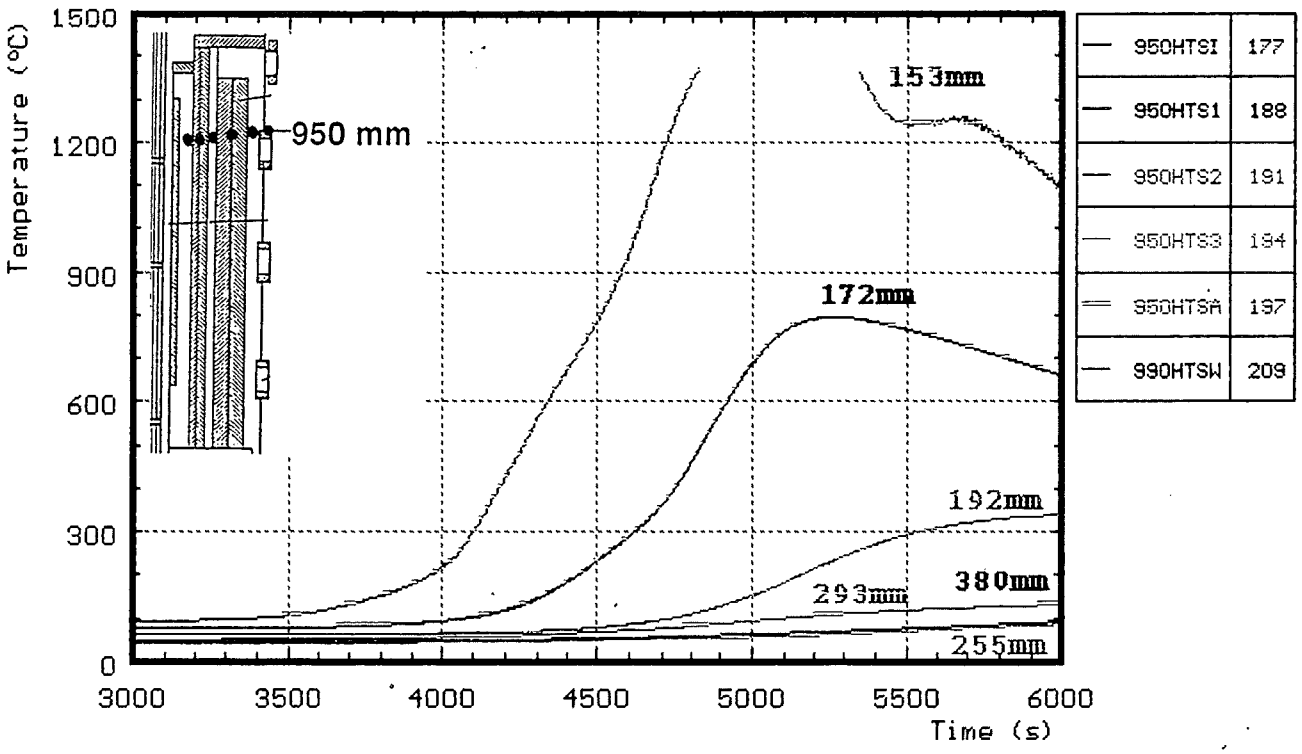

Fig. 68: CORA-10; Temperatures of HTS, Radial dependence at 950 mm elevation (3000-6000 s)

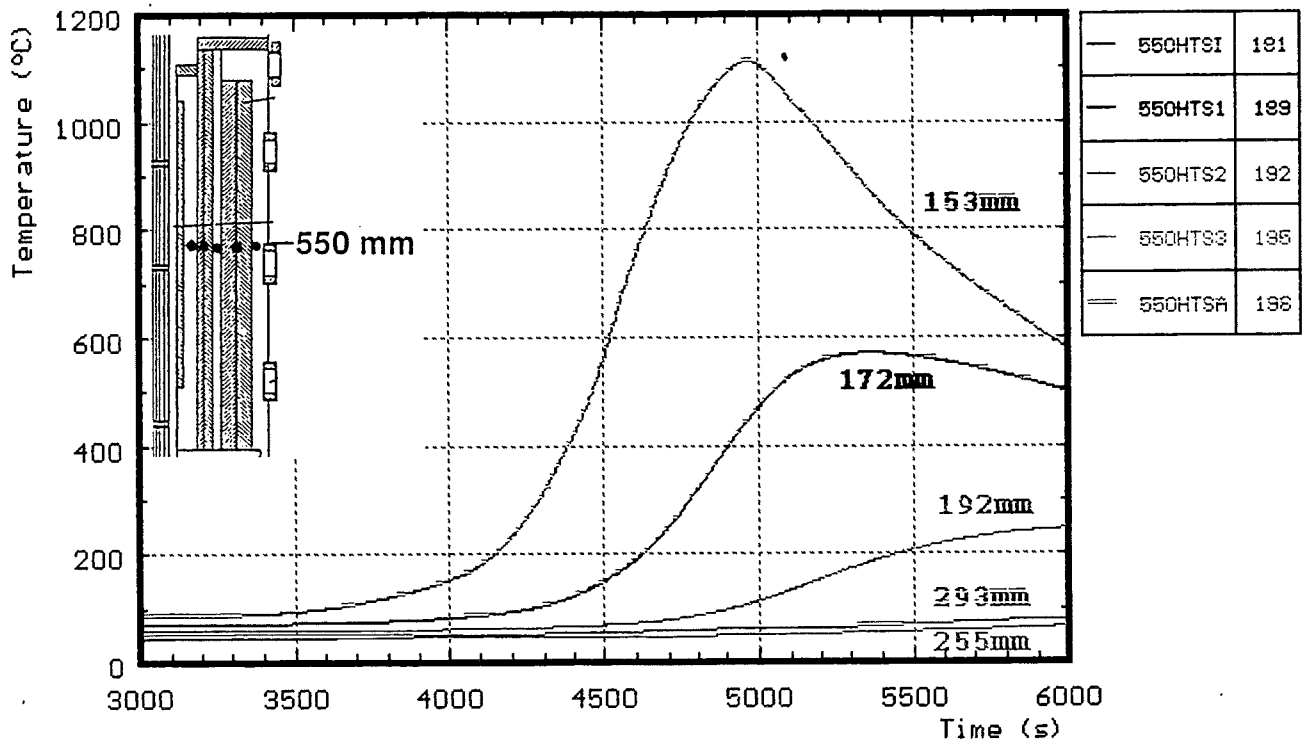

Fig. 69: CORA-10; Temperatures of HTS, Radial dependence at 550 mm elevation (3000-6000 s)

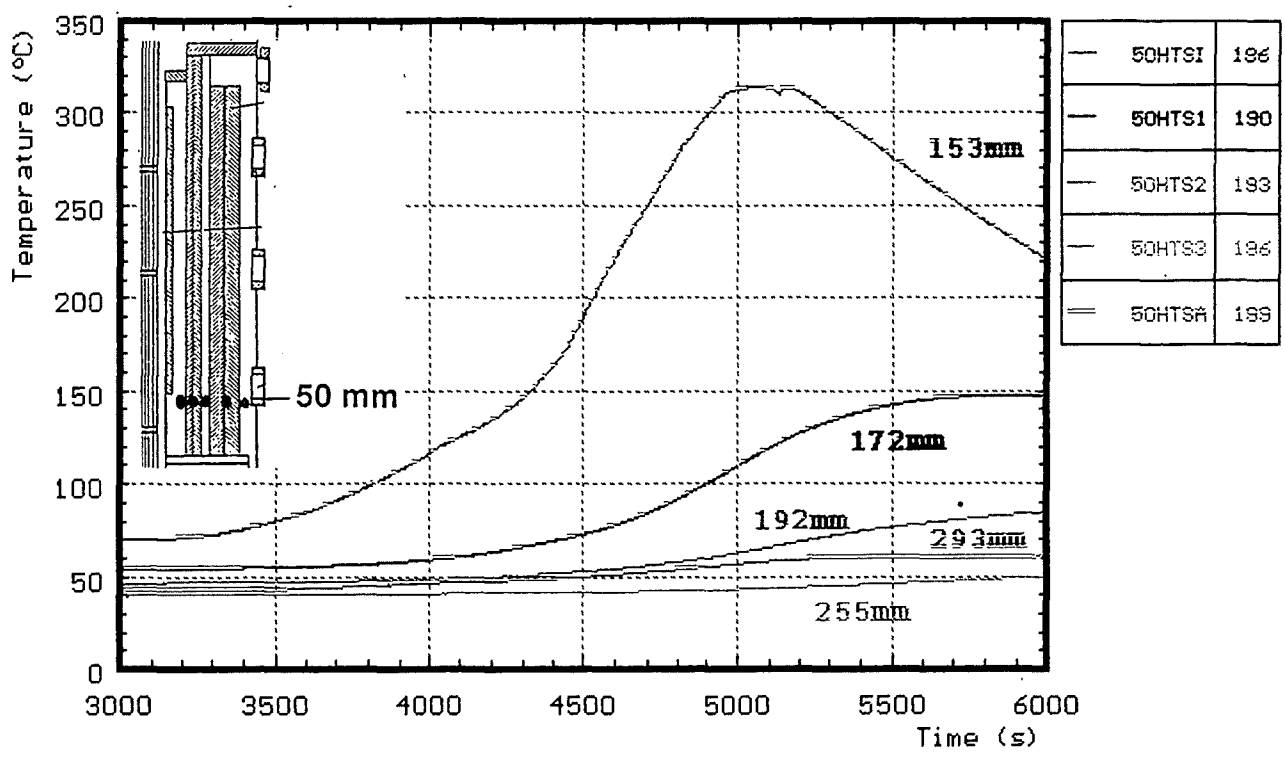

Fig. 70: CORA-10; Temperatures of HTS, Radial dependence at 50 mm elevation (3000-6000 s)

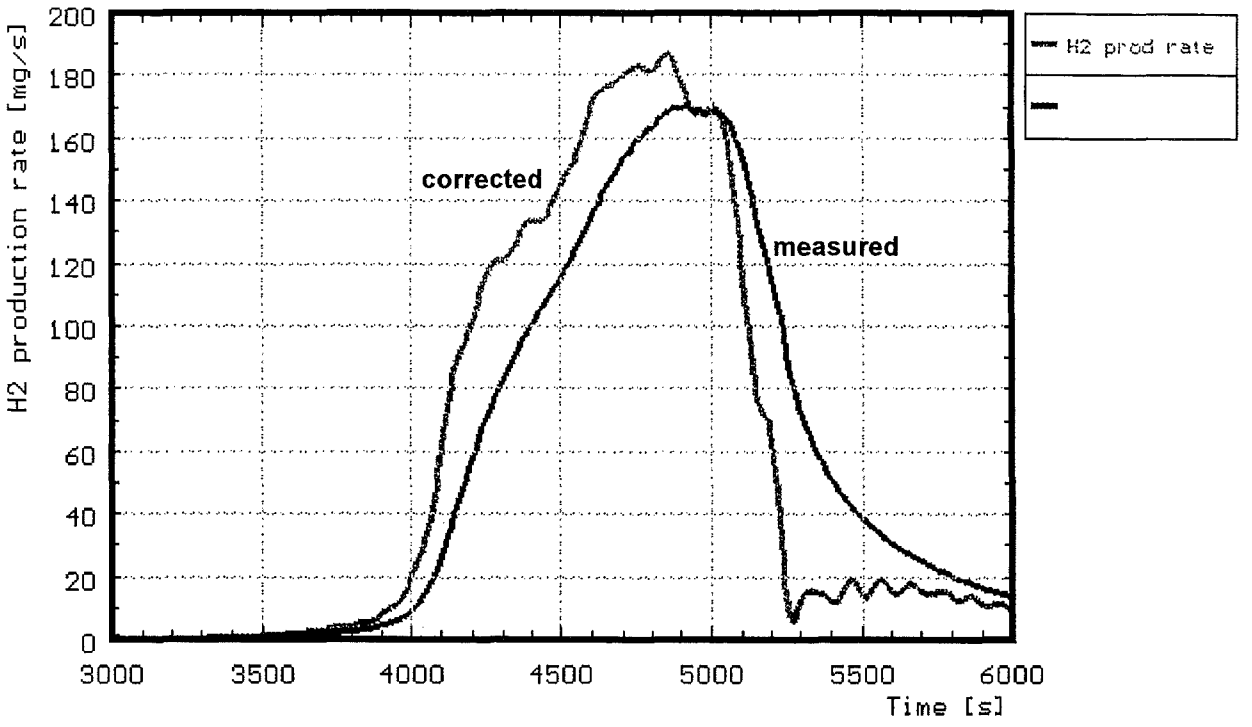

Fig. 71: Hydrogen production rate in test CORA-10

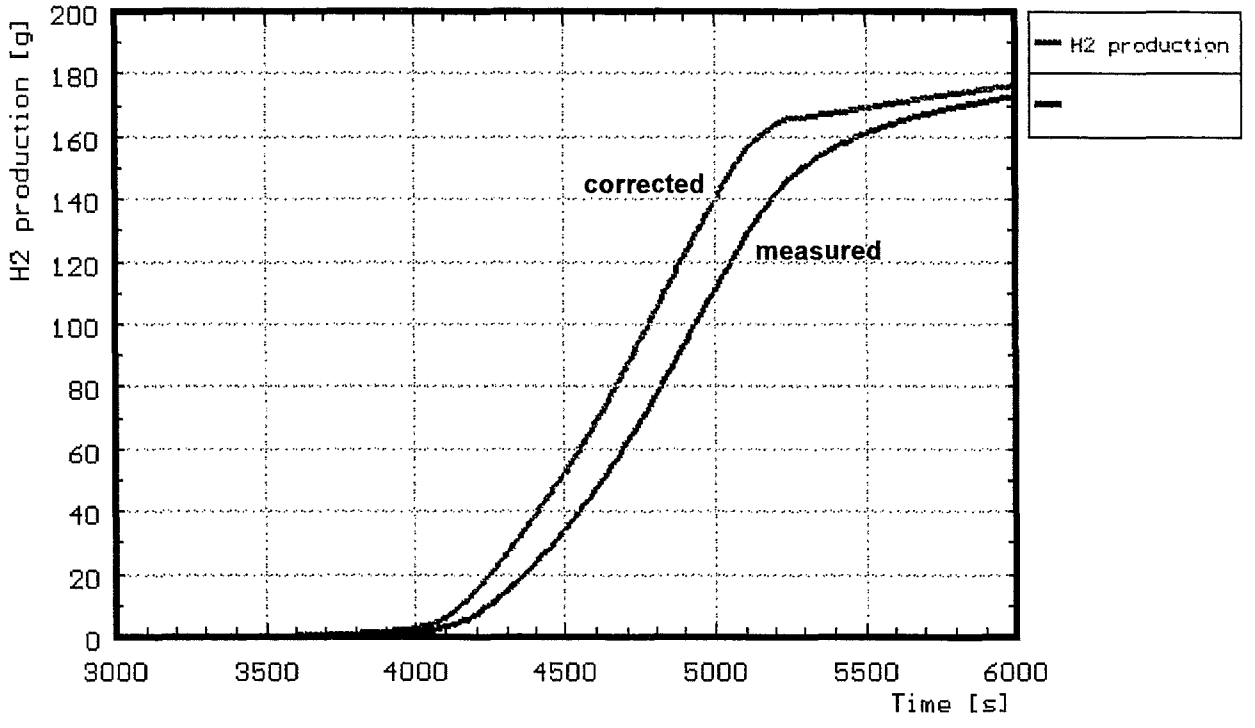

Fig. 72: Hydrogen production in test CORA-10; integral values

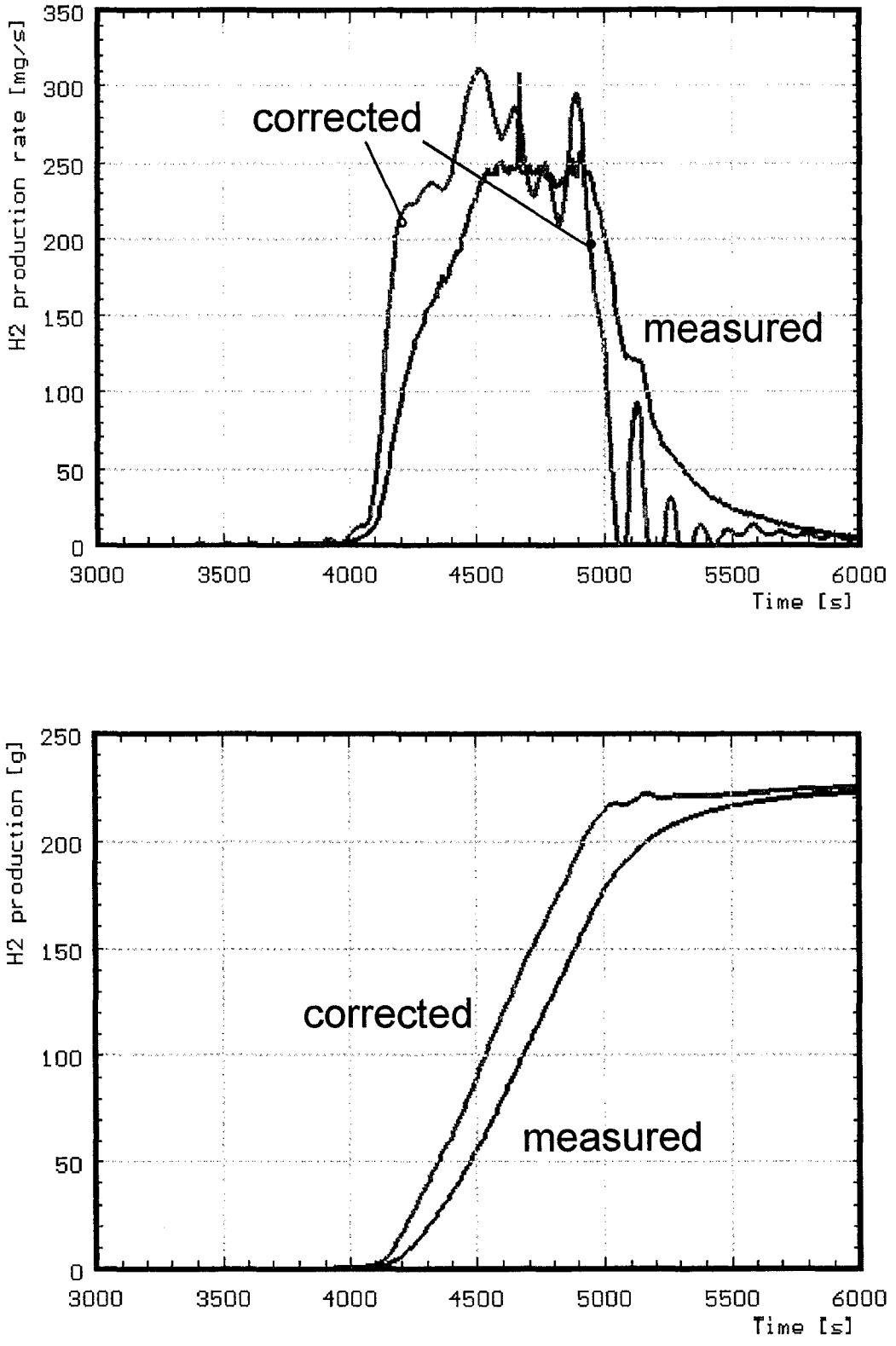

Fig. 72a: Hydrogen production in test CORA-29; production rate (top) and integral values (bottom)

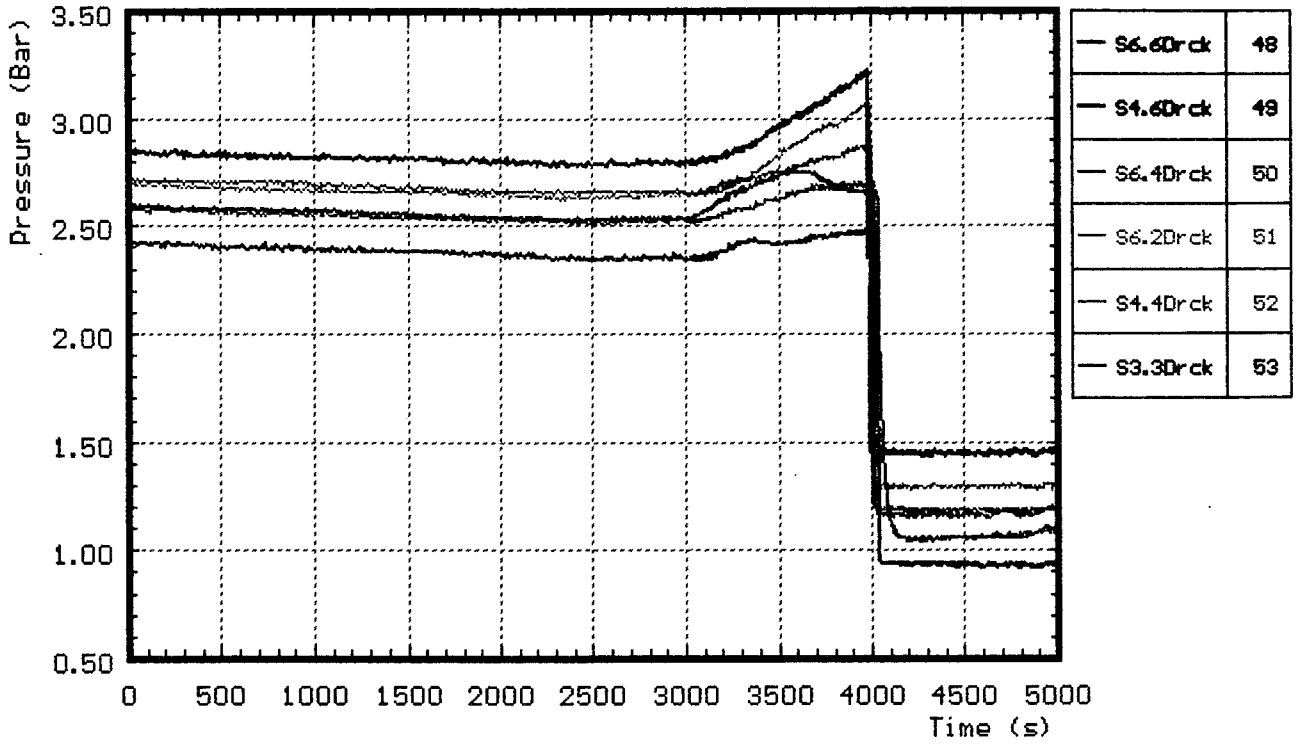

Fig. 73: CORA-10; Internal pressure of fuel rod simulators and absorber rods

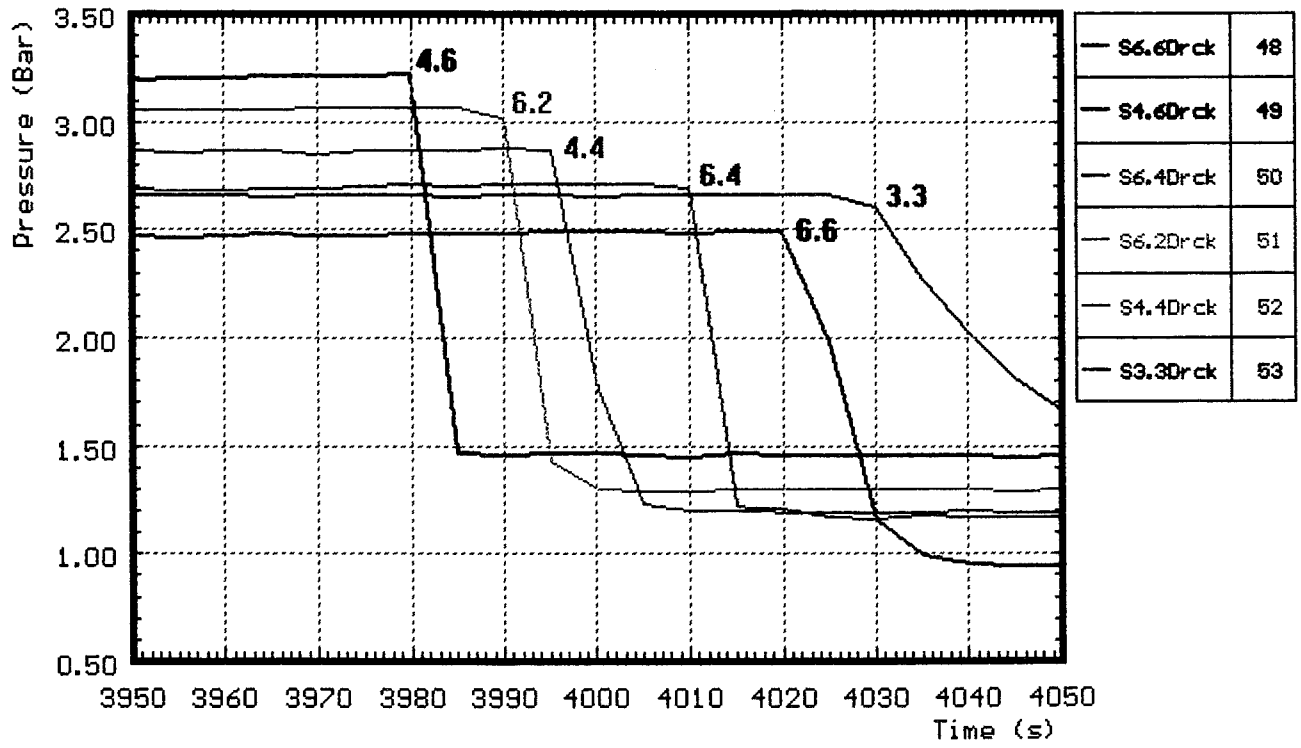

Fig. 74: CORA-10; Determination of failure time by pressure loss measurement

Pressure Loss Measurement		Video Measurements	
Failure Time of Rods		Start of Melt Movement	
Absorber rod 4.6	3980 s		
		3982 s	800 mm
		3982 s	600 mm
Absorber rod 6.2	3990 s		
		4000 s	800 mm

Fig. 75: CORA-10; Determination of failure of absorber rods

Failure temperature: 1230 °C

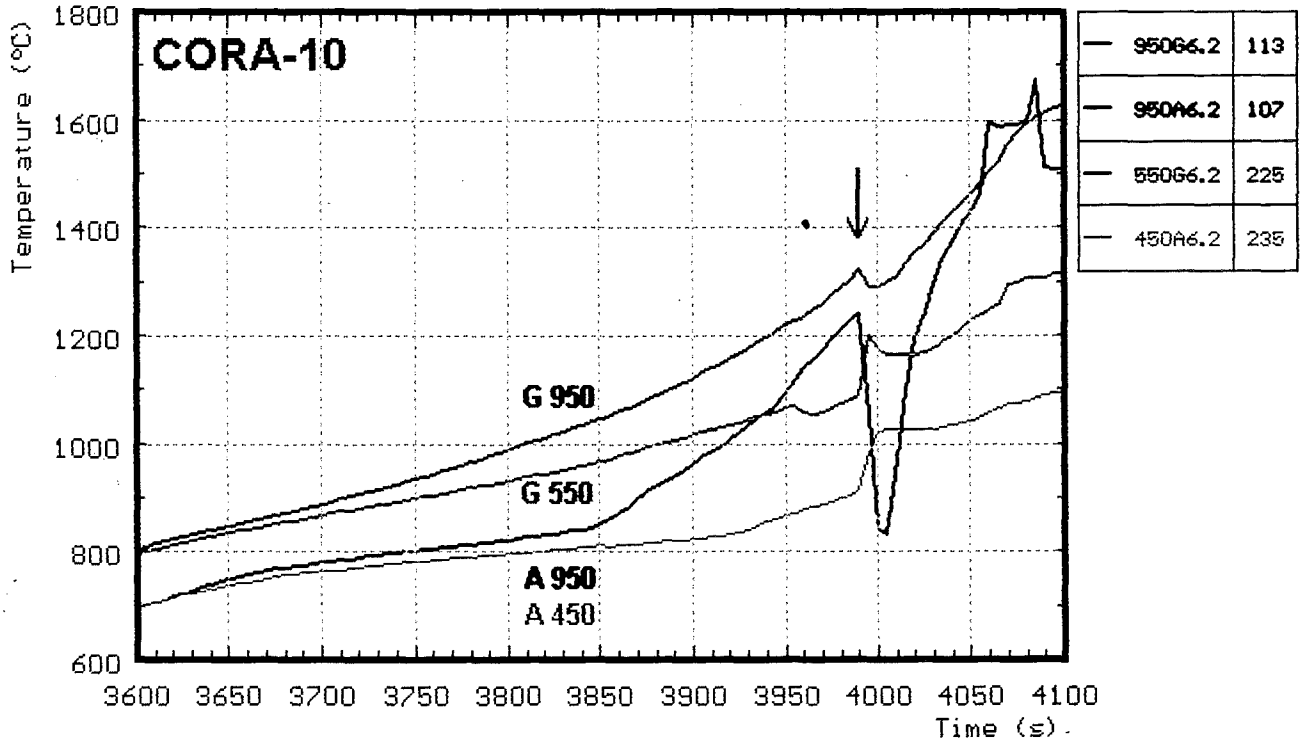

Fig. 76: CORA-10; Determination of failure of absorber rod 6.2 by irregularities in absorber and guide tube temperature measurements

Failure temperature: 1230 °C

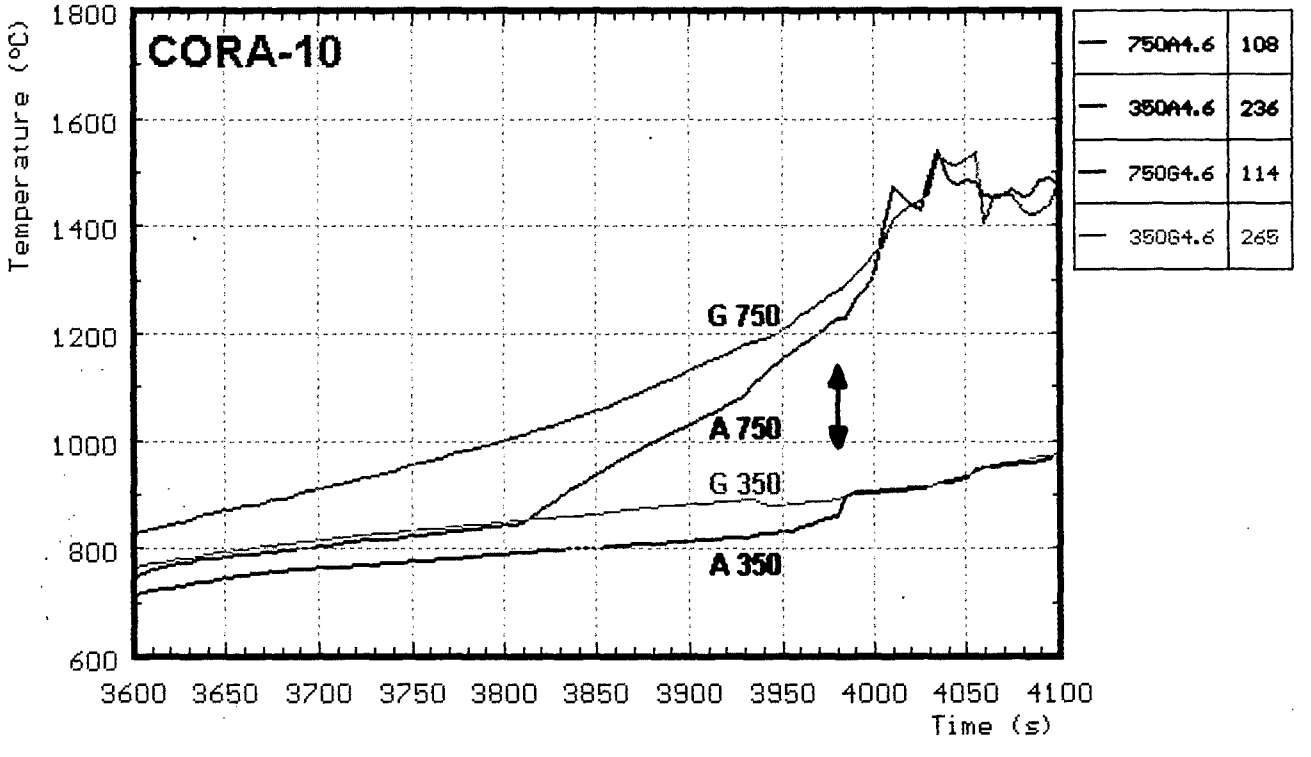

Fig. 77: CORA-10; Determination of failure of absorber rod 4.6 by irregularities in absorber and guide tube temperature measurements

Pressure loss measurement

	Failure time	Failure temperature
Unheated rod 4.4	3995s	1280°
Unheated rod 6.4	4010s	1310°
Unheated rod 6.6	4020s	1330°
Heated rod 3.3	4030s	1450°

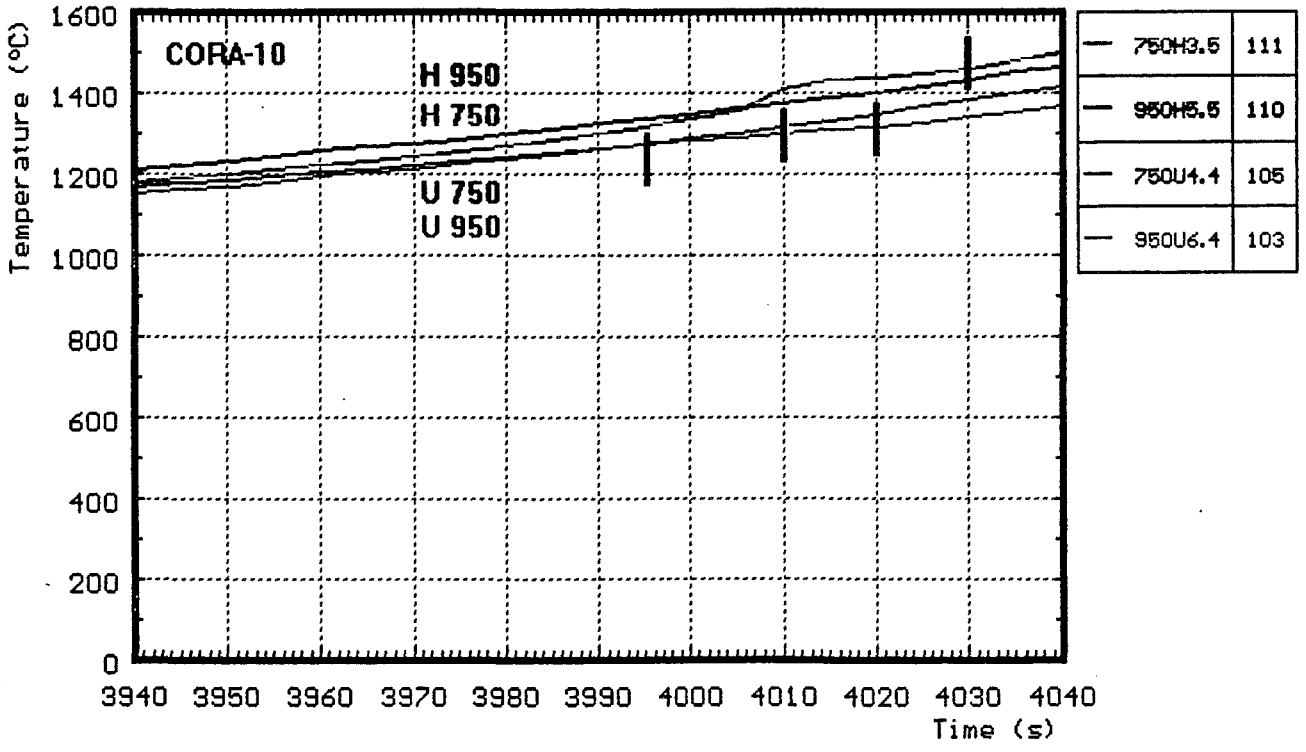

Fig. 78: CORA-10; Determination of failure of fuel rods by pressure loss measurement

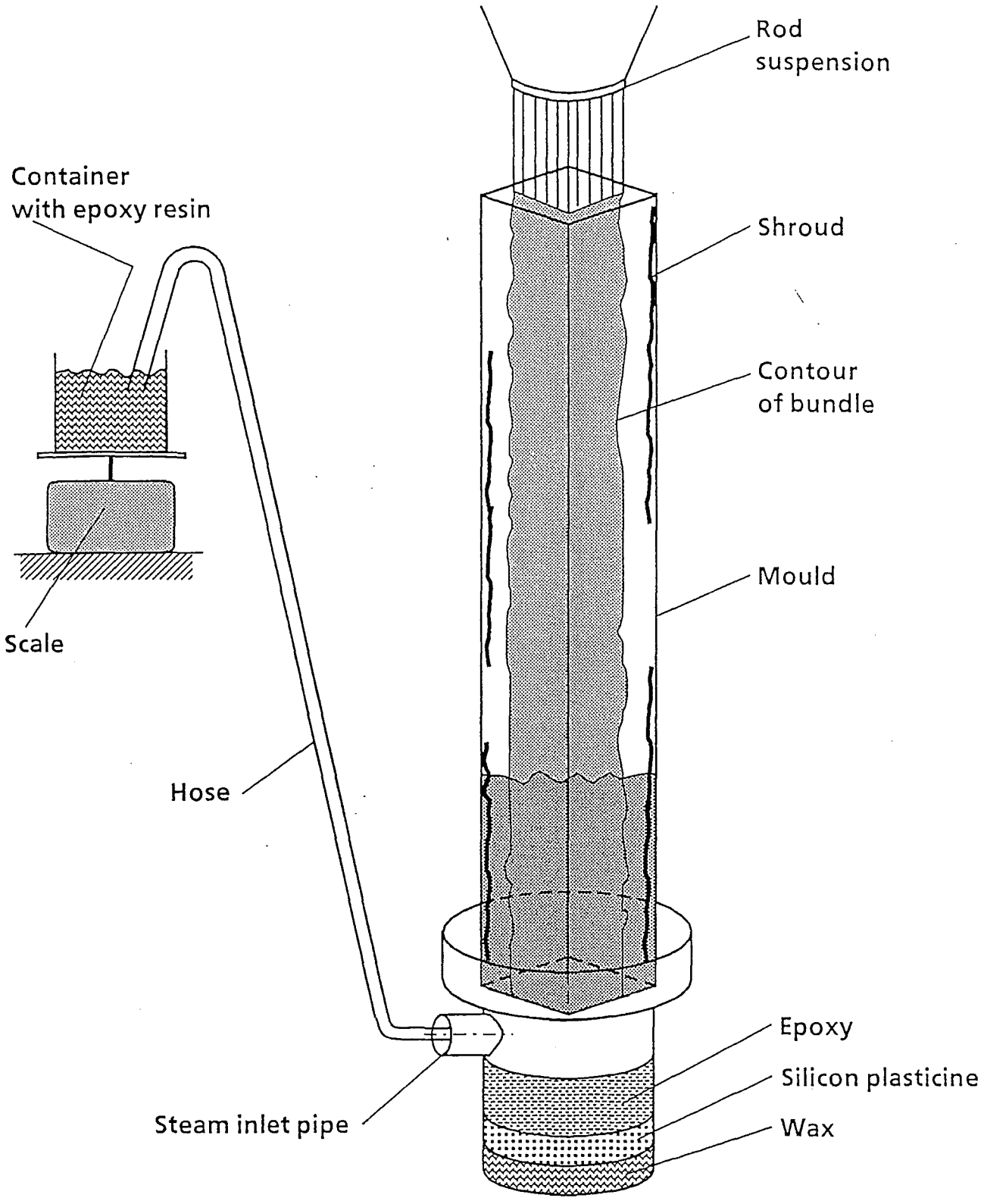

Fig. 79: CORA-10; Epoxying process of the tested bundle

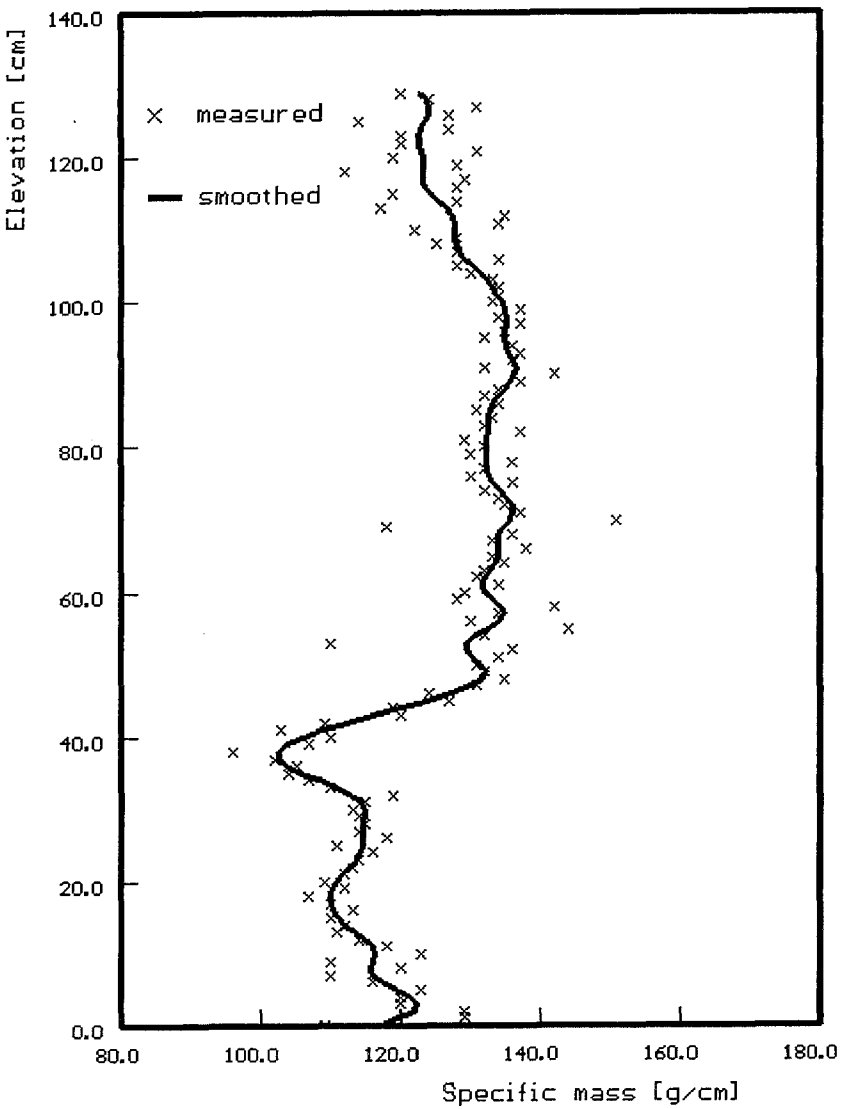

Fig. 80: CORA-10; Axial distribution of the bundle fill-up with epoxy resin

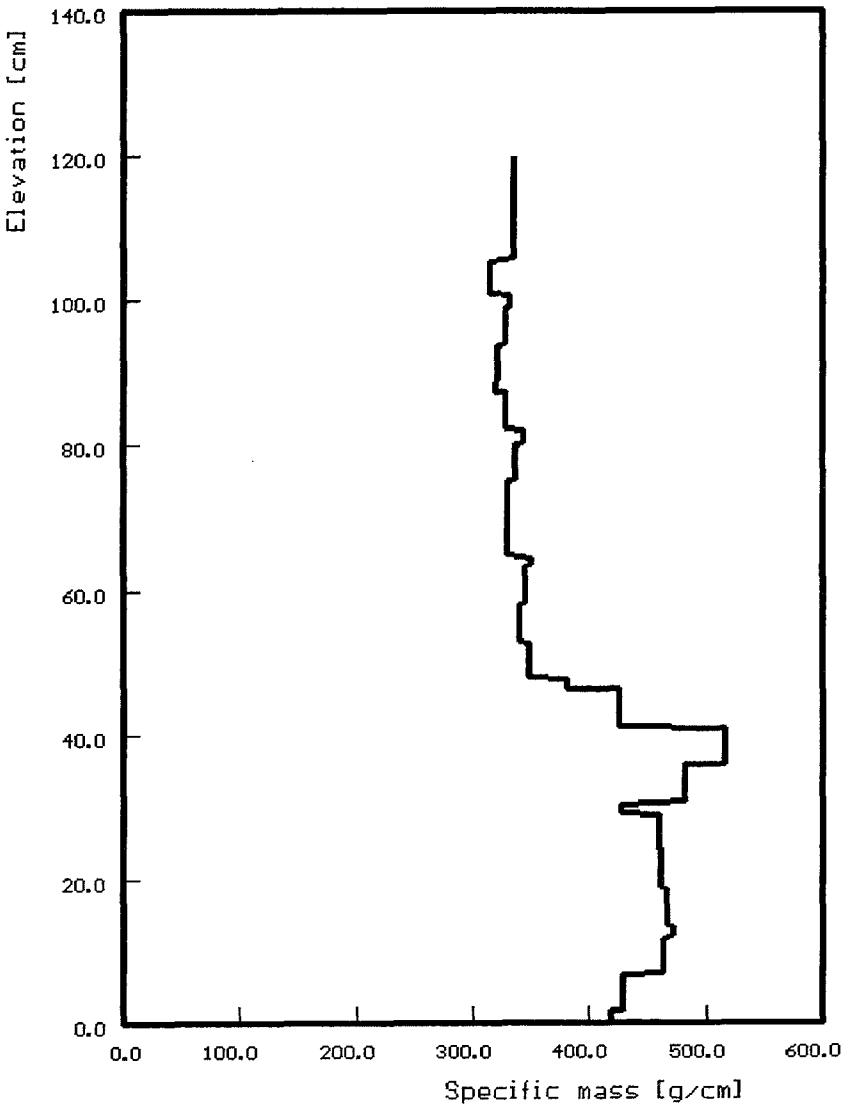

Fig. 81: CORA-10; Axial mass distribution of bundle segments filled with epoxy

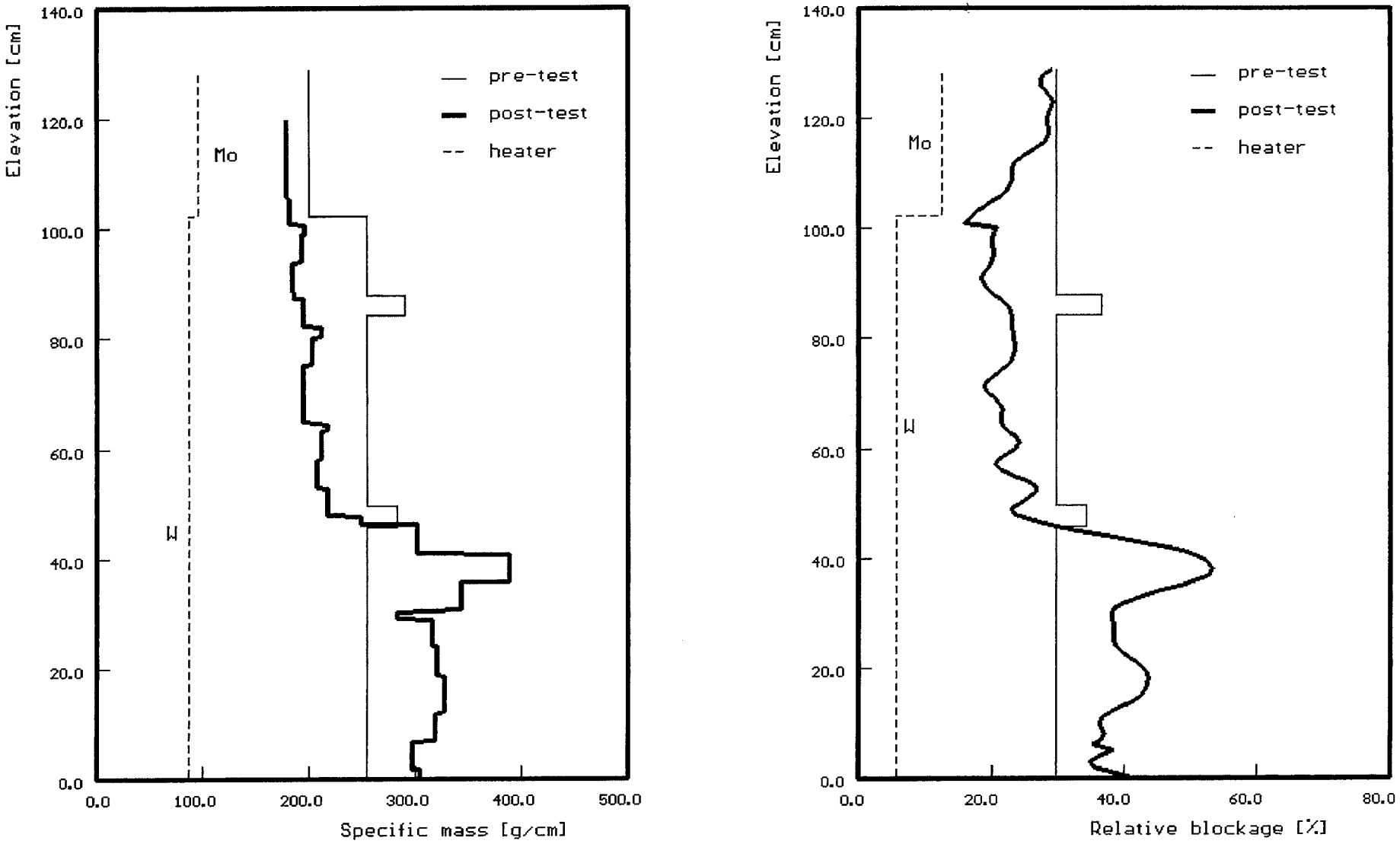

Fig. 82: Comparison of axial mass distribution and axial volume distribution after the test CORA-10

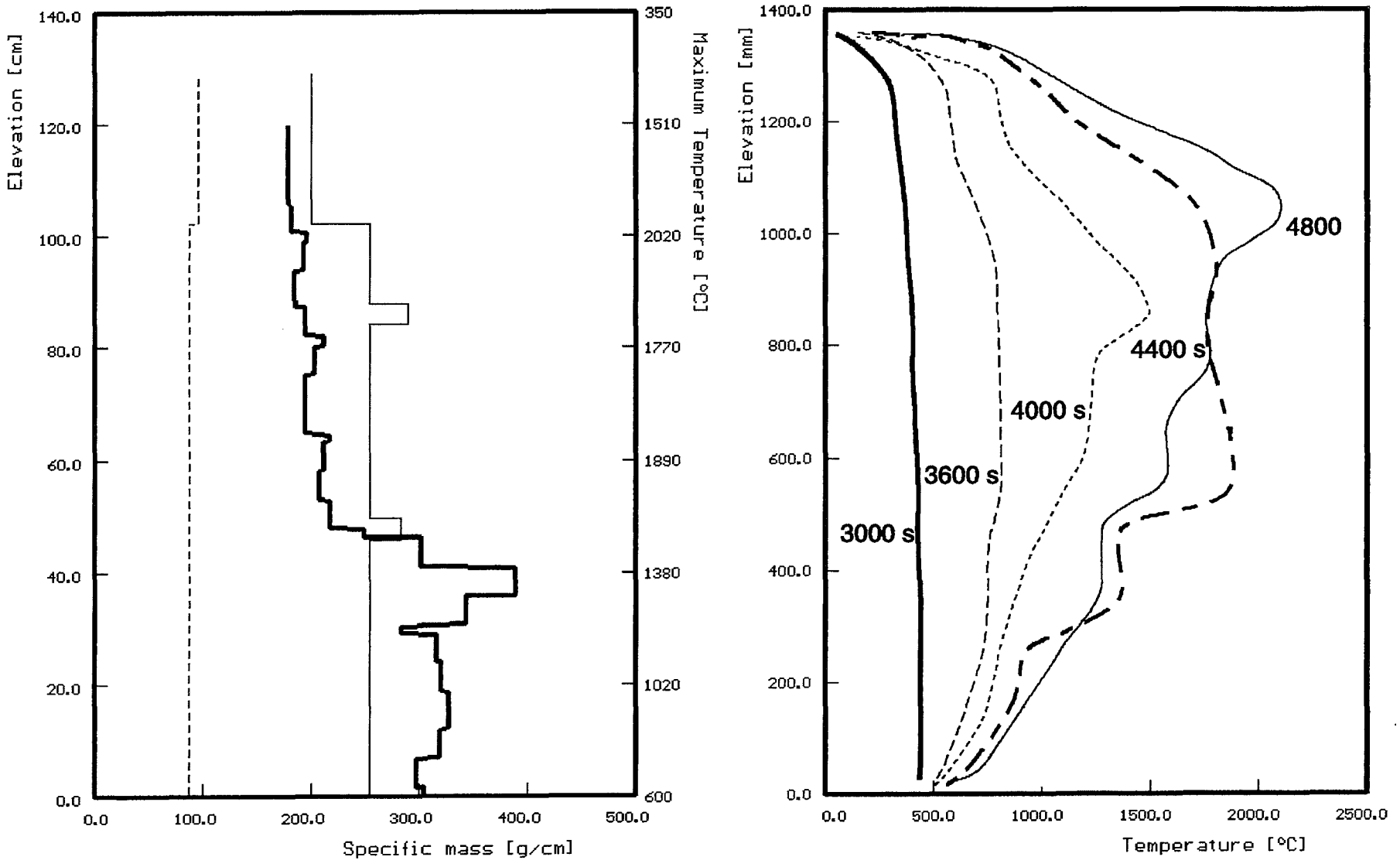

Fig. 83: **CORA 10; Axial mass distribution after the test and axial temperature distribution during the test**

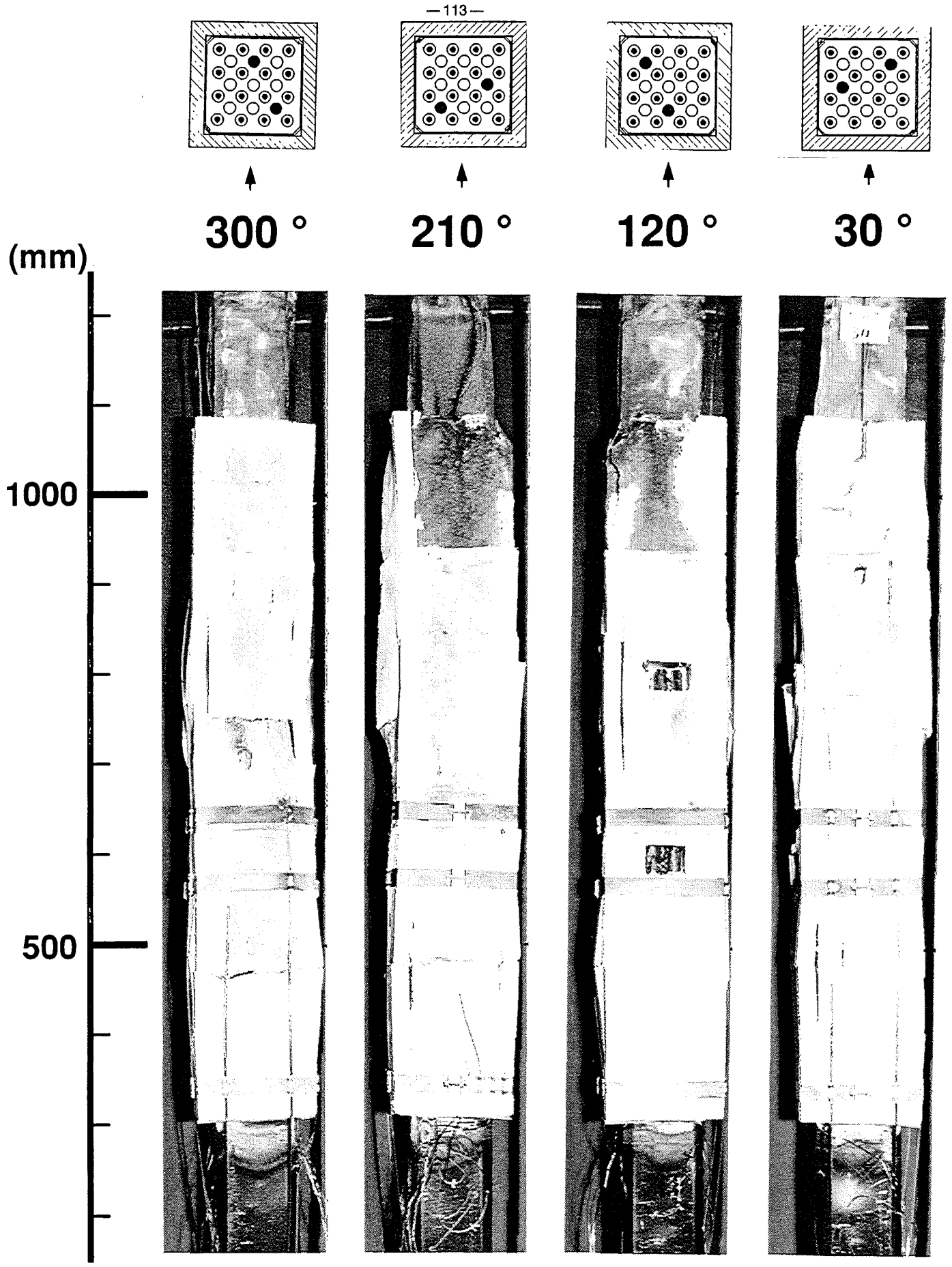

Fig. 84: CORA-10; Posttest appearance of the entire bundle length with the shroud insulation

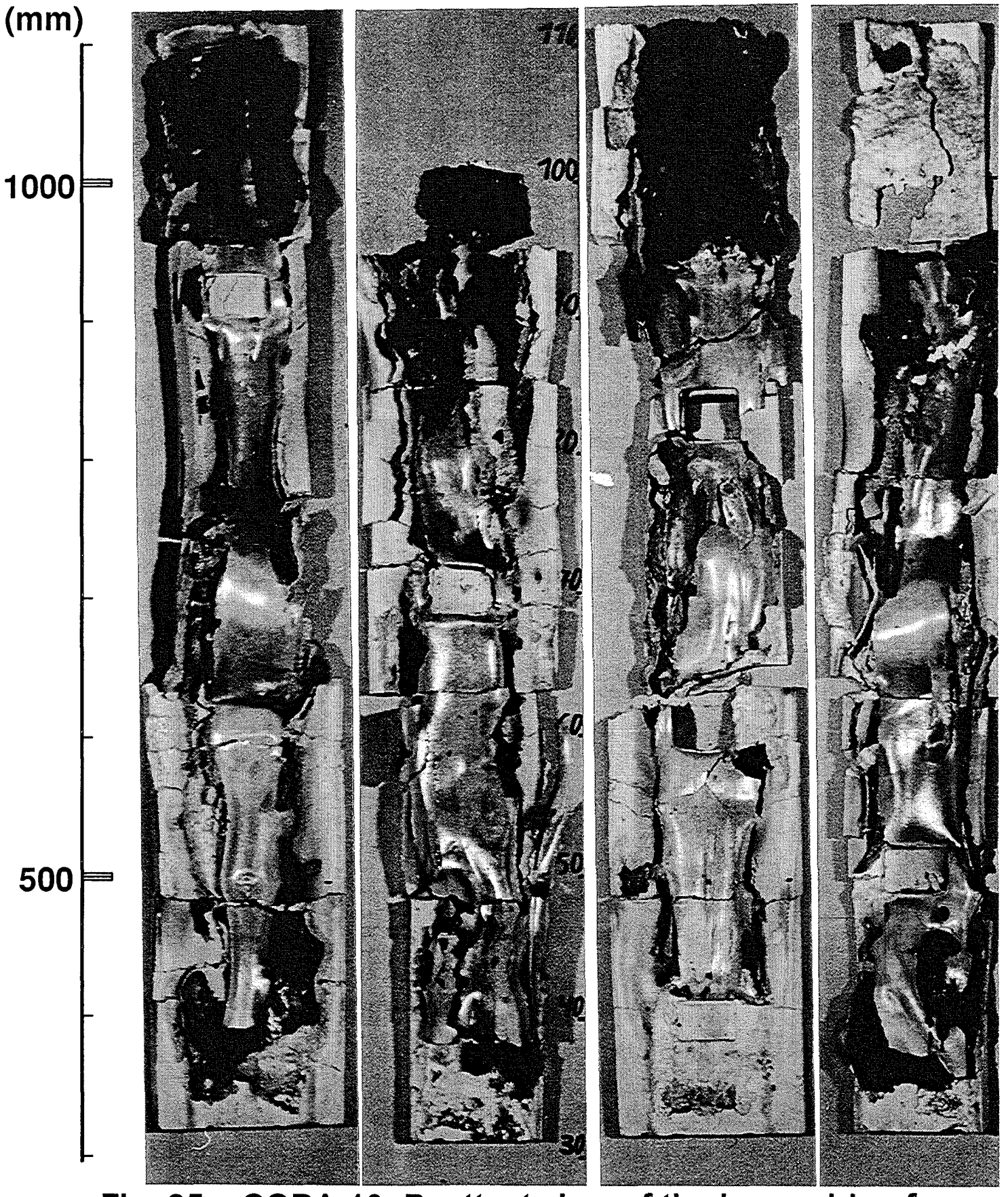

Fig. 85: CORA-10: Posttest view of the inner side of shroud insulation

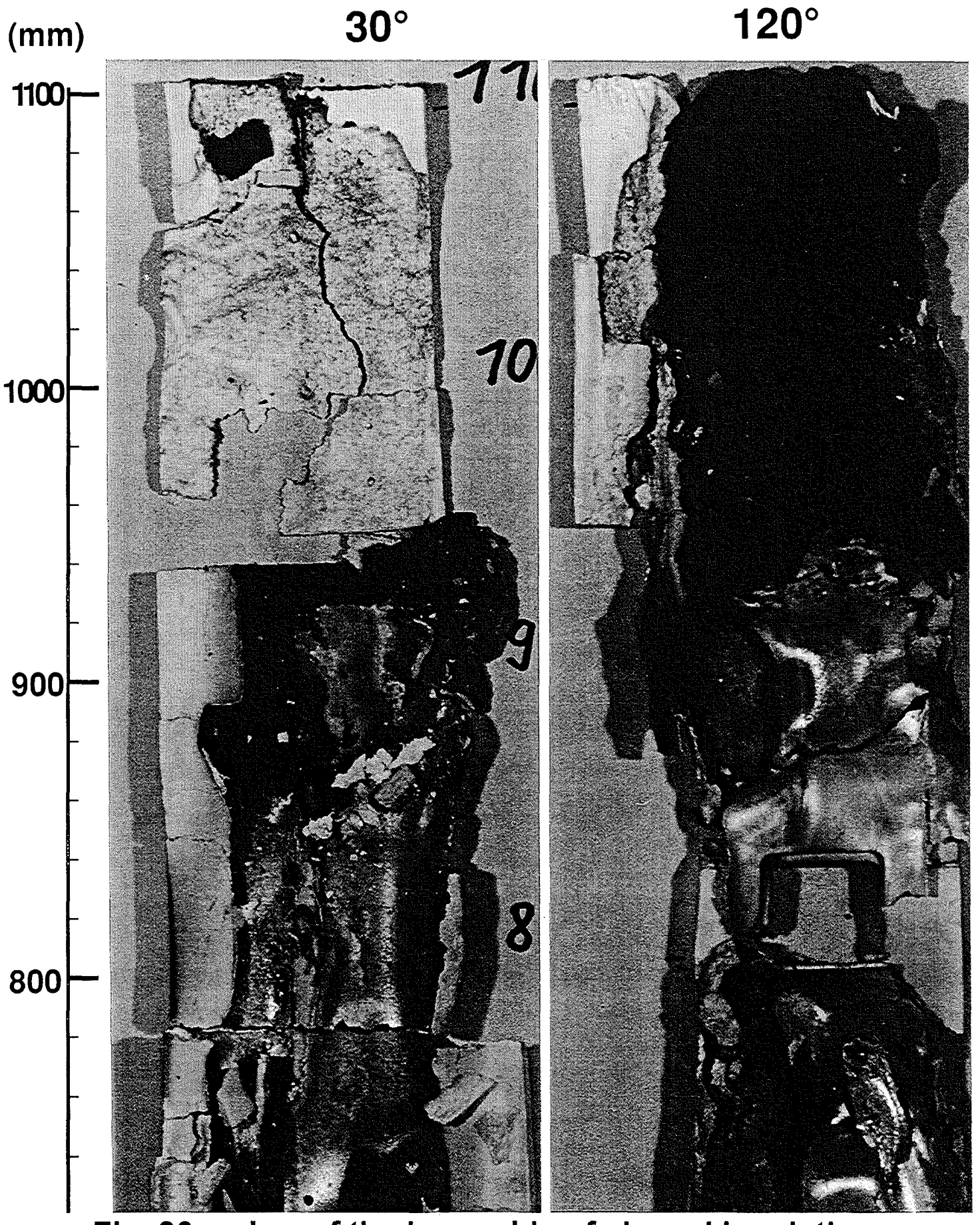

Fig. 86: view of the inner side of shroud insulation, 30° and 120° orientation

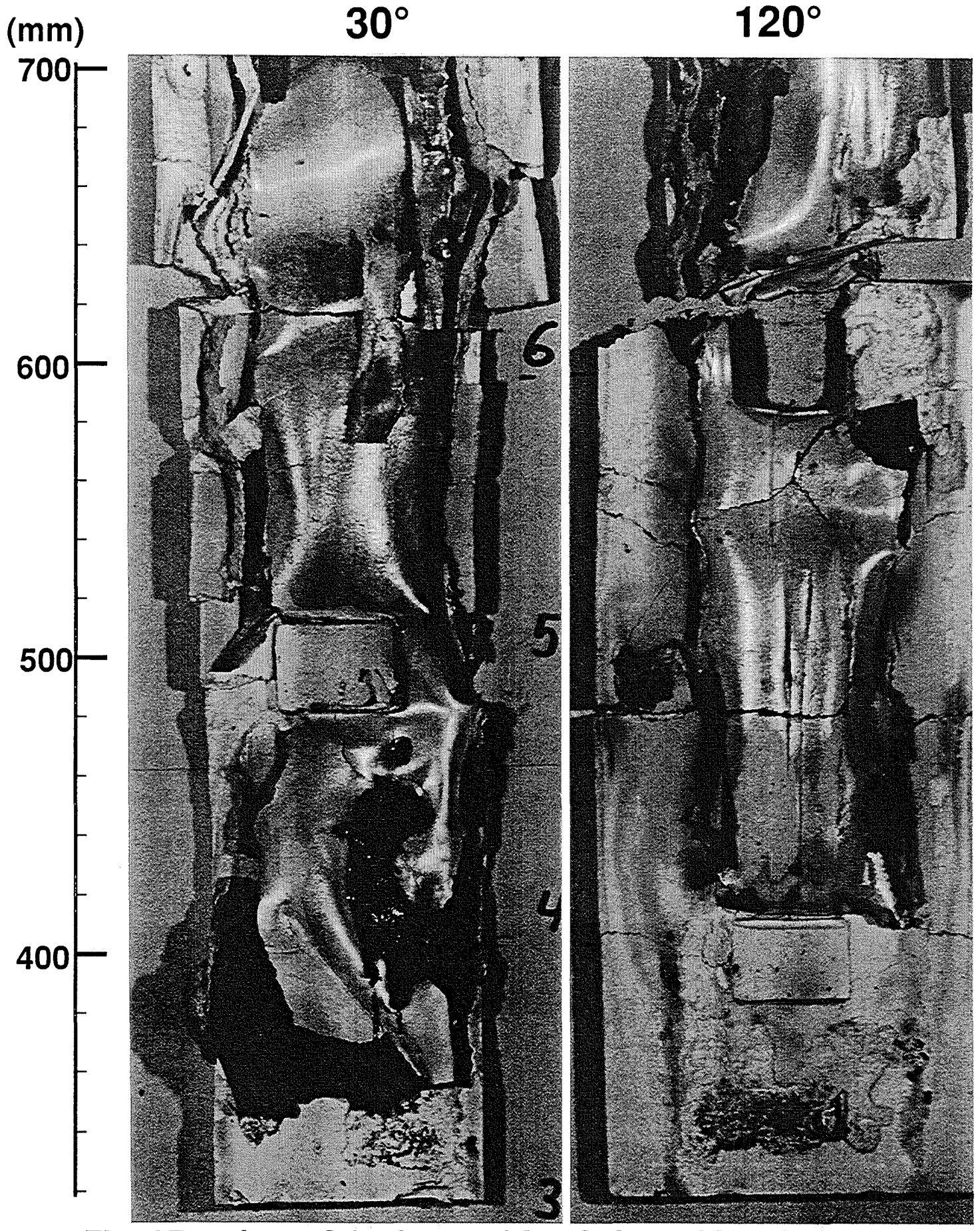

Fig. 87: view of the inner side of shroud insulation, 30° and 120° orientation

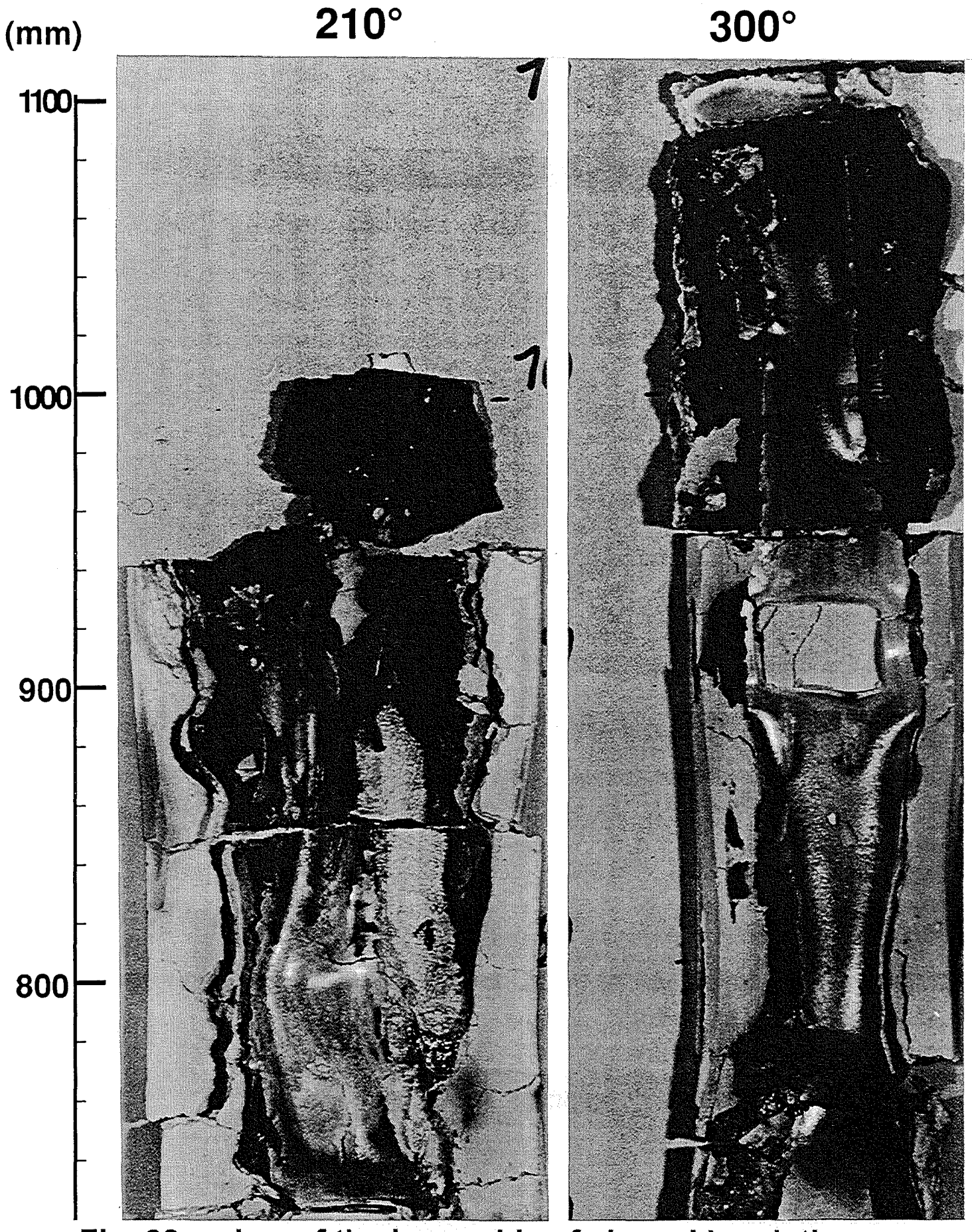

Fig. 88: view of the inner side of shroud insulation, 210° and 300° orientation

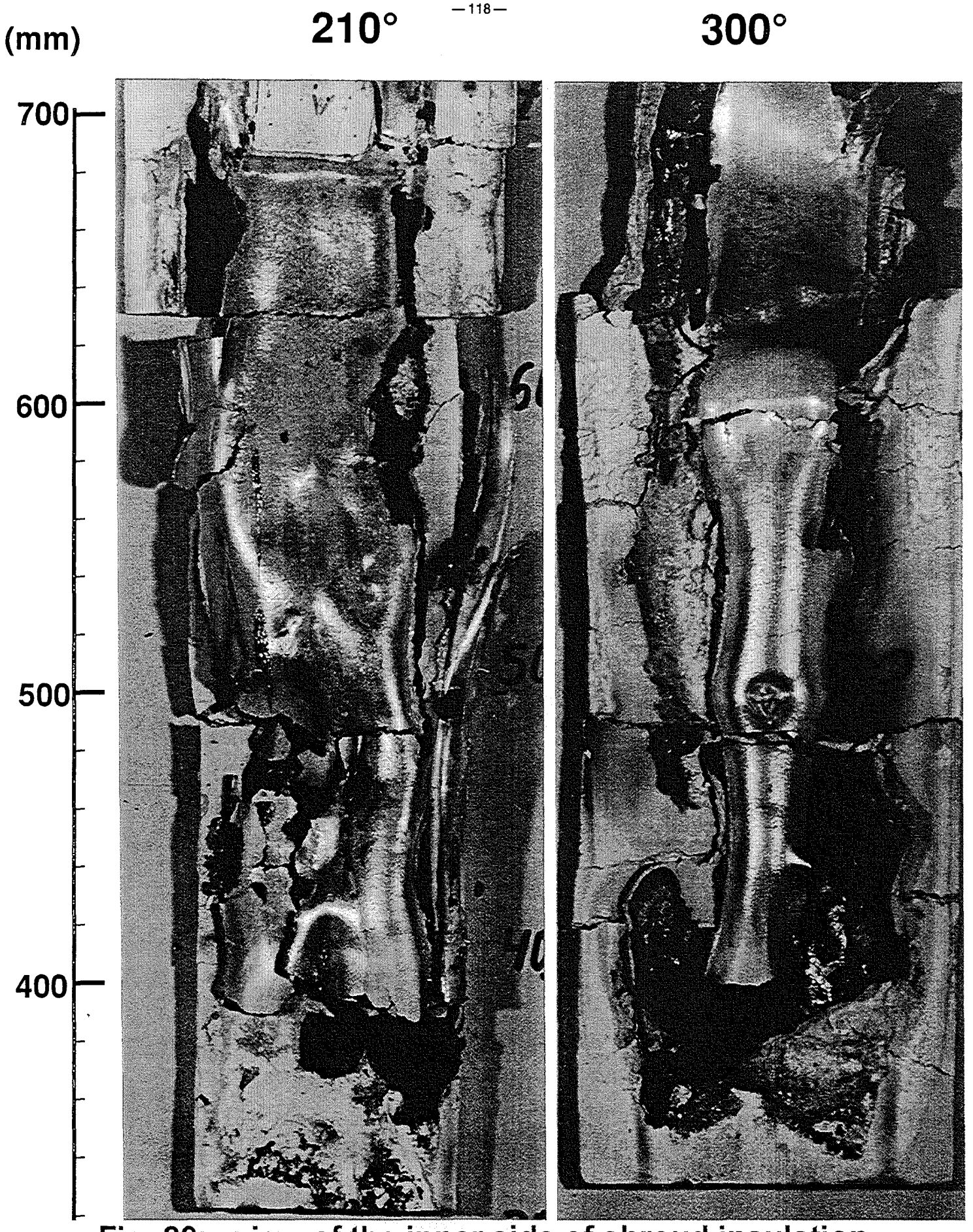

Fig. 89: view of the inner side of shroud insulation, 210° and 300° orientation

CORA-10; PWR

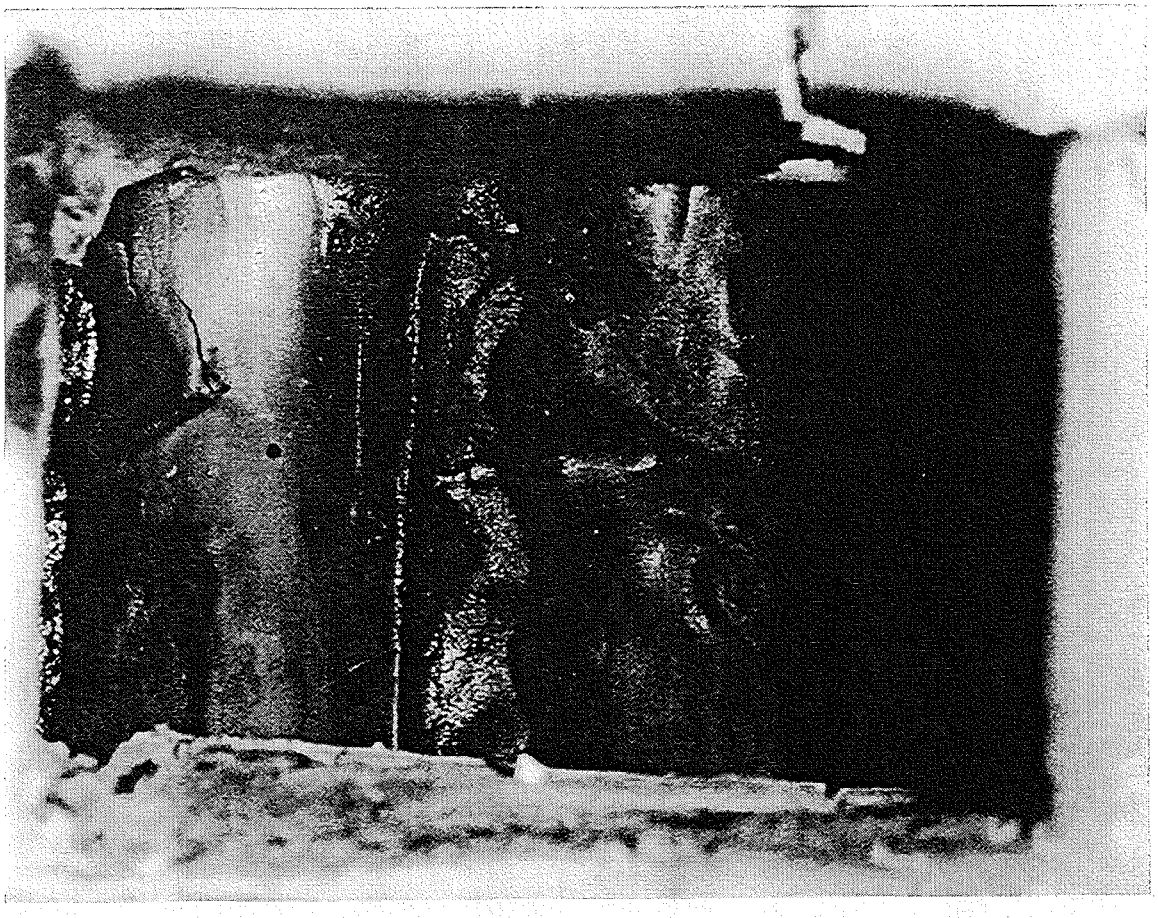

800 mm

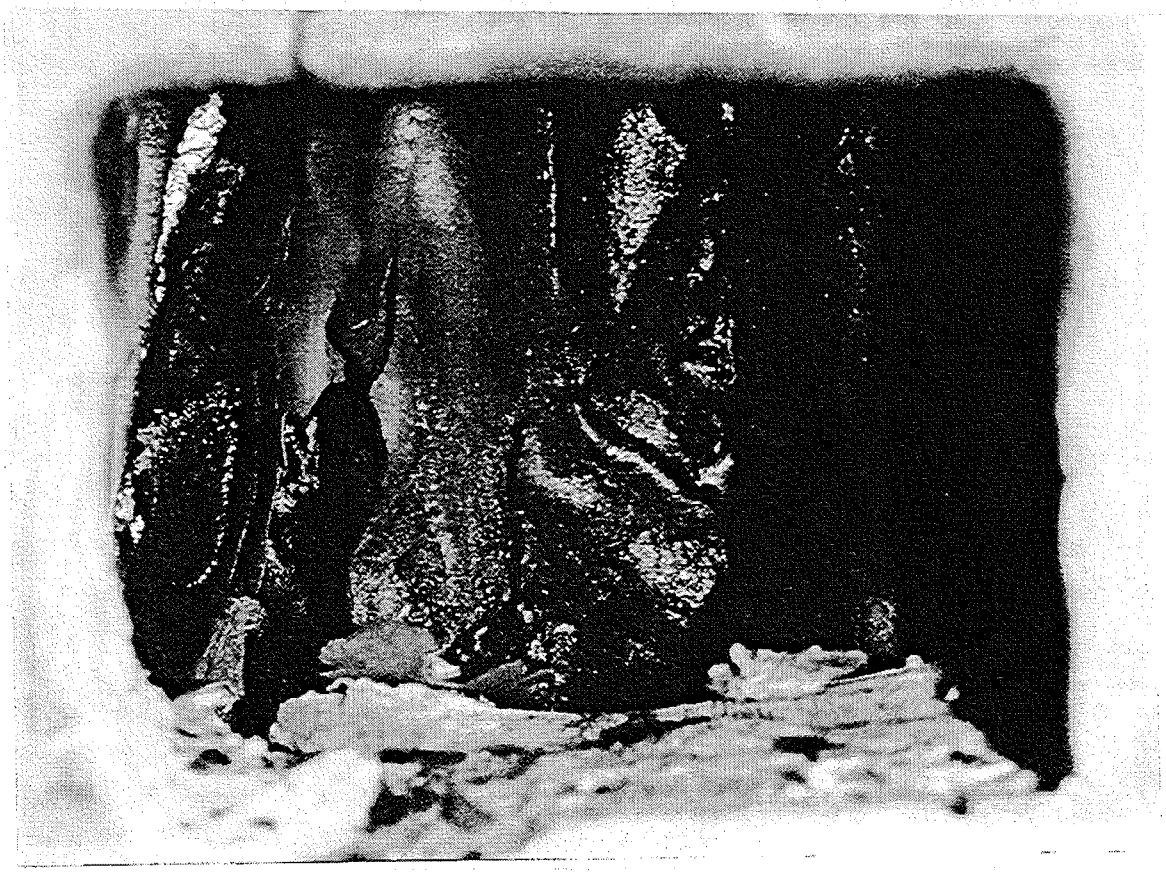

600 mm

Fig. 90: Windows at 800 mm and 600 mm

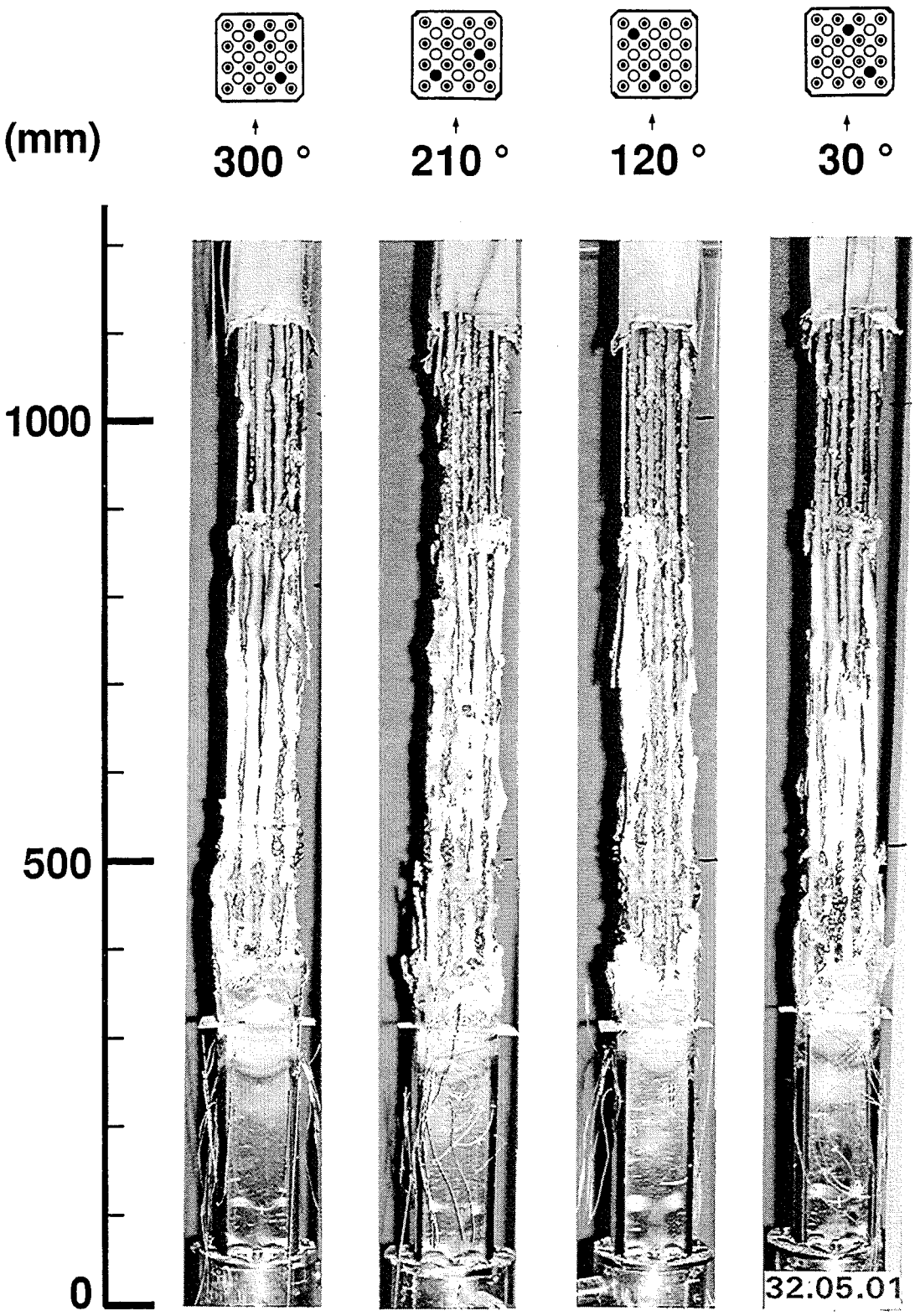

Fig. 91: CORA-10; Posttest appearance of the entire bundle lenght after removal of the shroud insulation

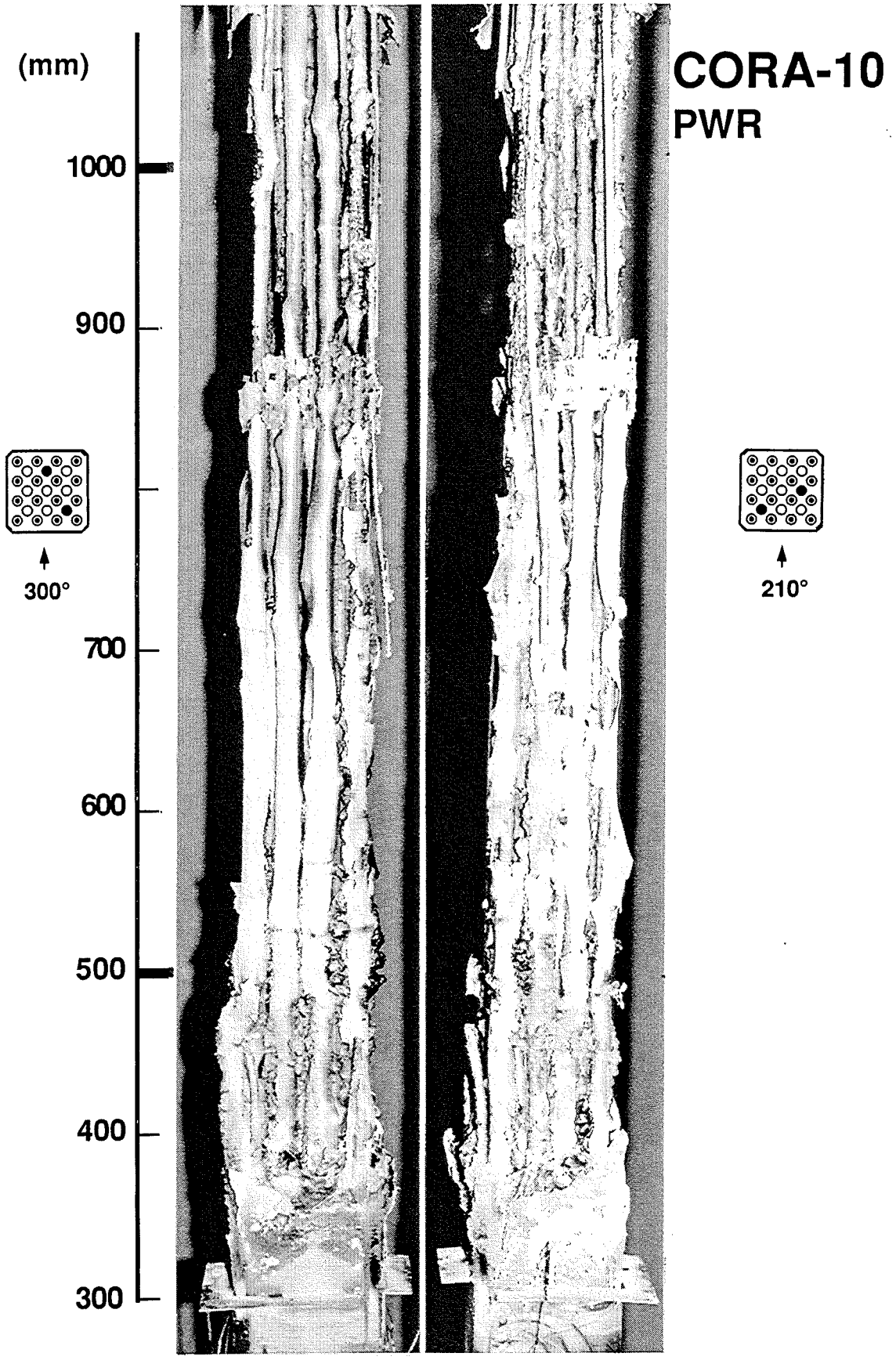

Fig. 92: Posttest view 300° and 210° orientation

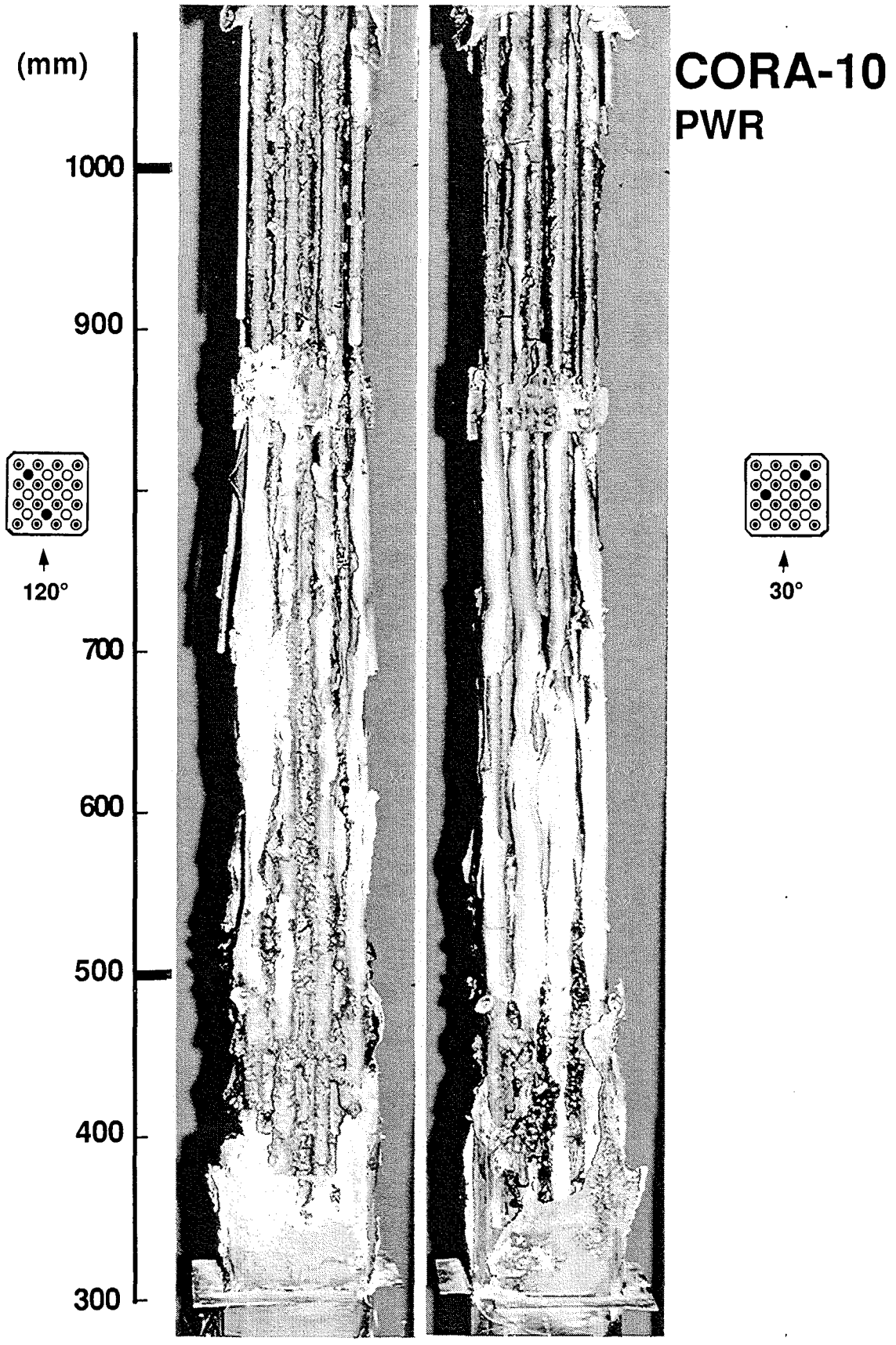

Fig. 93: Posttest view 120° and 30° orientation

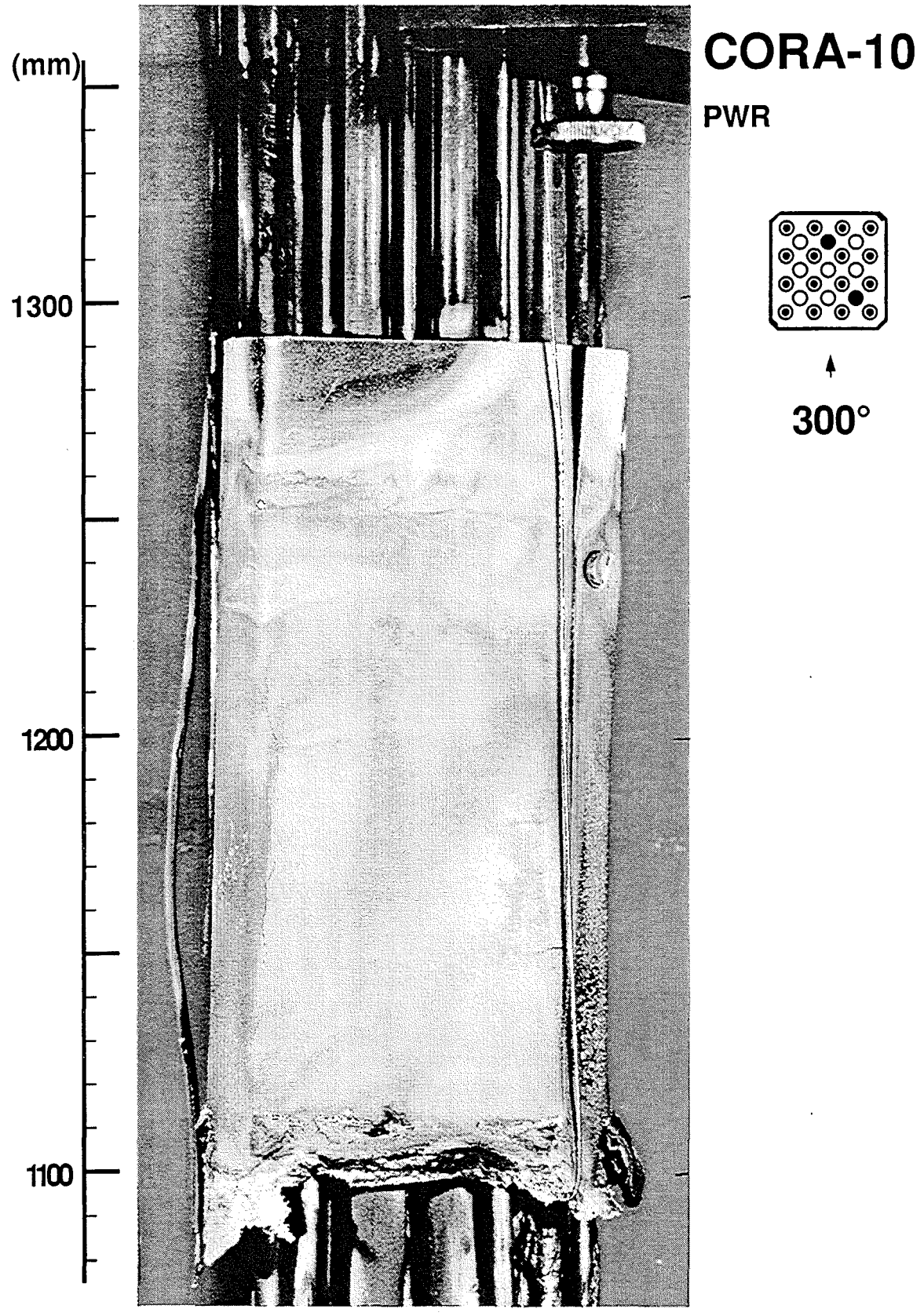

Fig. 94: Posttest view 300° orientation

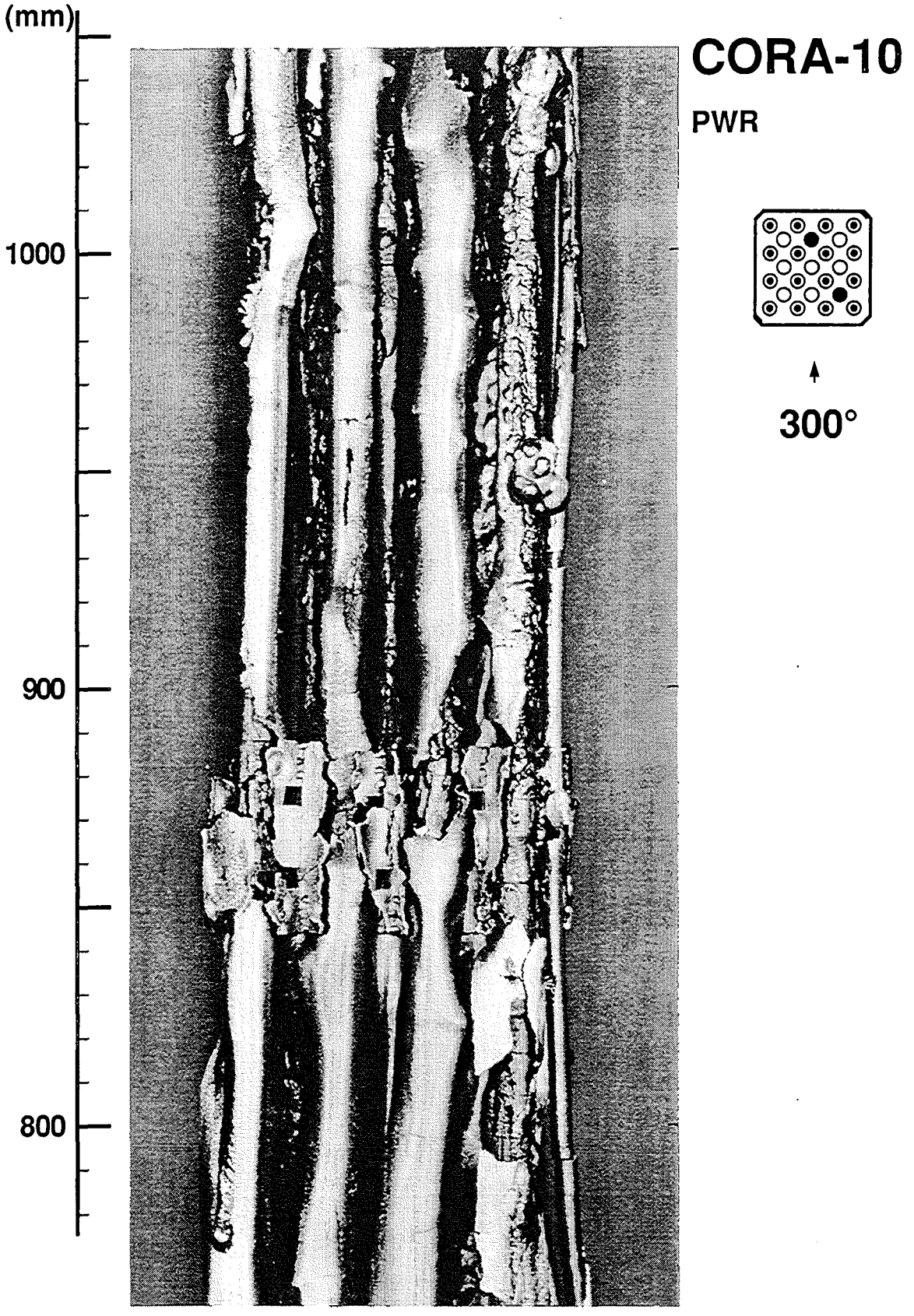

Fig. 95: Posttest view 300° orientation

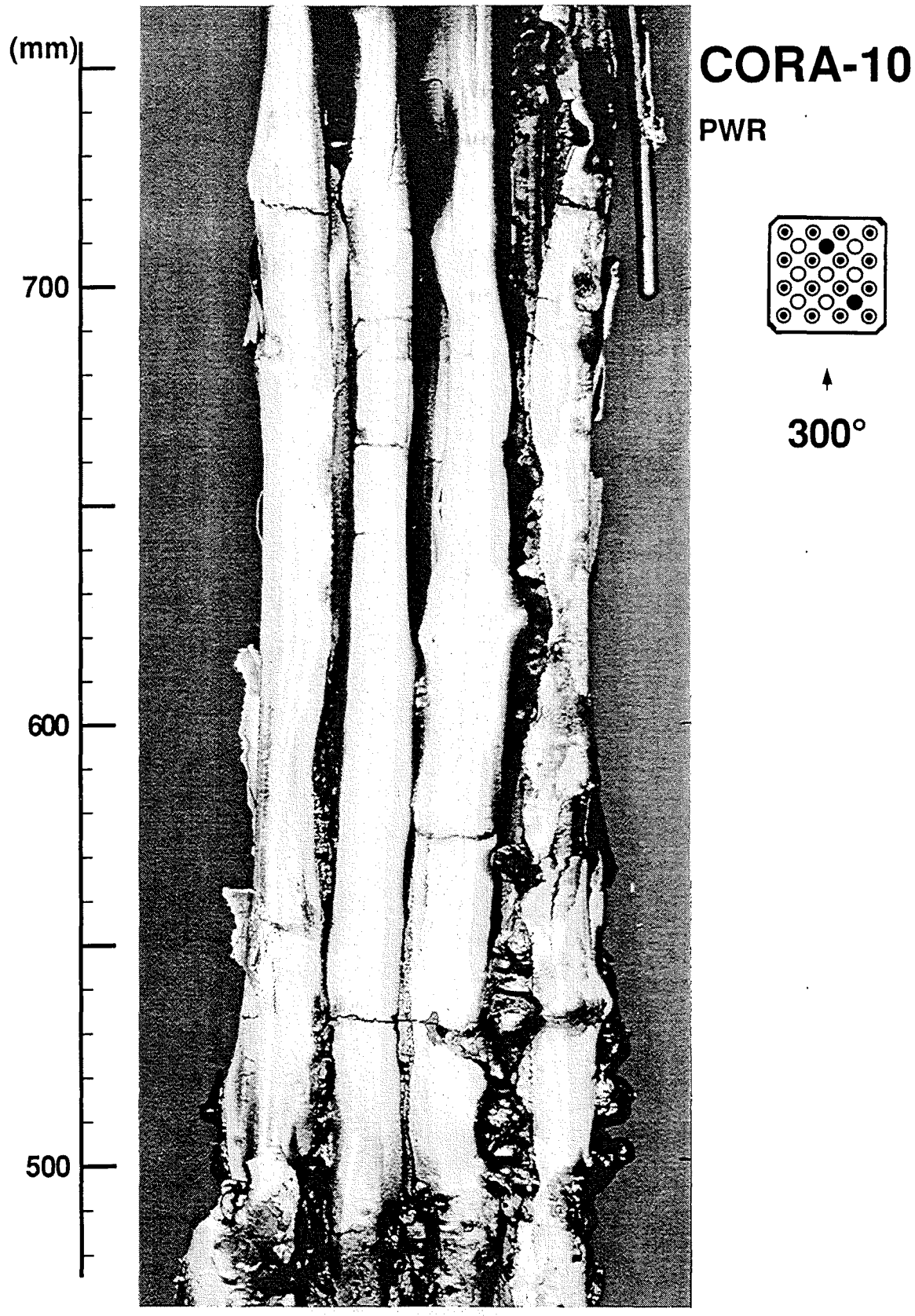

Fig. 96: Posttest view 300° orientation

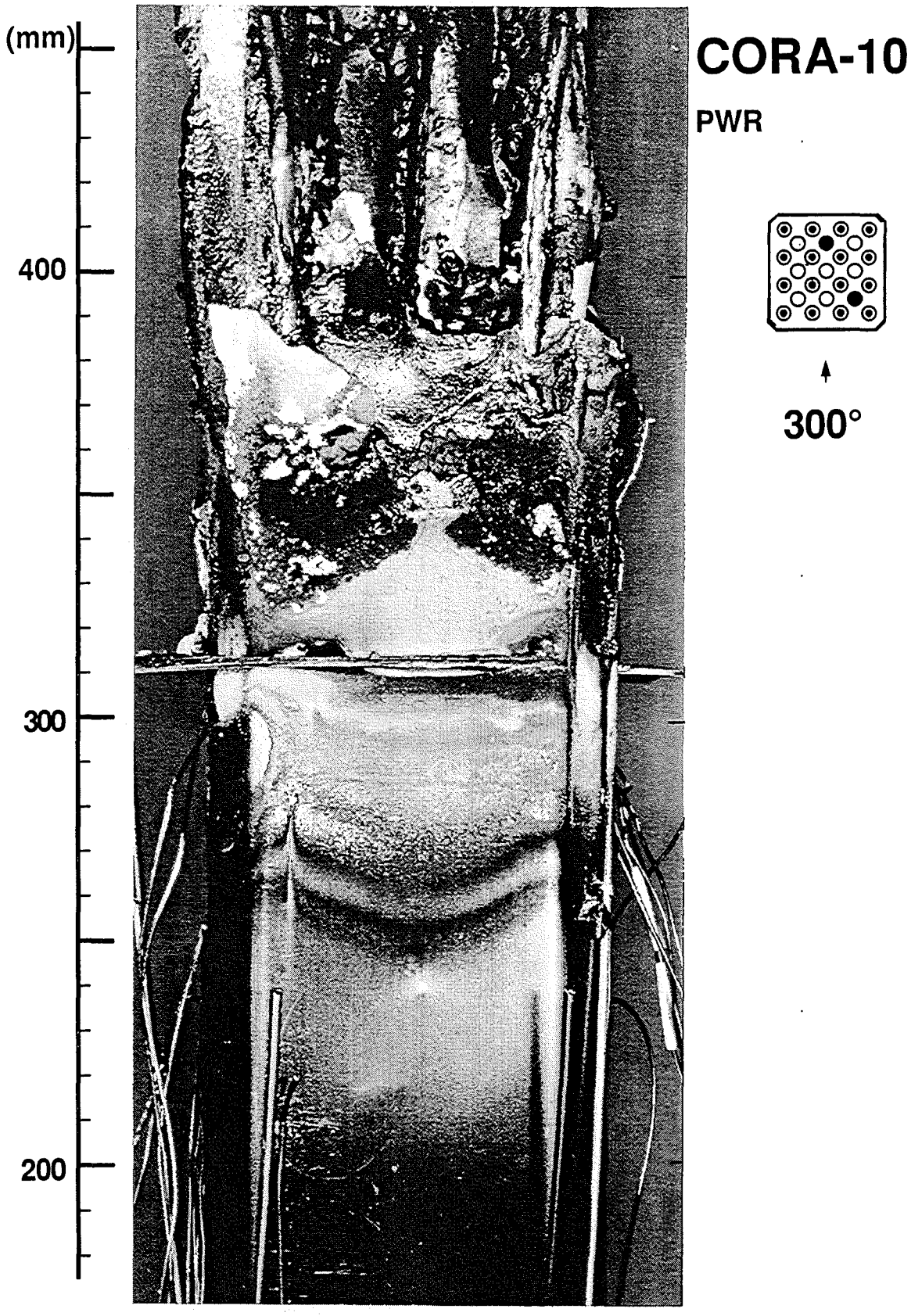

Fig. 97: Posttest view 300° orientation

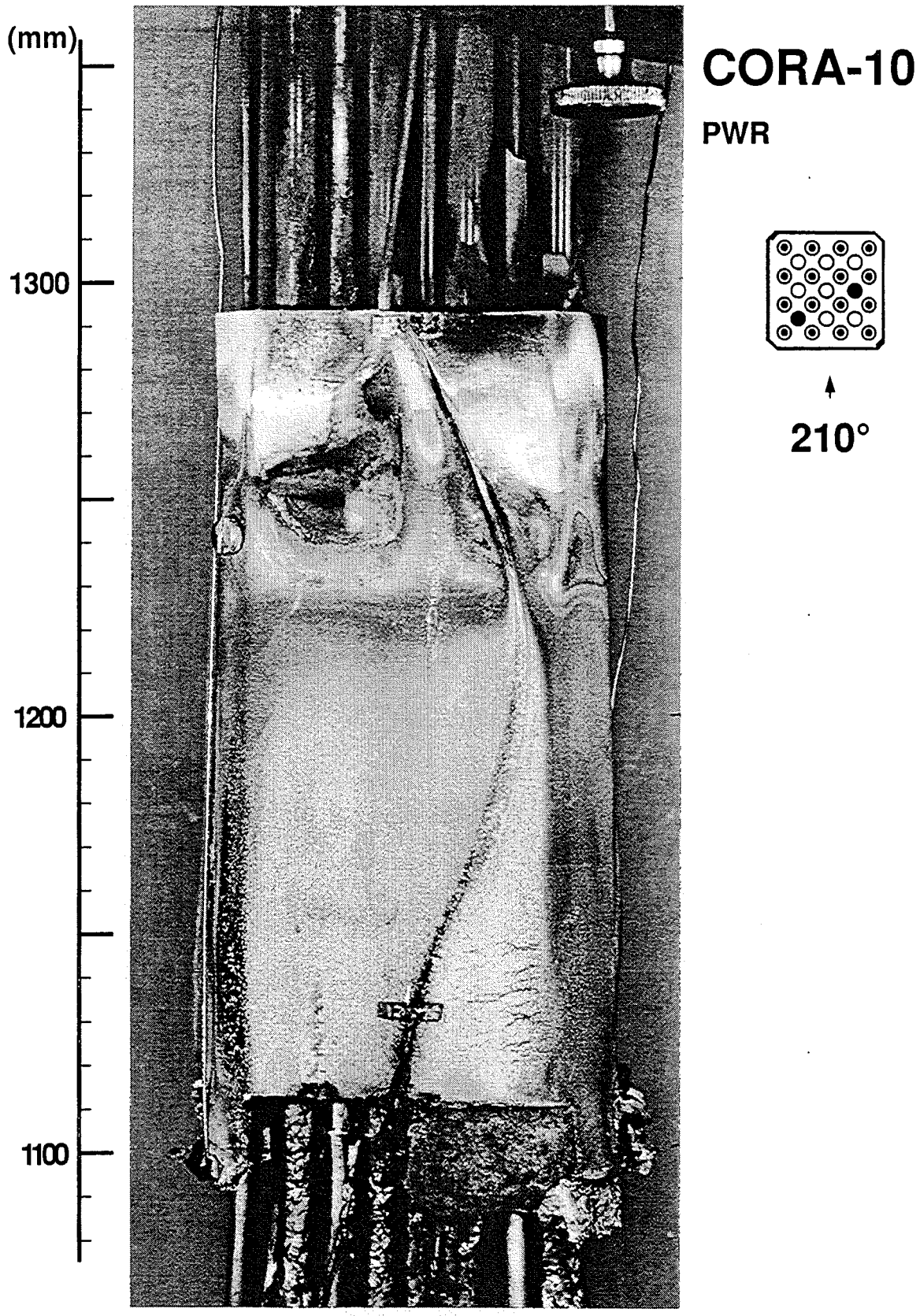

Fig. 98: Posttest view 210° orientation

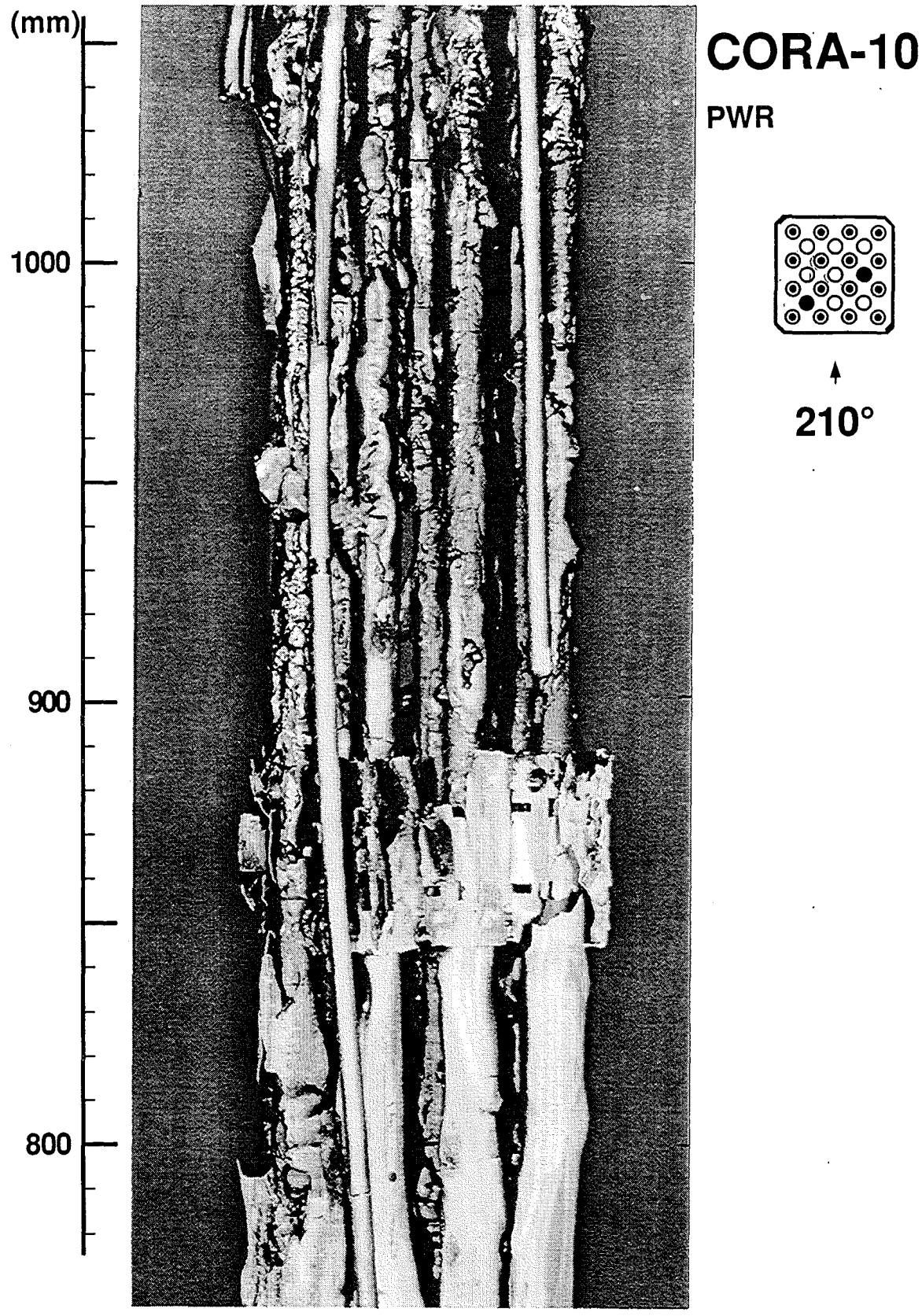

Fig. 99: Posttest view 210° orientation

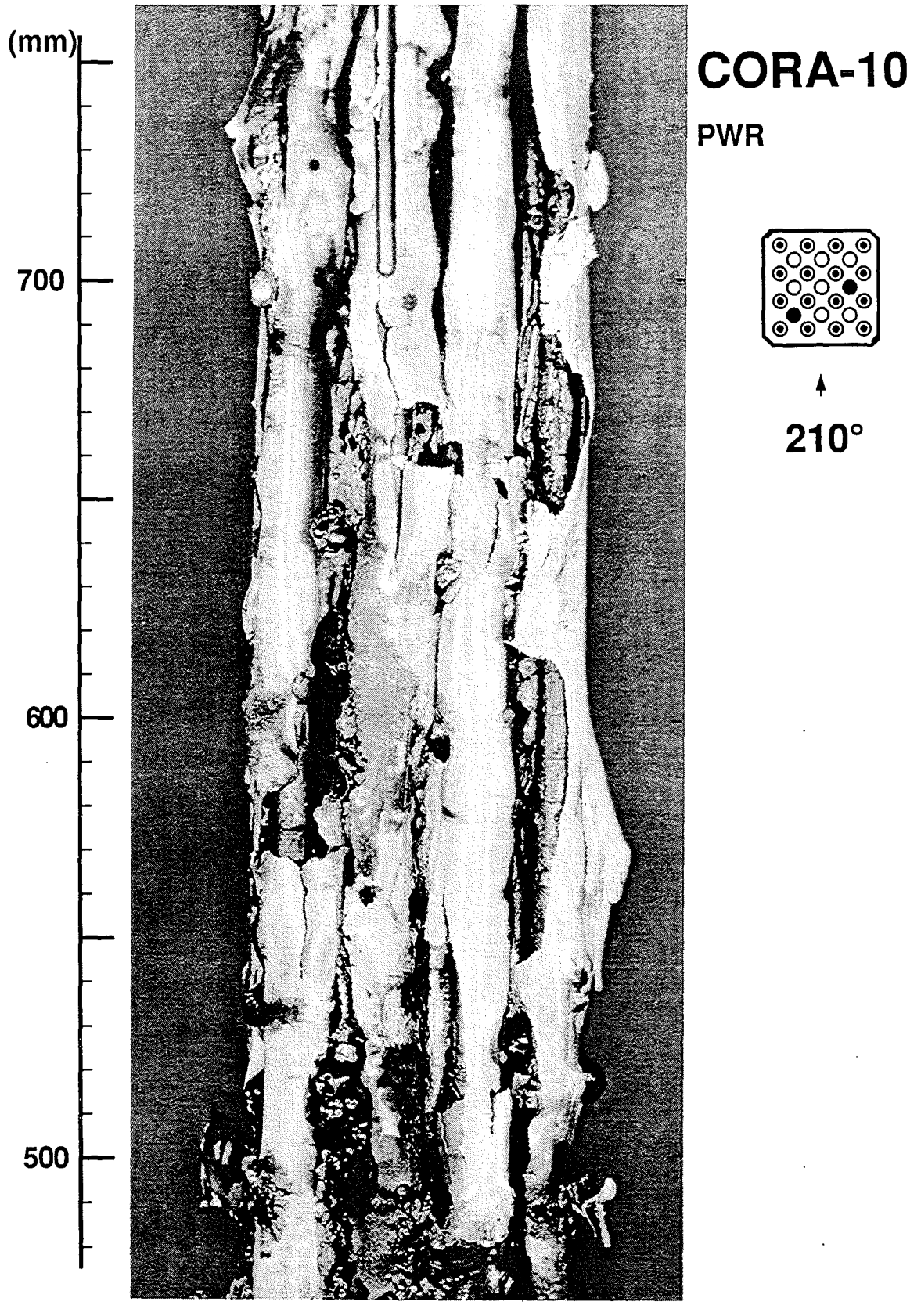

Fig. 100: Posttest view 210° orientation

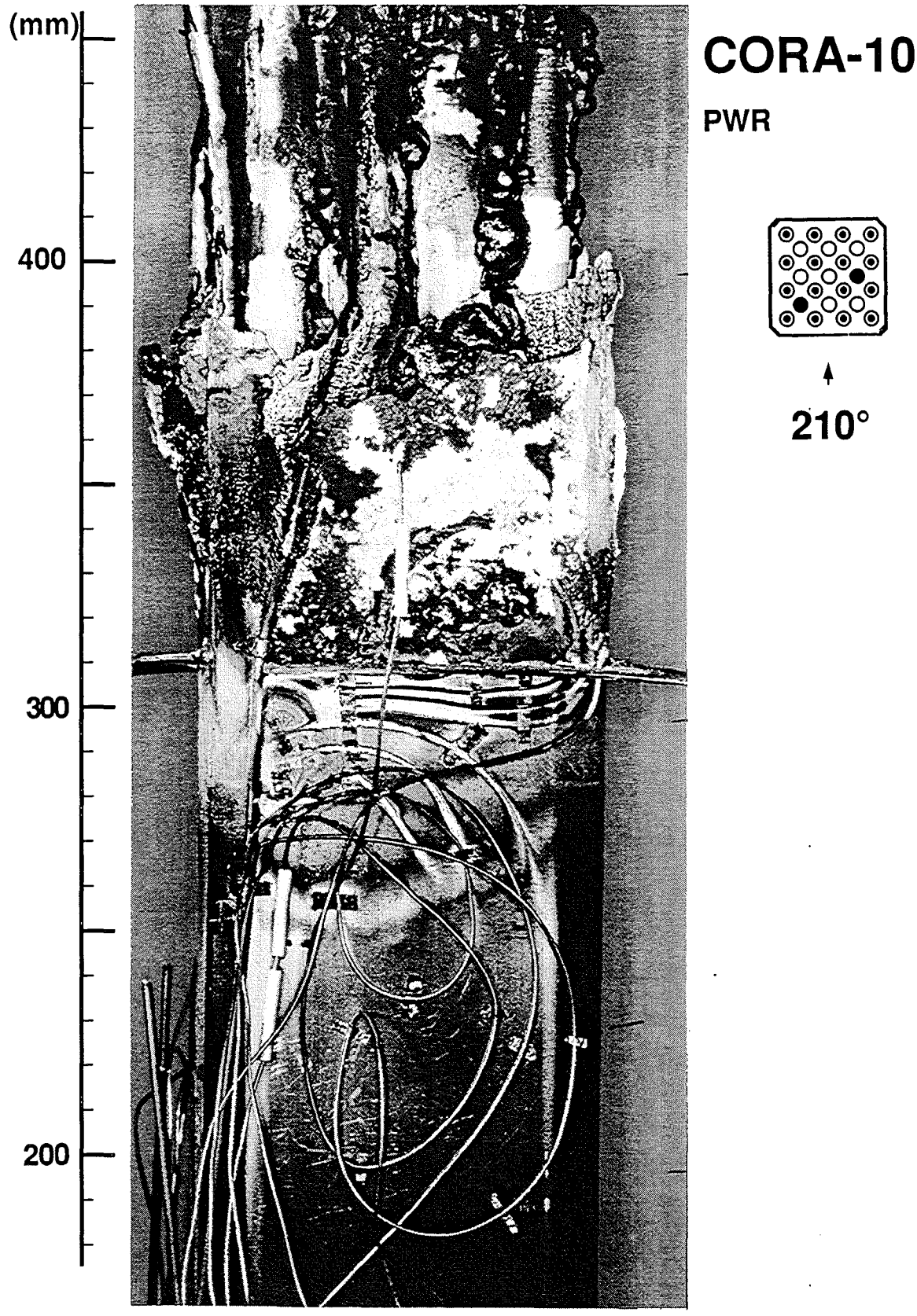

Fig. 101: Posttest view 210° orientation

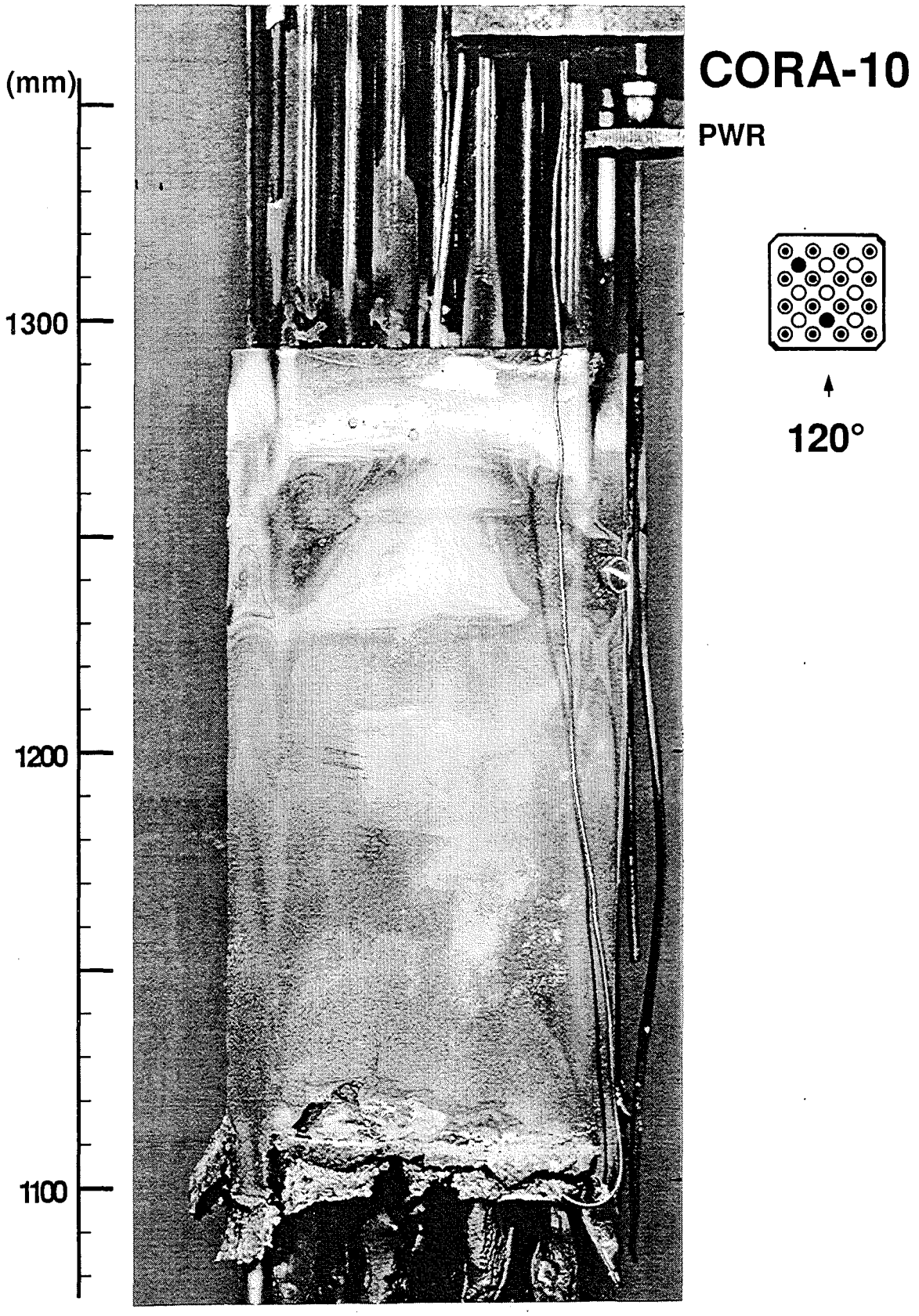

Fig. 102: Posttest view 120° orientation

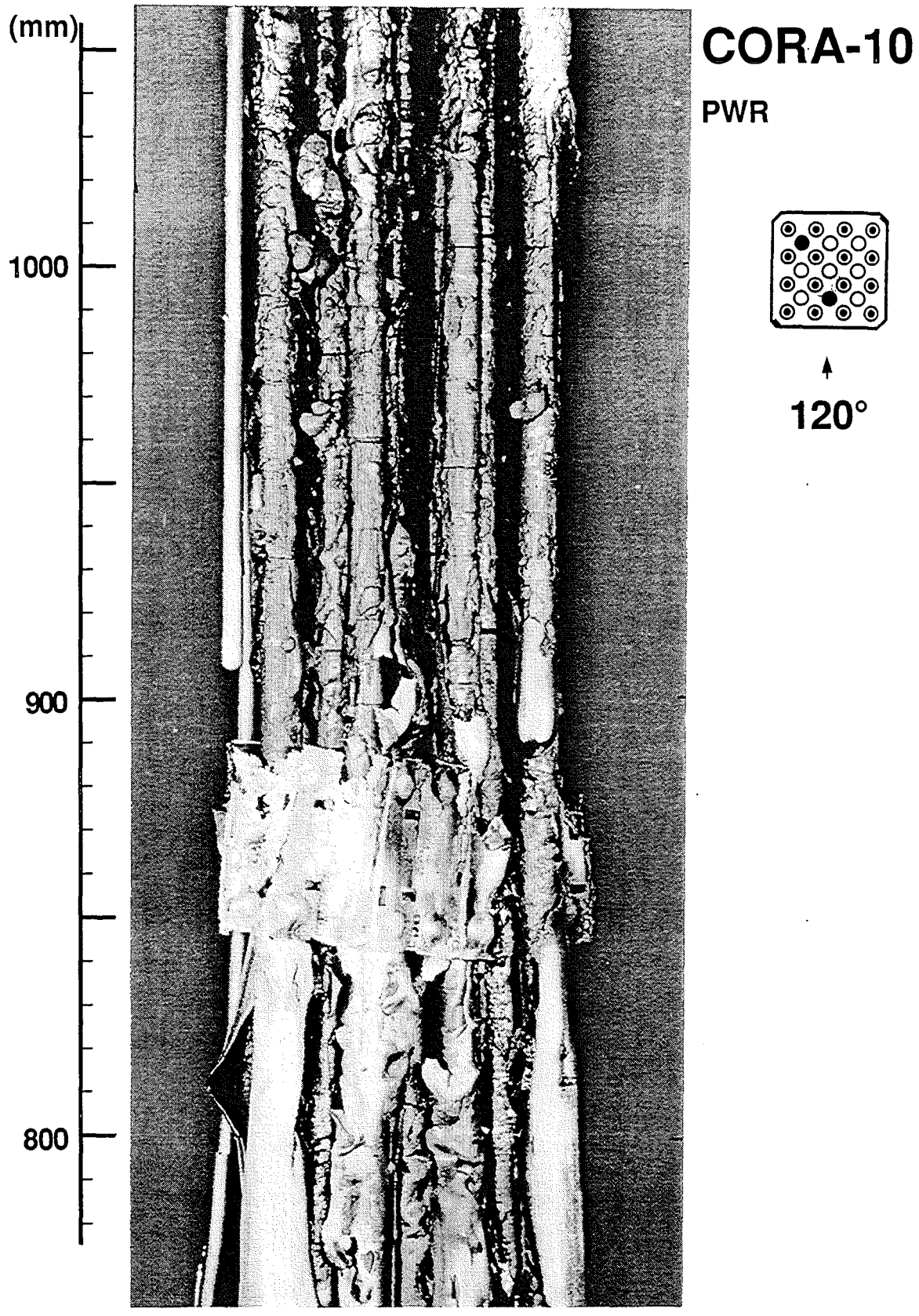

Fig. 103: Posttest view 120° orientation

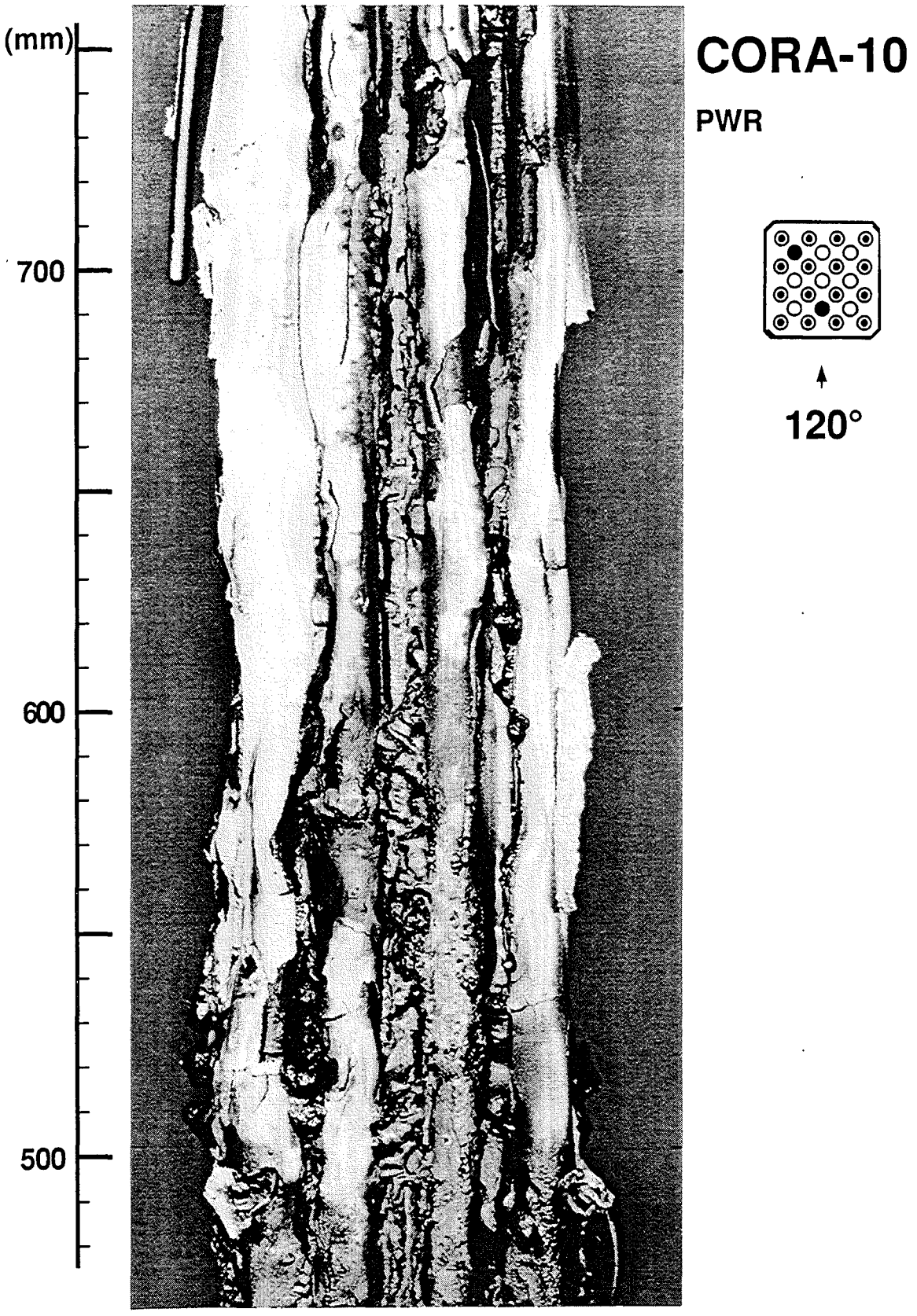

Fig. 104: Posttest view 120° orientation

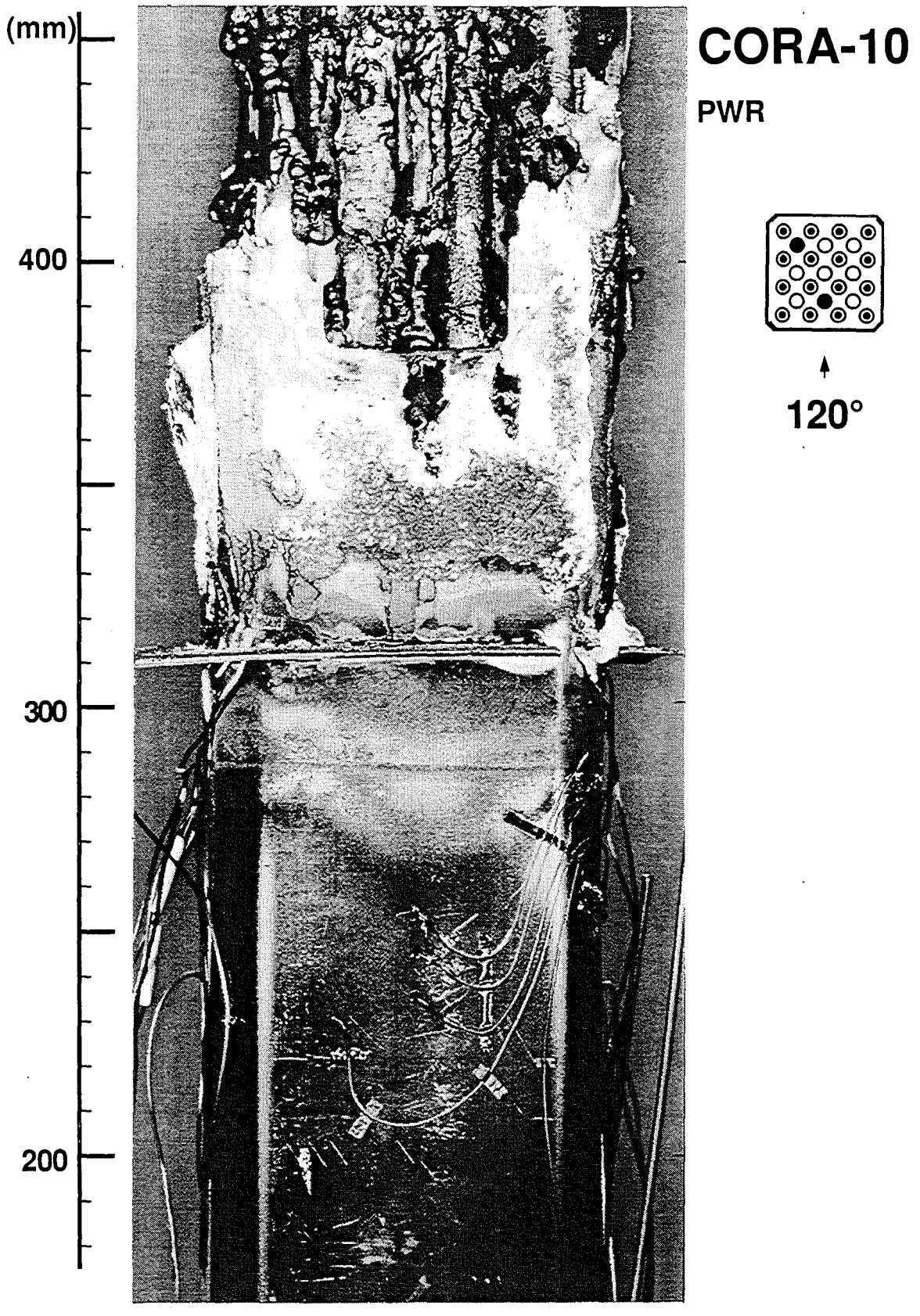

Fig. 105: Posttest view 120° orientation

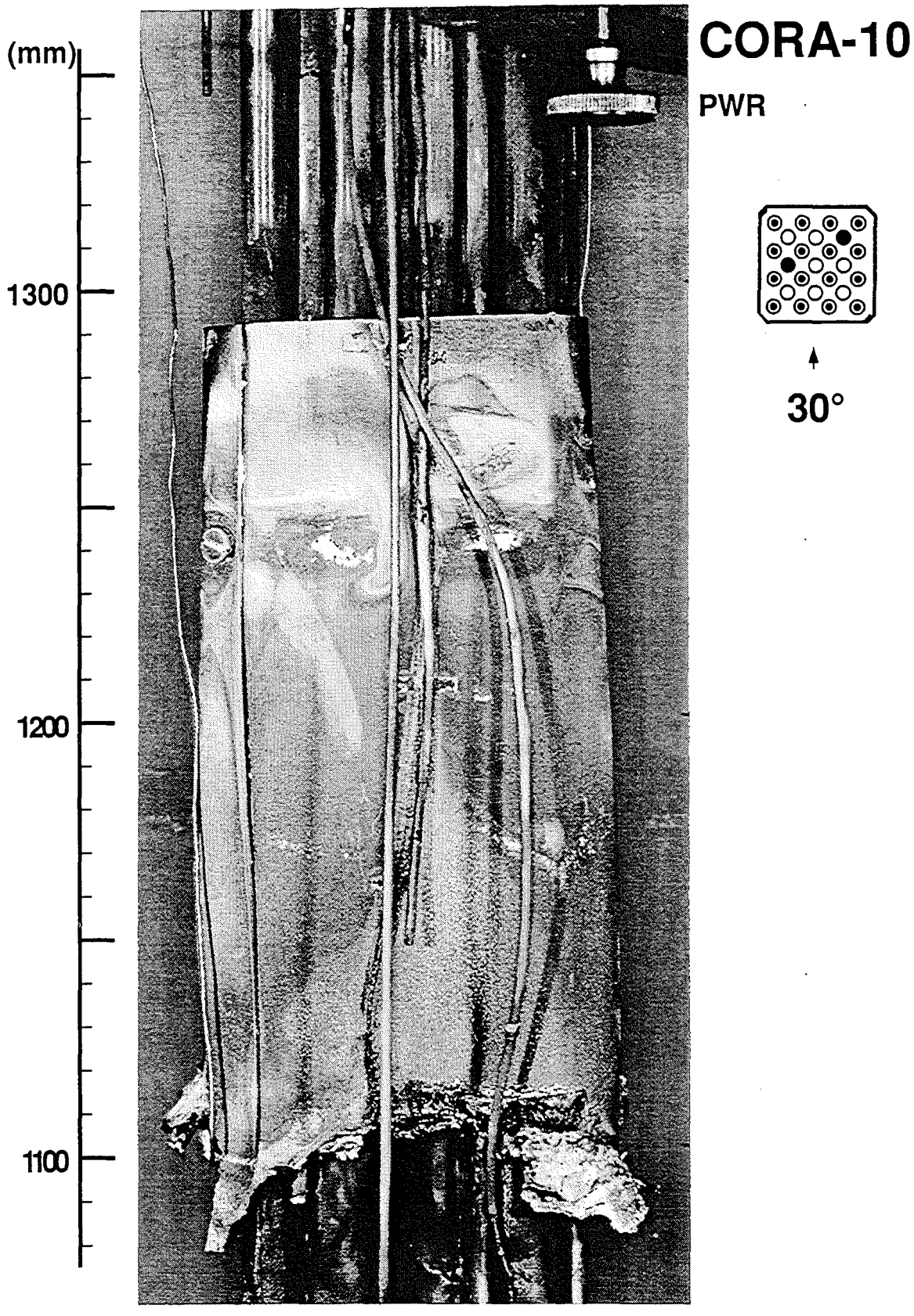

Fig. 106: Posttest view 30° orientation

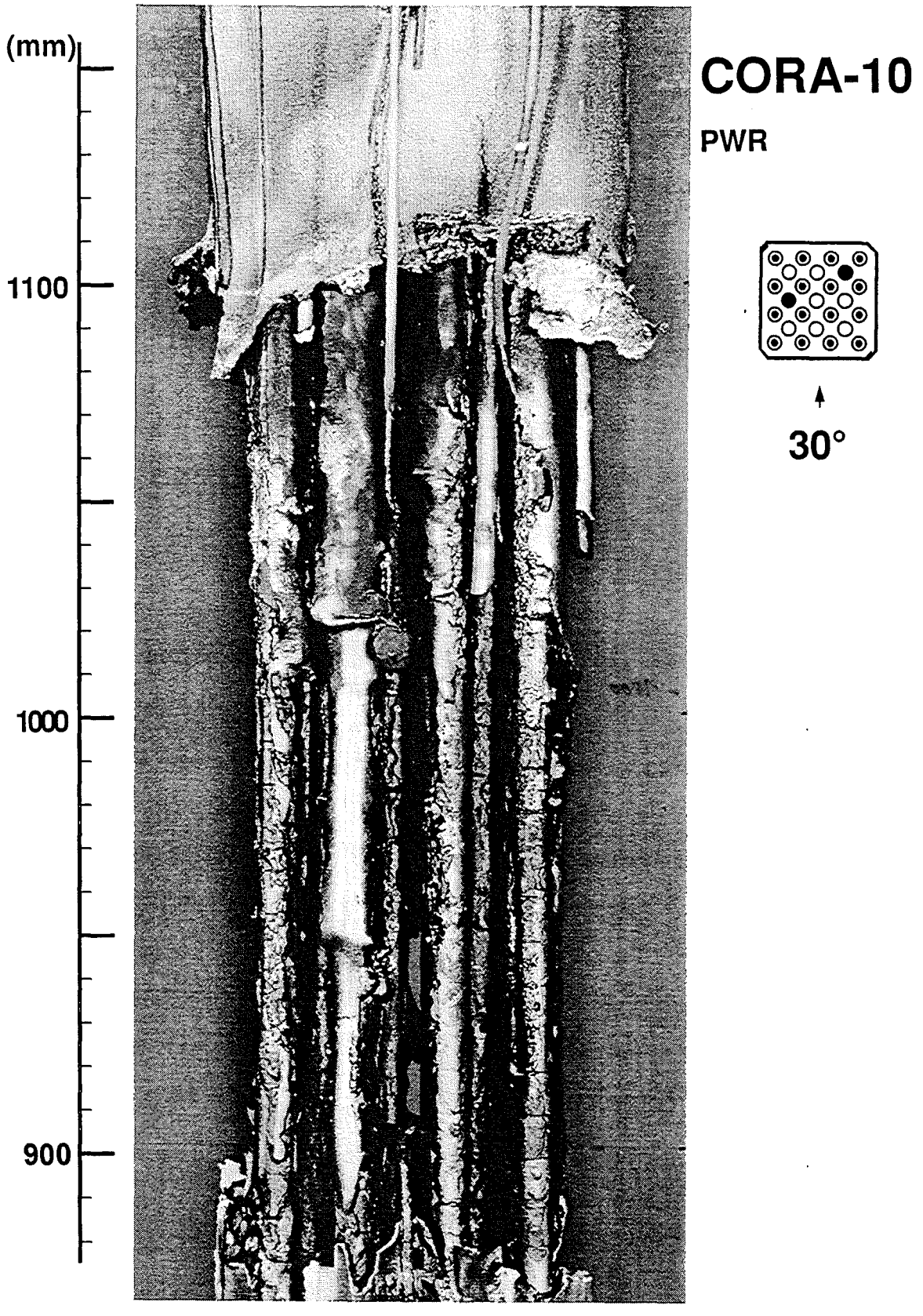

Fig. 107: Posttest view 30° orientation

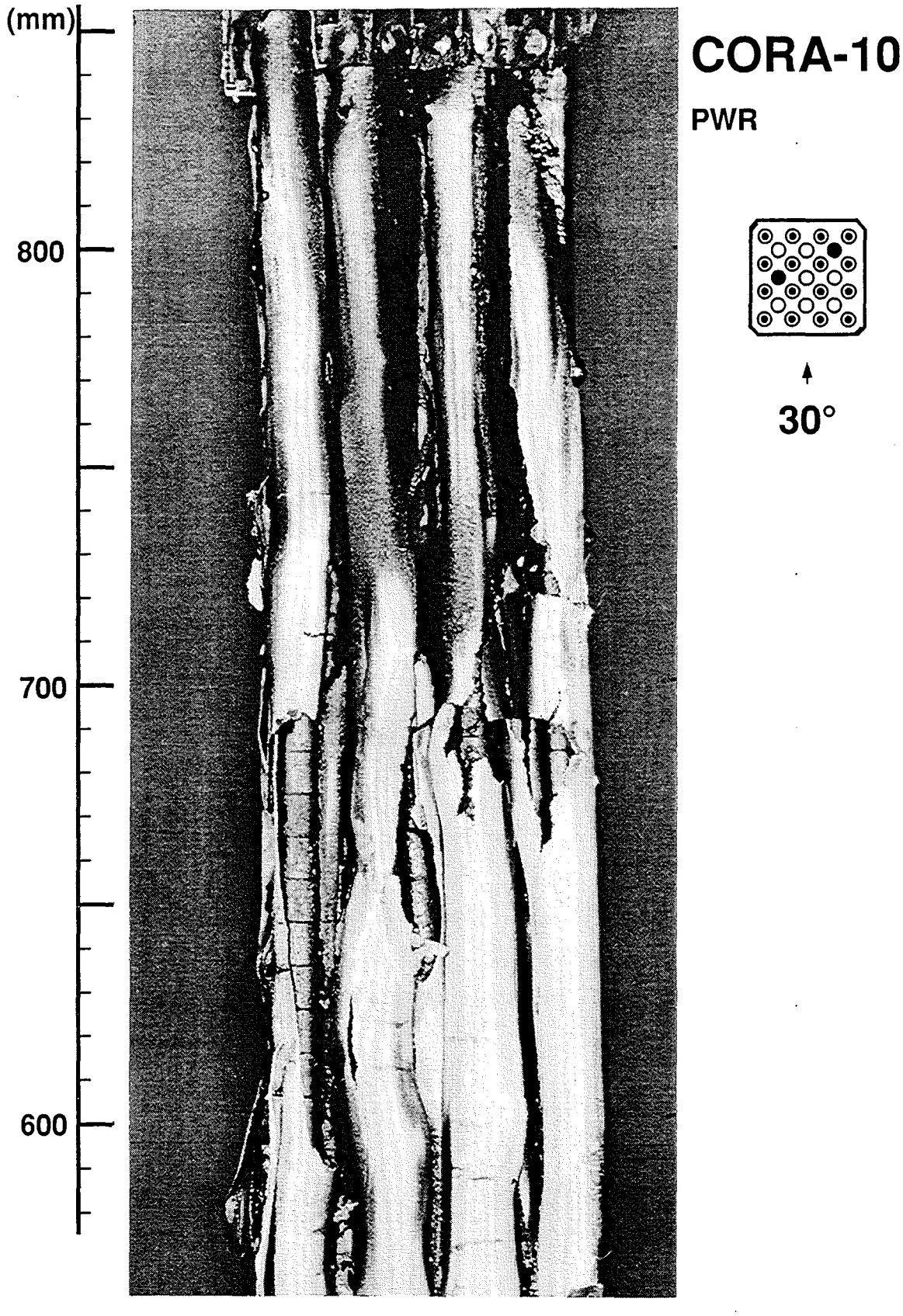

Fig. 108: Posttest view 30° orientation

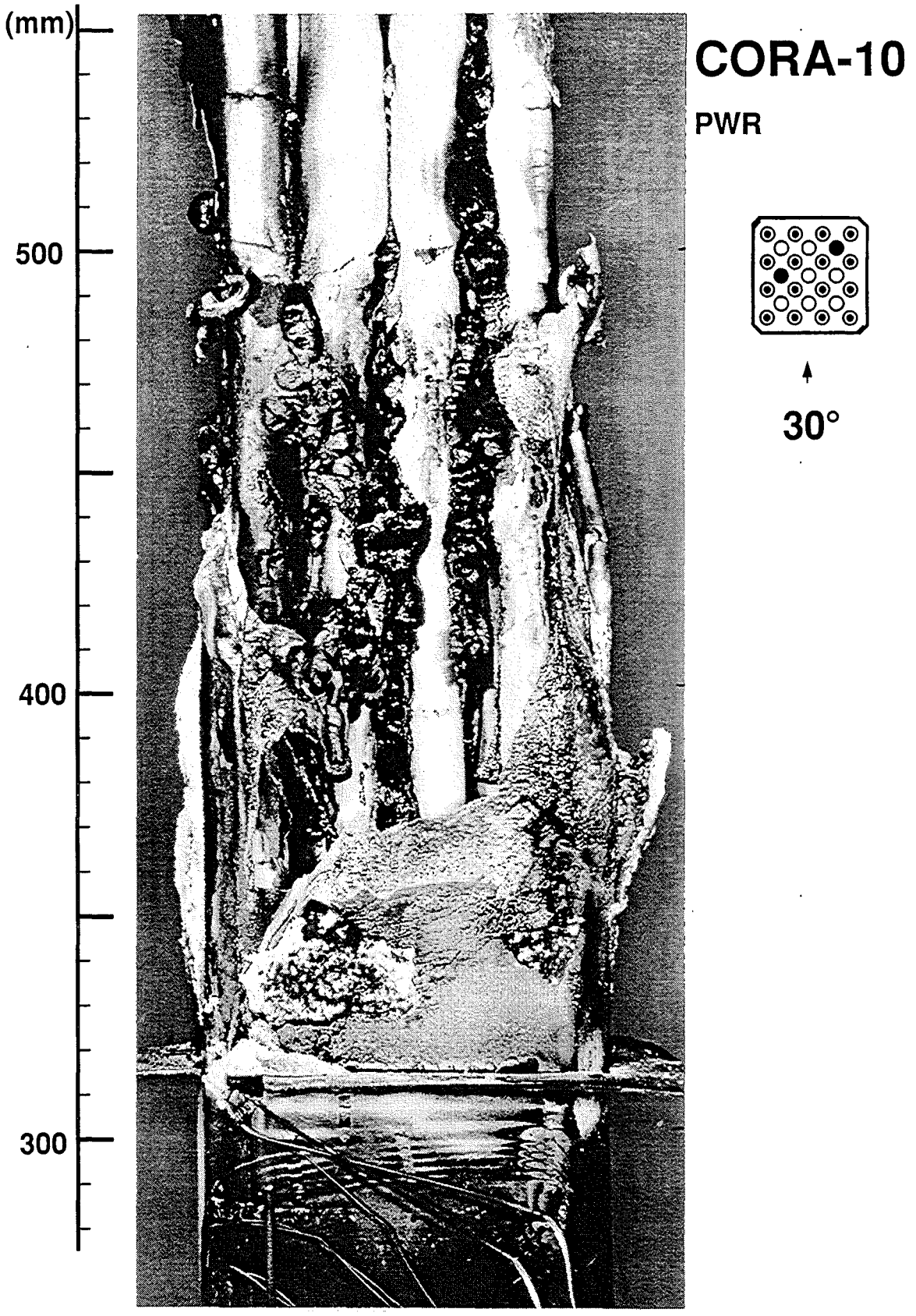

Fig. 109: Posttest view 30° orientation

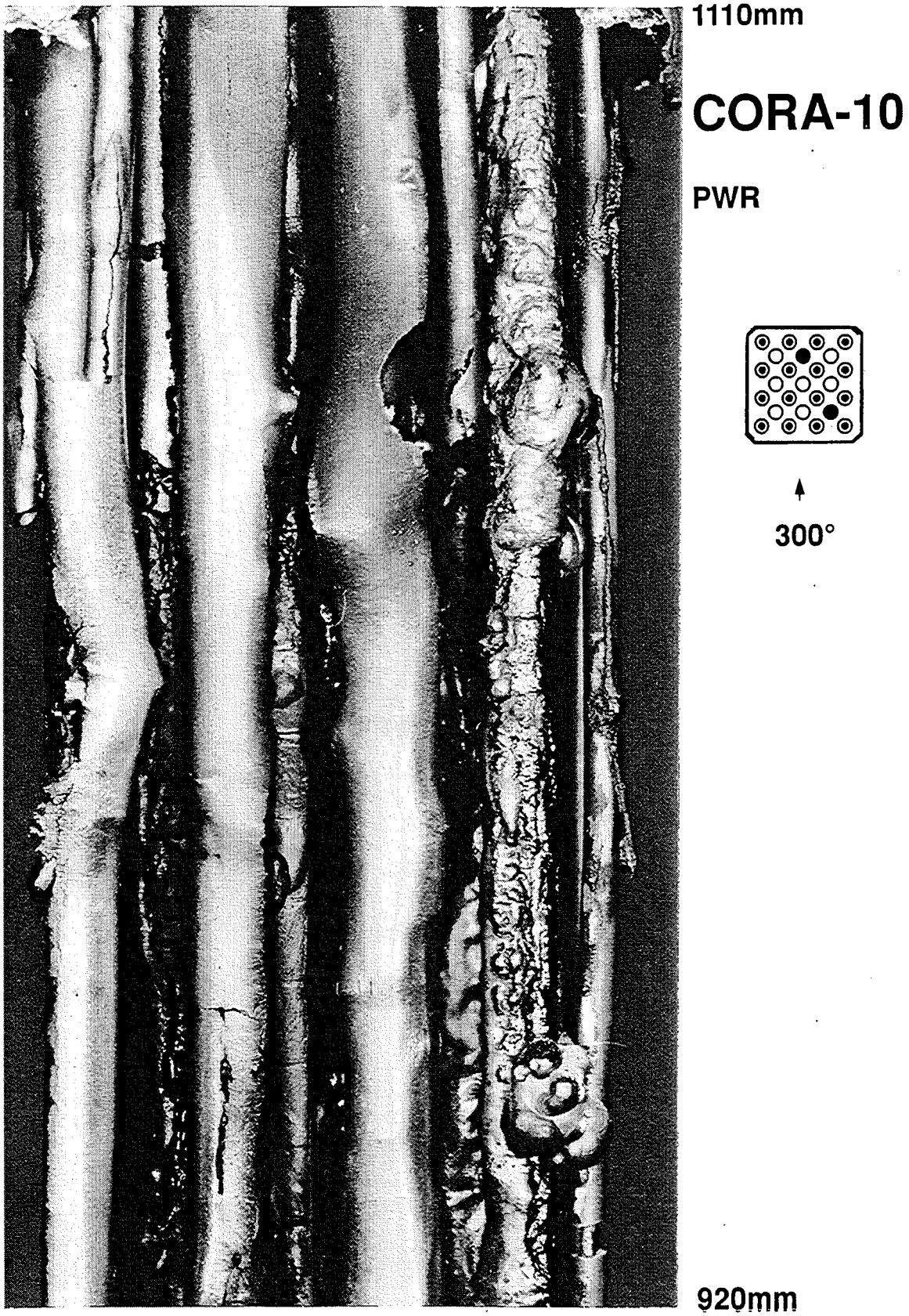

Fig. 110: Posttest view 300° orientation

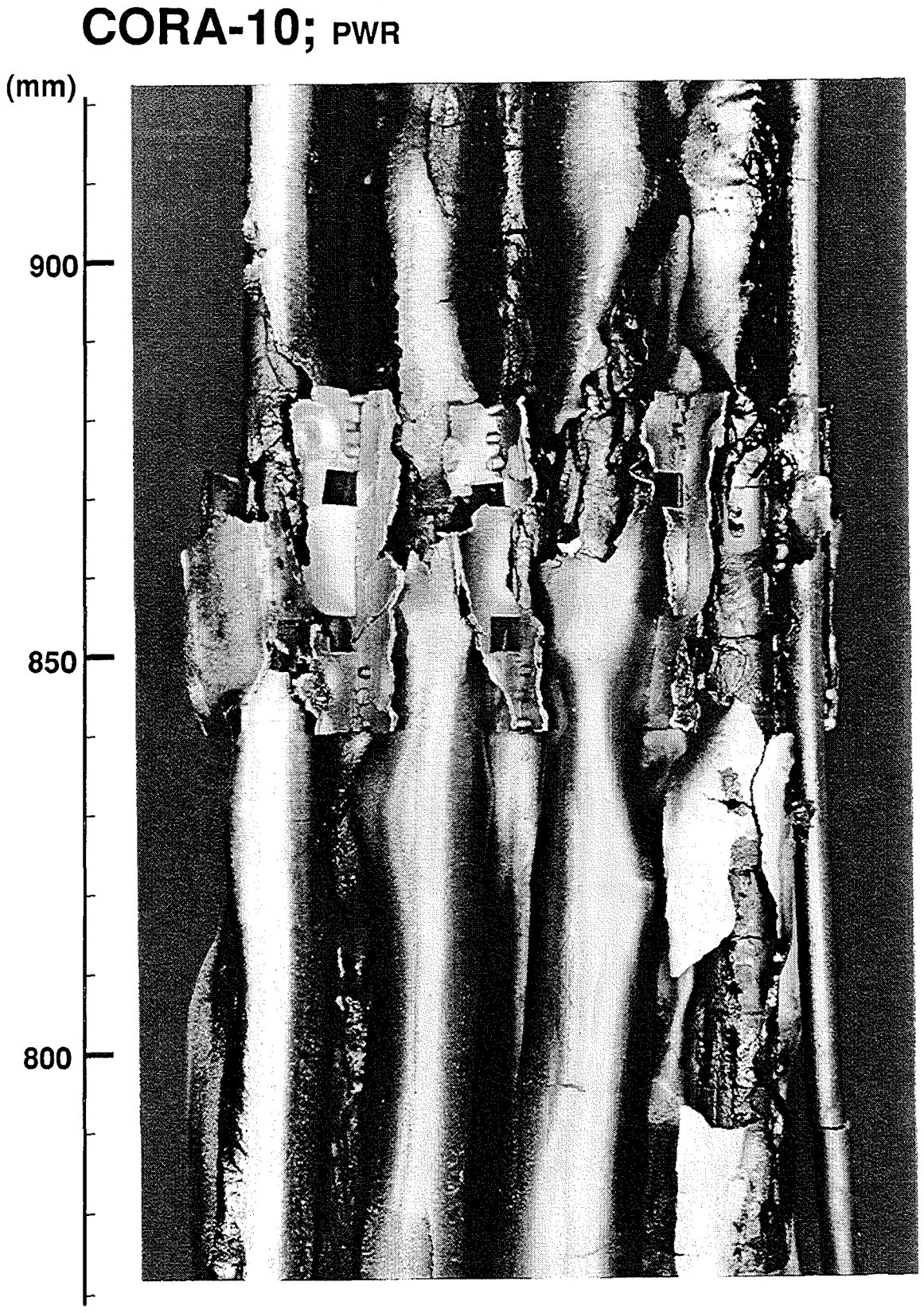

Fig. 111: Posttest view 300° orientation

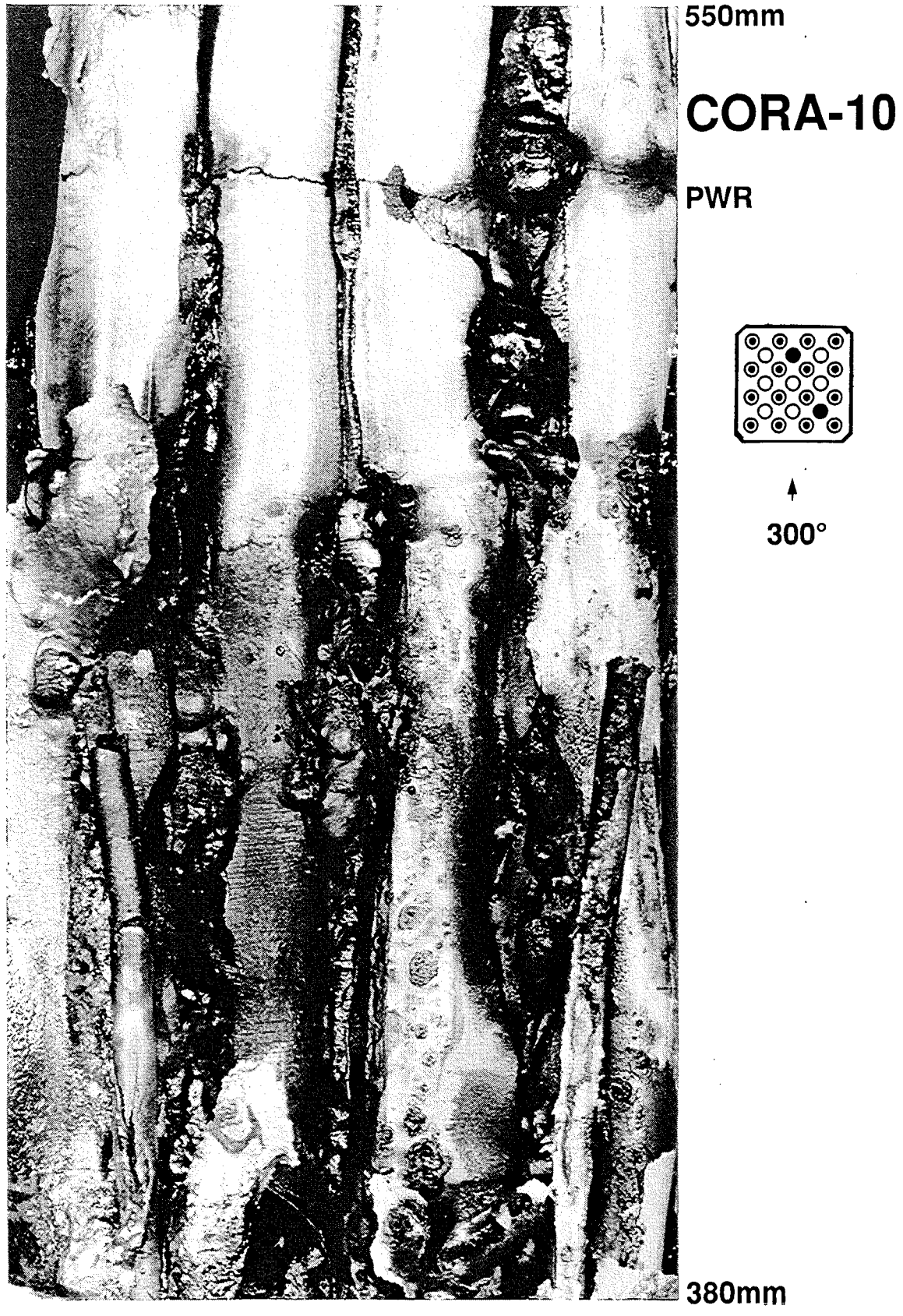

Fig. 112: Posttest view 300° orientation

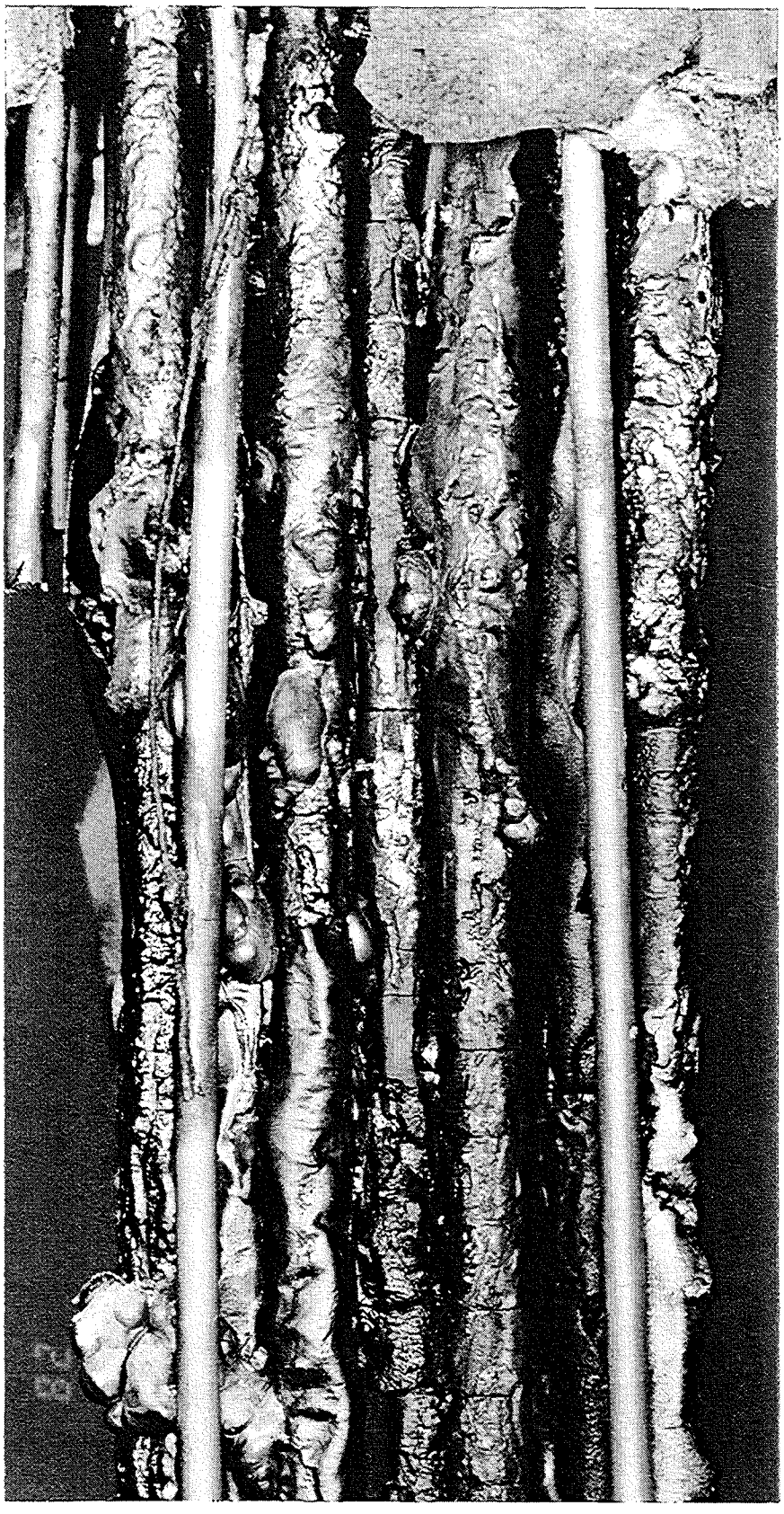

Fig. 113: Posttest view 210° orientation

CORA-10; PWR

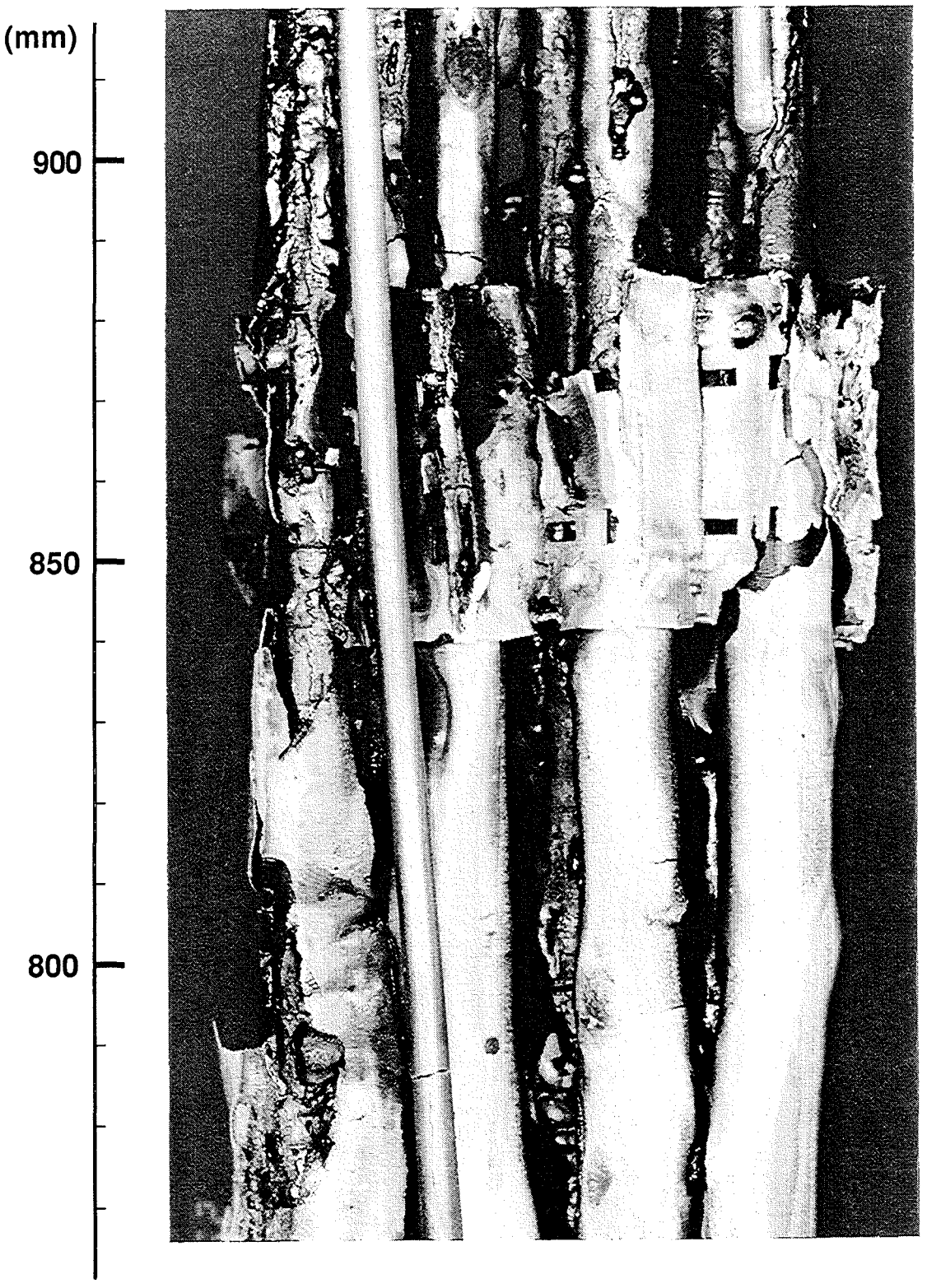

Fig. 114: Posttest view 210° orientation

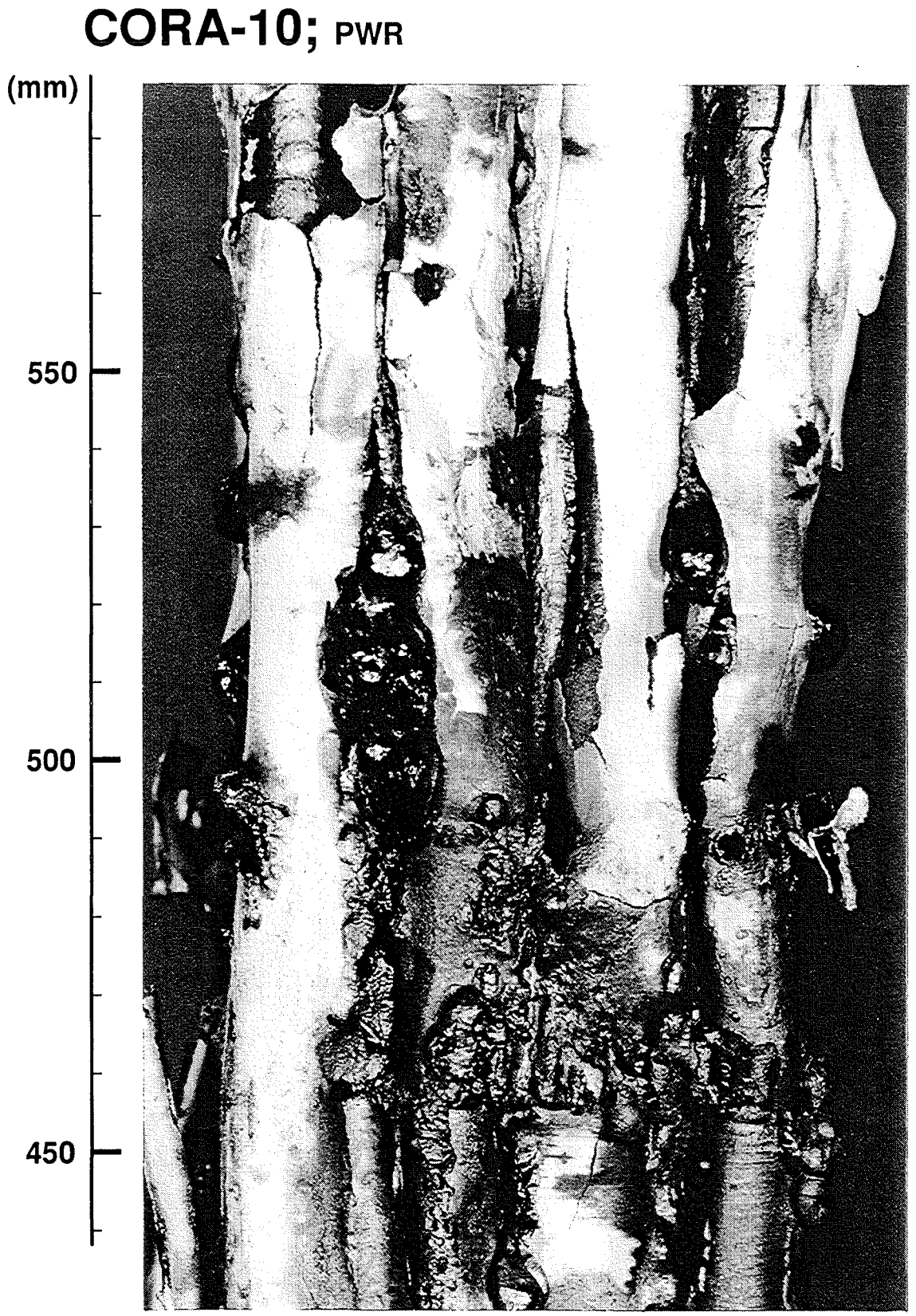

Fig. 115: Posttest view 210° orientation

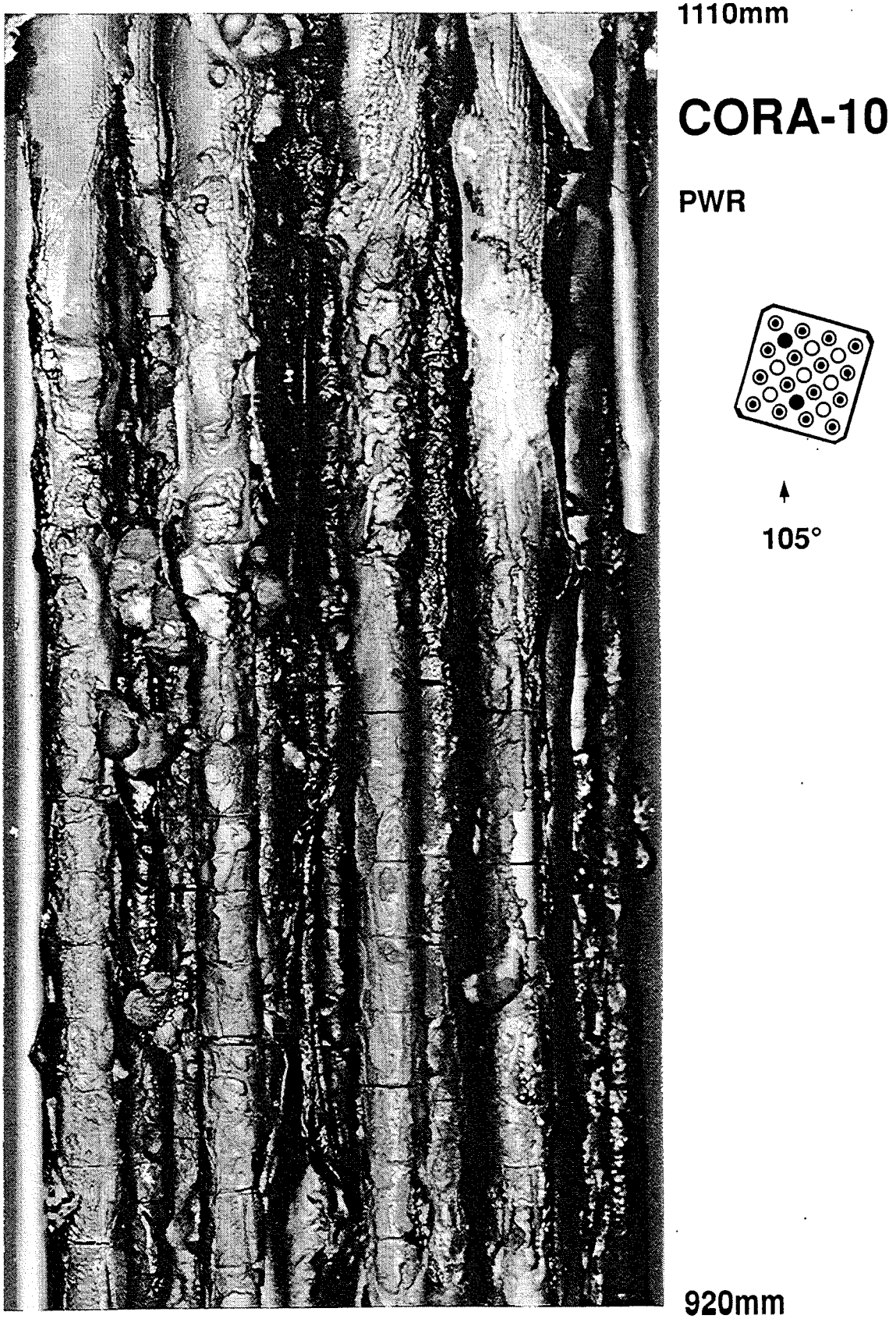

Fig. 116: Posttest view 105° orientation

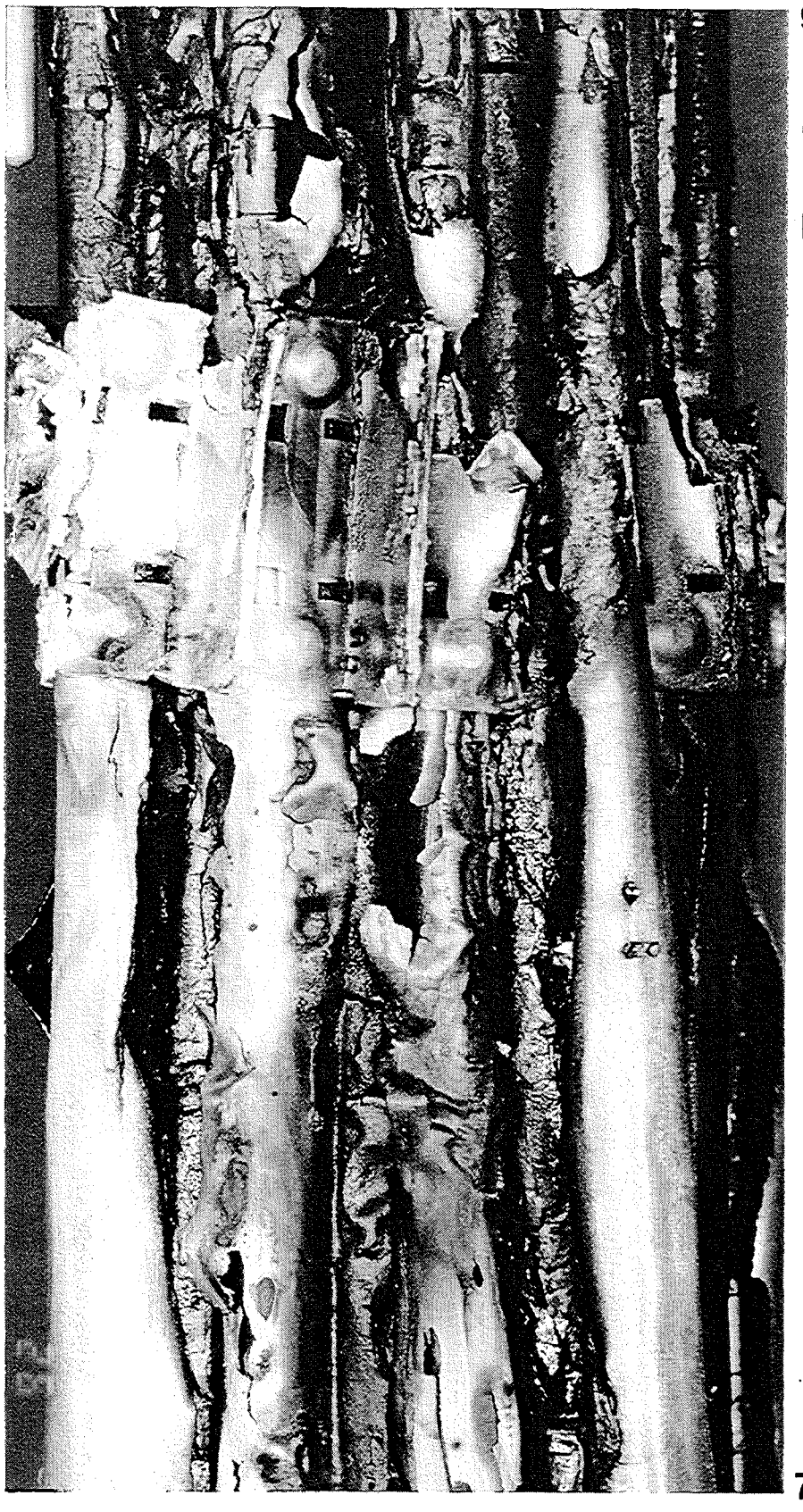

Fig. 117: Posttest view 105° orientation

Fig. 118: Posttest view 105° orientation

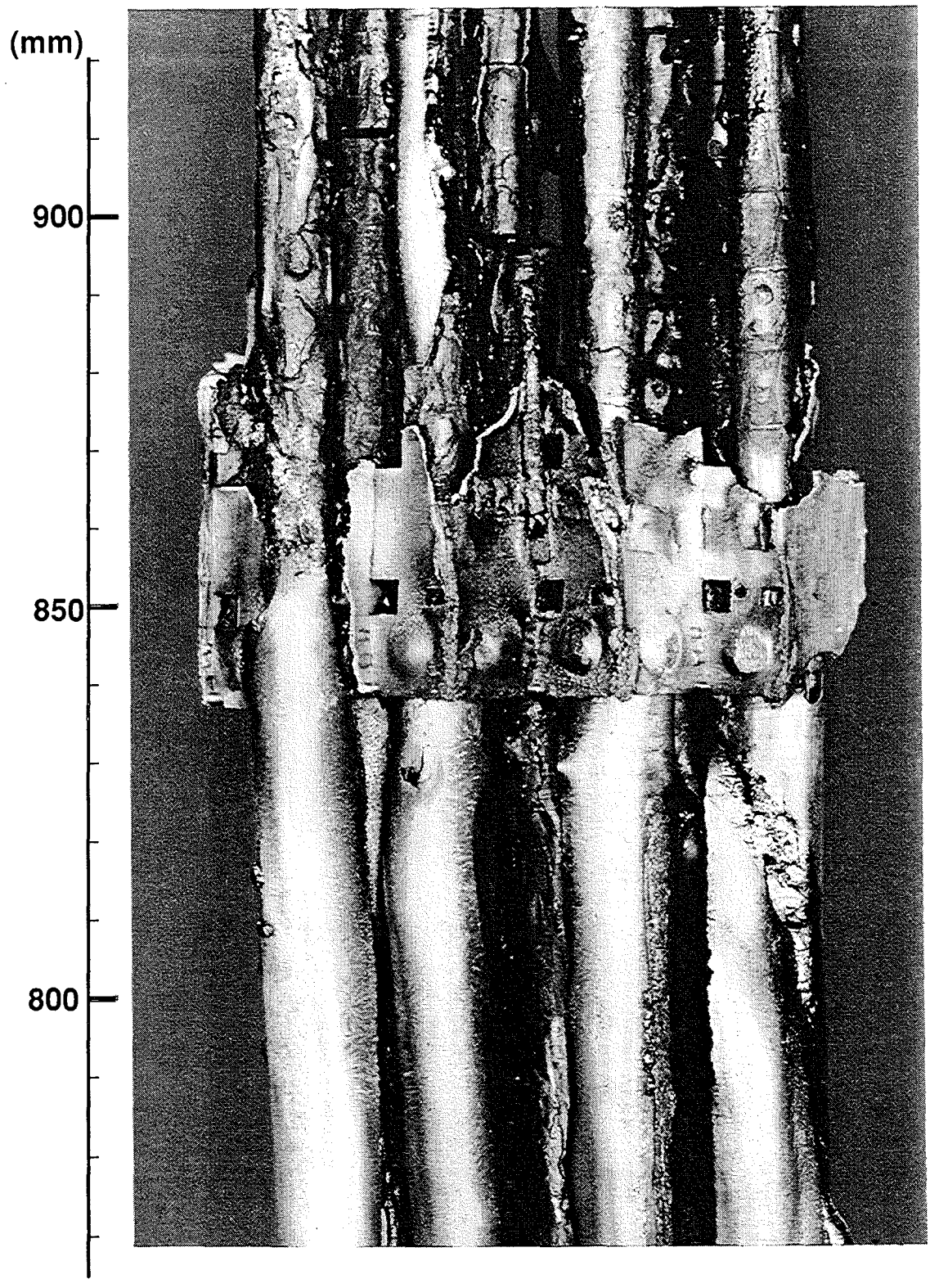

Fig. 119: Posttest view 30° orientation

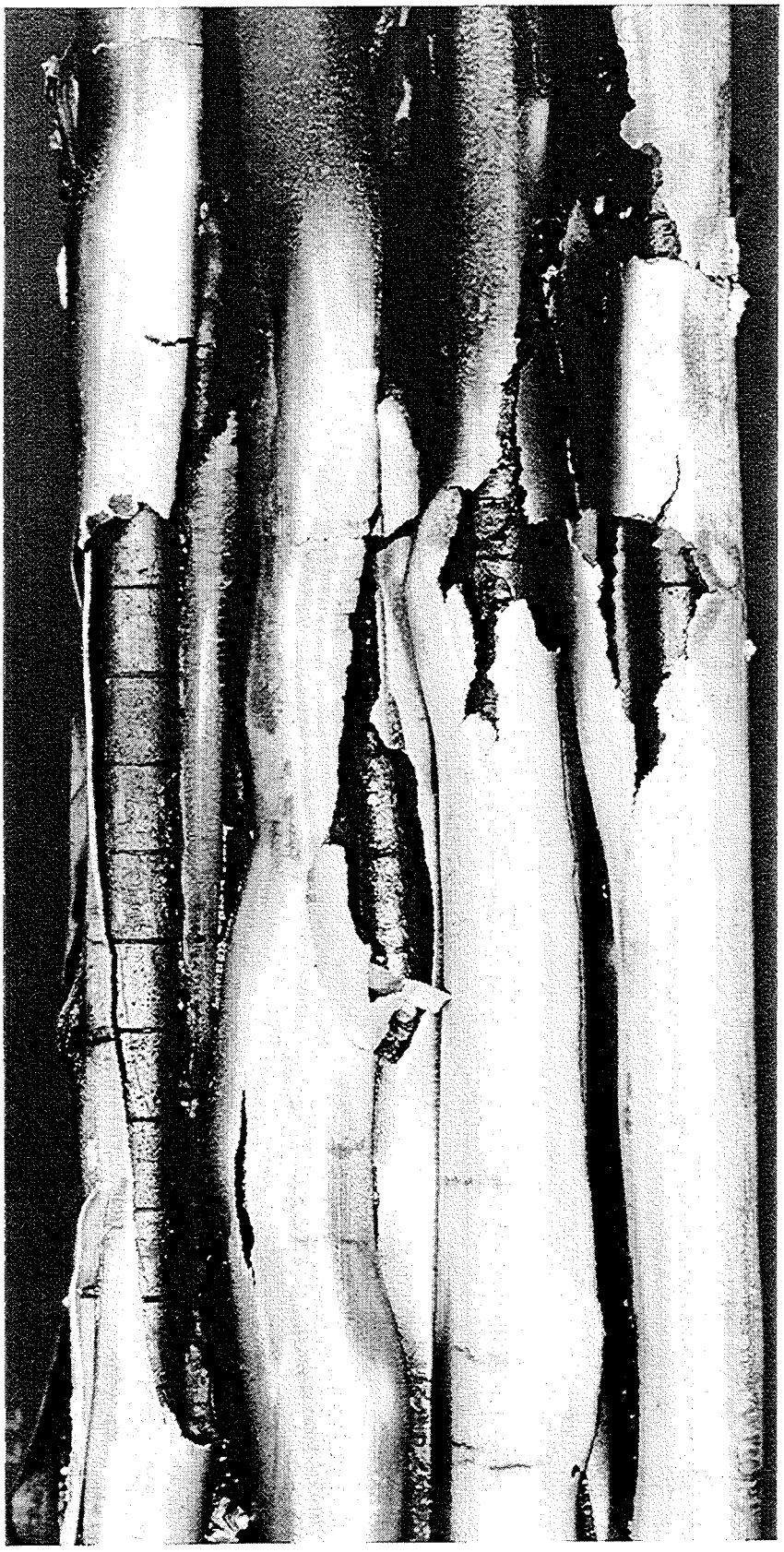

Fig. 120: Posttest view 30° orientation

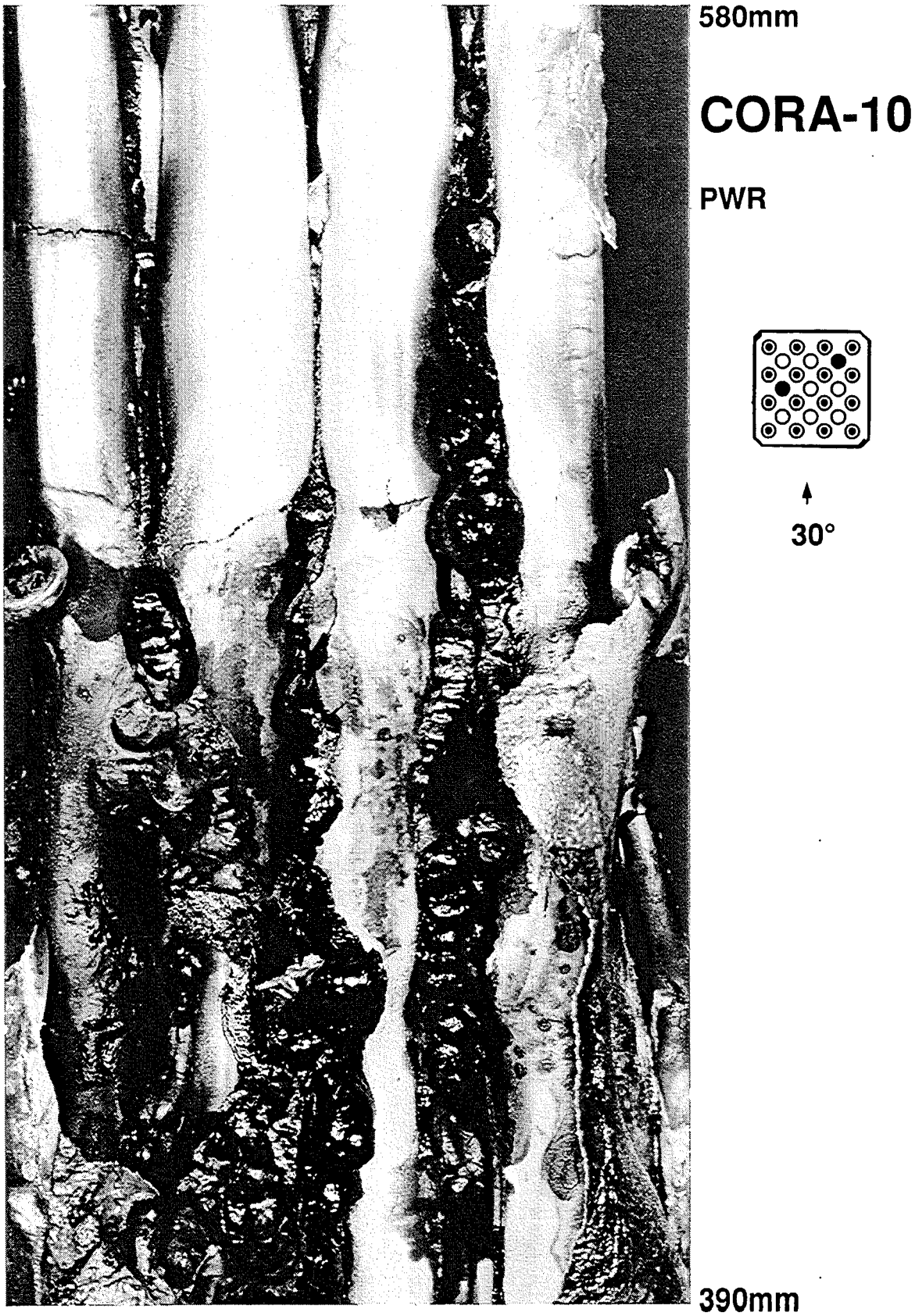

Fig. 121: Posttest view 30° orientation

Fig. 122: Posttest view 30° orientation

CORA-10; PWR

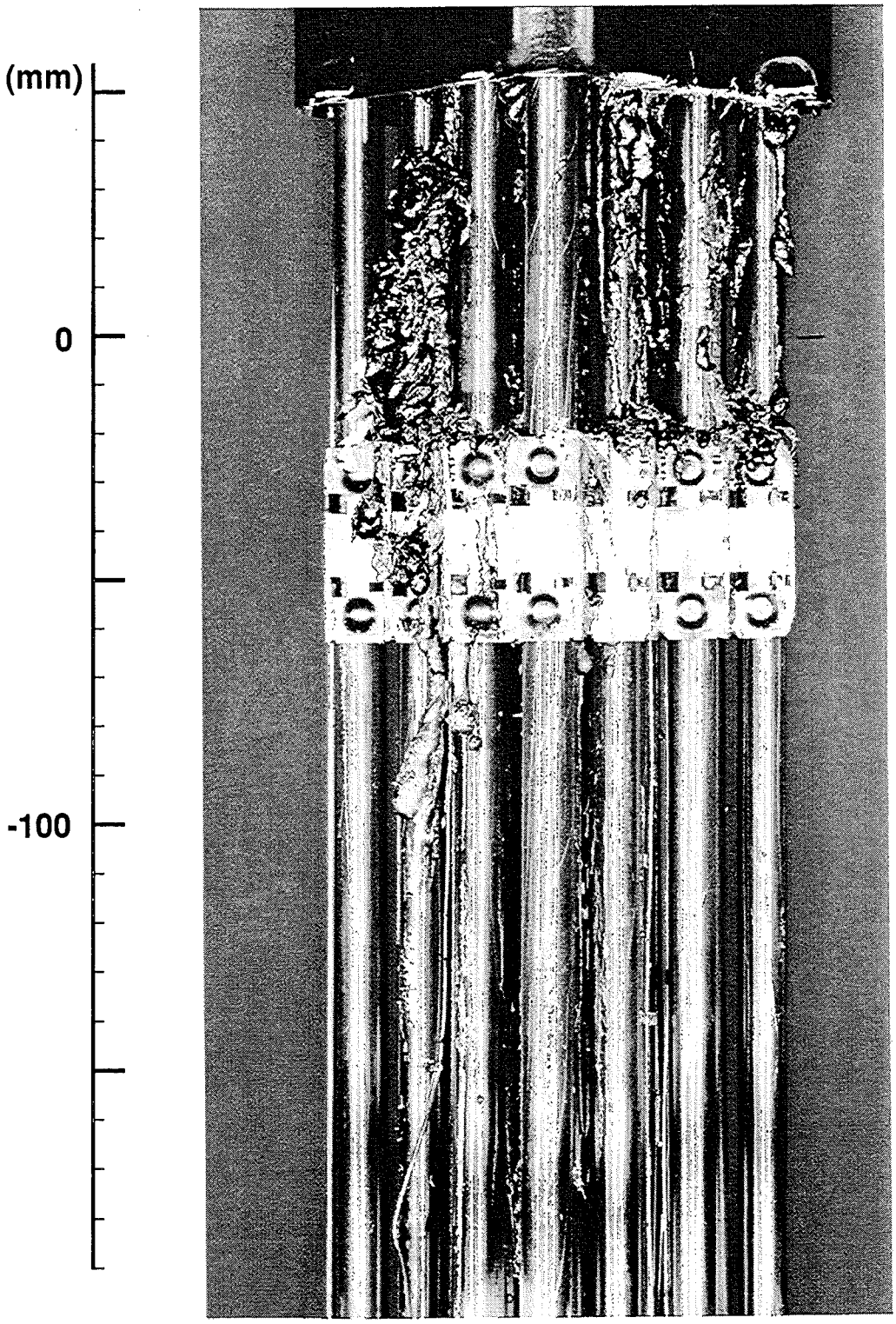

Fig. 123: Posttest view 160° orientation

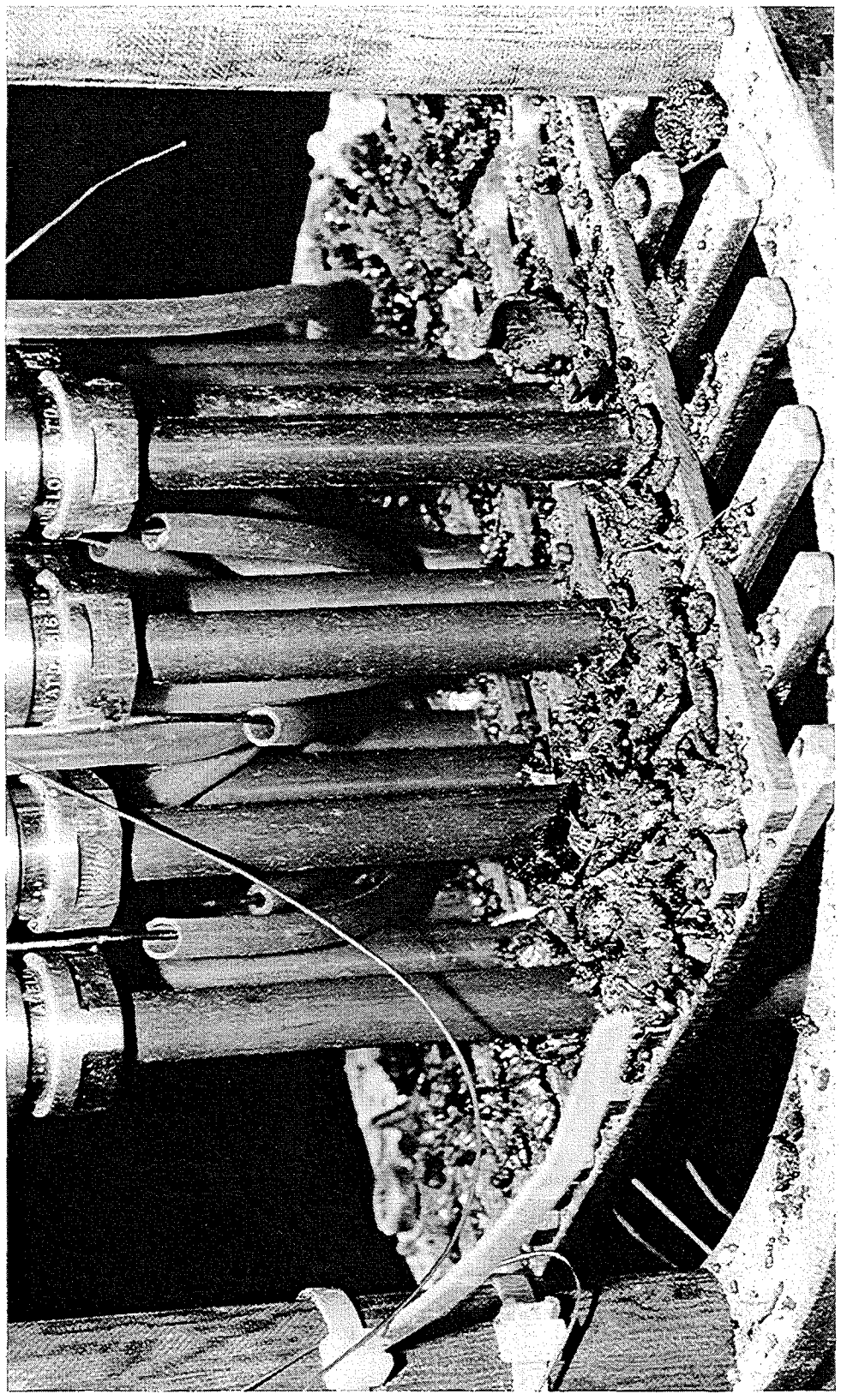

Fig. 124: Refrozen melt at the lower end of the bundle

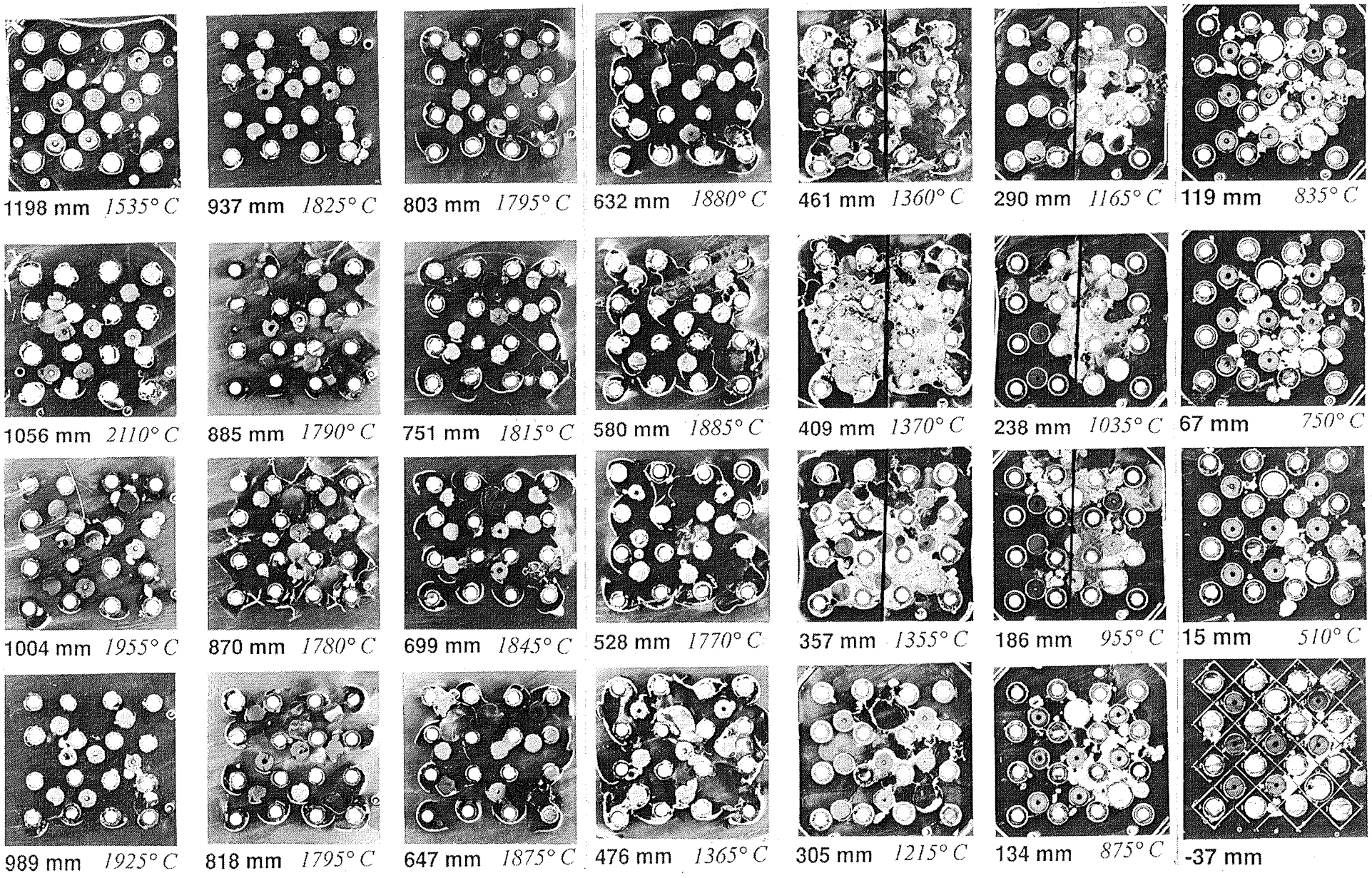

Fig. 125: Horizontal cross sections of bundle CORA-10, top view (1198 - -37 mm)

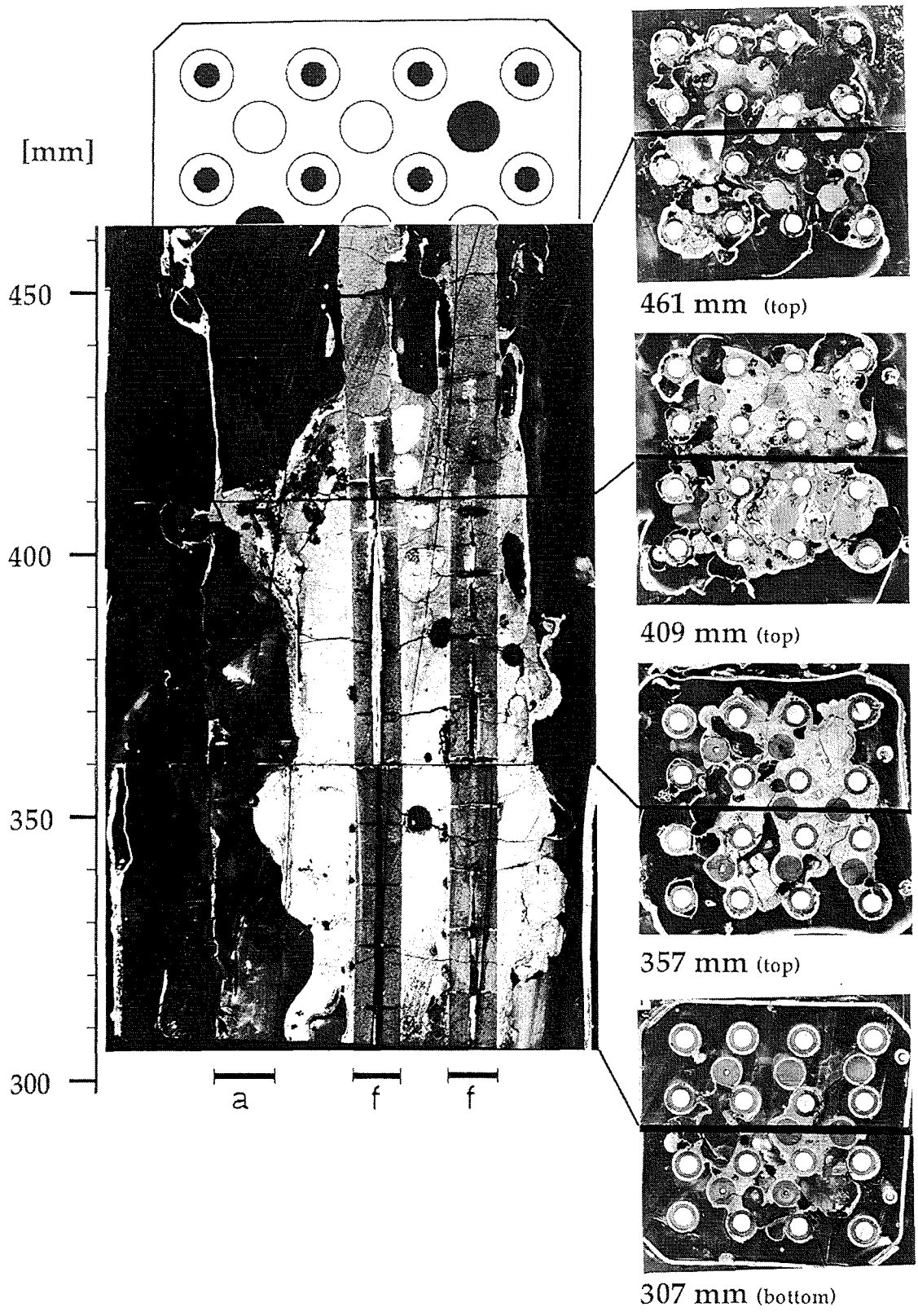

Fig. 126: CORA-10; Vertical cross section from 307 to 461 mm elevation

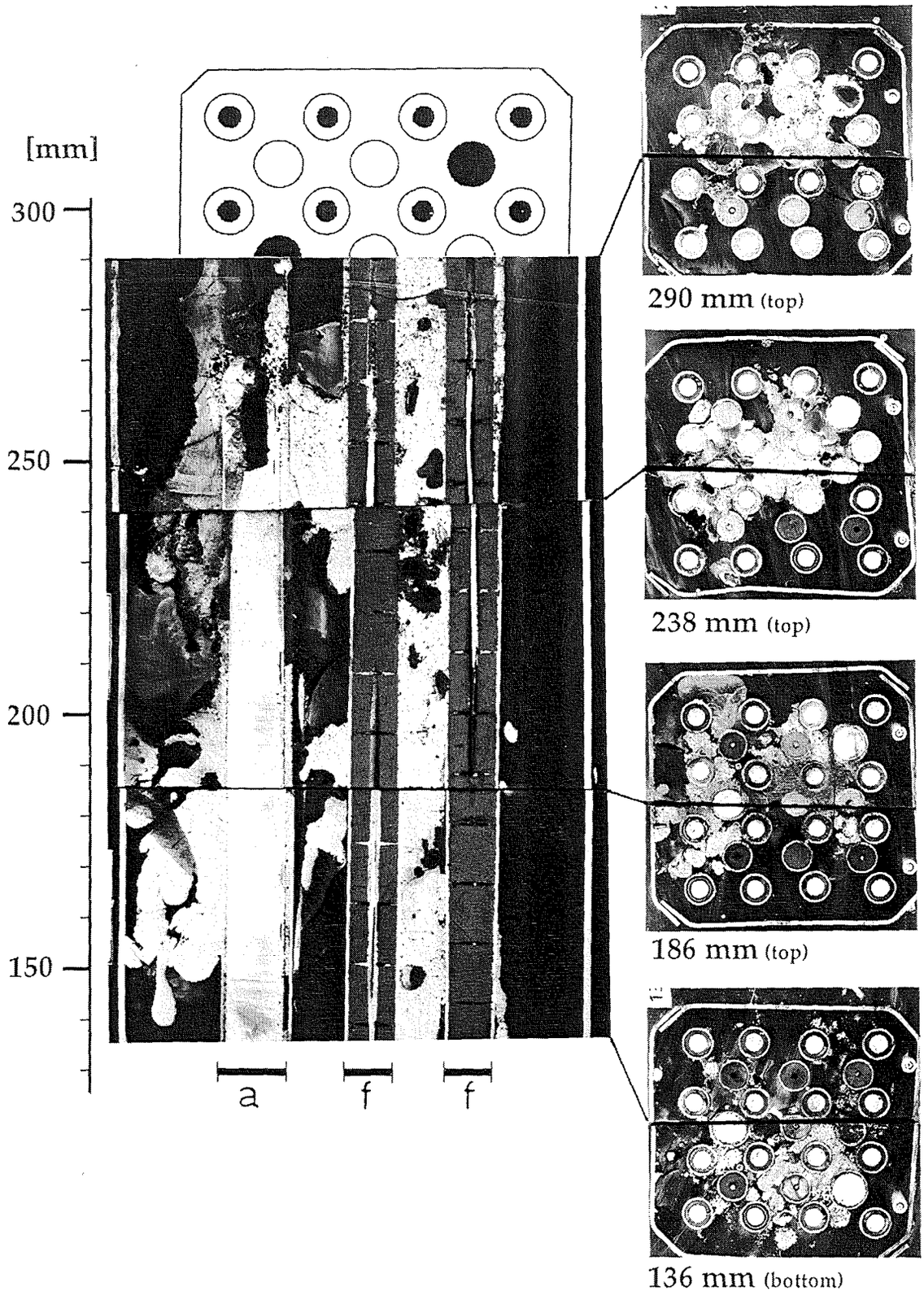

Fig. 127: CORA-10; Vertical cross section from 136 to 290 mm elevation

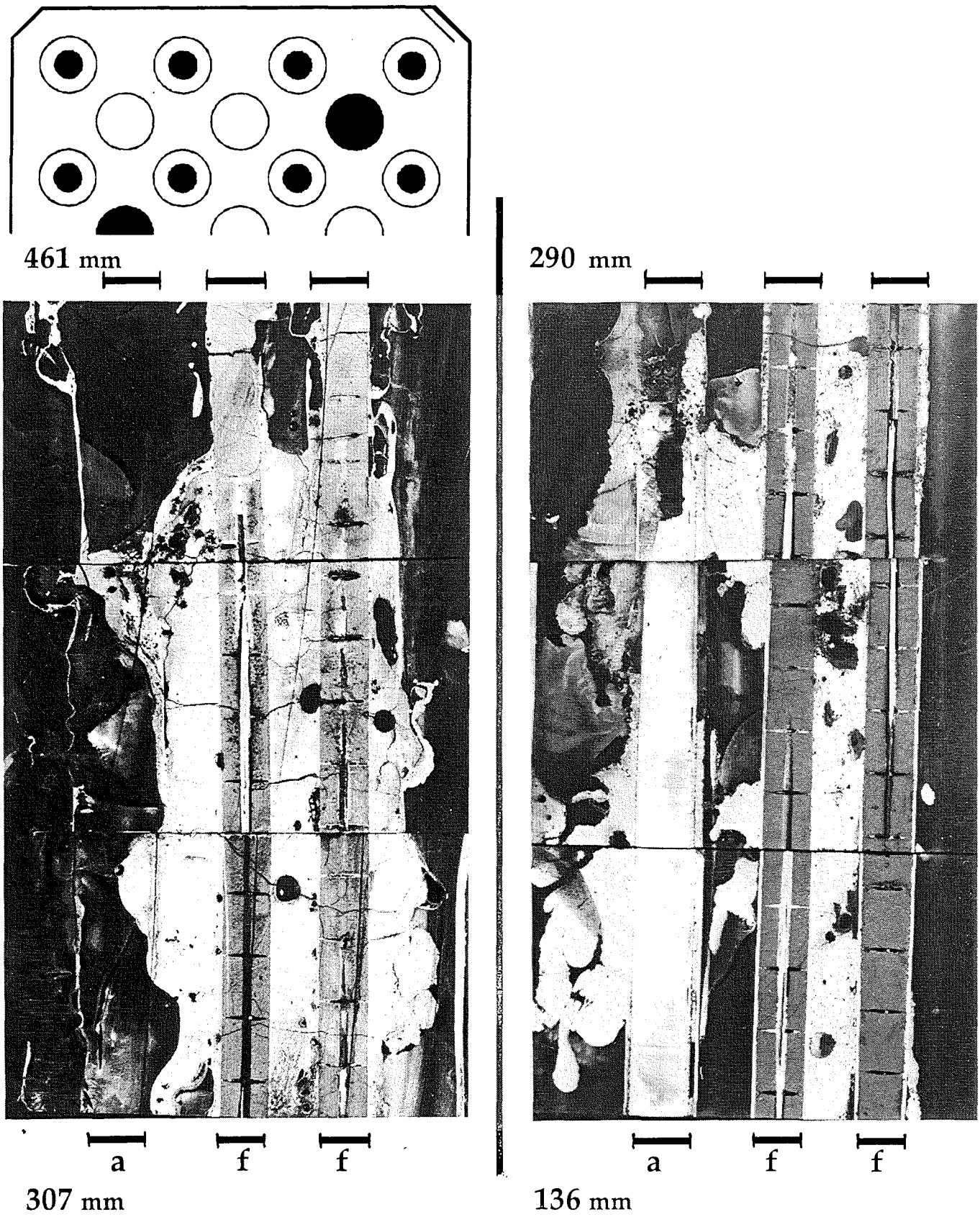

Fig. 128: CORA-10; Vertical cross sections from 136 to 290 mm elevation and from 307 to 461 mm elevation

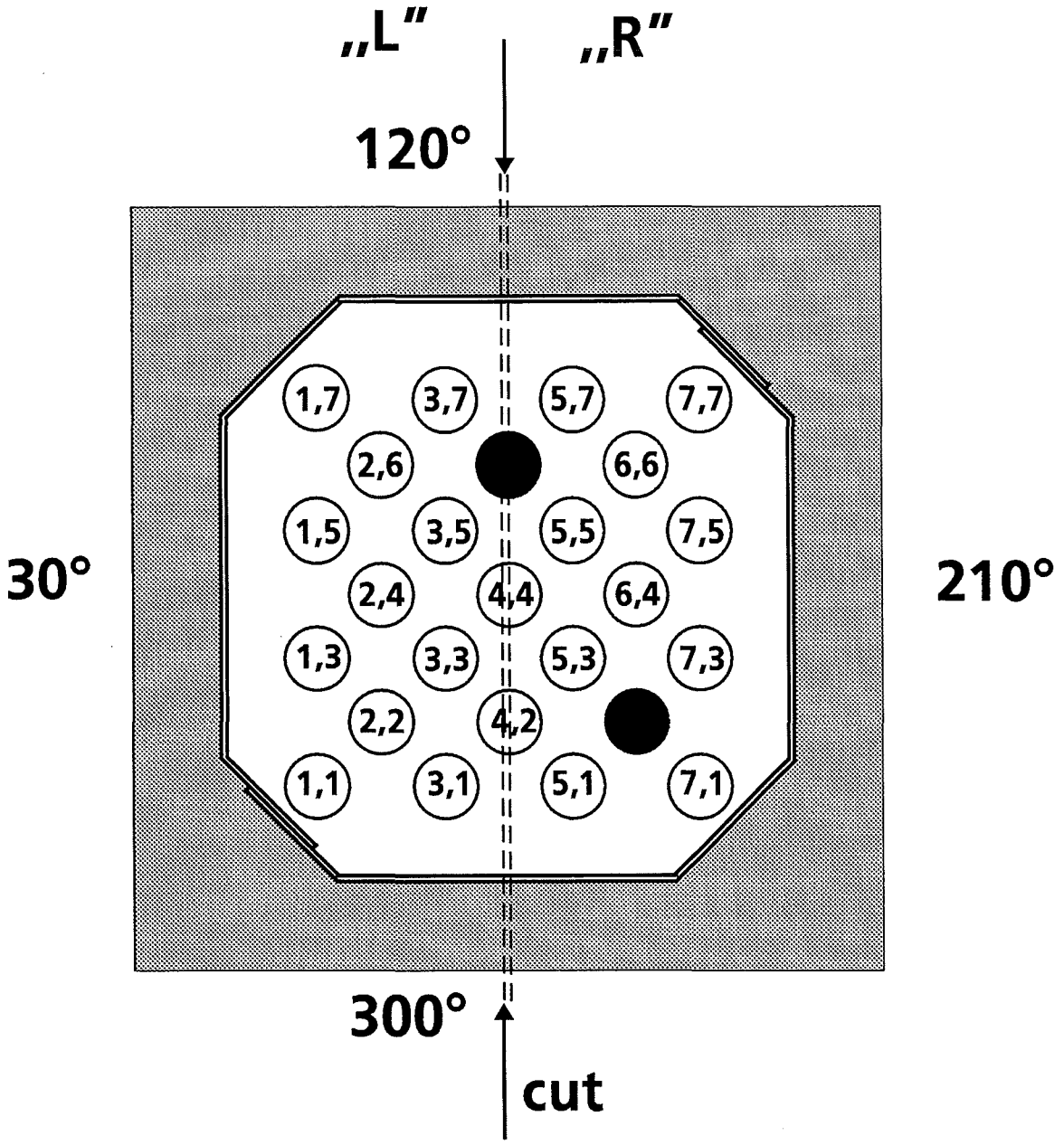

Top view

Fig. 128a: Locations of vertical cuts through samples CORA - 10-e, 10-f, 10-g, 10-h, 10-i and 10-j

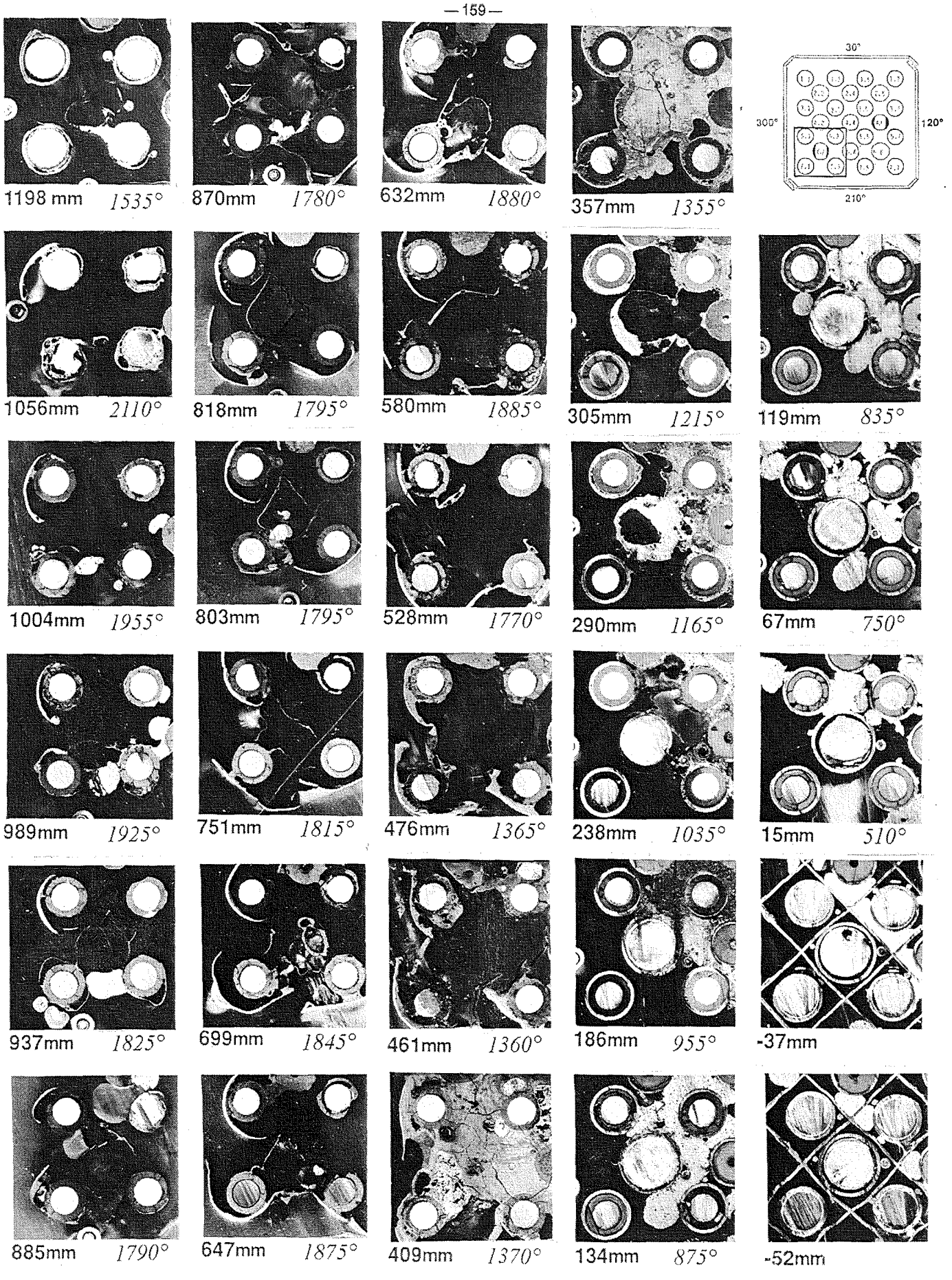

Fig. 129: CORA-10; Horizontal cross section of absorber region of absorber rod 6.2

APPENDIX A

Test Data of the pre-heating phase

Figures: A1 - A30

Complete set of cross sections

Figures: A31 - A42

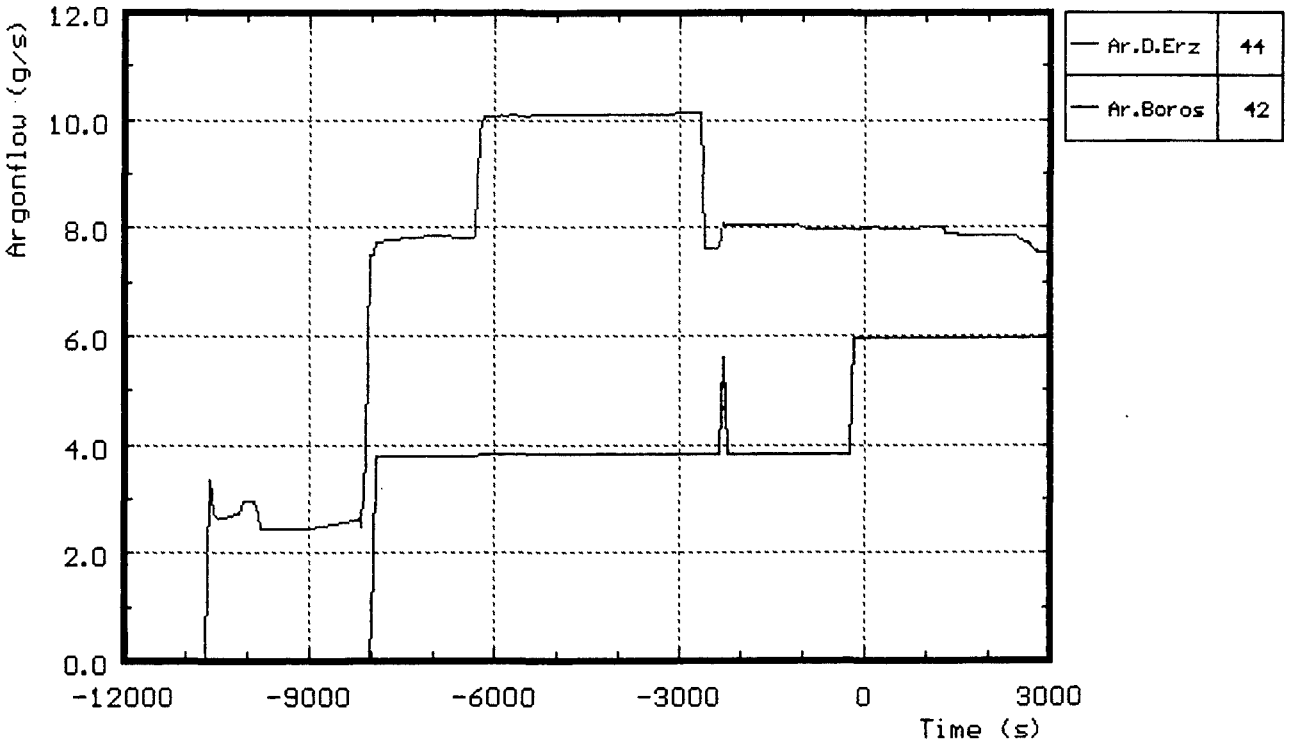

Fig. A1: CORA-10; Argon input before the test

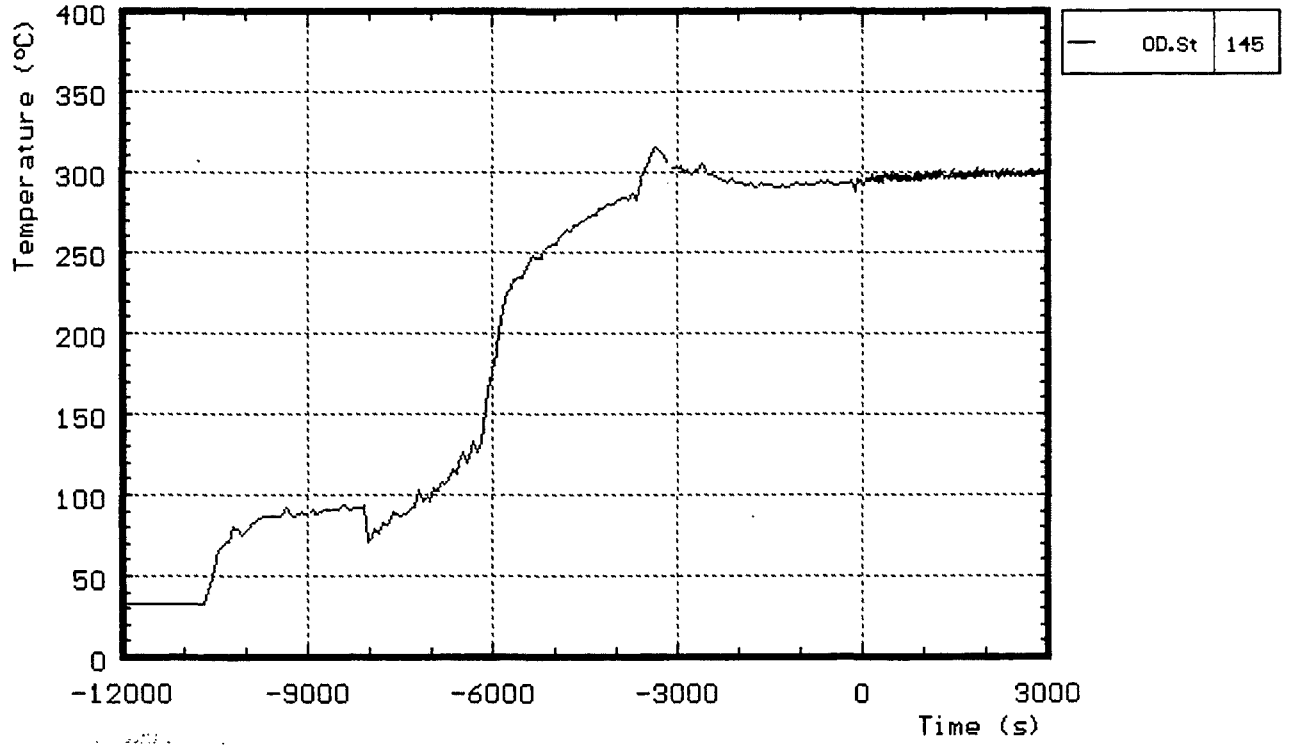

Fig. A2: CORA-10; Temperature at the entrance of the bundle prior to test

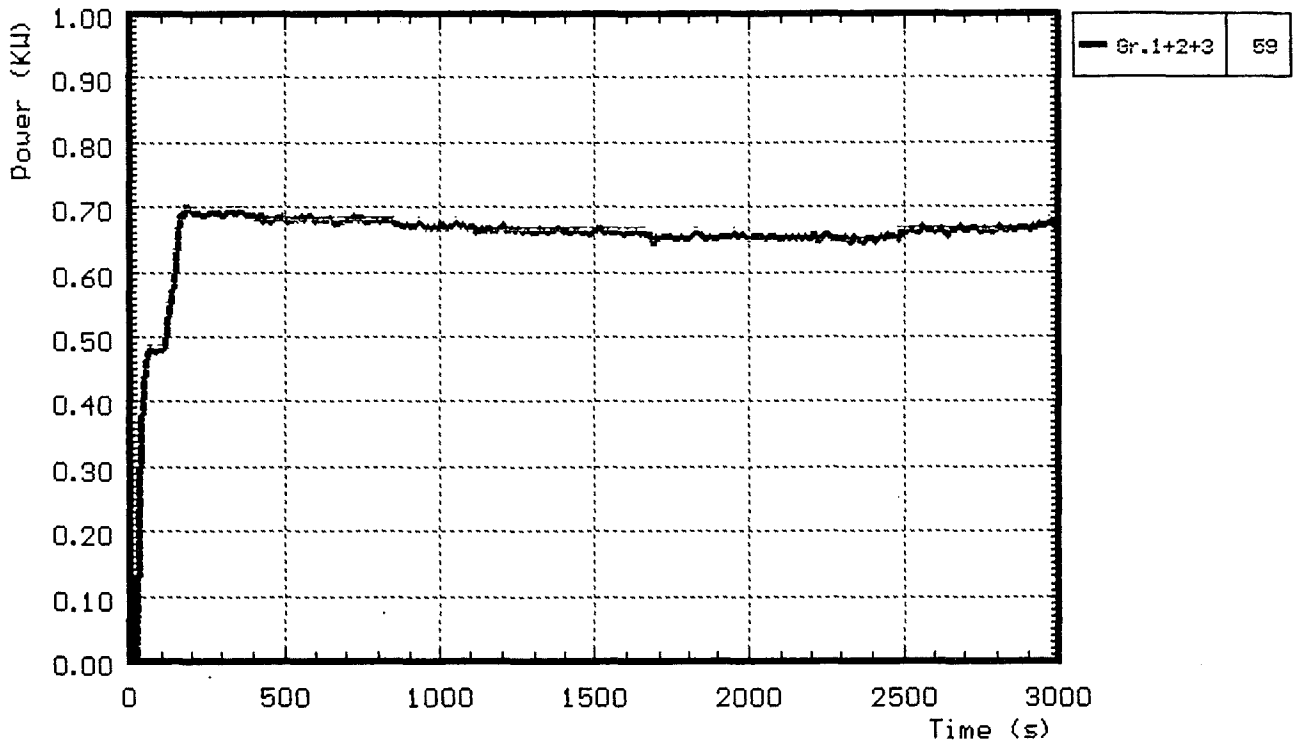

Fig. A3: CORA-10; Power input during the pre-heat phase

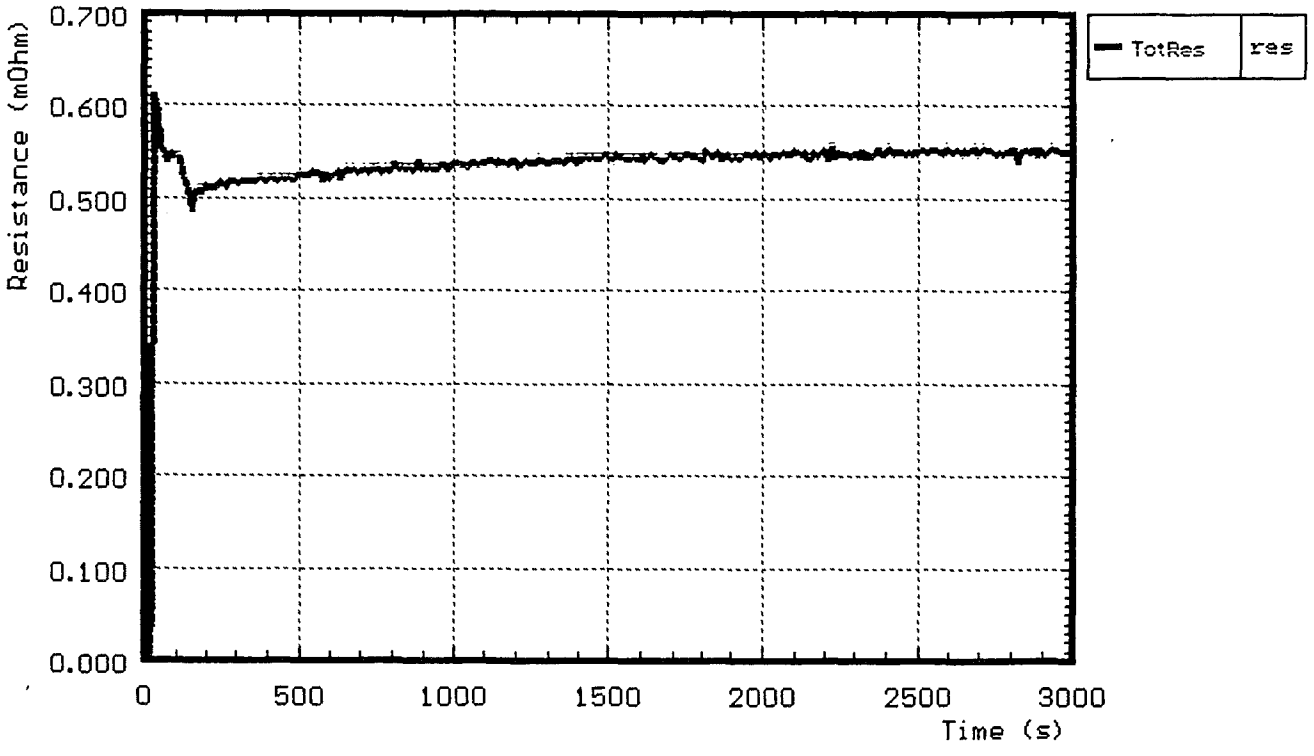

Fig. A4: CORA-10; Resistance during the pre-heat phase

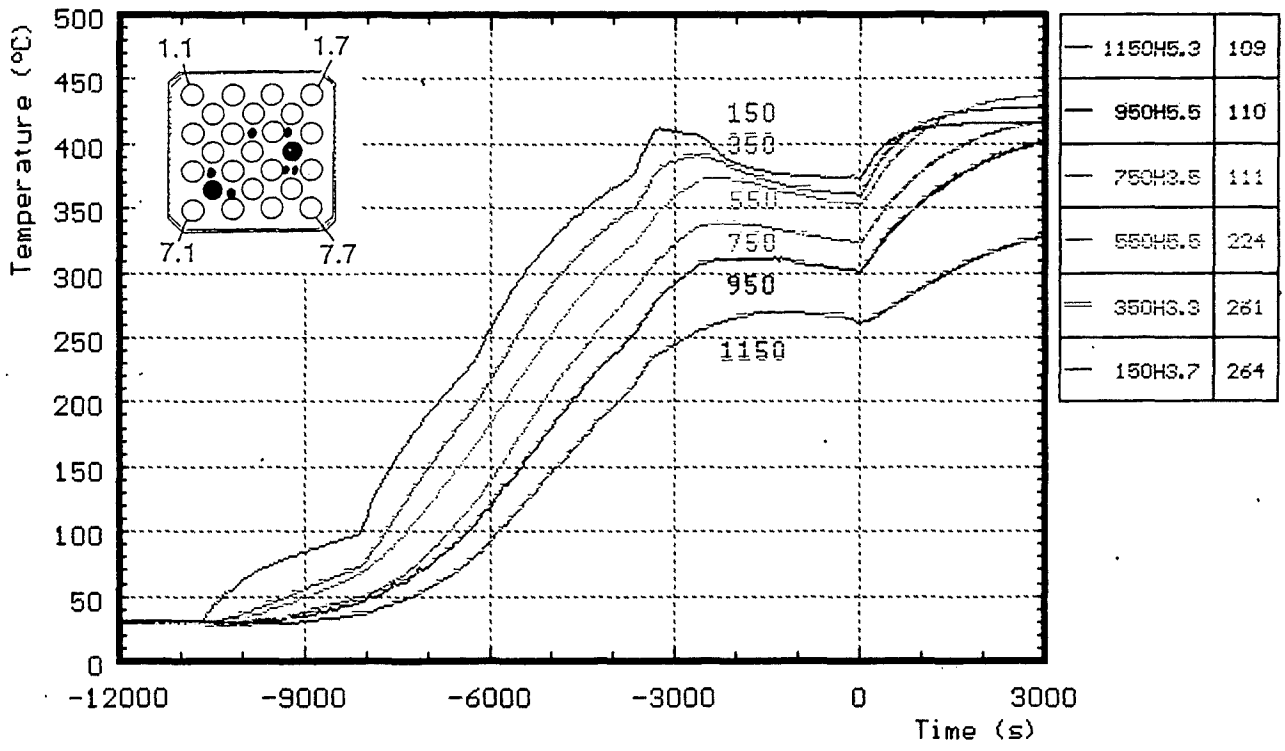

Fig. A5: CORA-10; Temperatures of heated rods, pre-heat phase

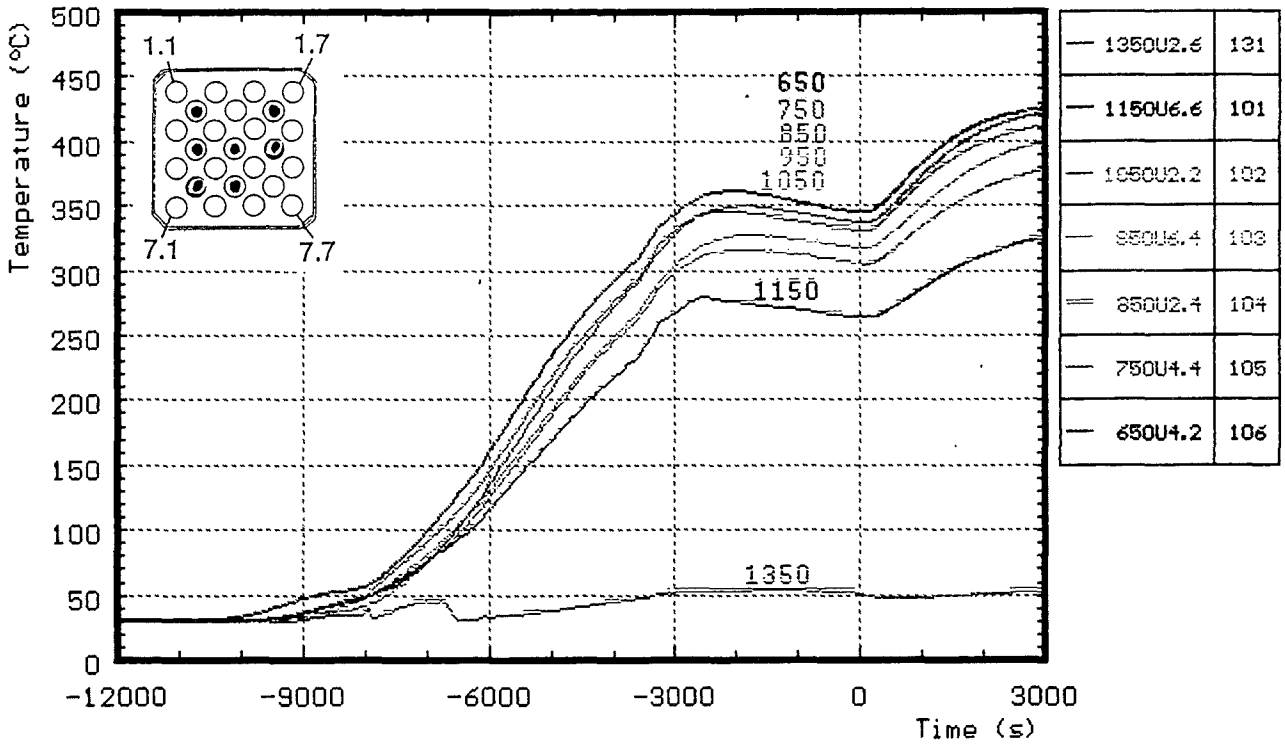

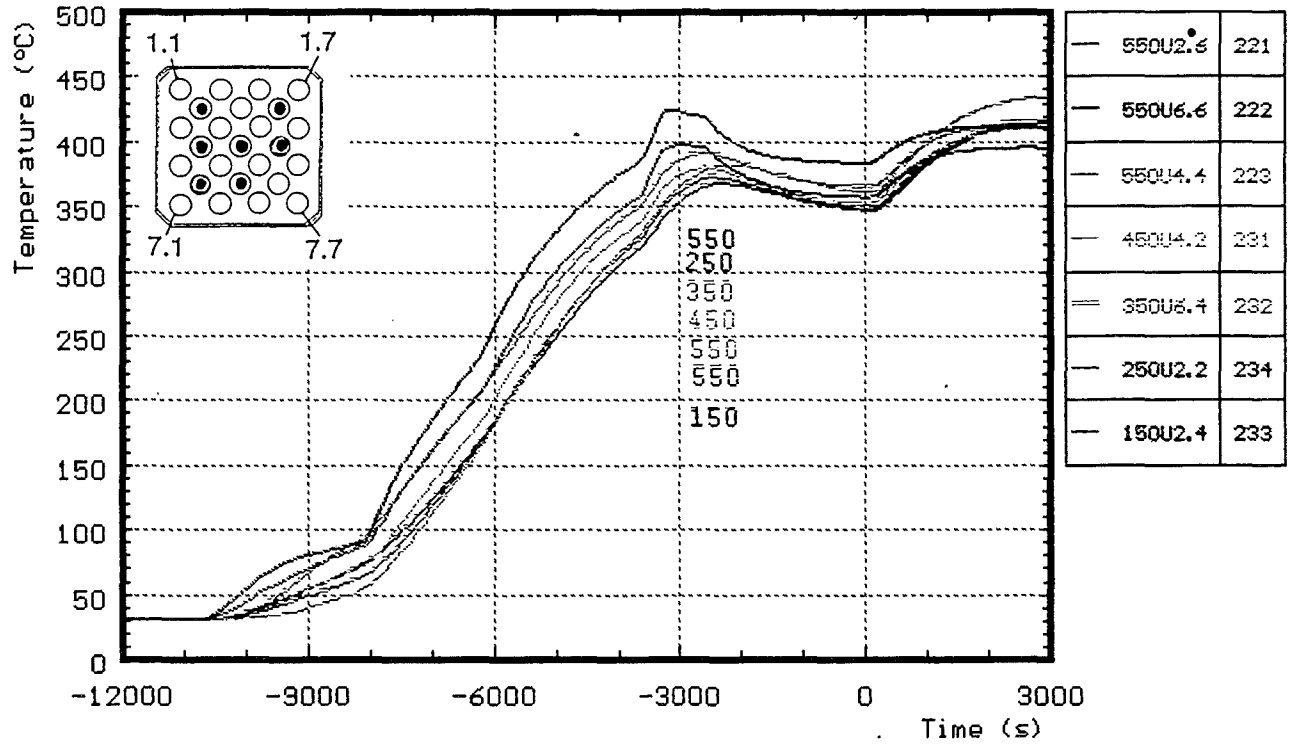

Fig. A6: CORA-10; Temperatures of unheated rods, pre-heat phase

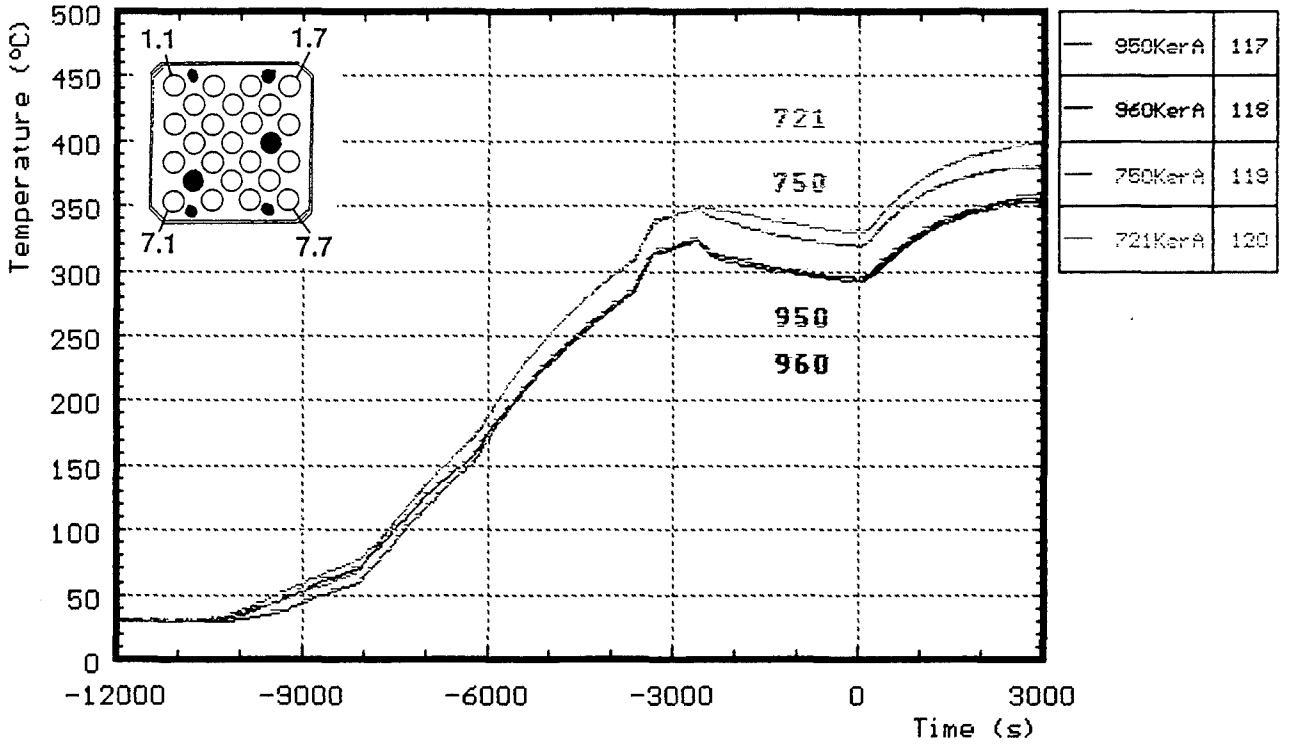

Fig. A7: CORA-10; Temperatures measured with ceramic protected TCs, pre-heat phase

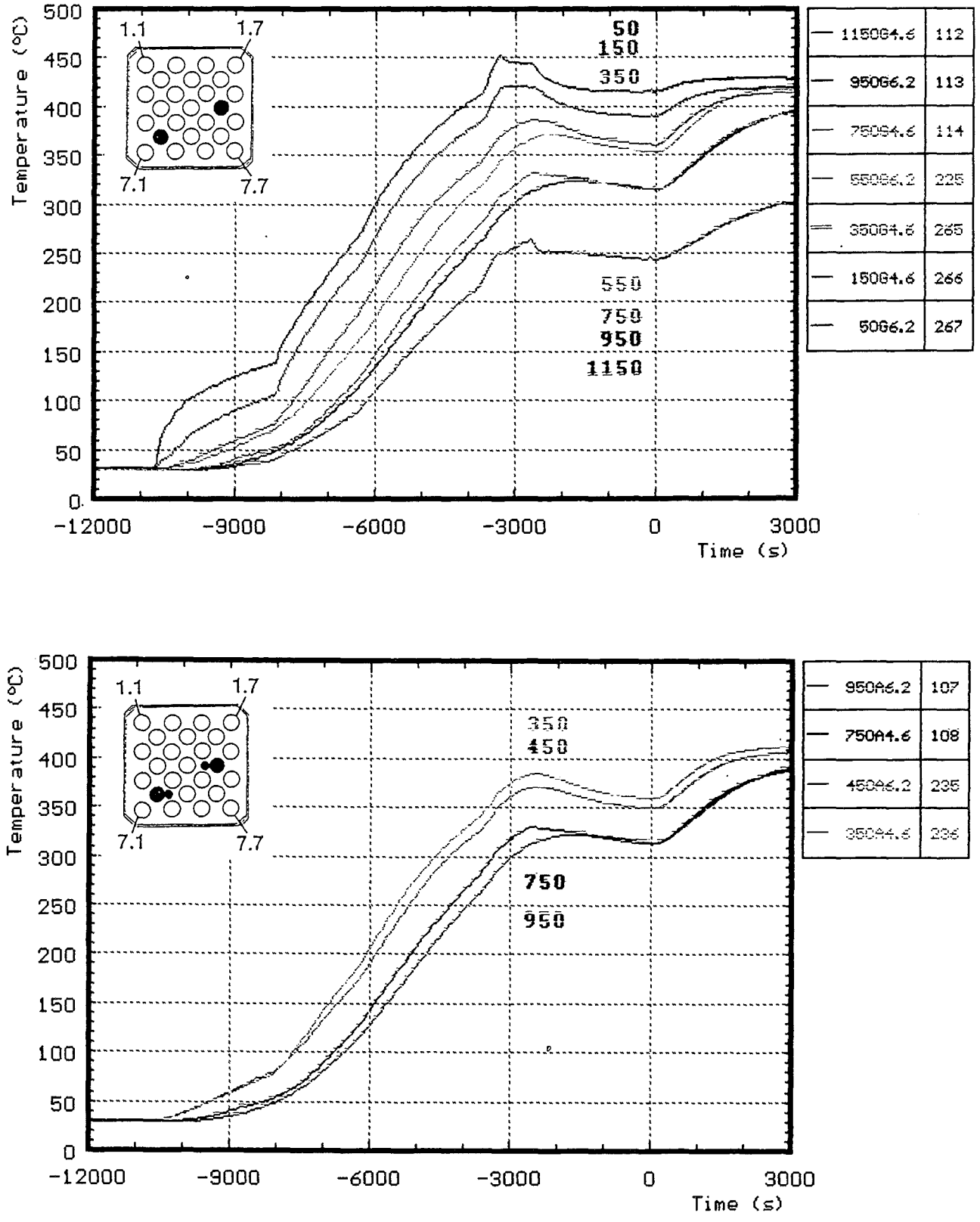

Fig. A8: CORA-10; Temperatures on the guide tubes and in the absorbers, pre-heat phase

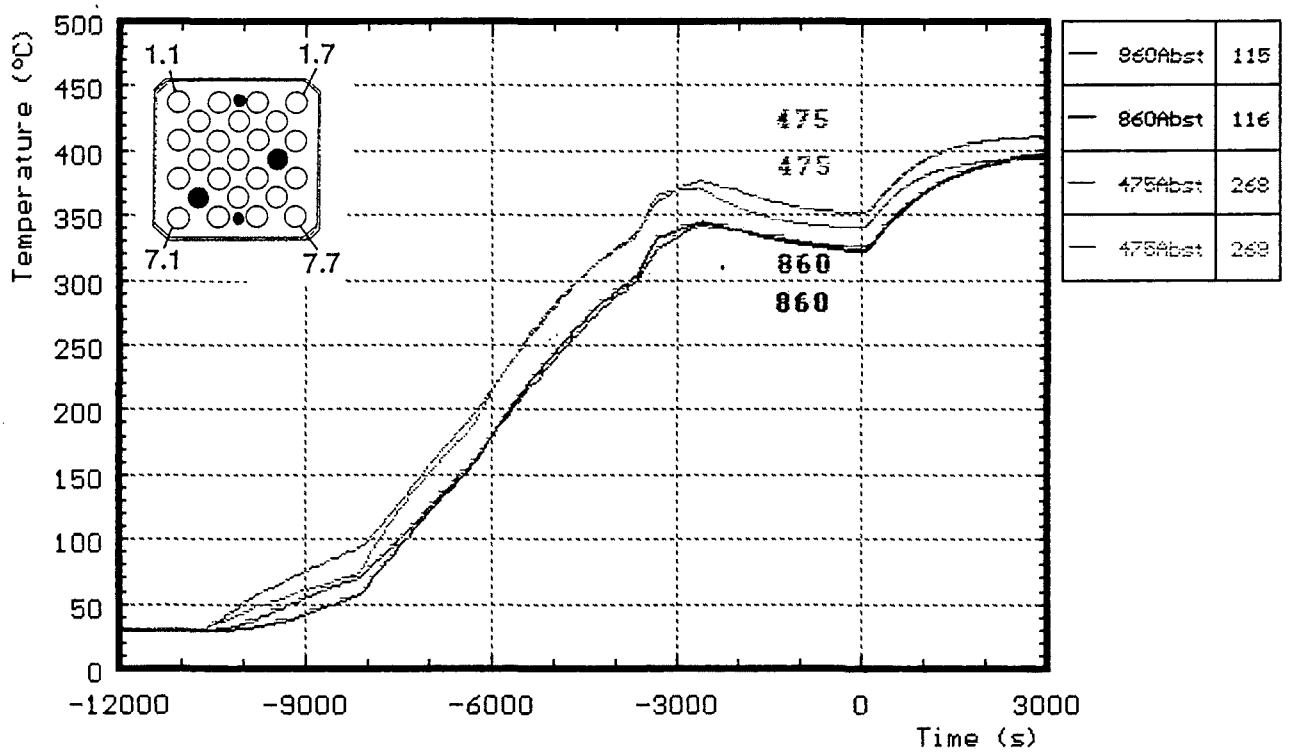

Fig. A9: CORA-10; Temperatures of the spacers; pre-heat phase

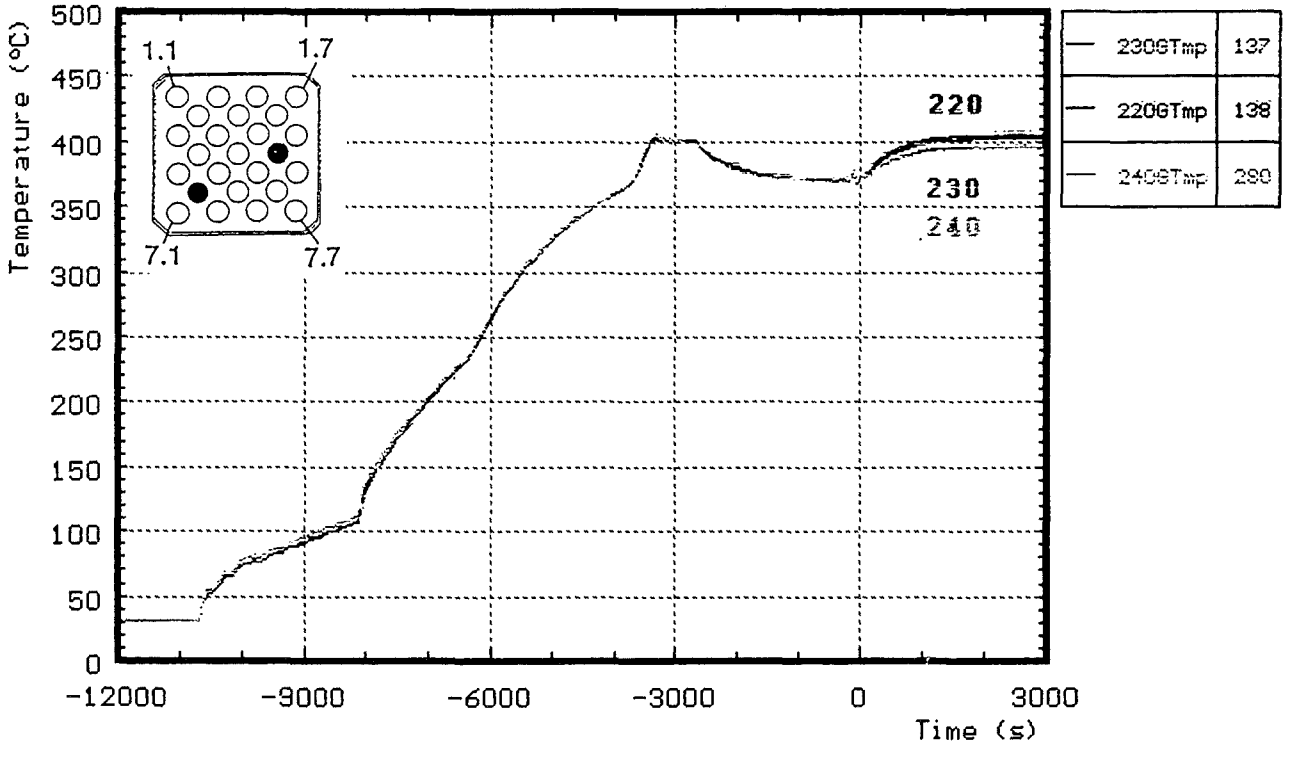

Fig. A10: CORA-10; Temperatures at lower end of bundle and shroud

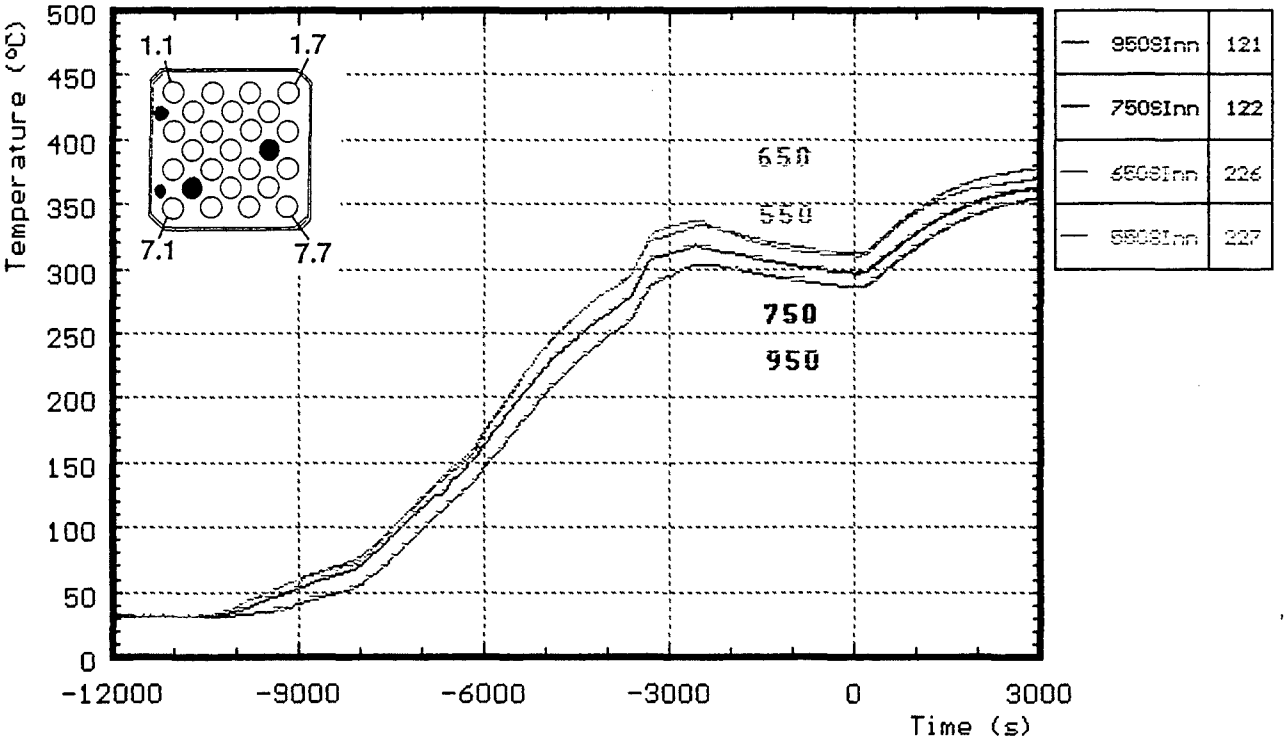

Fig. A11: CORA-10; Temperatures on the inner side of shroud; pre-heat phase

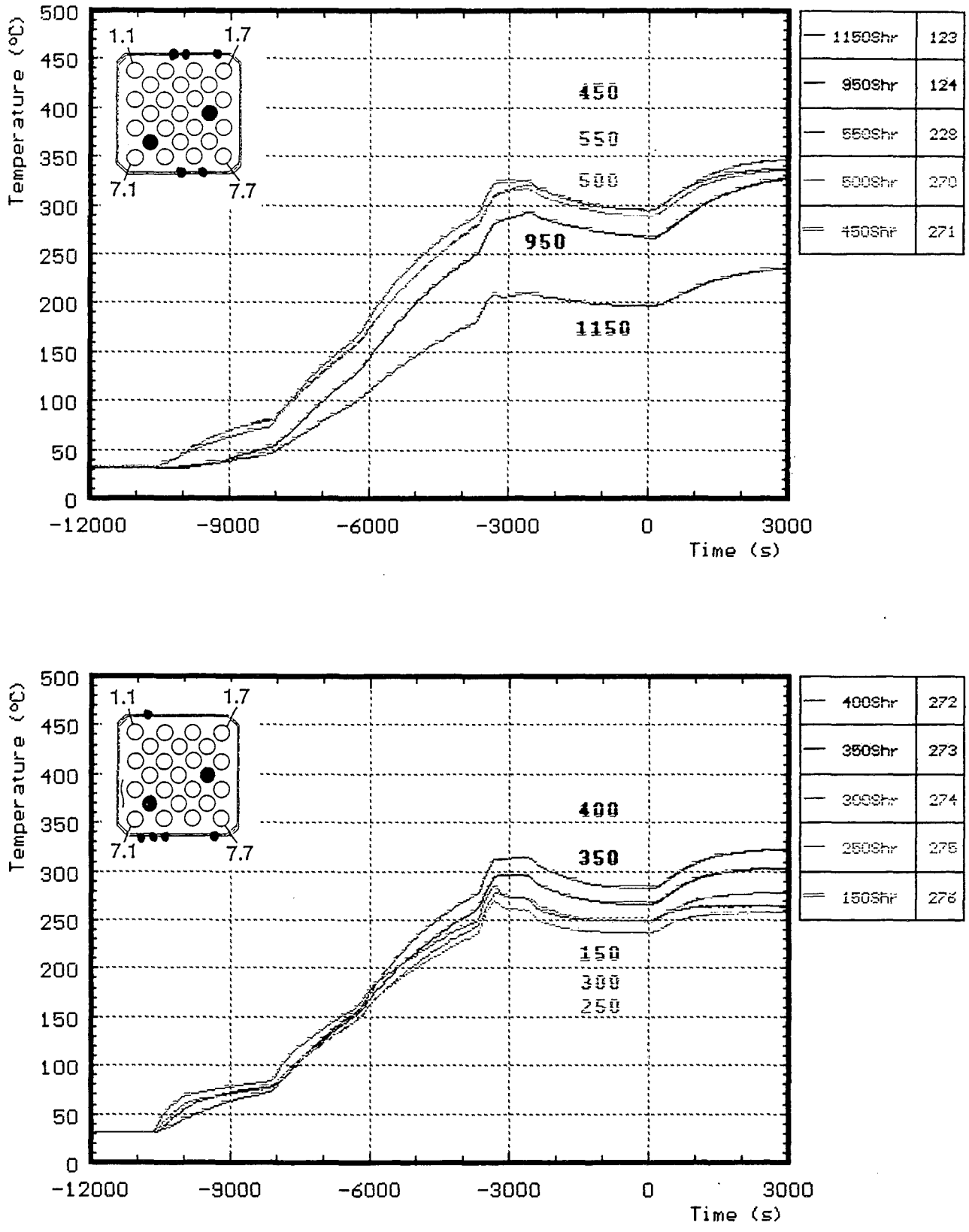

Fig. A12: CORA-10; Temperatures on the outer side of shroud, pre-heat phase

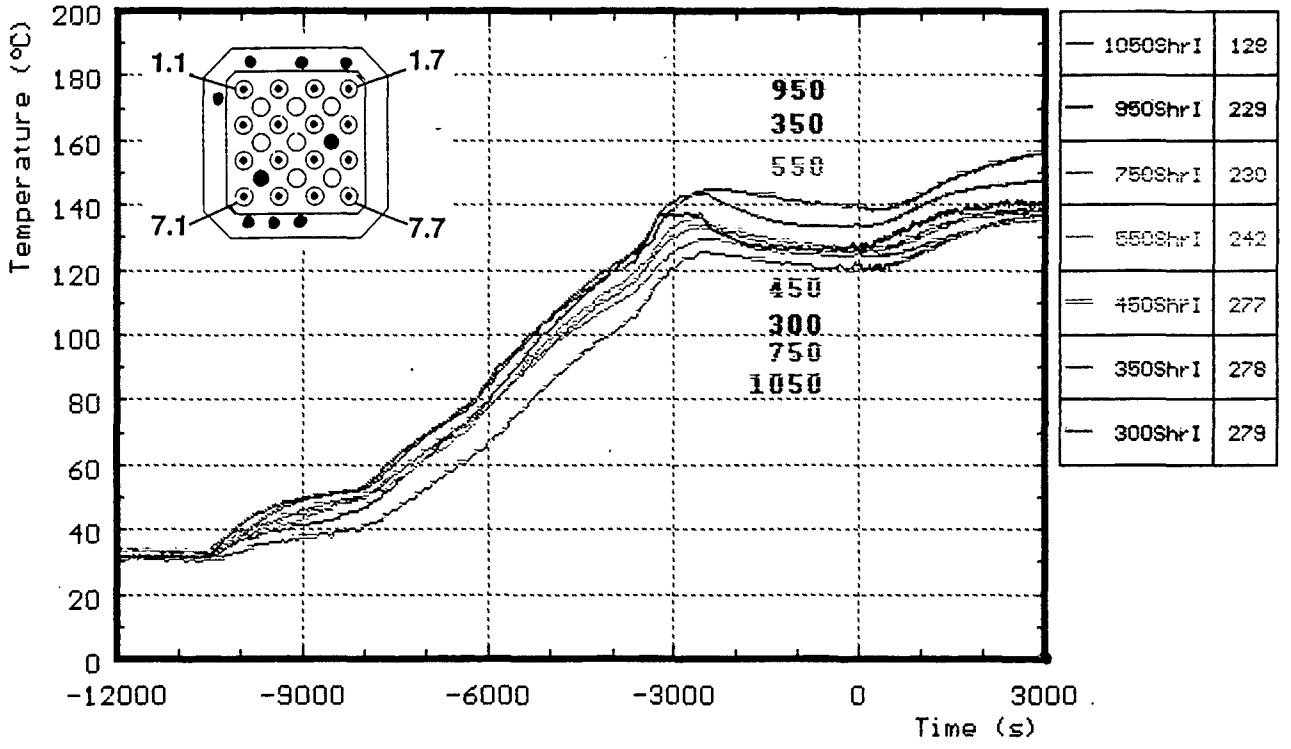

Fig. A13: CORA-10; Temperatures on shroud insulation; pre-heat phase

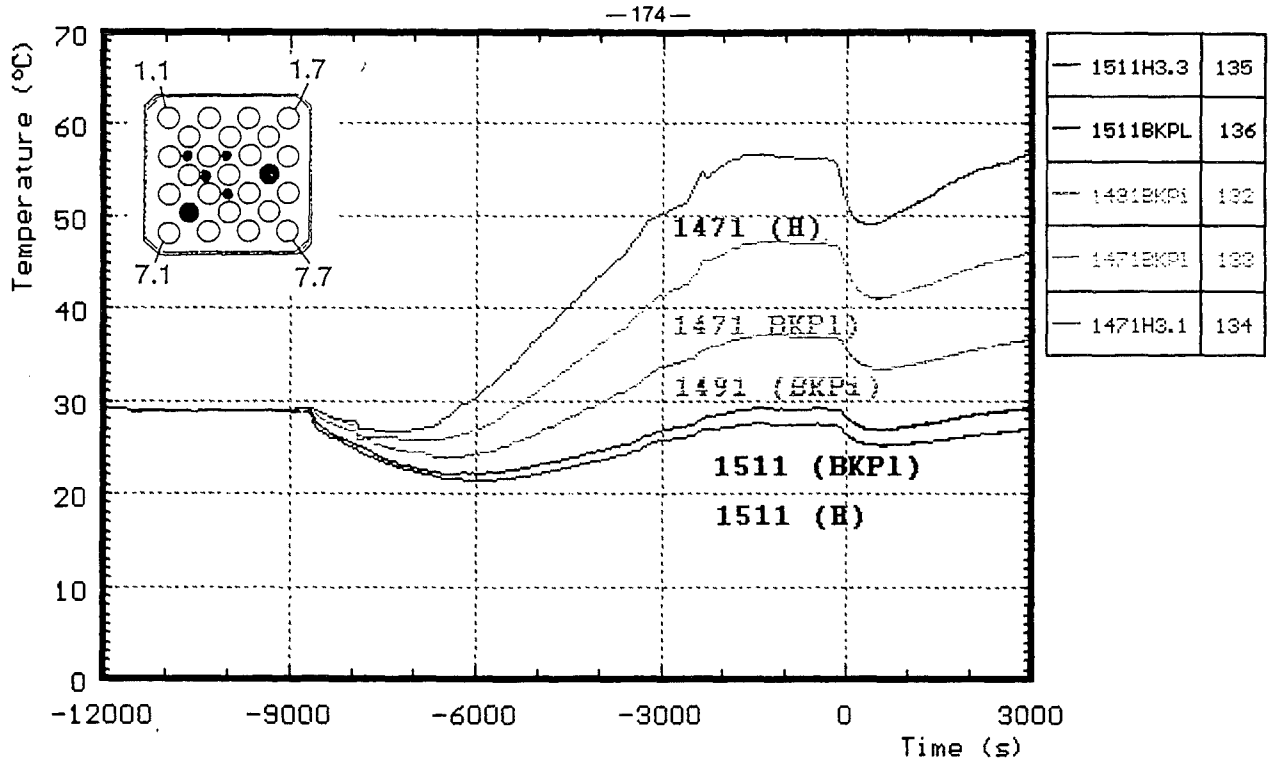

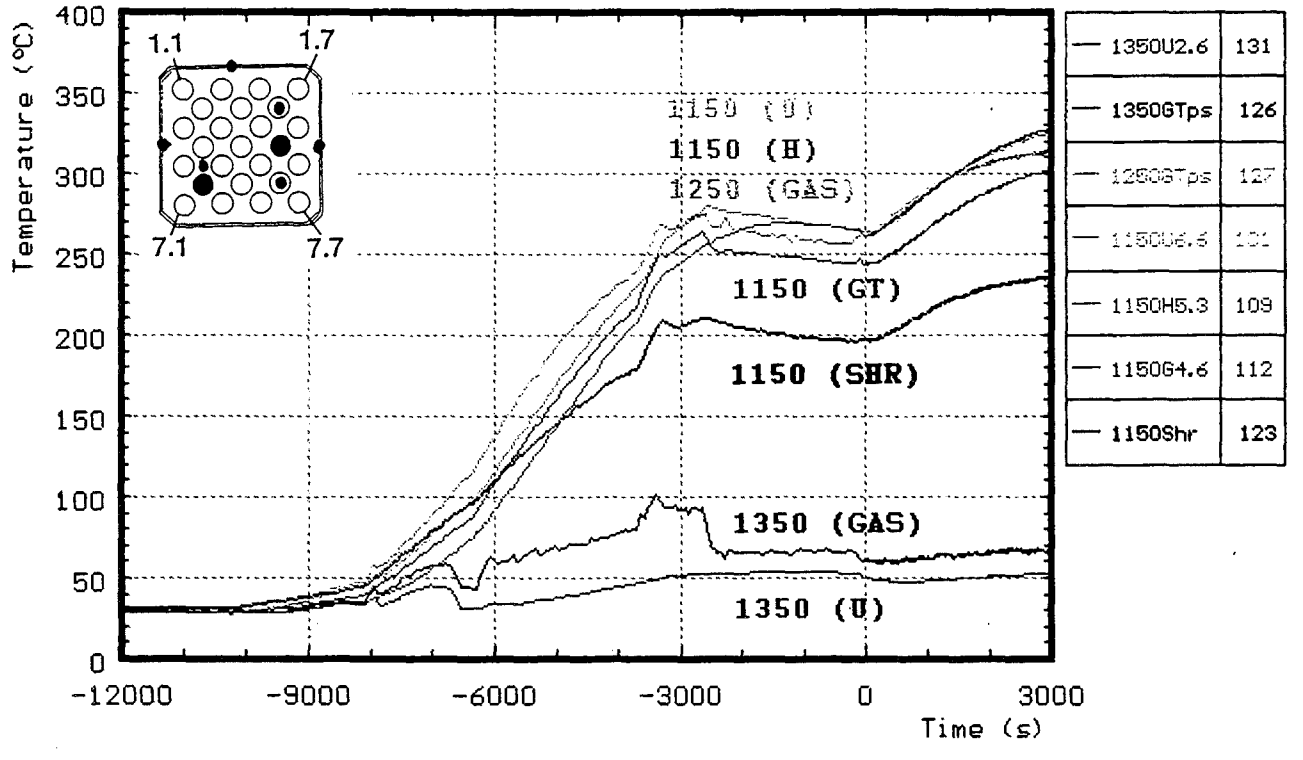

h : heated rods
u : unheated rods
gt : guide tube

shr : on shroud
BKPI : bundle heat plate
gas : gas temperature

Fig. A14: CORA-10; Temperatures at elevation given, pre-heat phase (1511-1471, 1350 - 1150mm)

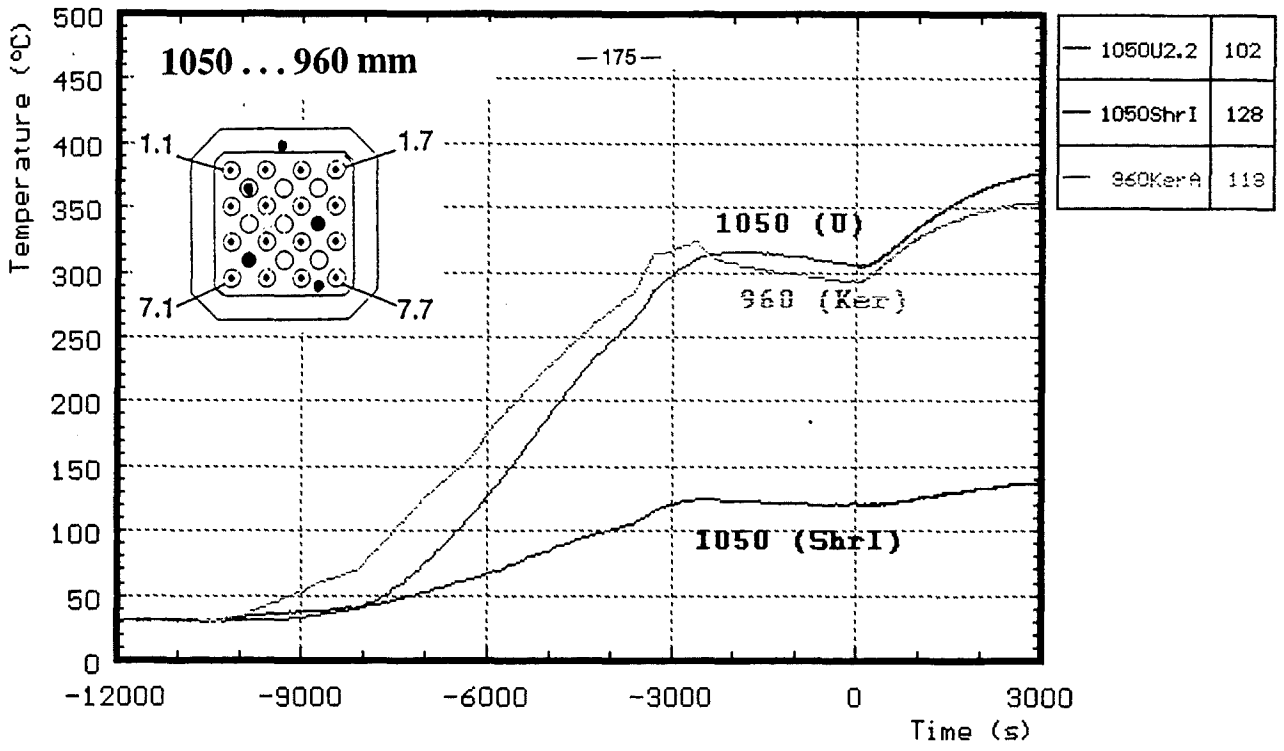

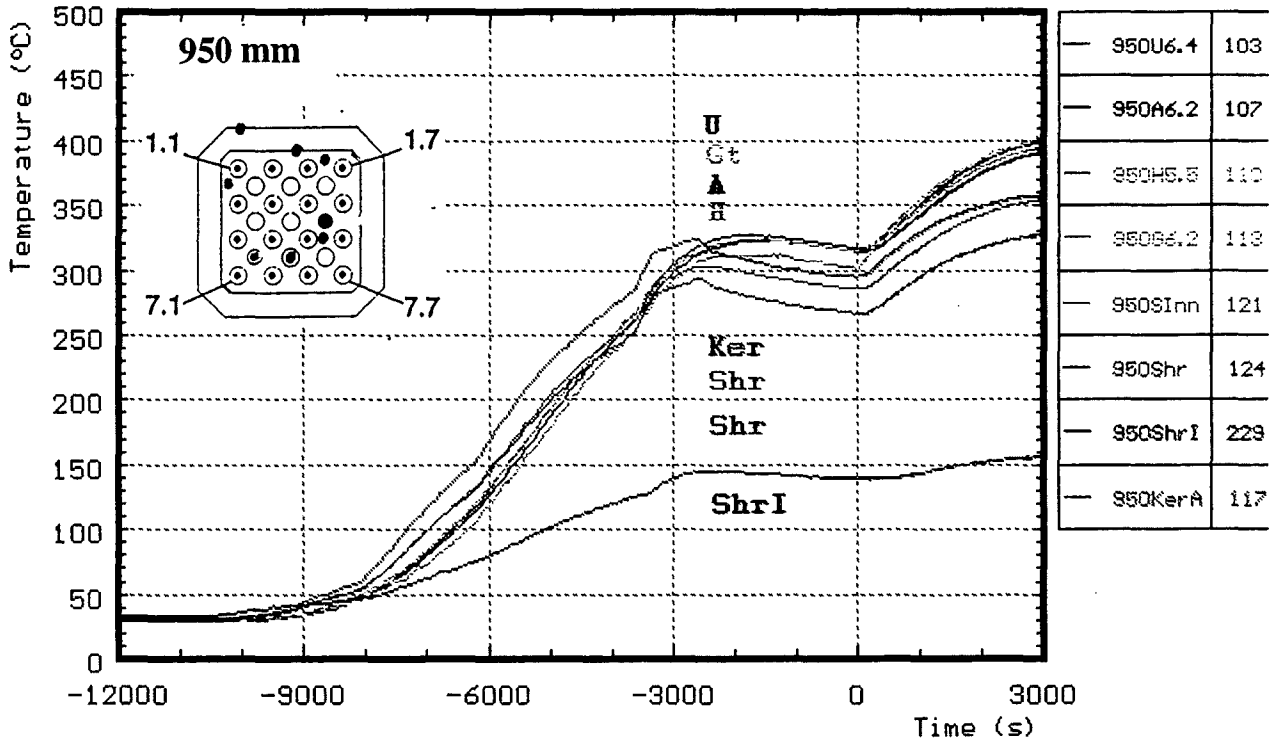

H : Heated rods
U : Unheated rods
Gt : Guide tube
A : In Absorber

Shr : On shroud
Shrl : Shroud insulation
ker : Ceramic protected thermocouples

Fig. A15: CORA-10; Temperatures at elevation given, pre-heat phase (1050-960, 950mm)

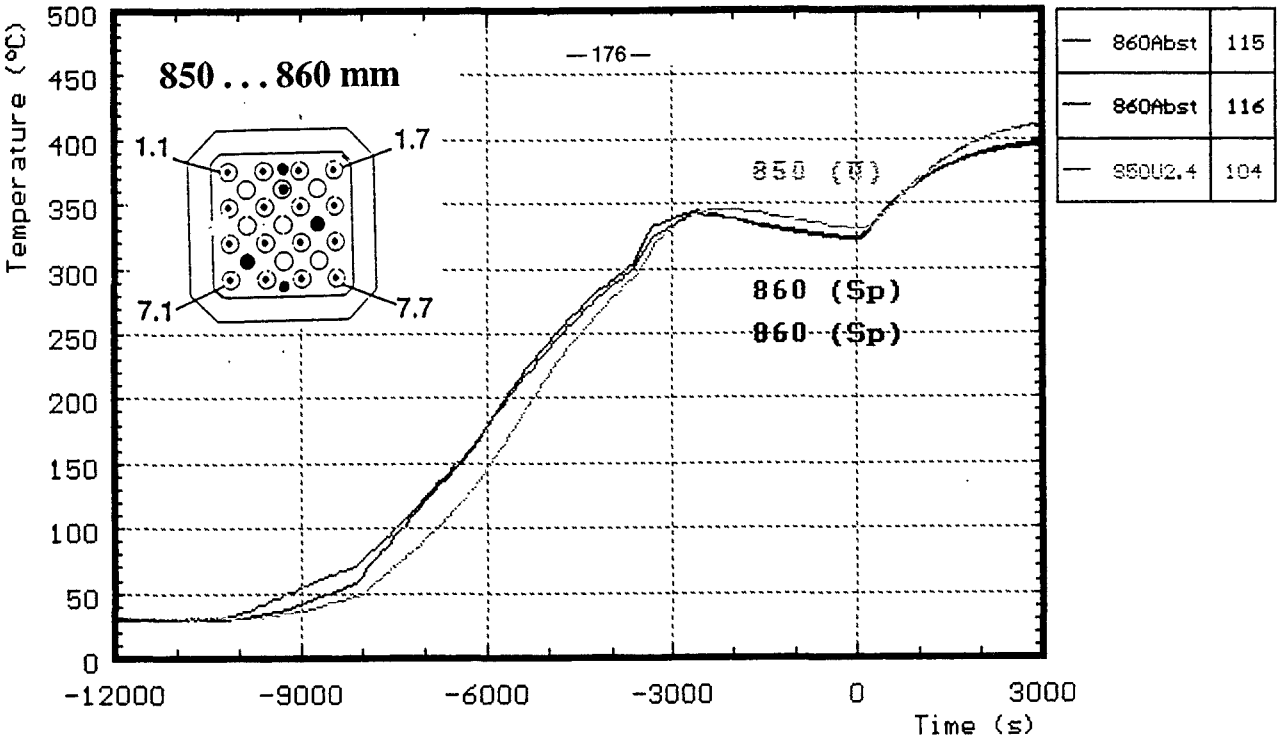

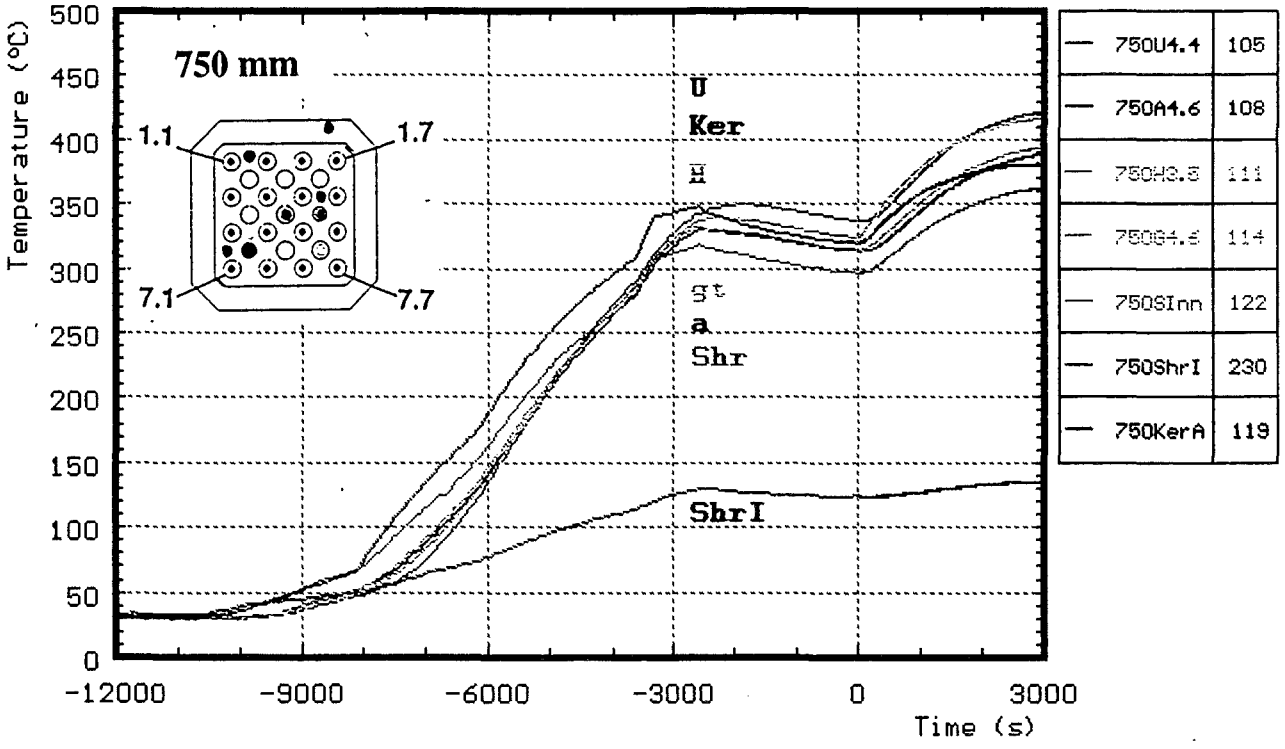

H : Heated rods
U : Unheated rods
Gt : Guide tube
A : In Absorber

Shr : On shroud
Shrl : Shroud insulation
ker : Ceramic protected thermocouples
Sp : Spacer

Fig. A16: CORA-10; Temperatures at elevation given, pre-heat phase (850-860, 750mm)

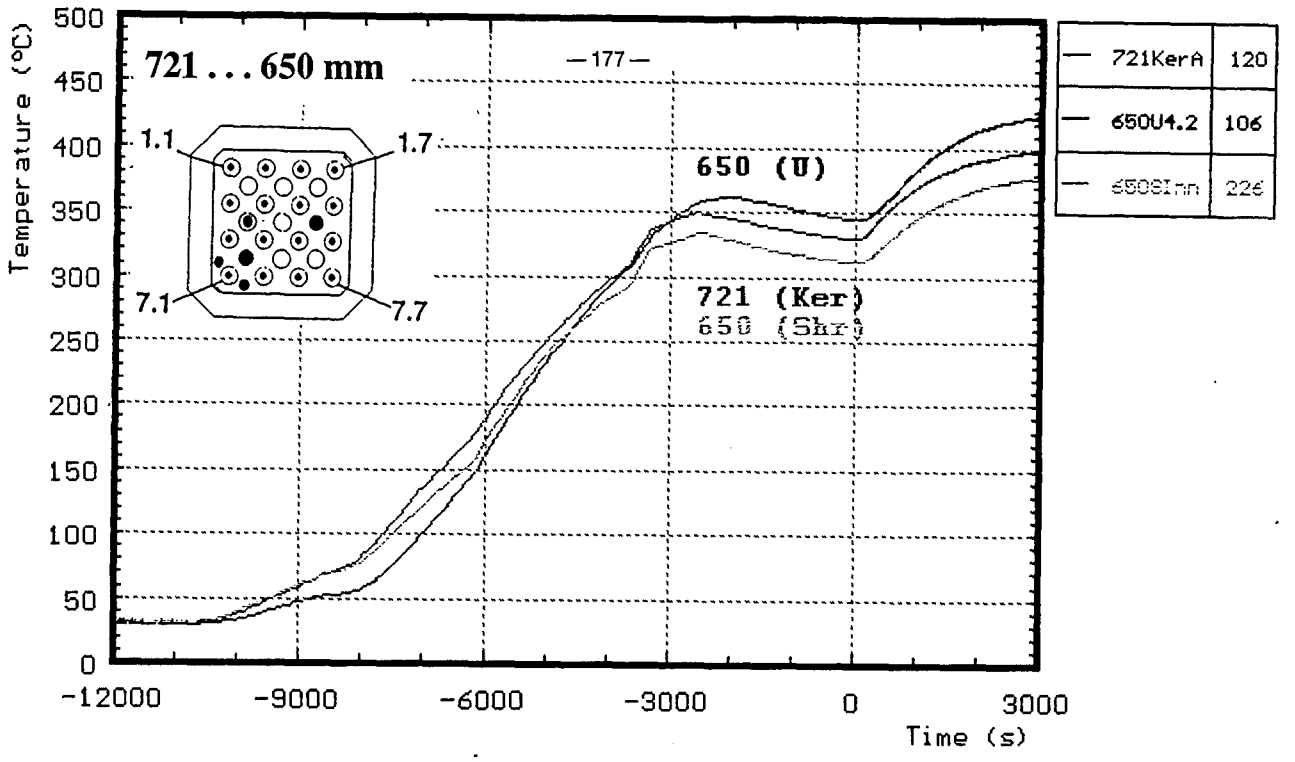

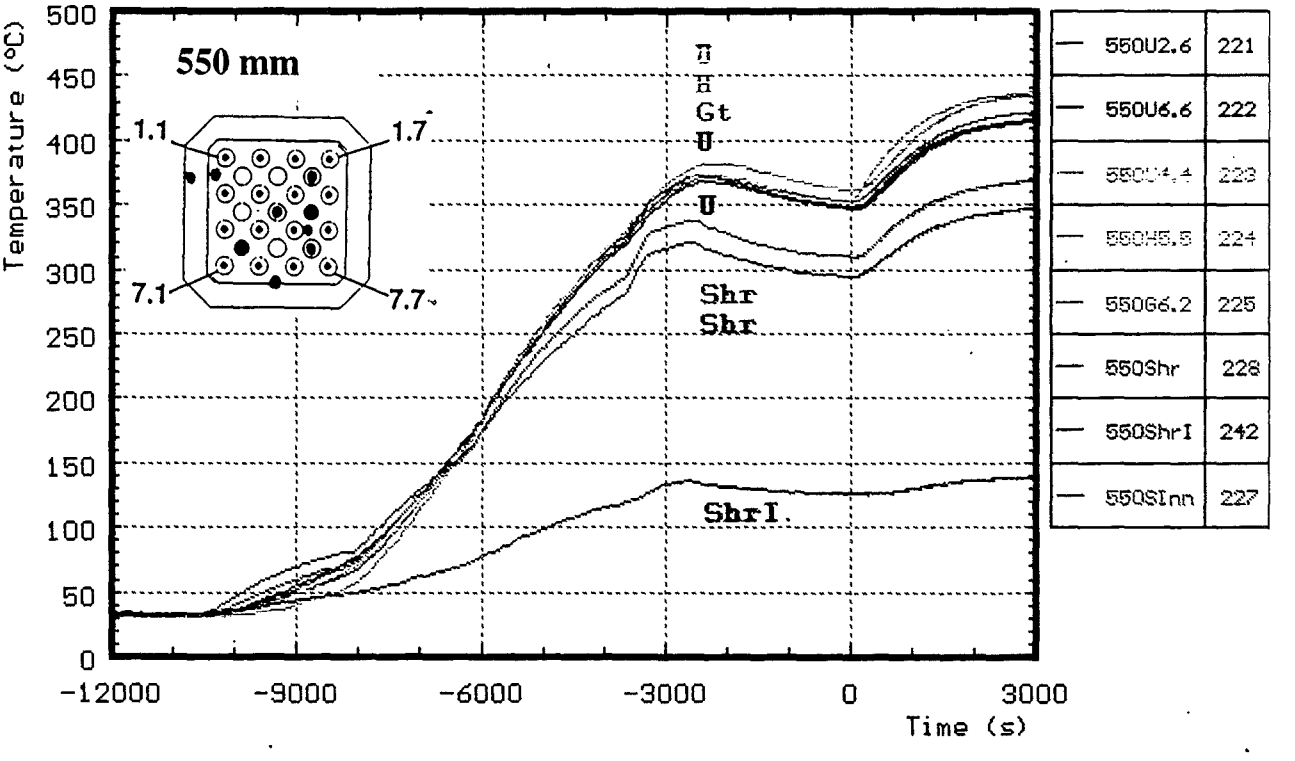

H : Heated rods
U : Unheated rods
Gt : Guide tube

Shr : On shroud
Shrl : Shroud insulation
Ker : Ceramic protected thermocouples

Fig. A17: CORA-10; Temperatures at elevation given, pre-heat phase (721-650, 550mm)

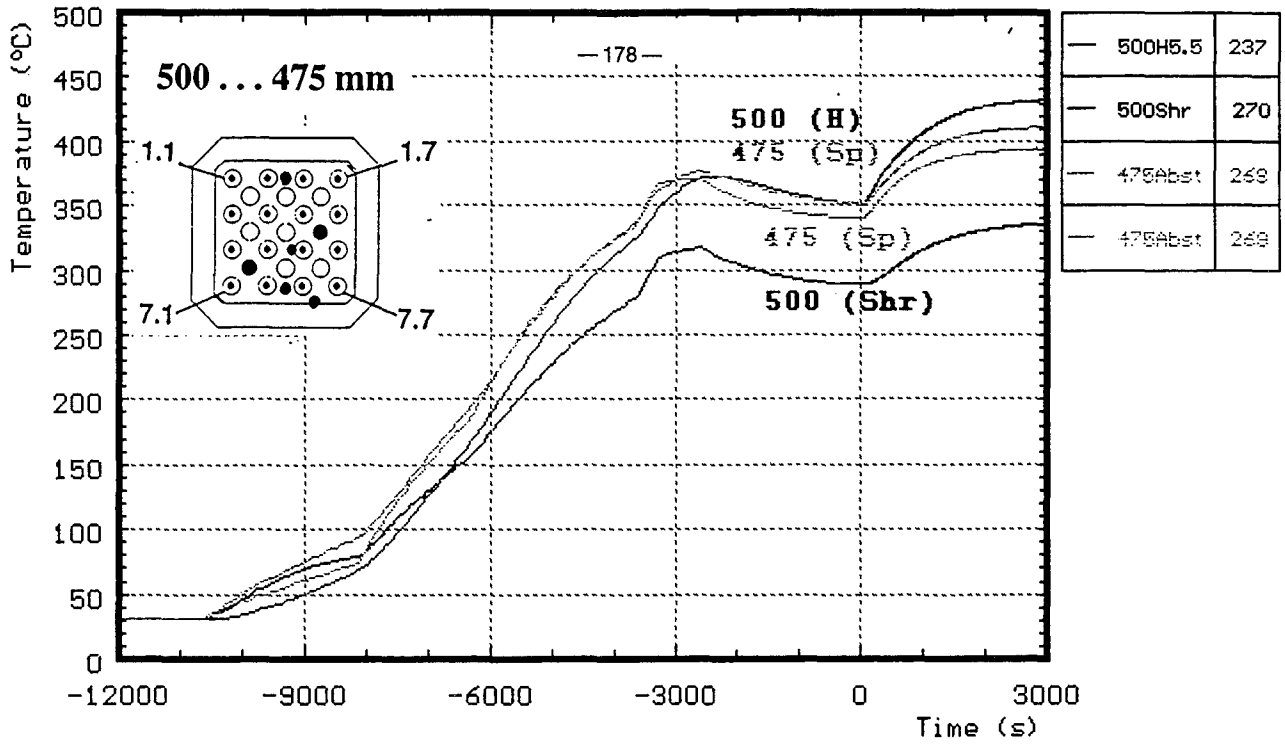

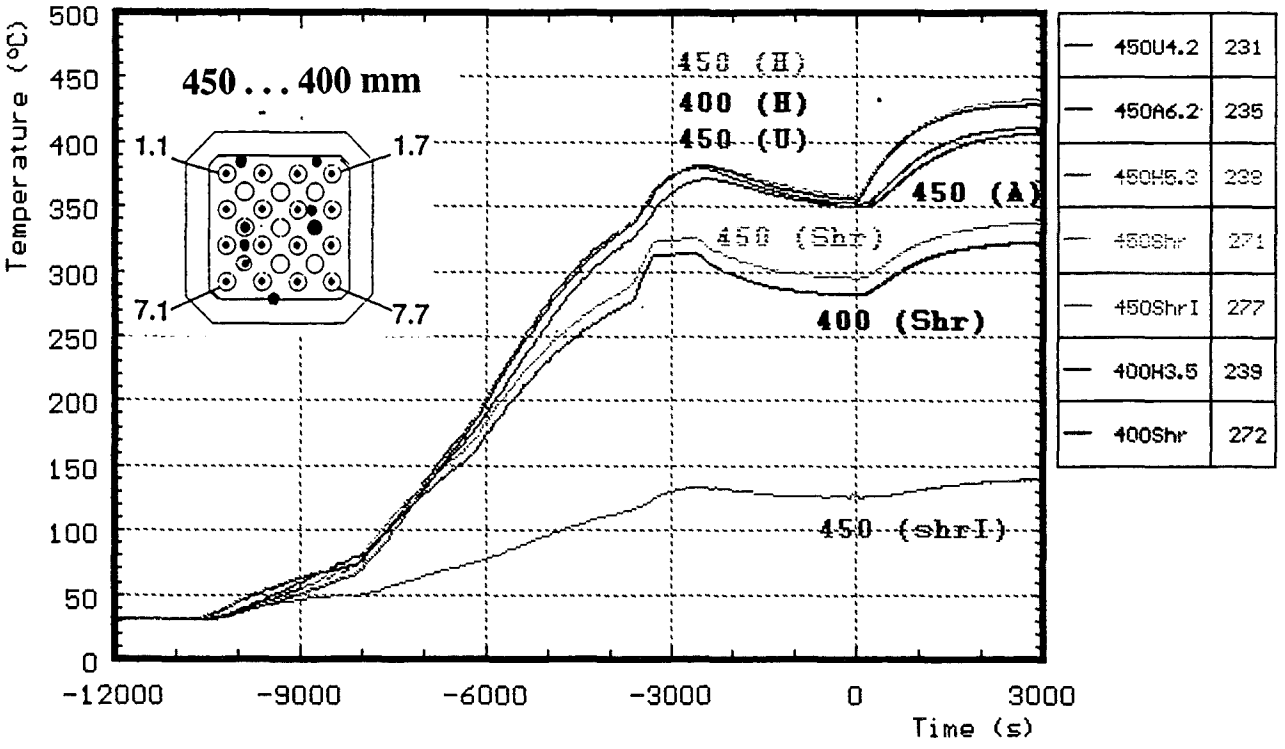

H : Heated rods
U : Unheated rods
Sp : Spacer

Shr : On shroud
Shrl : Shroud insulation
A : In absorber

Fig. A18: CORA-10; Temperatures at elevation given, pre-heat phase (500-475, 450-400mm)

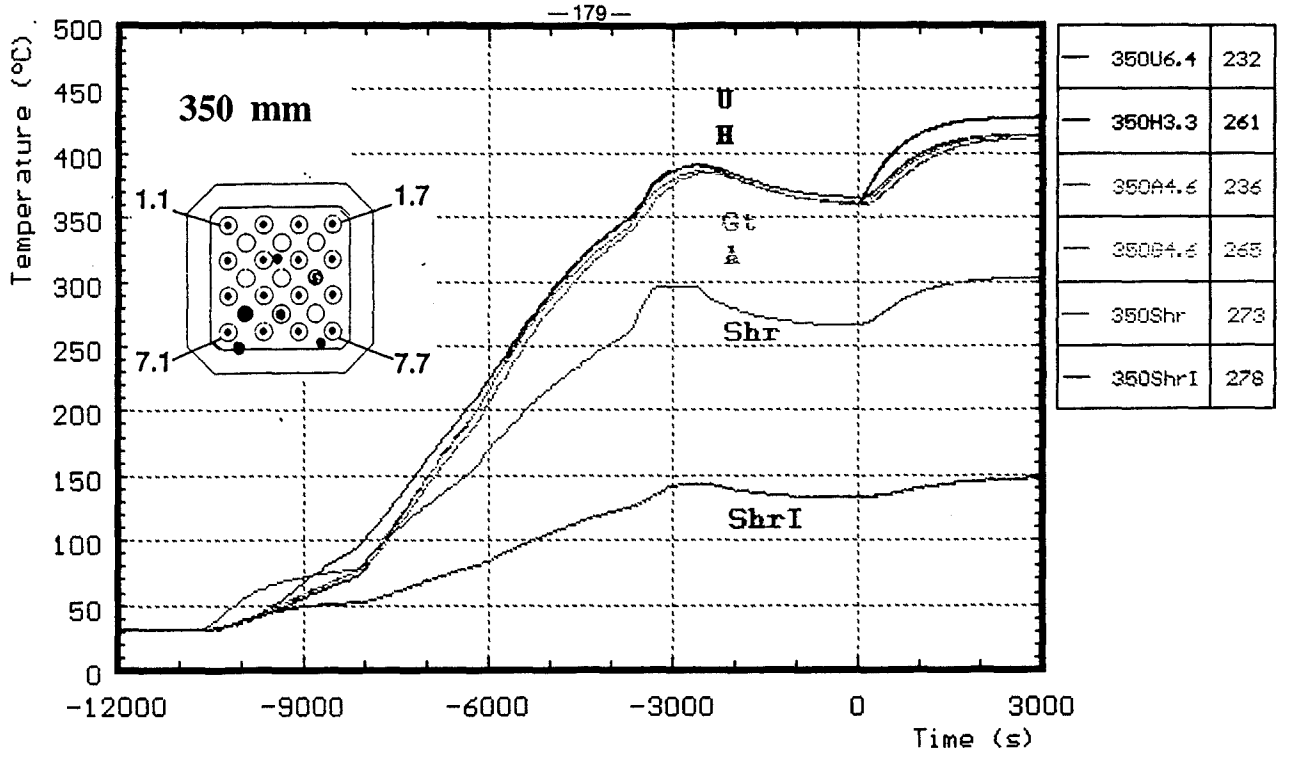

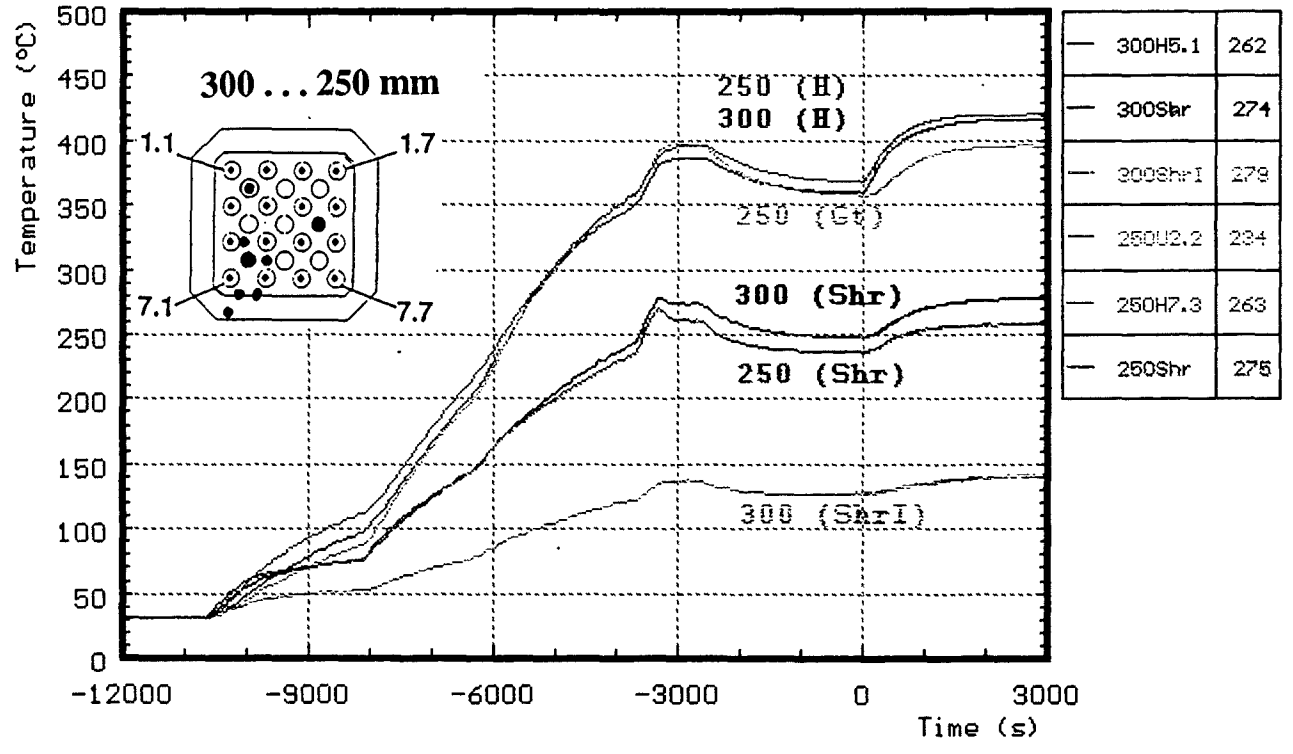

H : Heated rods
U : Unheated rods
Gt : Guide tube

Shr : On shroud
Shrl : Shroud insulation
A : In absorber

Fig. A19: CORA-10; Temperatures at elevation given, pre-heat phase (350, 300-250mm)

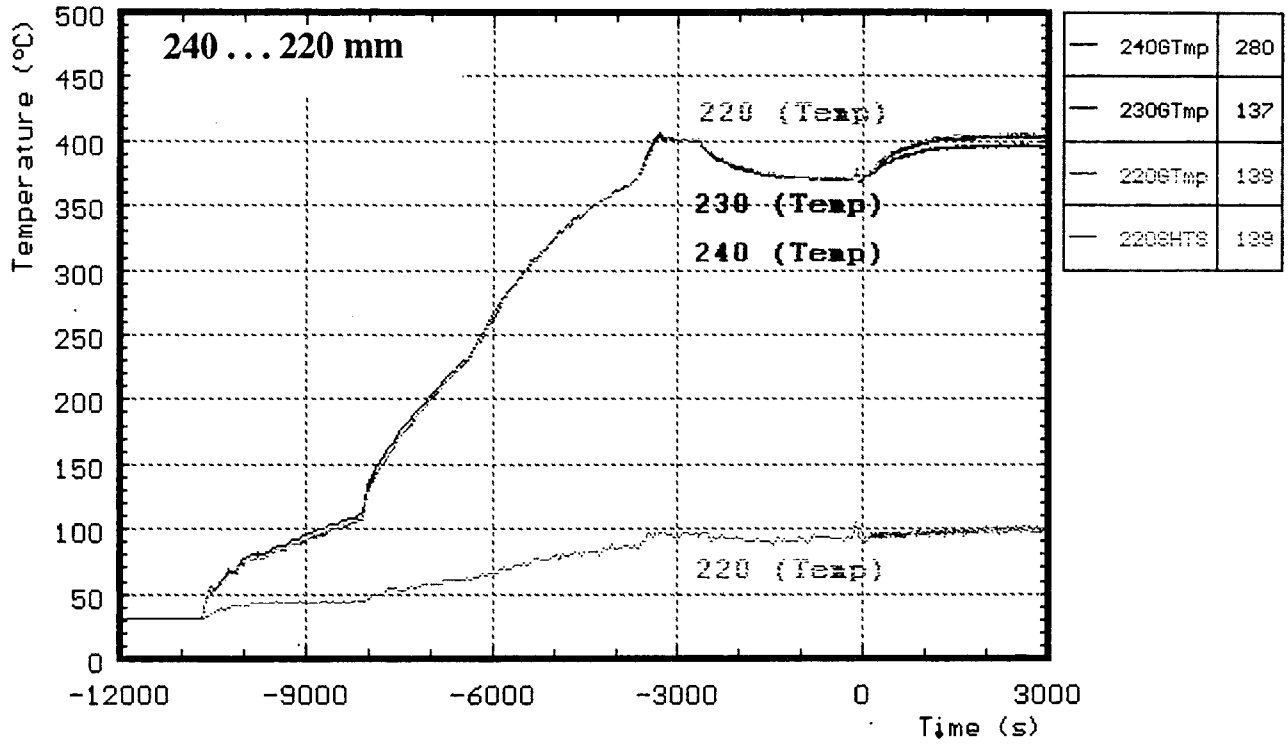

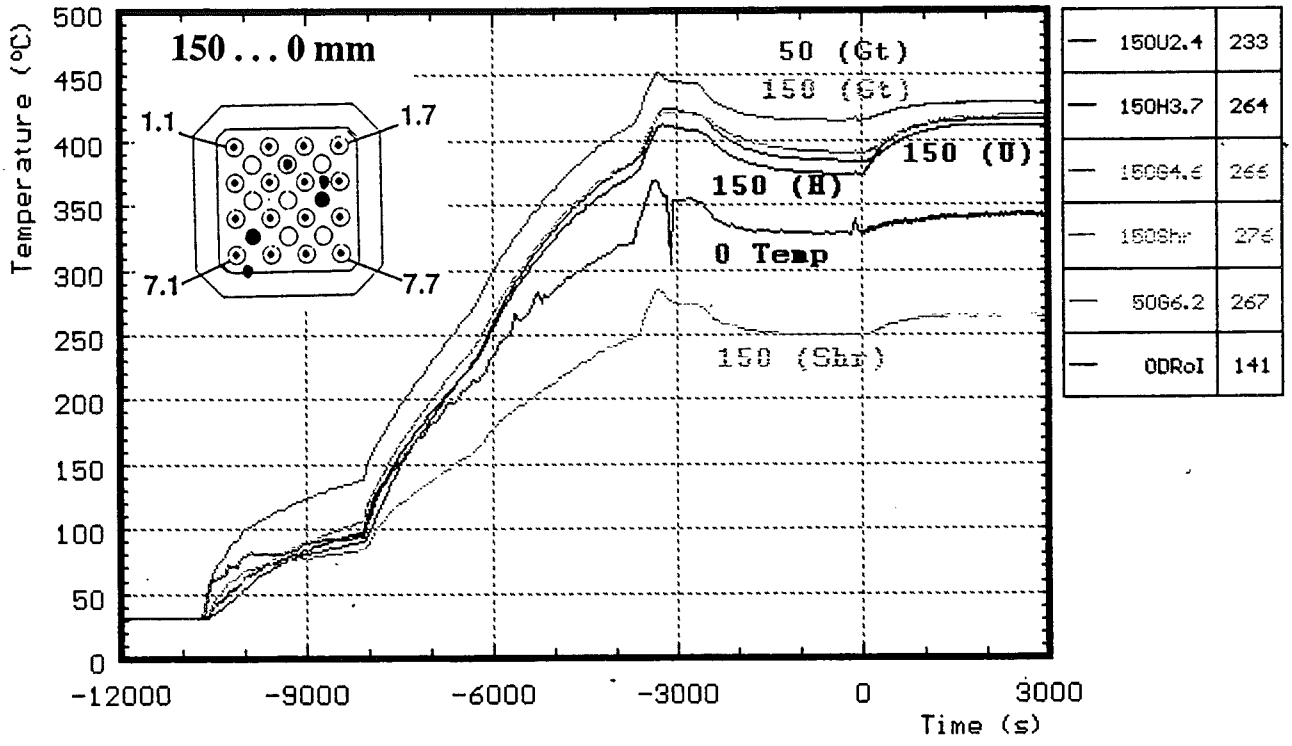

H : Heated rods
U : Unheated rods
Gt : Guide tube

Shr : On shroud
Temp : Between bundle and shroud

Fig. A20: CORA-10; Temperatures at elevation given, pre-heat phase (240-220, 150-0mm)

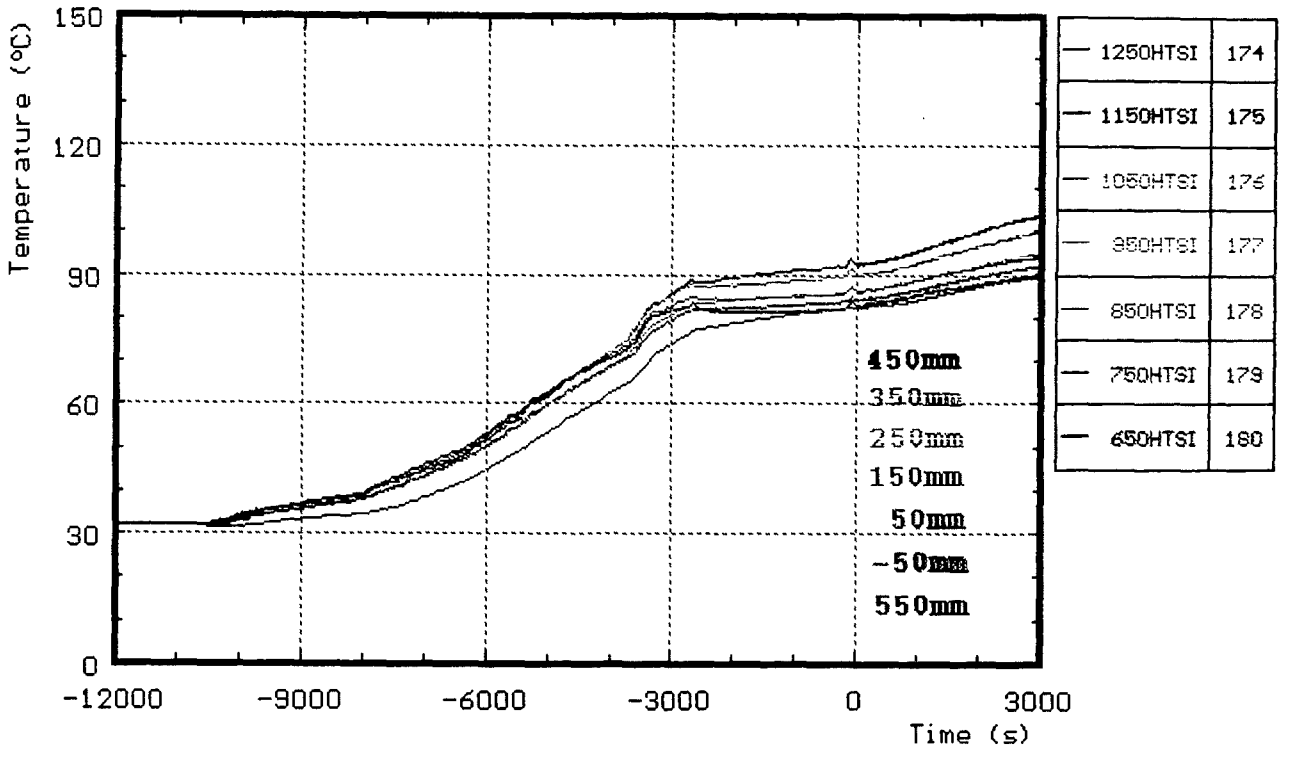

Fig. A21: CORA-10; Temperatures of HTS, pre-heat phase, inner surface at 153mm radius

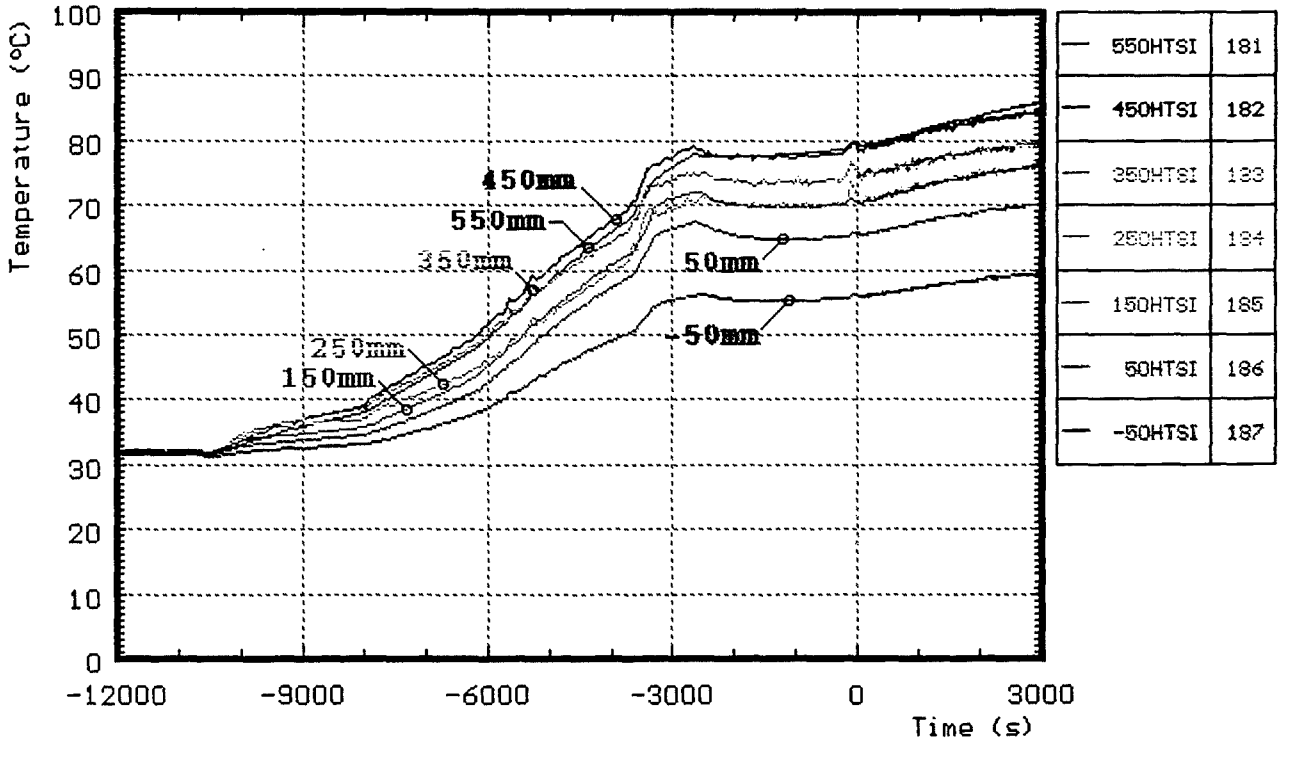

Fig. A22: CORA-10; Temperatures of HTS, pre-heat phase, inner surface at 153mm radius

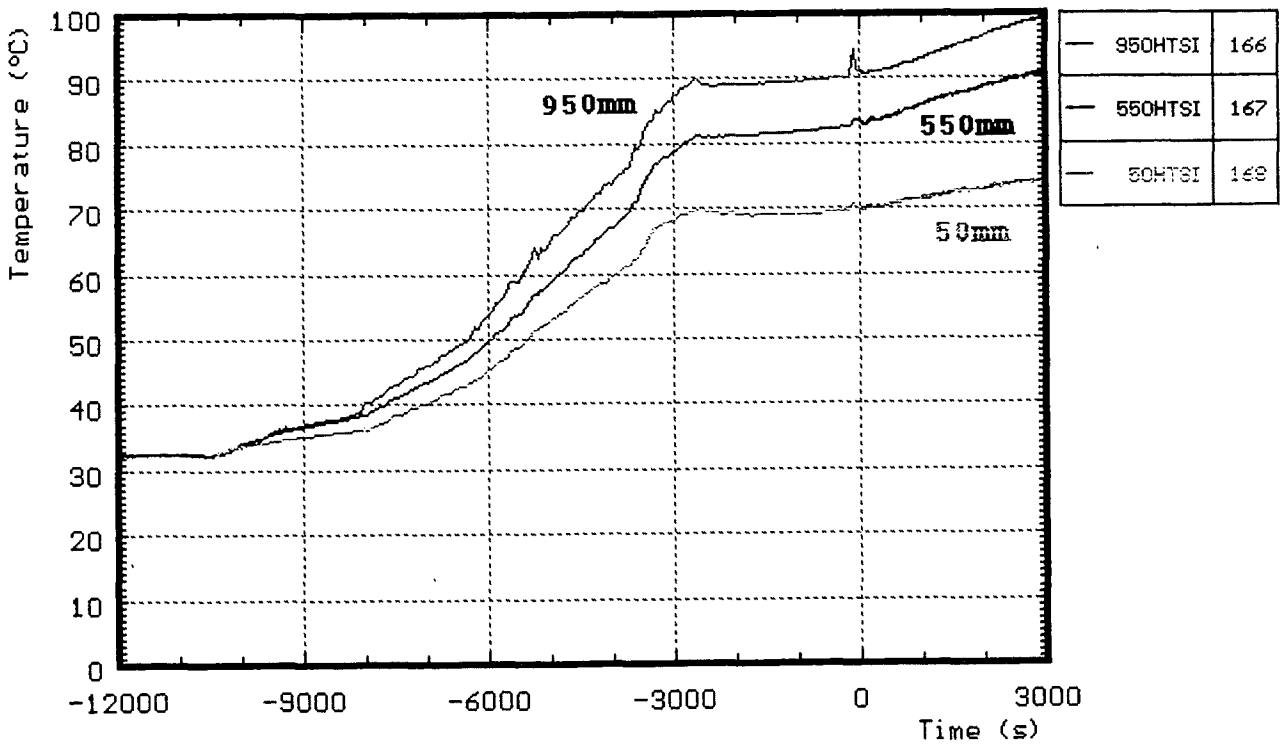

Fig. A23: CORA-10; Temperatures of HTS, pre-heat phase, inner surface at 153mm radius

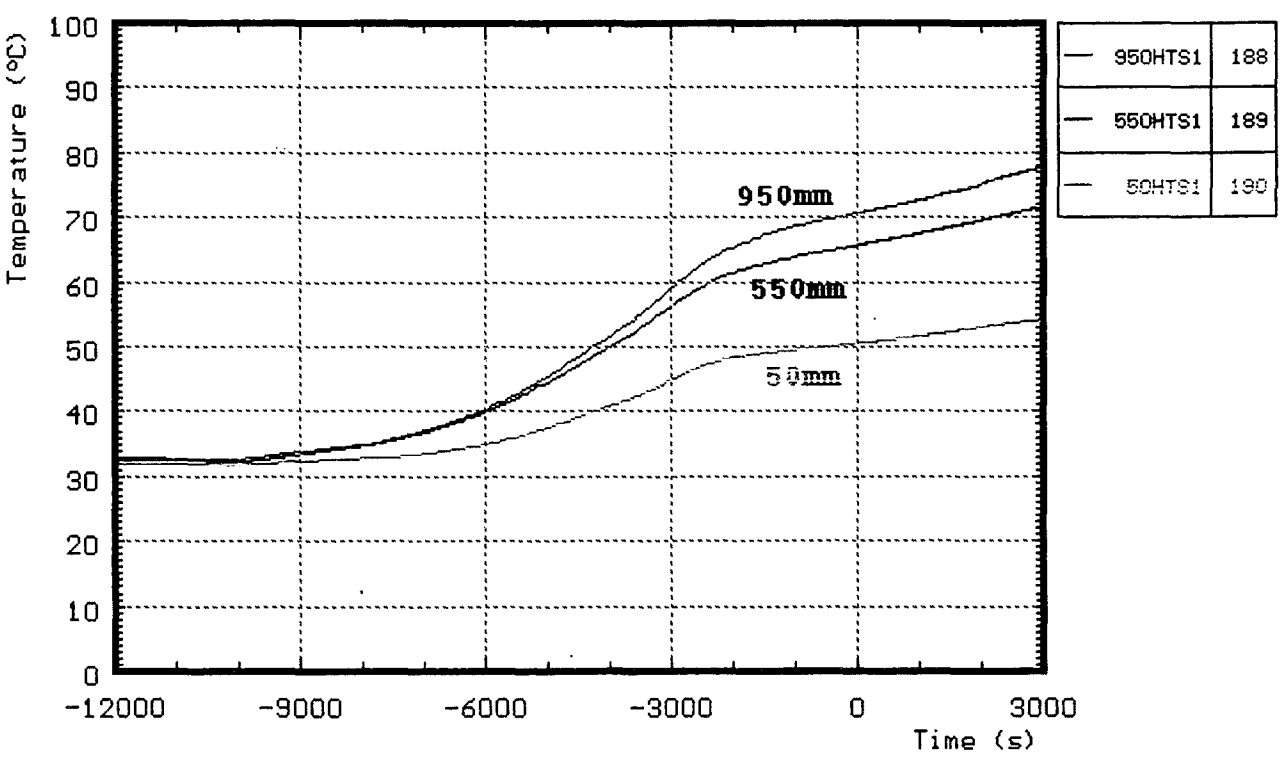

Fig. A24: CORA-10; Temperatures of HTS, pre-heat phase, at 192mm radius

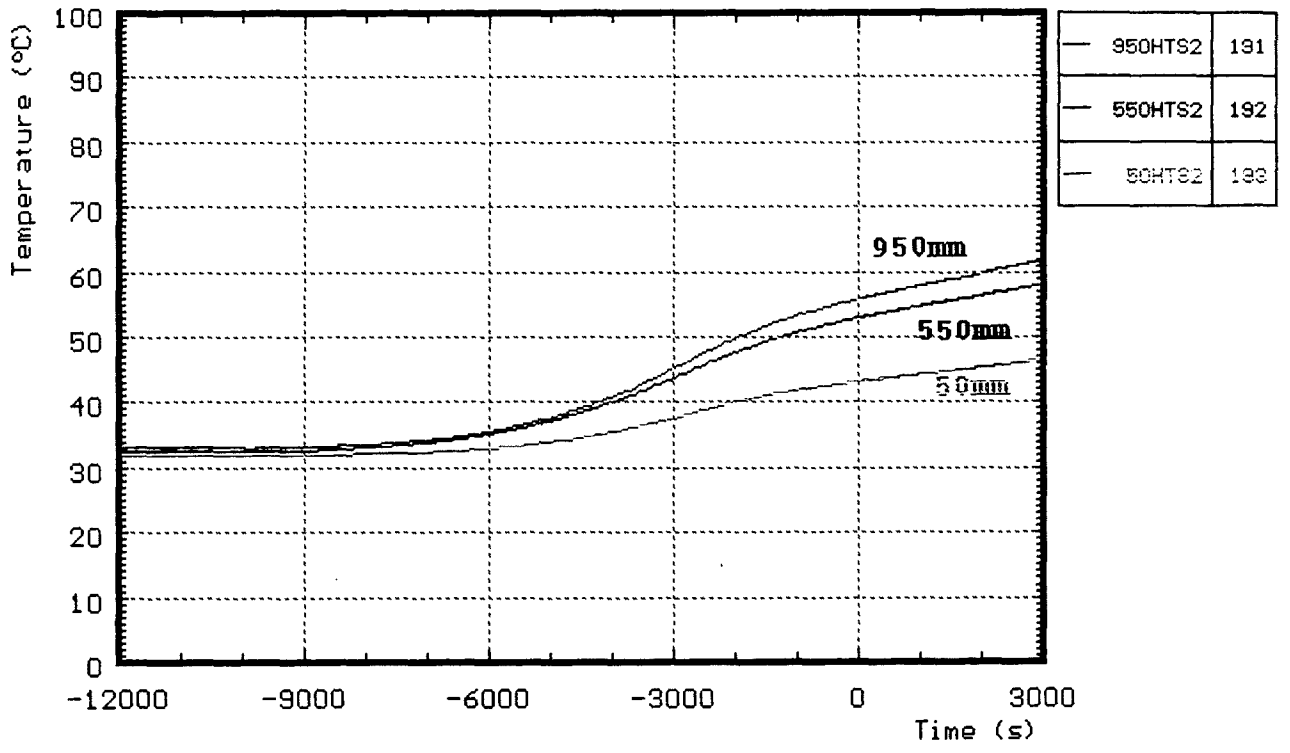

Fig. A25: CORA-10; Temperatures of HTS, pre-heat phase, at 192mm radius

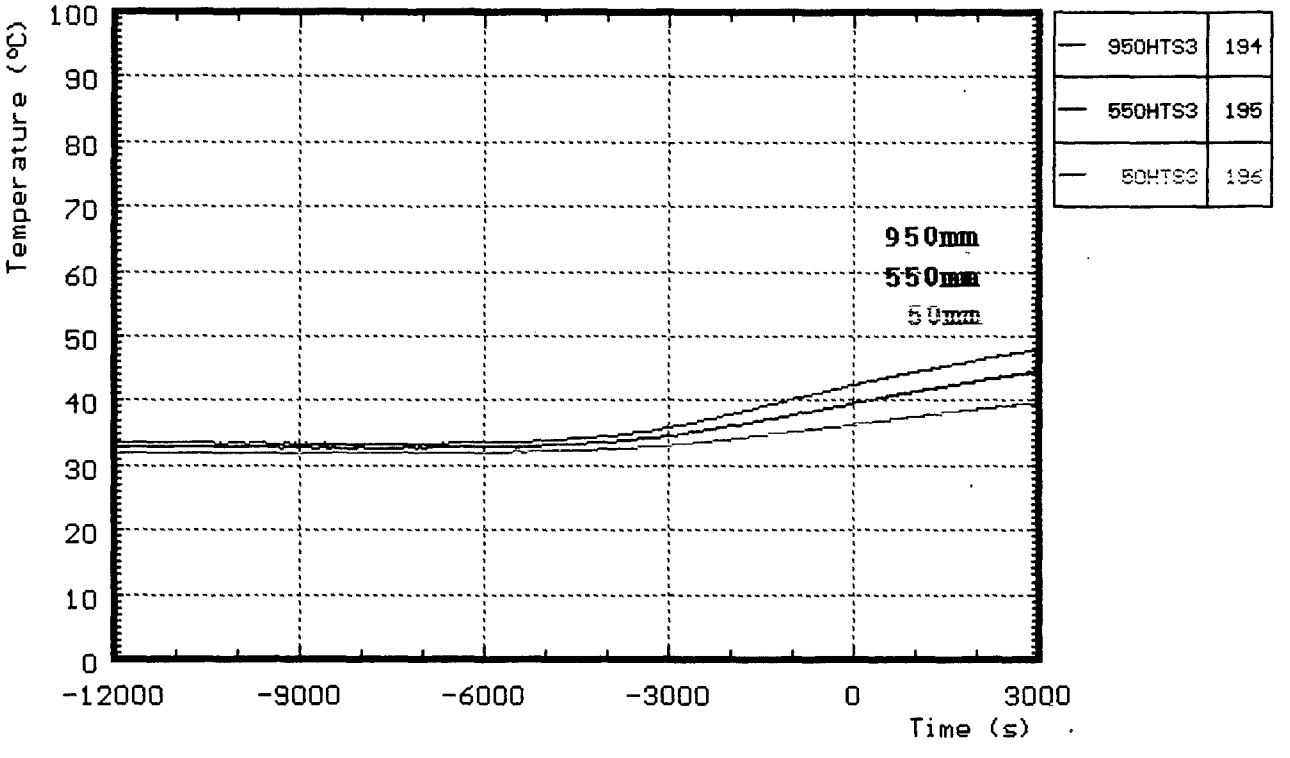

Fig. A26: CORA-10; Temperatures of HTS, pre-heat phase, at 255mm radius

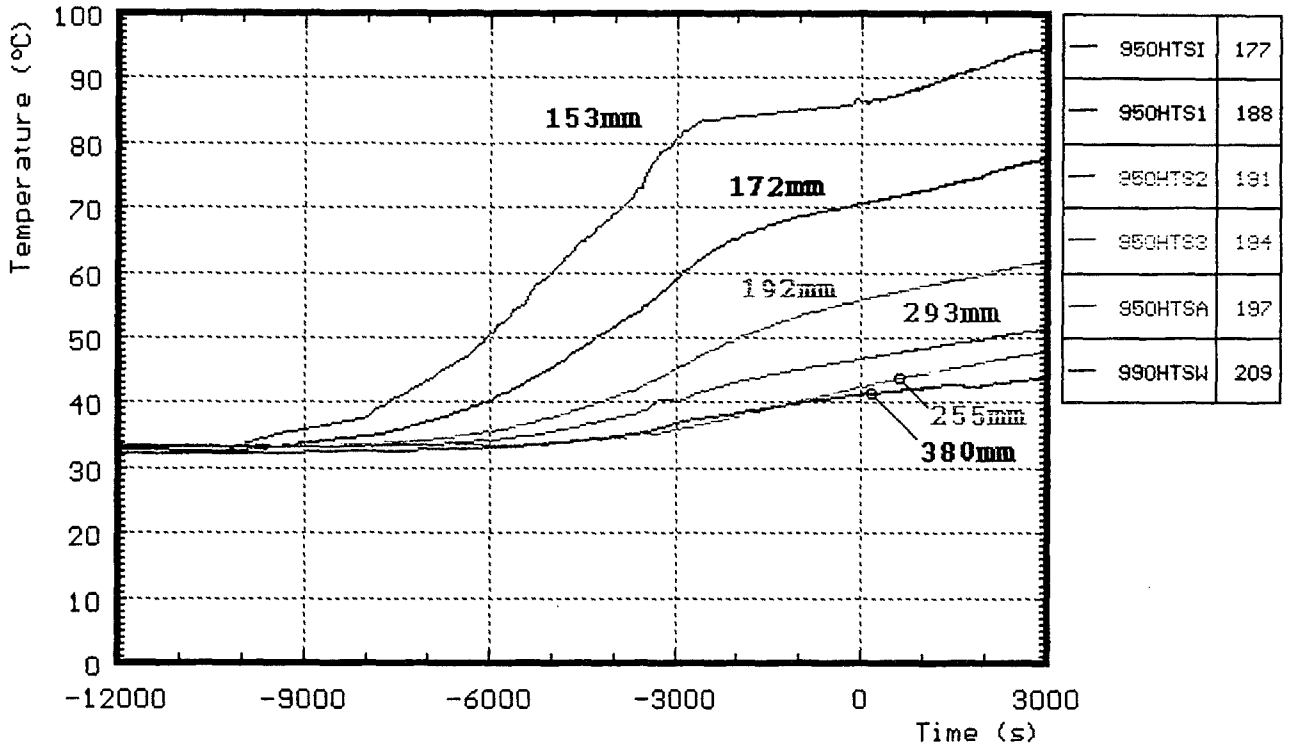

Fig. A27: CORA-10; Temperatures of HTS, pre-heat phase, at 950mm radius

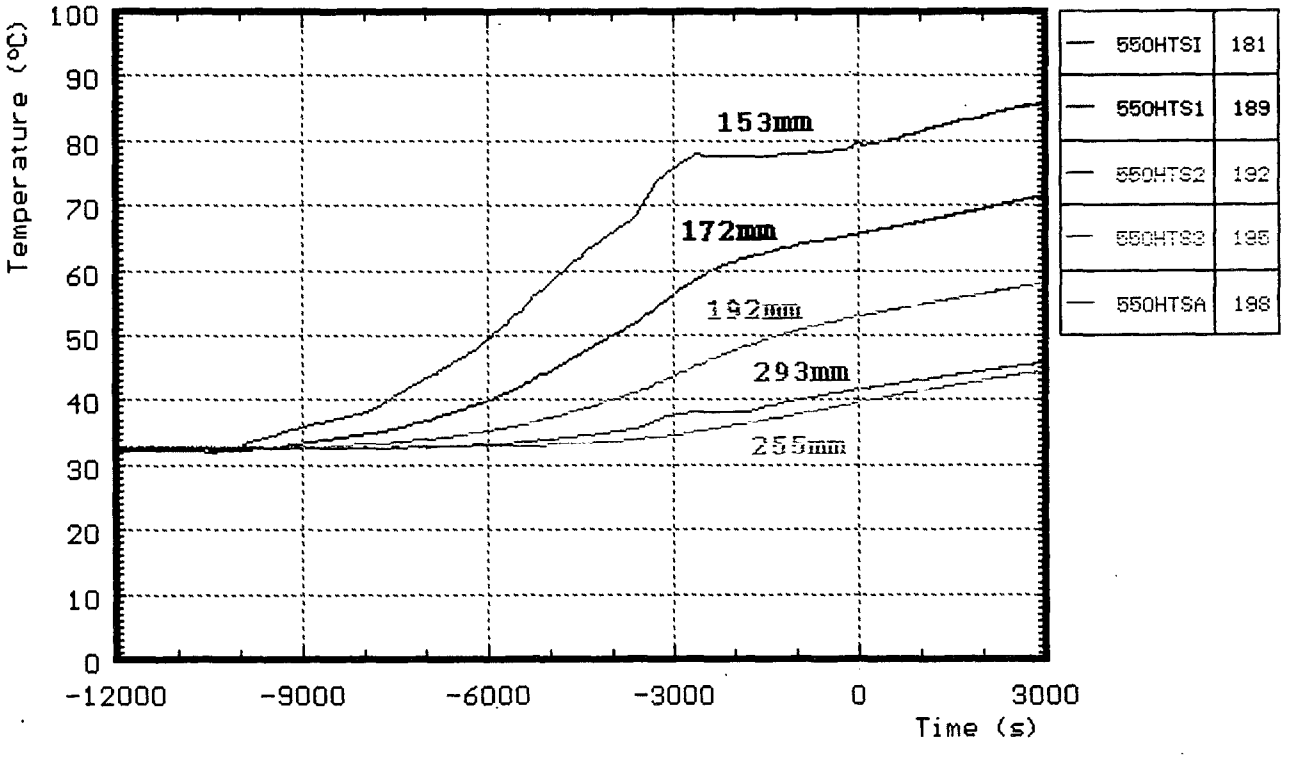

Fig. A28: CORA-10; Temperatures of HTS, pre-heat phase, at 550mm radius

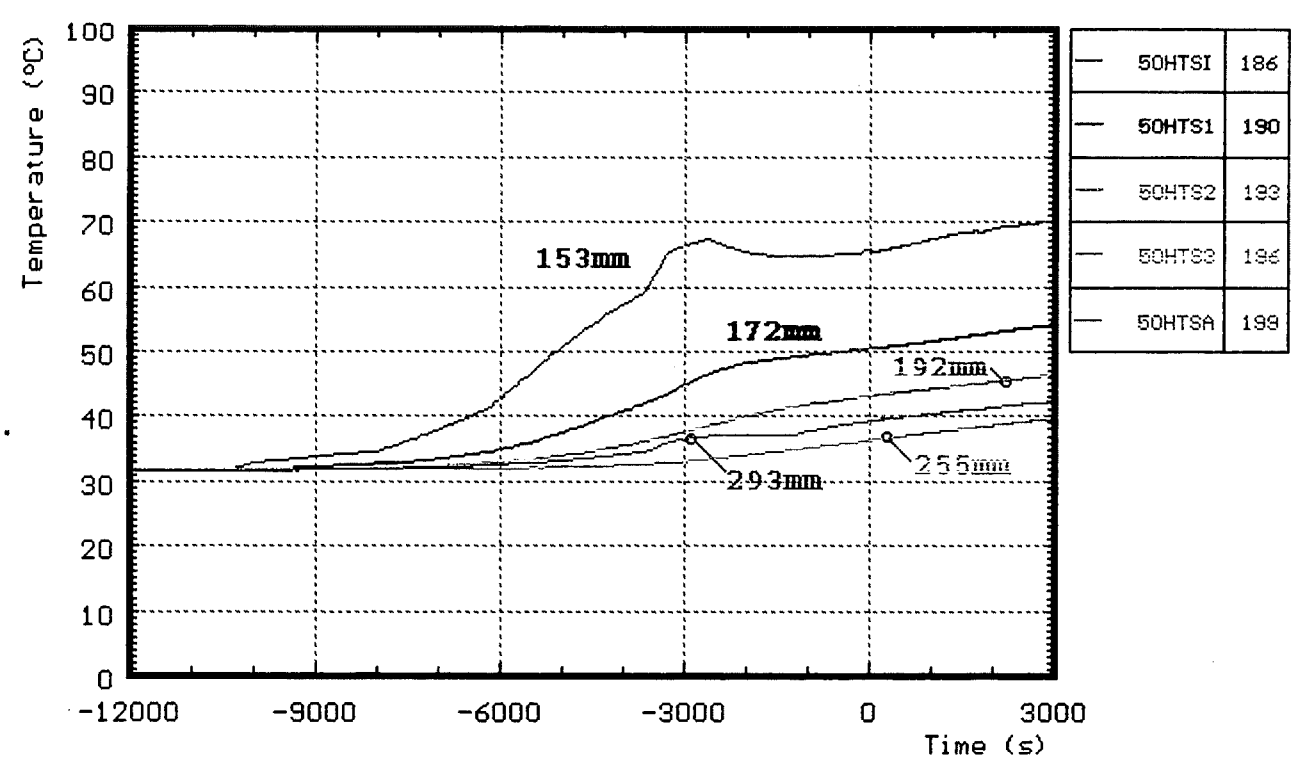

Fig. A29: CORA-10; Temperatures of HTS, pre-heat phase, at 50mm elevation

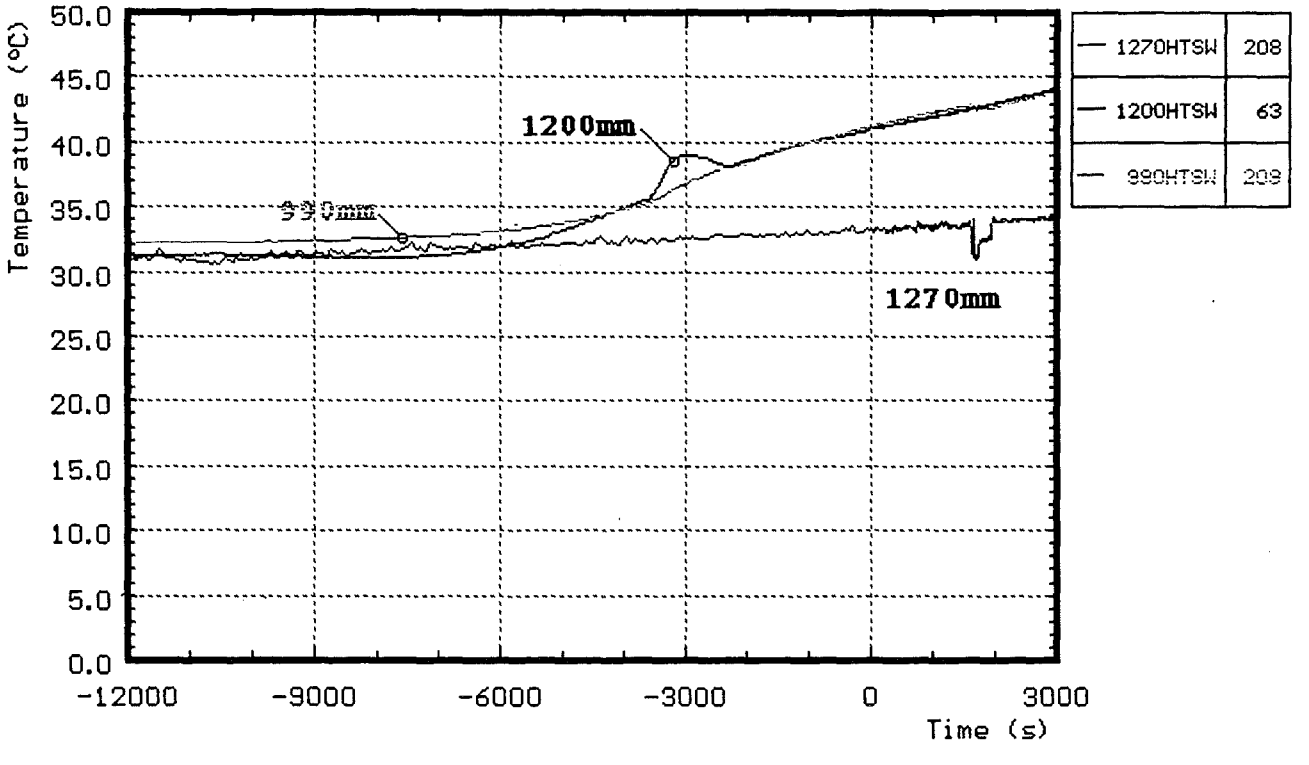

Fig. A30: CORA-10; Temperatures of HTS, pre-heat phase, on outer surface, 380 mm radius

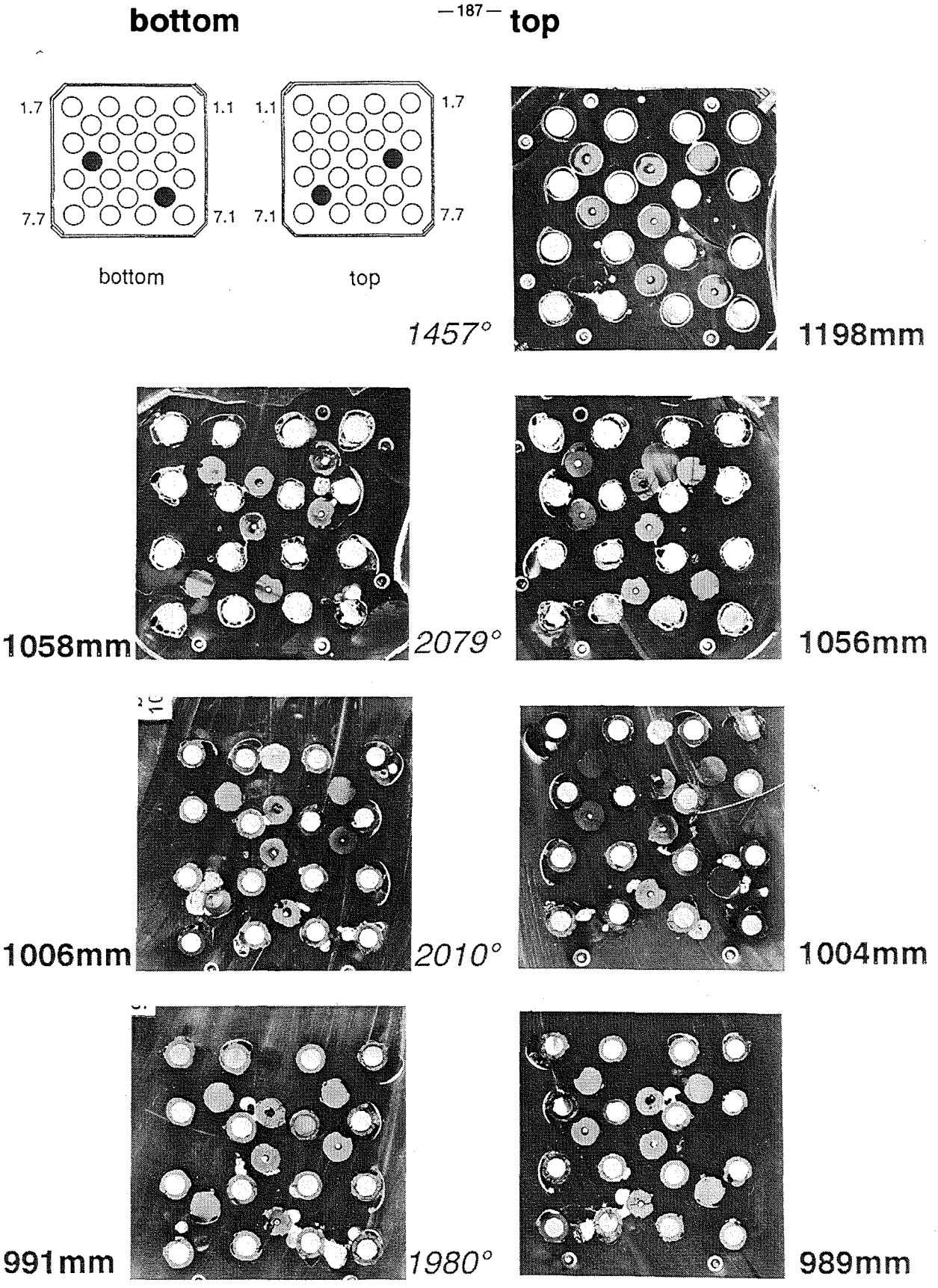

Fig. A31: Horizontal cross sections of bundle CORA-10, 1198 to 989 mm elevation

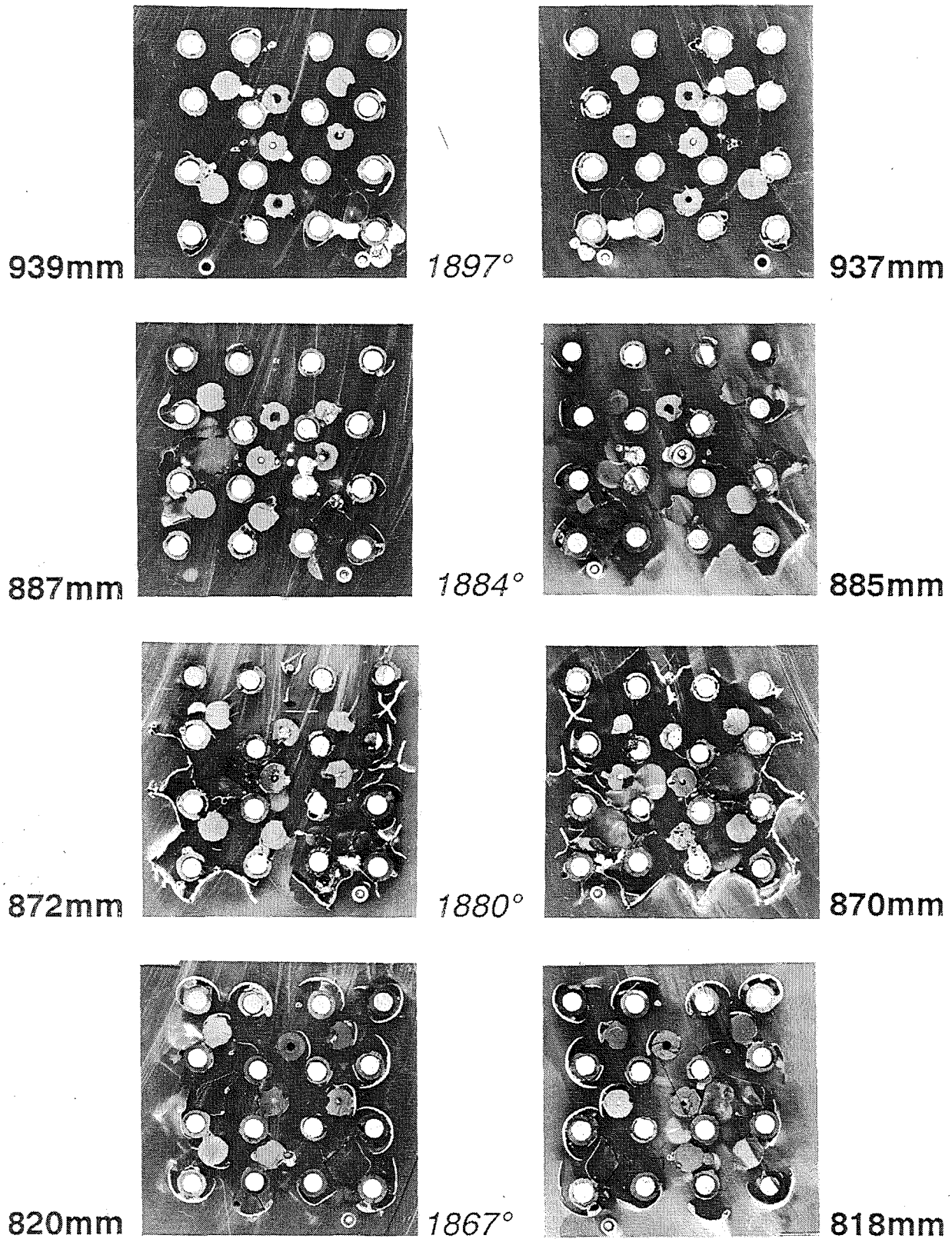

Fig. A32: Horizontal cross sections of bundle CORA-10, 939 to 818 mm elevation

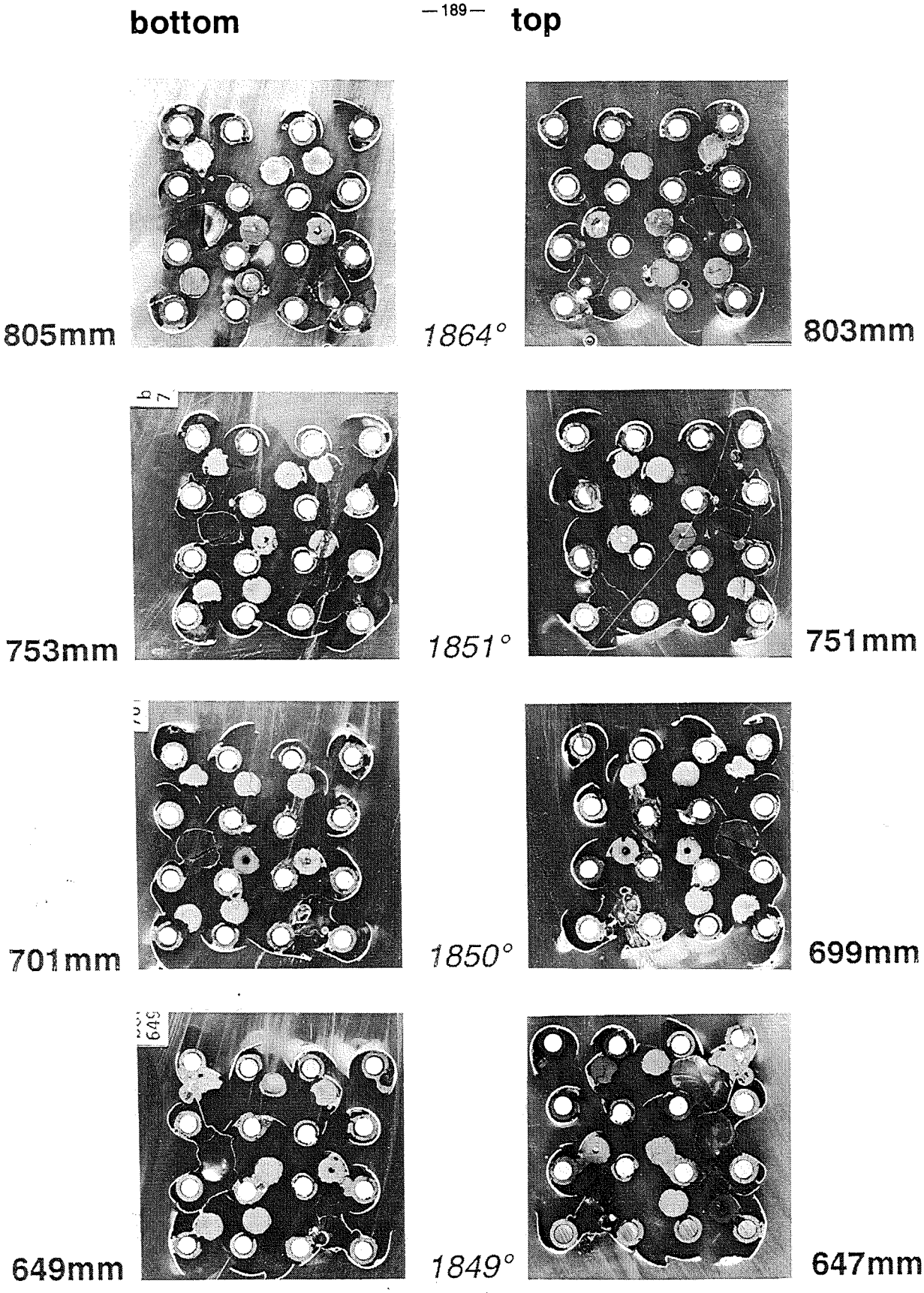

Fig. A33: Horizontal cross sections of bundle CORA-10, 805 to 647 mm elevation

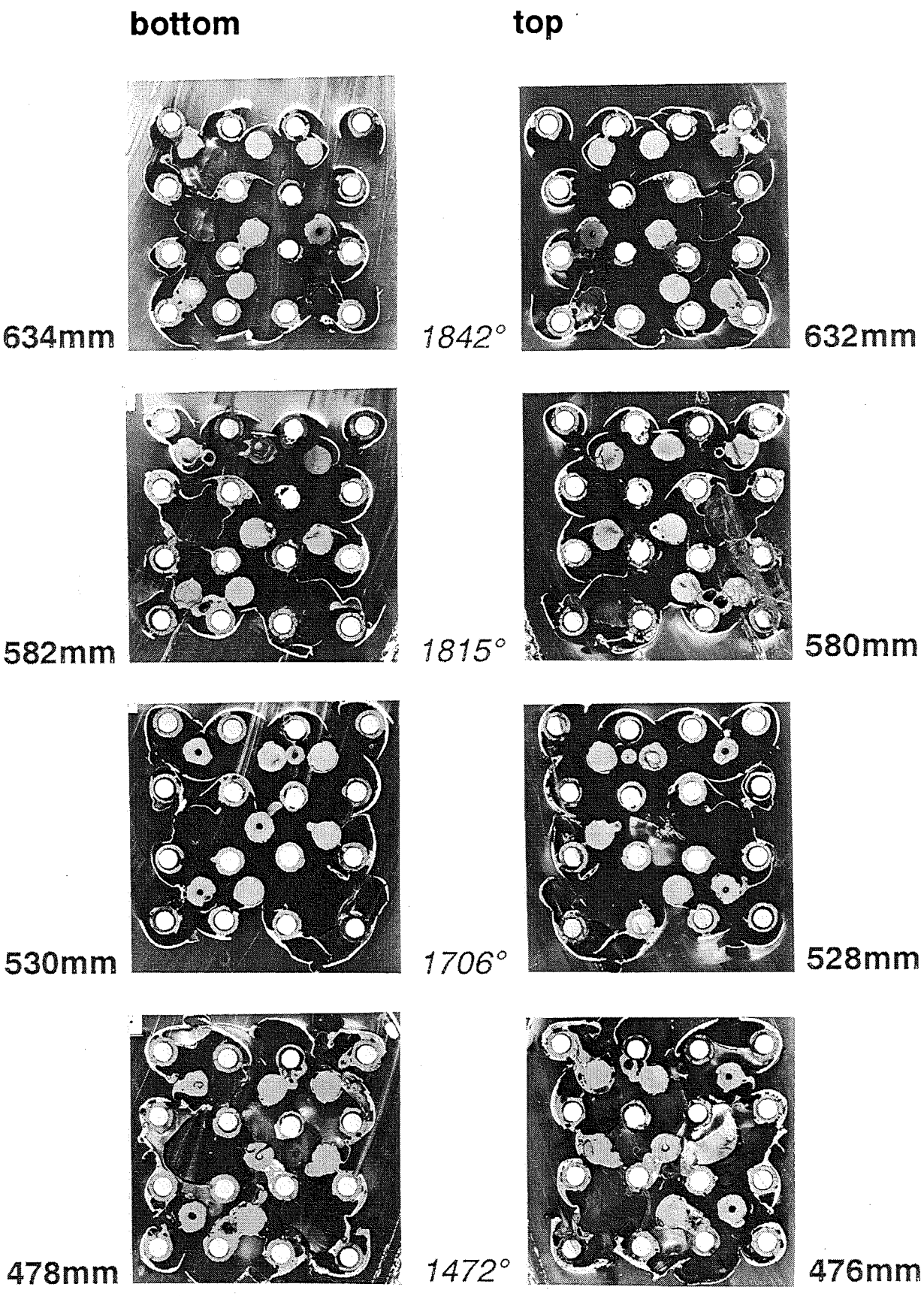

Fig. A34: Horizontal cross sections of bundle CORA-10, 634 to 476 mm elevation

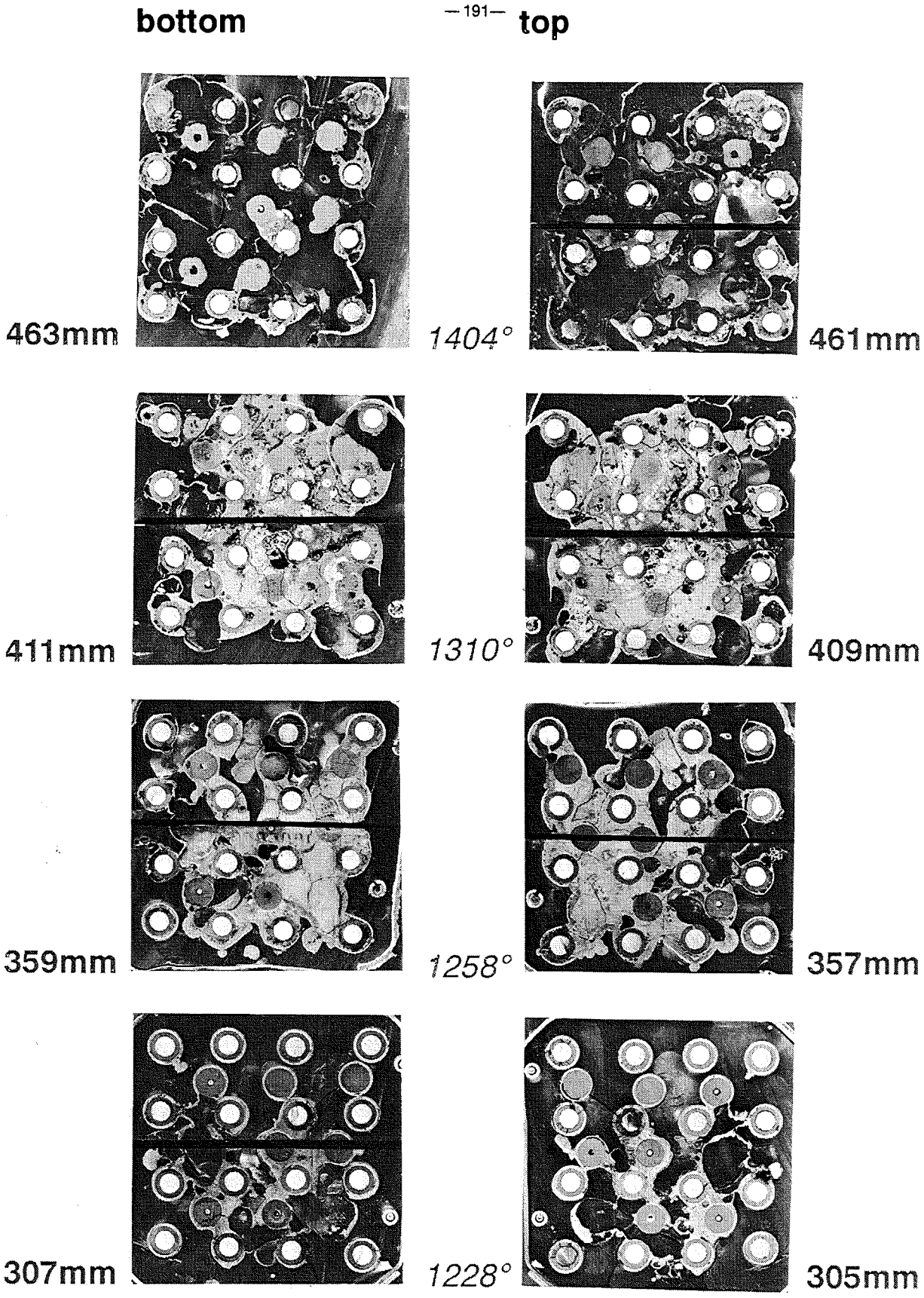

Fig. A35: Horizontal cross sections of bundle CORA-10, 463 to 305 mm elevation

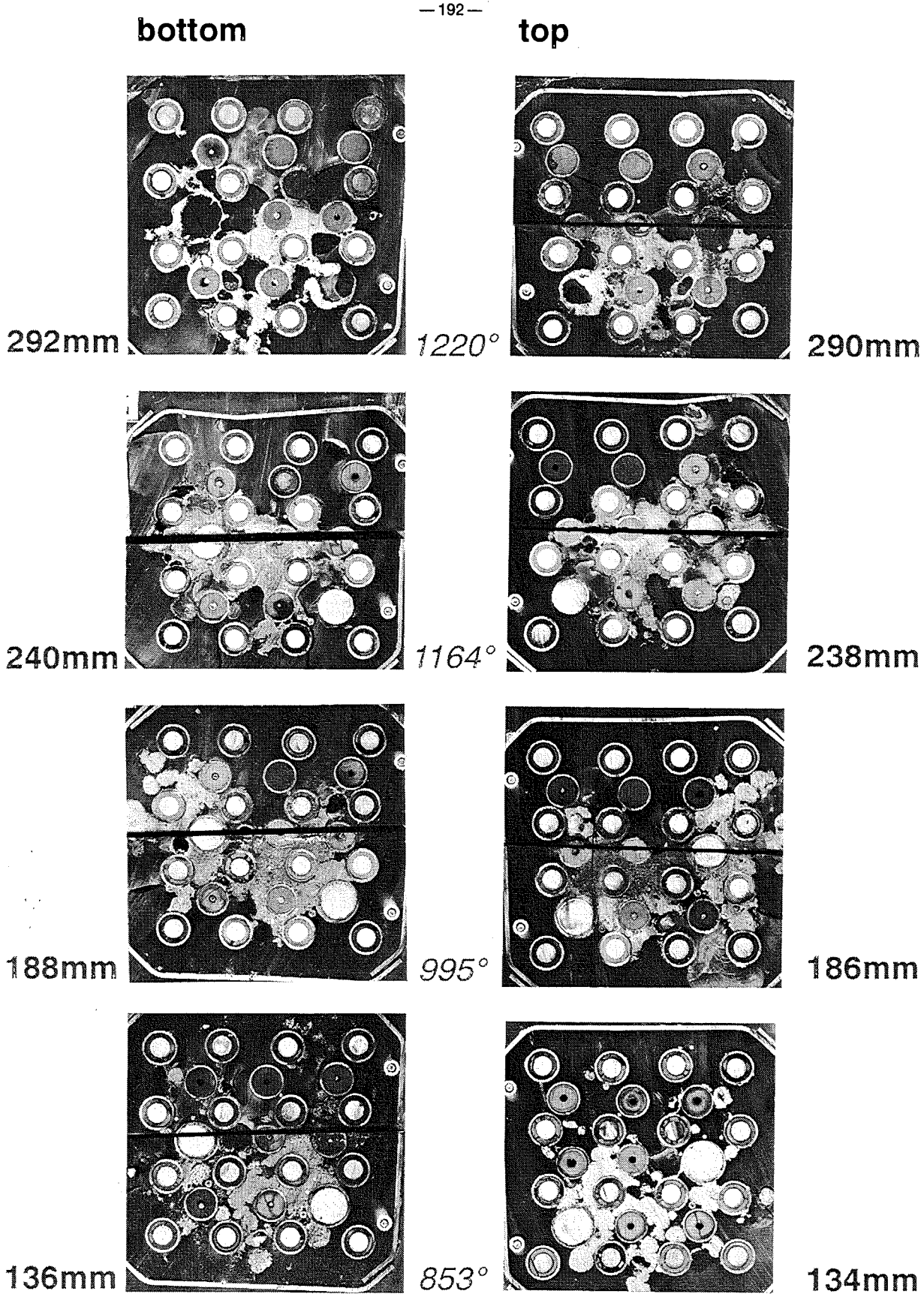

Fig. A36: Horizontal cross sections of bundle CORA-10, 292 to 134 mm elevation

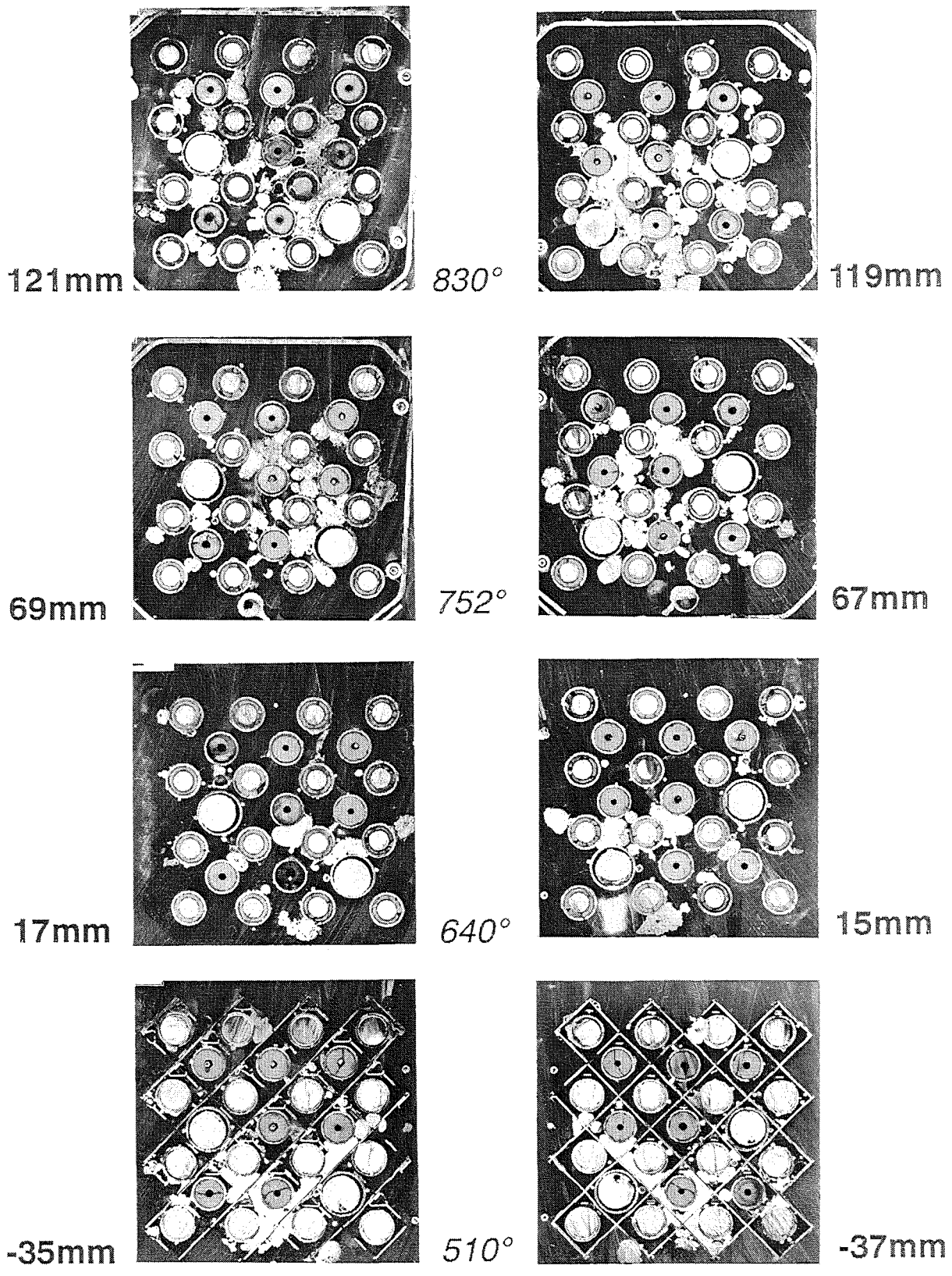

Fig. A37: Horizontal cross sections of bundle CORA-10, 121 to -37 mm elevation

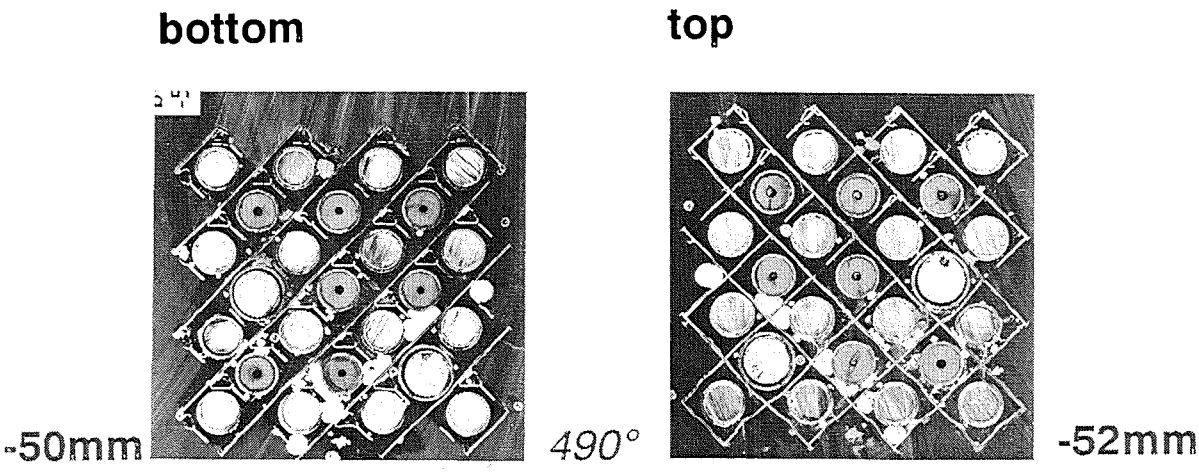

Fig. A38: Horizontal cross sections of bundle CORA-10, -50 to -52 mm elevation

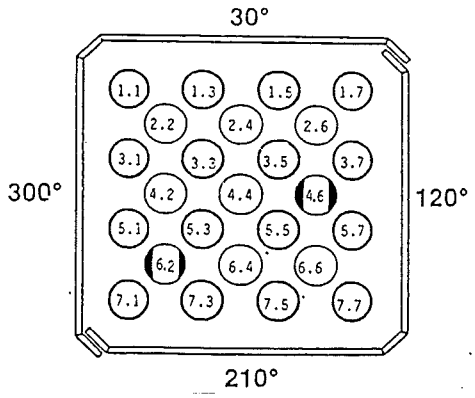

Absorberrod 4.6

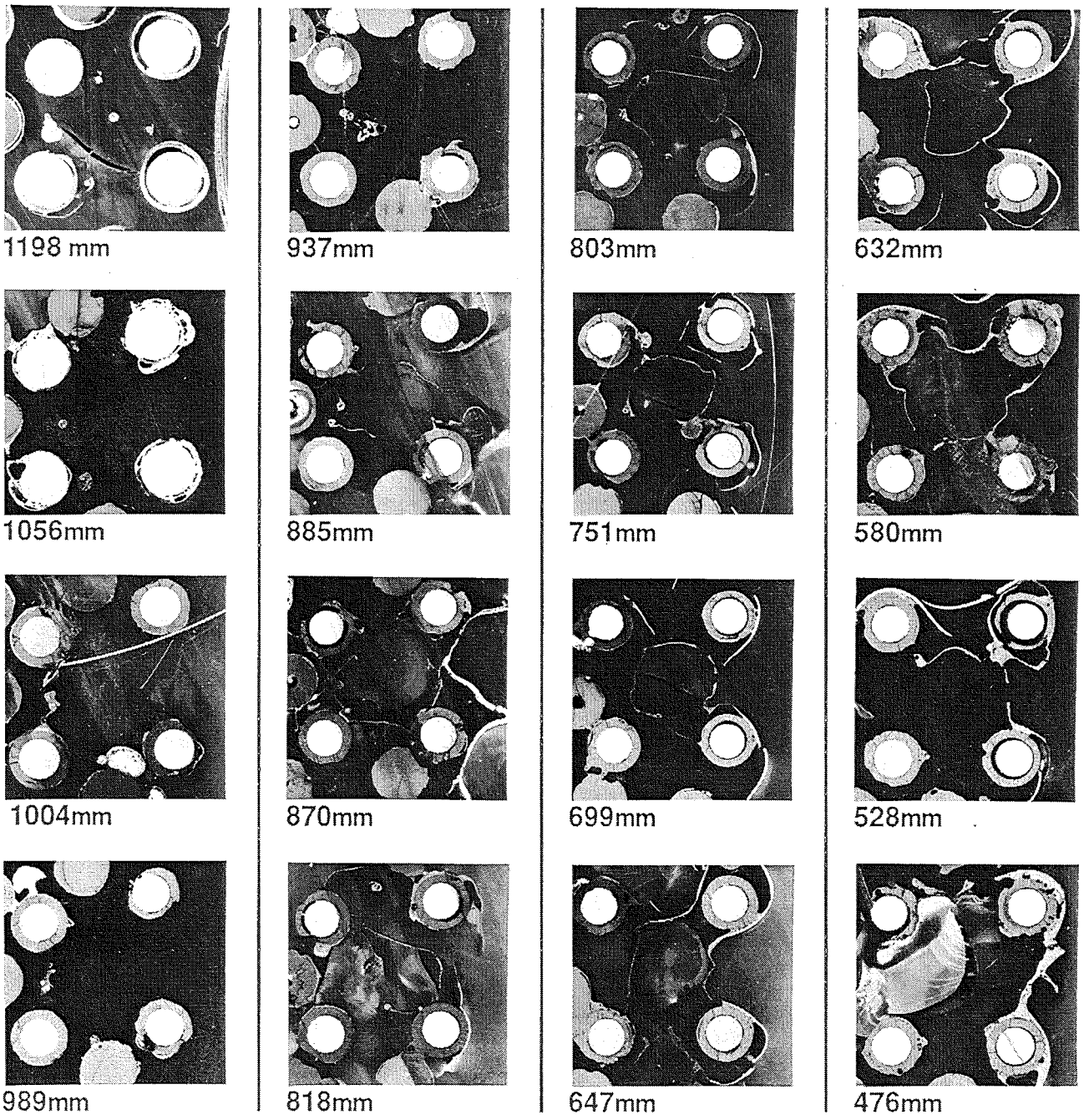

Fig. A39: CORA-10; Horizontal cross section of absorber region of absorber rod 4.6, 1198 to 476 mm elevation

Absorberrod 4.6

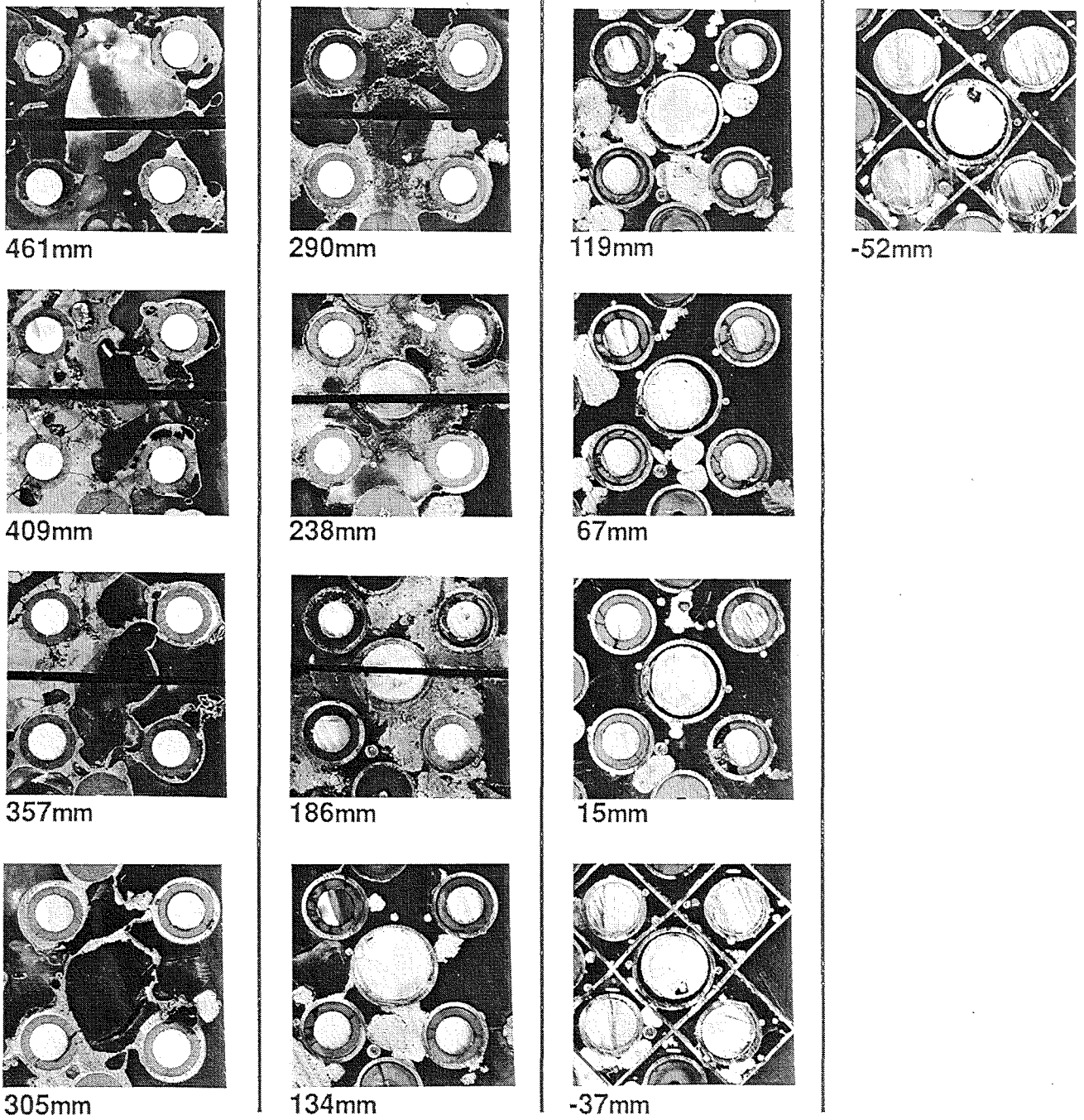

Fig. A40: CORA-10; Horizontal cross section of absorber region of absorber rod 4.6, 461 to -52 mm elevation

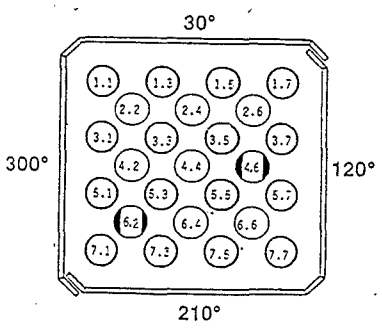

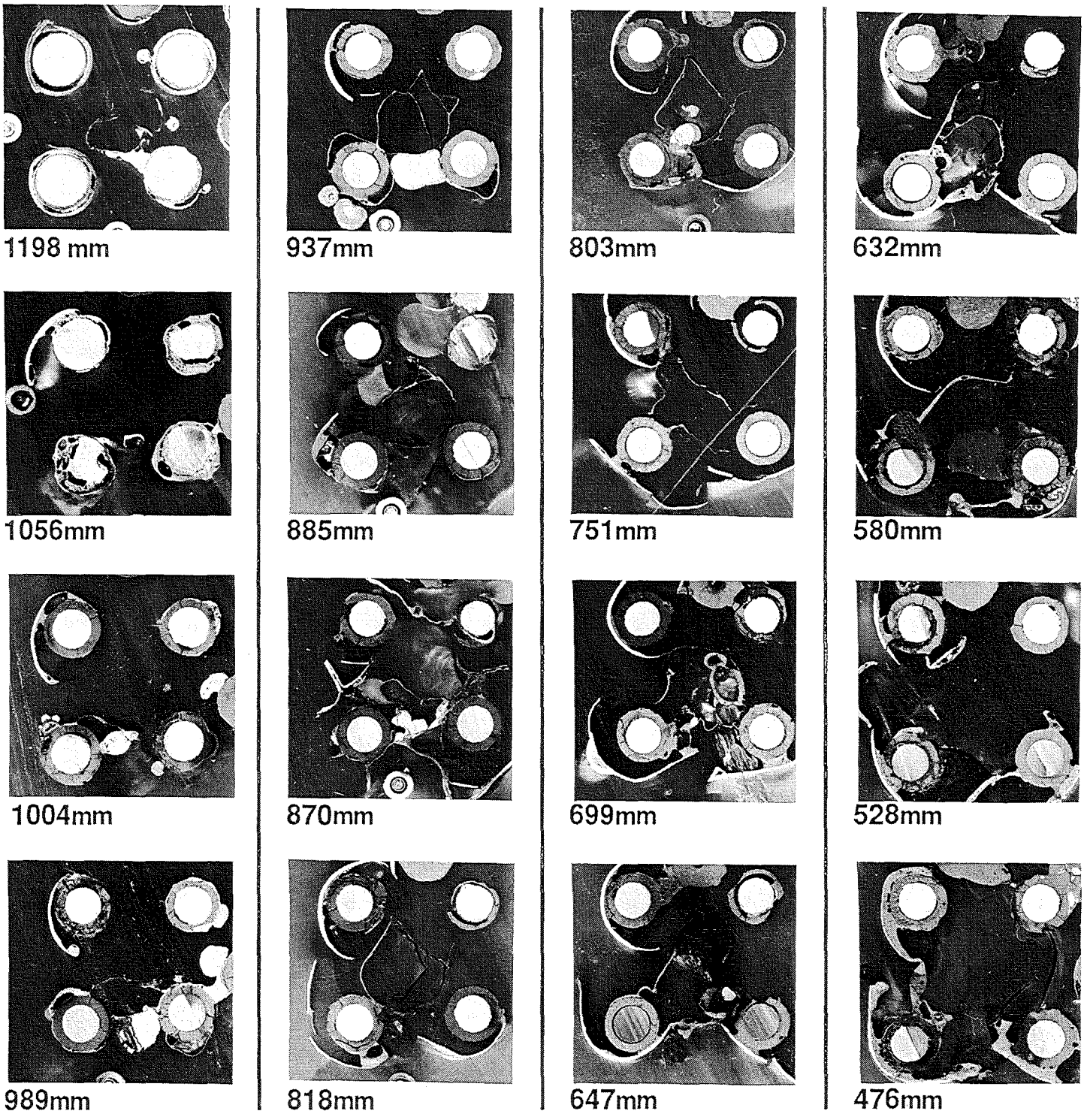

top view

Fig. A41: CORA-10; Horizontal cross sections of region of absorber rod 6.2, 1198 to 476 mm elevation

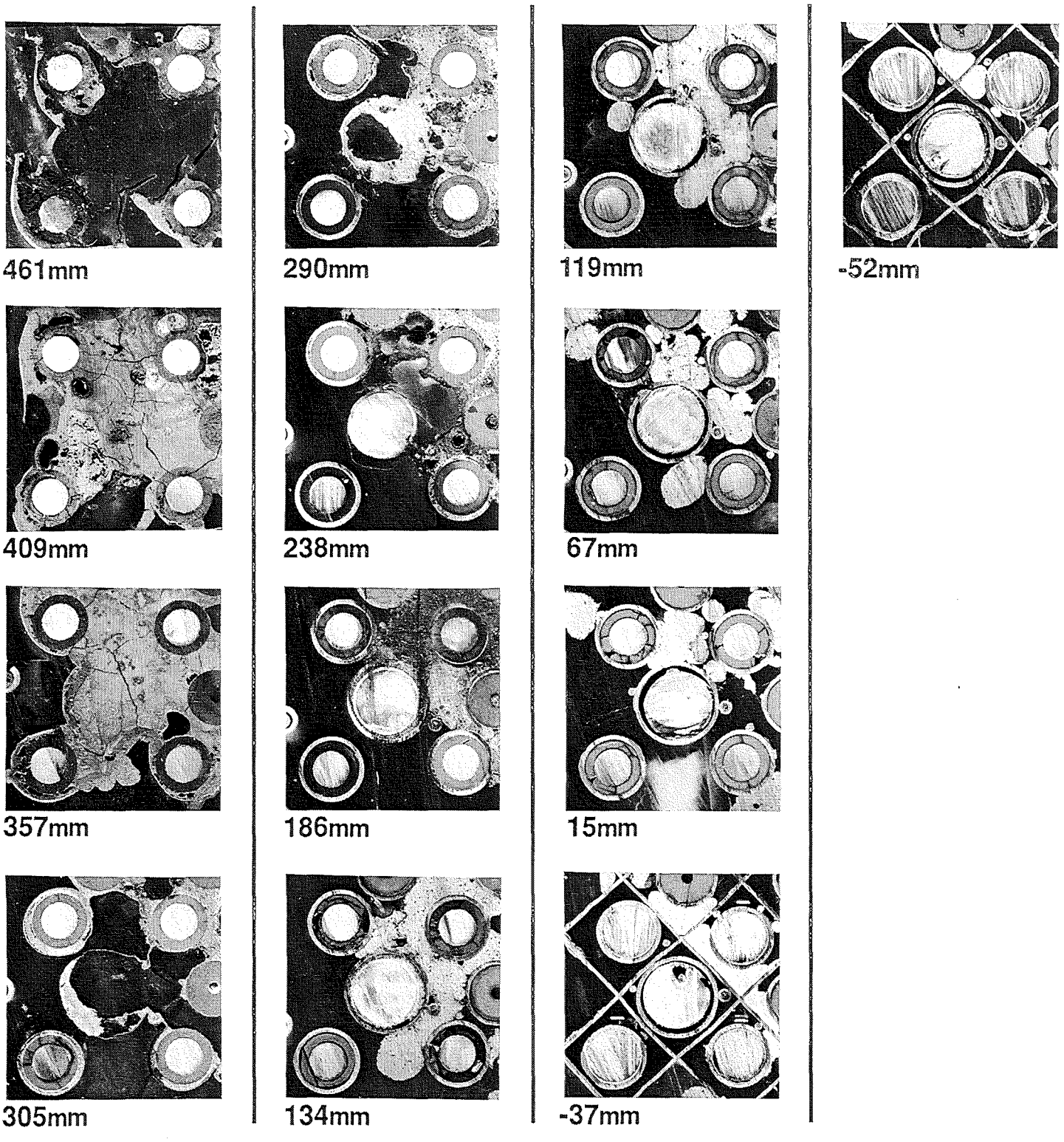

Fig. A42: CORA-10; Horizontal cross sections of region of absorber rod 6.2, 461 to -52 mm elevation